

# First-Principles Investigation of Puzzling Spin-Dependent Transport Phenomena in Molecular and Nanostructured Systems

Dissertation

with the aim of achieving a doctoral degree

at the Faculty of Mathematics, Informatics and Natural Sciences

Department of Chemistry

University of Hamburg

submitted by

Martin Sebastian Zöllner

2019

The present work was carried out in the period from October 2015 to September 2019 in the Institute of Inorganic and Applied Chemistry at the University of Hamburg in the group of Prof. Dr. Carmen Herrmann.

Dissertation accepted on the recommendation of  
Prof. Dr. Carmen Herrmann, examiner  
Prof. Dr. Robin Santra, co-examiner

Date of submission: 04.09.2019

Date of oral defense: 08.11.2019

Approval of dissertation: 12.02.2020

# Contents

<b>I. Abstract</b>	<b>v</b>
<b>II. Zusammenfassung</b>	<b>vii</b>
<b>III. List of Abbreviations</b>	<b>ix</b>
<b>1. Introduction</b>	<b>1</b>
<b>2. Theoretical Background</b>	<b>3</b>
2.1. Non-Relativistic Electronic Structure Theory . . . . .	3
2.1.1. Hartree–Fock Theory . . . . .	3
2.1.2. Density Functional Theory . . . . .	7
2.2. Relativistic Electronic Structure Theory . . . . .	9
2.2.1. Dirac Equation and Dirac–Coulomb–Breit Hamiltonian . . . . .	10
2.2.2. Current Density Functional Theory . . . . .	12
2.2.3. Quasirelativistic Hamiltonians . . . . .	14
2.2.4. Spin–Orbit Coupling as a Relativistic Effect . . . . .	16
2.2.5. Effective Single-Particle Hamiltonian Matrix and Overlap Matrix in Two-Component Electronic Structure Calculations . . . . .	18
2.3. Electron Transport Properties of Nanoscale Structures . . . . .	23
2.3.1. Landauer Approach . . . . .	23
2.3.2. Electron–Phonon Interactions in Electron Transport Calculations	26
<b>3. Large Magnetoresistance in TEMPO-OPE Single-Molecule Junctions</b>	<b>29</b>
3.1. Introduction . . . . .	29
3.2. Theoretical Methods to Investigate Magnetoresistance in Single-Molecule Junctions of TEMPO-OPE . . . . .	31

3.3.	Attempt to Identify Possible Origins of Magnetoresistance in TEMPO-OPE Single-Molecule Junctions . . . . .	34
3.3.1.	Influence of the Radical Part of the TEMPO-OPE Molecule on Electron Transport Properties . . . . .	35
3.3.2.	Possible Interaction between TEMPO Radical and Gold Electrodes	40
3.4.	Effect of Structural Changes on Electron Transport Properties at the example of Organic Radicals Similar to TEMPO-OPE . . . . .	42
3.5.	Conclusion . . . . .	48
<b>4.</b>	<b>Circular Photogalvanic Effect in Lead-(II)-Sulfide Nanosheets</b>	<b>49</b>
4.1.	Introduction . . . . .	49
4.2.	Theoretical Methods to Investigate the Circular Photogalvanic Effect in Lead-(II)-Sulfide Nanosheets . . . . .	58
4.3.	Band Structures and Origin of the Circular Photogalvanic Effect in (001)-Lead-(II)-Sulfide Nanosheets . . . . .	61
4.3.1.	Bulk Lead-(II)-Sulfide and Validation of the Methodology . . . . .	61
4.3.2.	(001)-Lead-(II)-Sulfide Nanosheets and the Effect of Spin–Orbit Coupling and an External Electric Field . . . . .	63
4.3.3.	Formulation of a Selection Mechanism for the Circular Photogalvanic Effect in (001)-Lead-(II)-Sulfide Sheets . . . . .	67
4.4.	Conclusion . . . . .	69
<b>5.</b>	<b>Chiral-Induced Spin Selectivity in Helical Molecules</b>	<b>70</b>
5.1.	Introduction . . . . .	70
5.2.	Theoretical Methods to Investigate Chiral-Induced Spin Selectivity . . . . .	75
5.3.	Derivations and Implementations of a Two-Component Landauer Approach and an effective Dephasing Model . . . . .	76
5.3.1.	Fock and Overlap Matrices from Two-Component DFT Calculations	77
5.3.2.	Two-Component Landauer Approach to include Spin–Orbit Coupling . . . . .	80

5.3.3.	Effective Dephasing Model to include Electron–Phonon Coupling	87
5.4.	Possible Origins of Chiral-Induced Spin Selectivity with First-Principles Methods: Analytical Considerations for the Landauer Approach . . . . .	94
5.4.1.	Conditions for P- and T-Symmetry of the Transmission Function	96
5.4.2.	Connection between Imaginary Parts of the Effective Single-Particle Hamiltonian Matrix and Removal of P-Symmetry of the Transmission Function . . . . .	97
5.4.3.	Indications for a Connection between Structural Symmetry of the Molecule and P-Symmetry of the Transmission Function . . . . .	99
5.5.	Possible Origins of Chiral Induced Spin Selectivity with First-Principles Methods: Insight from Density Functional Theory . . . . .	104
5.5.1.	Details on the Calculations and Structures of Perfect Symmetric Cumulenes . . . . .	105
5.5.2.	Details on the Analyzed Matrices of Perfect Symmetric Cumulenes	106
5.5.3.	Spin Polarization of Transmitted Electrons for Perfect Symmetric Cumulenes . . . . .	110
5.5.4.	Connection between Symmetry of the Cumulenes and Spin Polarization of the Transmitted Electrons: Analysis of Effective Single-Particle Hamiltonian Matrix . . . . .	112
5.5.5.	Connection between Magnitude of the Polarization of Transmitted Electrons and Imaginary Parts of the Effective Single-Particle Hamiltonian Matrix . . . . .	118
5.6.	Chiral-Induced Spin Selectivity from Electron Transport Calculations for Experimentally Relevant Systems . . . . .	125
5.6.1.	Oligopeptide and Helicene Molecules as Realistic Systems . . . . .	126
5.6.2.	Electron Transport Properties of Oligopeptides . . . . .	129
5.6.3.	Electron Transport Properties of the Helicene Molecule . . . . .	132
5.7.	Conclusion . . . . .	136

<b>6. Conclusion and Perspectives</b>	<b>139</b>
6.1. Summary . . . . .	139
6.2. Outlook . . . . .	141
<b>7. Acknowledgment</b>	<b>144</b>
<b>Appendix</b>	<b>146</b>
<b>A. Computational Methodology</b>	<b>146</b>
<b>B. Additional Data</b>	<b>151</b>
<b>C. Additional Derivations</b>	<b>158</b>
<b>D. List of Publications</b>	<b>162</b>
D.1. Published . . . . .	162
D.2. In Preparation . . . . .	162
<b>E. List of Chemicals</b>	<b>163</b>
<b>Bibliography</b>	<b>163</b>

# I. Abstract

The possibility to manipulate the electrical conductance of a system by addressing the electron's spin is a central feature in the scientific field of spintronics and is essential for the development of new computational devices. Besides the experimental exploration of new materials to improve existing or to develop new spintronic technologies, the fundamental understanding of the mechanisms leading to spin-dependent conductance is important. Such an understanding can allow to predict new materials for the field of spintronics.

In this work, the results of the attempt to gain insight into three puzzling experimental observations concerning electron transport in molecular and nanostructured systems are presented, based on density functional theory. These phenomena are the surprisingly large magnetoresistance in a molecular junction of an organic radical based on the oligo(*p*-phenyleneethynylene) (OPE) molecule, the circular photogalvanic effect (CPGE) in lead-(II)-sulfide (PbS) nanosheets, and the chiral-induced spin selectivity (CISS) effect observed for helical molecules. This work is able to give an explanation for the CPGE in PbS nanosheets. It is not be able to give a final explanation for the other effects, but provides theoretical results which can provide insight and which are helpful in further investigations.

Magnetoresistance describes the dependence of the conductance of a systems on a magnetic field. Regarding the OPE-based radical, electron transport calculations show that its singly-occupied molecular orbital does not participate in the electron transport. While this finding excludes mechanisms based on a direct interaction, no alternative mechanism can be confirmed based on the results of this work. Nevertheless, interactions of the singly-occupied orbitals of the radicals covering the electrode with the electrode are suggested to be a relevant factor for an interface-dominated mechanism, which could give further insight into the observed magnetoresistance in future studies.

The CPGE describes a current induced by illuminating a material with circularly polarized light. Band structure calculations identify the Rashba effect to be responsible for the CPGE in PbS nanosheets, although this effect is not expected for such a highly symmetric system. However, the calculations show that electric fields due to the applied gate voltage and the asymmetric interface are able to break space inversion symmetry, thus inducing a Rashba effect.

The CISS effect manifests itself in a surprisingly large spin filter property of helical all-organic molecules, based on spin-orbit coupling. As a fundamental understanding of the surprising magnitude of the effect does not exist, this work presents some attempts to provide one based on first-principles methods. The Landauer approach, a common method to calculate electron transport properties, is analyzed regarding its ability to describe the CISS effect. The symmetry of the first-principles effective single-particle Hamiltonian matrix and its imaginary elements are identified as being connected to the occurrence of the effect within the Landauer approach. The results are supported by calculations for perfect helical and perfect linear systems. Although the ability of the Landauer approach to describe the CISS effect is shown in principle, it fails to describe the correct order of magnitude. The results indicate that the effect of the asymmetry is covered by standard density functional theory based Landauer transport calculations, but the enhancement of the effect for helical systems is not. The identification of imaginary parts as the central quantity for chiral-induced spin selectivity can serve as a basis for further improvements of first-principles methodologies, providing further insight into chiral-induced spin selectivity and related effects in spin polarized nanoscopic structures.

## II. Zusammenfassung

Die Möglichkeit, die elektrische Leitfähigkeit eines Systems über den Spin des Elektrons zu beeinflussen, ist von zentraler Bedeutung im Bereich der Spintronik und ist essenziell für die Weiterentwicklung der Informationstechnologie. Neben der experimentellen Suche nach neuen Materialien zur Verbesserung vorhandener oder Entwicklung neuer Bauteile in der Spintronik ist das fundamentale Verständnis der Mechanismen, welche zur spinabhängigen Leitfähigkeit führen, ausschlaggebend, da es die Vorhersage von neuen Spintronikmaterialien ermöglicht.

In dieser Arbeit werden die Ergebnisse einer Untersuchung präsentiert, in welcher drei Phänomene mit unklarem Ursprung im Bereich des Elektronentransportes in molekularen und nanostrukturierten Systemen mittels Dichtefunktionaltheorie erklärt werden sollen. Diese Effekte sind der große Magnetwiderstand in einer *molecular junction* eines oligo(*p*-phenyleneethynylene) (OPE)-basierten organischen Radikals, der zirkularphtogalvanische Effekt (CPGE) in Bleisulfid (PbS)-Nanoblättern und der *chiral-induced spin selectivity* (CISS) Effekt in helikalen Molekülen. Während der CPGE in PbS-Nanoblättern in dieser Arbeit aufgeklärt werden kann, bleibt eine detaillierte theoretische Erklärung für die beiden anderen Effekte aus. Jedoch bieten die Ergebnisse dieser Arbeit eine hilfreiche Basis für weitere Untersuchungen.

Der Begriff „Magnetwiderstand“ beschreibt die Abhängigkeit des Leitwertes eines Systems von einem externen Magnetfeld. In Bezug auf das OPE-basierte Radikal zeigen Elektronentransportberechnungen, dass das einfach besetzte Orbital des Radikals nicht am Transport beteiligt ist. Während diese Erkenntnis einen auf einer direkten Wechselwirkung basierenden Mechanismus ausschließt, kann kein alternativer Mechanismus aufgrund der Ergebnisse dieser Arbeit bestätigt werden. Jedoch gibt es Anhaltspunkte für einen grenzflächendominierten Mechanismus, induziert durch Wechselwirkungen zwischen den Elektroden und den einfach besetzten Orbitalen von den auf der Elektrode adsorbierten Radikalen. Diese geben möglicherweise in weiteren Studien Einsicht in den

Magnetwiderstand.

Der CPGE bezeichnet einen durch Belichtung mit zirkular polarisiertem Licht induzierten Strom. Bandstrukturberechnungen zeigen, dass der Rashba-Effekt für den CPGE in PbS-Nanoblättern verantwortlich ist. Dies ist verwunderlich, da dieser Effekt für solch symmetrische Systeme untypisch ist. Die Berechnungen zeigen jedoch, dass ein elektrisches Feld, welches durch die Gate-Spannung und die nicht-symmetrischen Grenzflächen verursacht wird, die Inversionssymmetrie bricht und dadurch einen Rashba-Effekt induziert.

Der CISS-Effekt zeigt sich als überraschend große Spinfilterfähigkeit von organischen helikalen Molekülen, welche durch Spin–Bahn Kopplung hervorgerufen wird. Diese Arbeit zielt auf ein (noch fehlendes) Verständnis der Größenordnung des Effektes ab, basierend auf *first-principles*-Methoden. Eine häufig genutzte Technik zur Berechnung von Elektronentransporteigenschaften ist der Landauer-Ansatz, welcher in Bezug auf seine Fähigkeit zur grundlegenden Beschreibung des CISS-Effektes untersucht wird. Die Symmetrie der *first-principles*-basierten Matrix des effektiven Einteilchen-Hamiltonoperators und ihre imaginären Elemente können mit dem grundsätzlichen Vorhandensein des Effektes im Landauer-Ansatz in Verbindung gebracht werden. Dies wird durch Berechnungen von perfekten helikalen und perfekten linearen Systemen bestätigt. Trotz der Fähigkeit des Landauer-Ansatzes, den CISS-Effekt prinzipiell zu beschreiben, kann diese Methode die richtige Größenordnung des Effektes nicht wiedergeben. Dies weist darauf hin, dass zwar der Effekt der Asymmetrie durch den Landauer-Ansatz in Kombination mit Dichtefunktionaltheorie beschrieben wird, jedoch nicht die Verstärkung der Spin–Bahn Kopplung in helikalen Systemen. Die Identifikation der imaginären Elemente als zentrale Größe für CISS kann als Basis für weitere Verbesserungen von *first-principles*-Methodologien genutzt werden und zusätzliche Einsichten in den CISS-Effekt sowie verwandte Effekte in spinpolarisierten nanoskopischen Strukturen gewähren.

### III. List of Abbreviations

<b>cDFT</b>	current density functional theory
<b>CISS</b>	chiral-induced spin selectivity
<b>CPGE</b>	circular photogalvanic effect
<b>DFT</b>	density functional theory
<b>DNA</b>	deoxyribonucleic acid
<b>GGA</b>	generalized-gradient approximation
<b>GTO</b>	Gaussian-type orbital
<b>HF</b>	Hartree–Fock
<b>HOMO</b>	highest occupied molecular orbital
<b>IETS</b>	inelastic electron tunneling spectroscopy
<b>KS-DFT</b>	Kohn–Sham density functional theory
<b>LDA</b>	local-density approximation
<b>LUMO</b>	lowest unoccupied molecular orbital
<b>MRAM</b>	magnetic random access memory
<b>NEGF</b>	non-equilibrium Green’s function
<b>OPE</b>	oligo( <i>p</i> -phenyleneethynylene)
<b>PAW</b>	projector-augmented wave
<b>pDOS</b>	projected density of states
<b>QI</b>	quantum interference
<b>SCF</b>	self-consistent field
<b>SFO</b>	symmetrized fragment orbital
<b>SOC</b>	spin–orbit coupling
<b>SOMO</b>	singly occupied molecular orbital
<b>STO</b>	Slater-type orbital
<b>TEMPO</b>	2,2,6,6-tetramethylpiperidine-1-oxyl
<b>WBL</b>	wide band limit
<b>X2C</b>	exact two-component
<b>ZORA</b>	zeroth-order regular approximation

# 1. Introduction

To match the increasing demand of data-storage efficiency [1], computational power [2], and computational energy efficiency [3], the scientific field of spintronics offers promising alternatives to charge-only based transistors and data-storage devices [4].

Spintronics deals with the spin of the electron as a carrier of information [5]. A central phenomenon in this field is magnetoresistance, which describes the manipulation of the resistance with external magnetic fields [6]. Especially giant magnetoresistance [7, 8] and tunneling magnetoresistance [9–11] are of great importance for commonly used read heads in hard disc drives [12], where digital information is magnetically stored.

A problem of hard disc drives is the slow data writing/accessing process compared to electrical devices, which motivates the development of magnetoresistive random access memory, combining the persistent (non-volatile) data storage of hard disc drives with the fast data accessing and writing of random access memory [13].

Spintronics also offers the possibility of improving current transistors. Miniaturization has led to an increasing number of transistors per computer chip and to a speed-up of data processing [2]. However, this process faces a bottleneck in dissipating the produced heat, which has prevented a significant improvement of clock times despite the increasing number of transistors per chip so far [2]. In conventional transistors, ON and OFF are defined by differently charged states, and switching between these two states requires charges to move, which produces heat [14]. If ON and OFF were defined by spin states instead, a switching without moving charges would be possible, leading to much less heat production [5]. The possibility to build pure spin-based logic devices for instance was shown by Wiesendanger *et al.* [15].

Creating the magnetic fields for writing magnetically coded information/switching between spin-encoded ON and OFF states can be problematic for very small devices [12] and requires high currents, which are energy-consuming and again produce heat [14]. Alternative mechanisms are mandatory to improve spintronic computational devices. A manipulation of the spin degree of freedom with electric fields as in Rashba systems (spin transistor) [14] or with spin-polarized currents as for the spin-transfer torque [12, 13] are

promising alternatives.

Thus, both the exploration and the theoretical understanding of materials and mechanisms which allow for the creation of spin-polarized currents (spin filters), electrical manipulation of the spin, or magnetoresistance are very important in the field of spintronics. This work deals with the investigation of three puzzling spin-dependent transport phenomena, including spin-dependent properties due to unpaired electrons or due to spin-orbit coupling (SOC) in systems without unpaired electrons. These experimentally observed phenomena are namely the magnetoresistance for a molecular junction of 2,2,6,6-tetramethylpiperidine-1-oxyl functionalized oligo(*p*-phenyleneethynylene)<sup>1</sup>, the circular photogalvanic effect (CPGE) in (001)-lead-(II)-sulfide nanosheets<sup>2</sup>, and the chiral-induced spin selectivity (CISS) effect in helical molecular systems [4]. For all of these phenomena, the physical mechanism responsible for the experimentally observed behavior is currently unclear.

Although simple methods like tight-binding models can give insight into underlying mechanisms of electron-transport phenomena [18], the usage of model systems or the need of empirical or calculated parameters for tight-binding Hamiltonians limits its predictive capabilities. Thus, this work aims to describe the mentioned systems using first-principles methods, *i.e.*, methods which are only based on natural constants rather than system-specific input parameters [19], to provide fundamental insight into the origins of the phenomena under study.

---

<sup>1</sup> This is based on experiments done by Scheer *et al.* and is documented in a joint publication [16].

<sup>2</sup> This is based on experiments done by Klinke *et al.* and is documented in a joint publication [17].

## 2. Theoretical Background

The focus of this work lies on the description of spin and SOC effects on electron transport in molecular and solid-state systems. To understand the research and implementations done in this work, a short overview of the theoretical background is given in this part.

First, a short introduction to non-relativistic [20] and relativistic [21, 22] wave-function electronic-structure theory, as well as to density functional theory (DFT) [23] and current density functional theory (cDFT) (the relativistic counterpart of DFT) [21, 22] is given. Since DFT is the method of choice in this work, further explanations on the applied approximations to DFT and cDFT are given. Afterwards, SOC is introduced, focusing on its origin in the Dirac equation [21, 22] and on its effect on central quantities in these electronic-structure methods.

Finally, two methods to calculate the conductance of molecular junctions based on DFT are described: the so-called non-equilibrium Green's function approach and its "non-interacting" limit with leads in equilibrium, the Landauer approach [24].

### 2.1. Non-Relativistic Electronic Structure Theory

The equation of motion of quantum mechanics, the Schrödinger equation, neglects special relativity. This is a good approximation for many properties of systems consisting of light atoms, roughly up to the  $3d$  transition metals [21]. An often used approach to solve the Schrödinger equation is the Hartree–Fock (HF)-Theory. Throughout Section 2.1, atomic units are used (reduced Planck constant  $\hbar = 1$ , mass of the electron  $m_e = 1$ , elementary charge  $e = 1$ , dielectric constant of the vacuum  $4\pi\epsilon_0 = 1$ ) [20].

#### 2.1.1. Hartree–Fock Theory

In a non-relativistic description of electrons, an electronic system can be described with the time independent Schrödinger equation [20],

$$\hat{H}\Psi = E\Psi, \tag{2.1}$$

where  $\hat{H}$  is the non-relativistic Hamiltonian (operator of energy),

$$\hat{H} = \hat{T}_e + \hat{T}_N + \hat{V}_{ee} + \hat{V}_{NN} + \hat{V}_{eN}, \quad (2.2)$$

which includes the operators of the electronic kinetic energy  $\hat{T}_e$ , the nuclear kinetic energy  $\hat{T}_N$ , the electron–electron interaction  $\hat{V}_{ee}$ , the nucleus–nucleus interaction  $\hat{V}_{NN}$ , and the electron–nucleus interaction  $\hat{V}_{eN}$ . The system is completely defined by a wave function  $\Psi$ , which is an eigenfunction of  $\hat{H}$ .  $\Psi$  depends on the electronic spatial coordinates  $\mathbf{r}$  as well as on the nuclear spatial coordinates  $\mathbf{R}$ .

In practice, the Born–Oppenheimer approximation [20] is commonly used, assuming  $\hat{T}_N$  to be zero, since the motions of the heavy nuclei are much slower than the motions of the light electrons, *i.e.*, the electrons react instantaneously to the movement of the nuclei. As a consequence,  $\Psi$  can be separated into an electronic wave function  $\Psi_e(\mathbf{r}, \{\mathbf{R}\})$  and a nuclear wave function  $\Psi_N(\mathbf{R})$ ,

$$\Psi = \Psi_e(\mathbf{r}, \{\mathbf{R}\}) \cdot \Psi_N(\mathbf{R}), \quad (2.3)$$

where the electronic wave function depends explicitly on the electronic degrees of freedom and only parametrically on the degrees of freedom of the nuclei. The resulting electronic Hamiltonian,

$$\hat{H}_e = \hat{T}_e + \hat{V}_{ee} + \hat{V}_{eN} + \hat{V}_{NN} \quad (2.4)$$

can then be used to solve the electronic Schrödinger equation,

$$\hat{H}_e \Psi_e(\mathbf{r}, \{\mathbf{R}\}) = E_e \Psi_e(\mathbf{r}, \{\mathbf{R}\}). \quad (2.5)$$

$\hat{H}_e$  can then be written in detail as (neglecting  $V_{NN}$ , which is an additive constant for a fixed set of nuclei) [20]

$$\hat{H}_e = -\frac{1}{2} \sum_i^N \nabla_i^2 - \sum_{i=1}^N \sum_{I=1}^M \frac{Z_I}{|\mathbf{r}_i - \mathbf{R}_I|} + \sum_i^N \sum_{j>i}^N \frac{1}{|\mathbf{r}_i - \mathbf{r}_j|}, \quad (2.6)$$

where  $\nabla_i$  is the nabla operator acting on electron  $i$ ,  $Z_I$  is the charge number of nucleus  $I$ ,  $\mathbf{r}_i$  is the position of electron  $i$ , and  $\mathbf{R}_I$  is the position of nucleus  $I$ .

A possible way to describe the wave function of an electronic system with  $N$  electrons is a Slater determinant [20],

$$\Phi^{SD} = \frac{1}{\sqrt{N!}} \begin{vmatrix} \chi_1(\mathbf{x}_1) & \chi_2(\mathbf{x}_1) & \cdots & \chi_N(\mathbf{x}_1) \\ \chi_1(\mathbf{x}_2) & \chi_2(\mathbf{x}_2) & \cdots & \chi_N(\mathbf{x}_2) \\ \vdots & \vdots & \cdots & \vdots \\ \chi_1(\mathbf{x}_N) & \chi_2(\mathbf{x}_N) & \cdots & \chi_N(\mathbf{x}_N) \end{vmatrix}, \quad (2.7)$$

which fulfills the Pauli principle.  $\Phi^{SD}$  is built using single-electron functions  $\chi_a(\mathbf{x}_i)$  (spin orbitals), where  $a$  is an index describing the orbital and  $\mathbf{x}_i$  contains the spatial coordinates  $\mathbf{r}_i$  and spin coordinate  $s_i$  of electron  $i$ . Spin orbitals are built as a product of a spatial orbital  $\psi_i(\mathbf{r}_j)$  and a spin function  $\sigma_i(s_j)$ ,

$$\chi_i(\mathbf{x}_j) = \psi_i(\mathbf{r}_j) \cdot \sigma_i(s_j). \quad (2.8)$$

$\sigma_i$  is either  $\alpha$  for a positive or  $\beta$  for a negative spin along the quantization direction.

Using the Born–Oppenheimer Hamiltonian,  $\Phi_{SD}$ , the variational principle<sup>3</sup>, and assuming a closed-shell system (no unpaired electrons), one arrives at the closed-shell spatial HF equation [20],

$$\hat{f}(\mathbf{r}_1)\psi_j(\mathbf{r}_1) = \epsilon_j\psi_j(\mathbf{r}_1), \quad (2.9)$$

where  $\epsilon_j$  is the energy of orbital  $\psi_j$ , and  $\hat{f}(\mathbf{r}_1)$  is an effective single-particle Hamiltonian, called Fock operator,

$$\hat{f}(\mathbf{r}_1) = \hat{h}(\mathbf{r}_1) + \sum_{i=1}^{N/2} [2\hat{J}_i(\mathbf{r}_1) - \hat{K}_i(\mathbf{r}_1)]. \quad (2.10)$$

Here,  $\hat{h}(\mathbf{r}_1)$  is the one-electron operator,

$$\hat{h}(\mathbf{r}_1) = -\frac{1}{2}\nabla_1^2 - \sum_{I=1}^M \frac{Z_I}{|\mathbf{r}_1 - \mathbf{R}_I|}, \quad (2.11)$$

---

<sup>3</sup> The variational principle states that the energy corresponding to the ground state wave function of a system is smaller than that of any other wave function used to describe the system [20]. Within an approximate ansatz for the wave function  $\Psi_{\text{approx}}$ , the best approximation to the ground state is found by minimizing  $\langle \Psi_{\text{approx}} | \hat{H} | \Psi_{\text{approx}} \rangle$ .

$\hat{J}_i$  is the Coulomb operator,

$$\hat{J}_i(\mathbf{r}_1)\psi_j(\mathbf{r}_1) = \left[ \int d\mathbf{r}_2 \psi_i^*(\mathbf{r}_2) \frac{1}{|\mathbf{r}_1 - \mathbf{r}_2|} \psi_i(\mathbf{r}_2) \right] \psi_j(\mathbf{r}_1), \quad (2.12)$$

and  $\hat{K}_i$  is the exchange operator,

$$\hat{K}_i(\mathbf{r}_1)\psi_j(\mathbf{r}_1) = \left[ \int d\mathbf{r}_2 \psi_i^*(\mathbf{r}_2) \frac{1}{|\mathbf{r}_1 - \mathbf{r}_2|} \psi_j(\mathbf{r}_2) \right] \psi_i(\mathbf{r}_1). \quad (2.13)$$

Since the Fock operator depends on the orbitals, these equations have to be solved iteratively by a self-consistent field (SCF) algorithm. In practice, spatial parts of the orbitals  $\psi_j(\mathbf{r})$  are often expanded in a linear combination of atomic orbitals [20]

$$\psi_j(\mathbf{r}) = \sum_{\mu} c_{\mu j} \phi_{\mu}(\mathbf{r}) \quad (2.14)$$

where  $c_{\mu j}$  is a weighting or molecular-orbital coefficient and  $\phi_{\mu}(\mathbf{r})$  is a so called atom-centered basis function. There are several choices of  $\phi_j(\mathbf{r})$ , in particular the Slater-type orbital (STO) and the Gaussian-type orbital (GTO). Applying the atom-centered expansion in Equation (2.14), one arrives at the Roothaan–Hall equations [20],

$$\mathbf{FC} = \mathbf{SC}\epsilon. \quad (2.15)$$

where  $\mathbf{F}$  is the Fock matrix,  $\mathbf{S}$  is the overlap matrix, and  $\epsilon$  is a diagonal matrix with elements

$$\epsilon_{ij} = \delta_{ij}\epsilon_i. \quad (2.16)$$

Matrix elements of  $\mathbf{F}$  and  $\mathbf{S}$  are then defined as

$$S_{\mu\nu} = \int d\mathbf{r}_1 \phi_{\mu}^*(\mathbf{r}_1) \phi_{\nu}(\mathbf{r}_1) \quad (2.17)$$

$$\begin{aligned} F_{\mu\nu} &= \int d\mathbf{r}_1 \phi_{\mu}^*(\mathbf{r}_1) \hat{f}(\mathbf{r}_1) \phi_{\nu}(\mathbf{r}_1) = \int d\mathbf{r}_1 \phi_{\mu}^*(\mathbf{r}_1) \hat{h}_1(\mathbf{r}_1) \phi_{\nu}(\mathbf{r}_1) \\ &+ \sum_{\lambda\sigma}^{N/2} \mathbf{P}_{\lambda\sigma} \left[ \int \int d\mathbf{r}_1 d\mathbf{r}_2 \frac{\phi_{\mu}^*(\mathbf{r}_1) \phi_{\nu}^*(\mathbf{r}_1) \phi_{\sigma}(\mathbf{r}_2) \phi_{\lambda}(\mathbf{r}_2)}{|\mathbf{r}_1 - \mathbf{r}_2|} \right. \\ &\left. - \frac{1}{2} \int \int d\mathbf{r}_1 d\mathbf{r}_2 \frac{\phi_{\mu}^*(\mathbf{r}_1) \phi_{\lambda}^*(\mathbf{r}_1) \phi_{\sigma}(\mathbf{r}_2) \phi_{\nu}(\mathbf{r}_2)}{|\mathbf{r}_1 - \mathbf{r}_2|} \right]. \end{aligned} \quad (2.18)$$

They are important quantities in practice for the calculation of properties of molecular systems. In Equation (2.18),  $\mathbf{P}$  is the density matrix whose elements are calculated as

$$\mathbf{P}_{\lambda\sigma} = 2 \sum_i^{N/2} c_{\lambda i} c_{\sigma i}^*. \quad (2.19)$$

Although HF theory provides a solution to the Schrödinger equation, it only describes the electronic system with a set of effective single-particle equations, and the many-body interaction of the electrons is reduced to a mean-field description [20]. The missing electron–electron interactions in HF theory are called electron correlation. A possible tool to address this correlation is DFT [23], which is discussed in detail in the following section.

### 2.1.2. Density Functional Theory

The most frequently employed method to calculate the electronic properties of molecular systems is DFT [25]. DFT is an approach which, in contrast to methods based on the Schrödinger equation, describes properties of an electronic system solely by using the electron density  $\rho(\mathbf{r})$  [23].

The foundation of the applicability of DFT was given by Hohenberg and Kohn by introducing the Hohenberg–Kohn theorems [23]. The first Hohenberg–Kohn theorem describes the connection between the electronic ground-state wave function  $\Psi_0$  and the electron density of the ground state  $\rho_0(\mathbf{r})$ :  $\rho_0(\mathbf{r})$  defines the external potential resulting from the nuclei except for an additive constant, which means that the Hamiltonian is completely defined through  $\rho_0(\mathbf{r})$  and, therefore,  $\rho_0(\mathbf{r})$  also defines  $\Psi_0$ .

The possibility to find  $\rho_0(\mathbf{r})$  is derived via the second Hohenberg–Kohn theorem, which states that  $\rho_0(\mathbf{r})$  is the electron density  $\rho(\mathbf{r})$  with the lowest energy,

$$E[\rho(\mathbf{r})] \geq E[\rho_0(\mathbf{r})]. \quad (2.20)$$

This allows the calculation of  $\rho_0(\mathbf{r})$  using the variational principle.

Although Hohenberg and Kohn showed that it is possible to find  $\rho_0(\mathbf{r})$  and to use it to calculate electronic properties in principle, it is very difficult in practice to calcu-

late the energy with  $\rho(\mathbf{r})$  only, in particular for systems with inhomogeneous electron densities such as molecules. This was solved by Kohn–Sham density functional theory (KS-DFT) [23]. Kohn and Sham proposed to describe a system of electrons, *i.e.*, interacting fermions, based on a reference system of non-interacting fermions, assuming that their  $\rho_0(\mathbf{r})$  is the same as for the interacting system. The wave function of the non-interacting system is exactly described by a single Slater determinant, which is again built using single electron functions, also called Kohn–Sham orbitals. Consequently, the energy can be calculated as (neglecting the nucleus–nucleus interactions)

$$E[\rho(\mathbf{r})] = T[\rho(\mathbf{r})] + J[\rho(\mathbf{r})] + E_{Ne}[\rho(\mathbf{r})] + E_{XC}[\rho(\mathbf{r})], \quad (2.21)$$

where  $J[\rho(\mathbf{r})]$  is the classical electron–electron Coulomb interaction,

$$J[\rho(\mathbf{r})] = \frac{1}{2} \int \frac{\rho(\mathbf{r})\rho(\mathbf{r}')}{|\mathbf{r} - \mathbf{r}'|} d\mathbf{r}d\mathbf{r}', \quad (2.22)$$

$E_{Ne}[\rho(\mathbf{r})]$  is the classical electron–nucleus interaction,

$$E_{Ne}[\rho(\mathbf{r})] = - \sum_{I=1}^M Z_I \int d\mathbf{r} \frac{\rho(\mathbf{r})}{|\mathbf{R}_I - \mathbf{r}|}, \quad (2.23)$$

$T[\rho(\mathbf{r})]$  is the kinetic energy of the non-interacting fermions, which is calculated using the spatial part  $\psi_i^{\text{KS}}(\mathbf{r})$  of the Kohn–Sham orbitals,

$$T[\rho(\mathbf{r})] = - \sum_{i=1}^N \langle \psi_i^{\text{KS}}(\mathbf{r}) | \frac{1}{2} \nabla^2 | \psi_i^{\text{KS}}(\mathbf{r}) \rangle, \quad (2.24)$$

and  $E_{XC}[\rho(\mathbf{r})]$  is the exchange–correlation functional.  $E_{XC}[\rho(\mathbf{r})]$  contains the deviation of the non-interacting fermion’s  $T[\rho(\mathbf{r})]$  from  $T[\rho(\mathbf{r})]$  of the interacting fermions as well as the non-classical electron–electron interactions of the interacting system, *i.e.*, the exchange–correlation energy. The density of the system with  $N$  fermions can be calculated as

$$\rho(\mathbf{r}) = \sum_{i=1}^N |\psi_i^{\text{KS}}(\mathbf{r})|^2. \quad (2.25)$$

In analogy to HF theory, a set of effective single-particle equations, the so-called Kohn–Sham equations, are obtained as

$$\hat{h}^{\text{KS}}(\mathbf{r})\psi_i^{\text{KS}}(\mathbf{r}) = \epsilon_i\psi_i^{\text{KS}}(\mathbf{r}), \quad (2.26)$$

where again an effective single-particle Hamiltonian  $\hat{h}^{\text{KS}}$ , the Kohn–Sham Hamiltonian,

$$\hat{h}^{\text{KS}}(\mathbf{r}) = -\frac{1}{2}\nabla^2 + v_{\text{eff}}(\mathbf{r}), \quad (2.27)$$

is obtained. It contains the kinetic energy (first term) as well as the effective potential  $v_{\text{eff}}$ , which is defined as

$$v_{\text{eff}} = v_{\text{ext}}(\mathbf{r}) + \int \frac{\rho(\mathbf{r}')}{|\mathbf{r} - \mathbf{r}'|} d\mathbf{r}' + \frac{\delta E_{\text{XC}}[\rho]}{\delta \rho(\mathbf{r})}, \quad (2.28)$$

describing the external potential  $v_{\text{ext}}(\mathbf{r})$  of the nuclei, the electron–electron interaction and the exchange–correlation potential. These equations again have to be solved self-consistently, and the  $\psi^{\text{KS}}(\mathbf{r})$  are expanded using atom-centered basis functions.

Since the exact  $E_{\text{XC}}$  is unknown, its contribution to the total energy is approximated [23]. Although a lot of such approximations exist, the common exchange–correlation functionals can be categorized into the following species [23]: within the local-density approximation (LDA), the energy is calculated as for a system with a homogeneous electron density. The so-called generalized-gradient approximation (GGA) uses the first derivative of the electron density additionally, and the meta-GGA also the second derivative. Such functionals are called pure functionals, since they are completely based on KS-DFT. In contrast, hybrid functionals combine KS-DFT with wave-function based methods, calculating a fraction of the exchange energy using HF theory.

## 2.2. Relativistic Electronic Structure Theory

A drawback of wave function theory and standard DFT is that the electron’s spin-degree of freedom has to be postulated rather than resulting naturally from the fundamental equations, and their inconsistency with Einstein’s principle of special relativity [21]. This is in particular relevant for systems containing heavy atoms [26] and for certain properties of systems consisting of light atoms, such as nuclear magnetic resonance properties [27]. In this section, an overview of the foundations of relativistic electronic-structure theory is given. While atomic units were used in Section 2.1,  $\hbar$ ,  $e$ , and  $m_e$  are written explicitly in the following, while  $4\pi\epsilon_0 = 1$  remains. Such units are commonly used in relativistic literature [21, 22].

### 2.2.1. Dirac Equation and Dirac–Coulomb–Breit Hamiltonian

According to the principle of special relativity derived by Einstein, equations describing physical properties must be invariant under a Lorentz transformation and must obey the principle of equivalence of time and space variables: the non-relativistic Schrödinger equation violates both [21]. An equation describing the motion of a single electron in an electromagnetic potential consistent with Einstein’s principle of special relativity was derived by Dirac, which is known as the Dirac equation (here given in its time-independent form) [21],

$$\left[ c\boldsymbol{\alpha} \cdot (\mathbf{p} + e\mathbf{A}) + \beta m_e c^2 - eV \right] \Psi_{\text{Dirac}} = E\Psi_{\text{Dirac}}. \quad (2.29)$$

$c$  is the speed of light,  $\mathbf{A}$  is a vector potential due to magnetic fields,  $V$  is a scalar potential due to electric fields (like the potential of the nuclei),  $\boldsymbol{\alpha}$  is a vector  $(\boldsymbol{\alpha}^1, \boldsymbol{\alpha}^2, \boldsymbol{\alpha}^3)$ ,

$$\boldsymbol{\alpha}^i = \begin{pmatrix} \mathbf{0}_2 & \boldsymbol{\sigma}_i \\ \boldsymbol{\sigma}_i & \mathbf{0}_2 \end{pmatrix}, i = (1, 2, 3), \quad (2.30)$$

containing  $2 \times 2$  null matrices  $\mathbf{0}_2$  and  $\boldsymbol{\sigma}_i$  as the Pauli spin matrices,

$$\boldsymbol{\sigma}_1 = \begin{pmatrix} 0 & 1 \\ 1 & 0 \end{pmatrix}, \quad (2.31)$$

$$\boldsymbol{\sigma}_2 = \begin{pmatrix} 0 & -i \\ i & 0 \end{pmatrix}, \quad (2.32)$$

$$\boldsymbol{\sigma}_3 = \begin{pmatrix} 1 & 0 \\ 0 & -1 \end{pmatrix}, \quad (2.33)$$

which are connected to the spin  $\mathbf{s}$  as

$$\frac{\hbar}{2}\boldsymbol{\sigma} = \mathbf{s}. \quad (2.34)$$

$\beta$  is a matrix of the form

$$\beta = \begin{pmatrix} \mathbf{1}_2 & \mathbf{0}_2 \\ \mathbf{0}_2 & -\mathbf{1}_2 \end{pmatrix}, \quad (2.35)$$

where  $\mathbf{1}_2$  is the identity matrix of the size two and  $\Psi_{\text{Dirac}}$  is the wave function, being a four-component complex vector. It is often written as two spinors,

$$\Psi_{\text{Dirac}} = \begin{pmatrix} \Psi^L \\ \Psi^S \end{pmatrix}, \quad (2.36)$$

where  $\Psi^L$  is the so-called large component describing the electronic and  $\Psi^S$  the small component describing the positronic states.  $\Psi^L$  and  $\Psi^S$  can then also be separated into their spin components [28]

$$\Psi^L = \begin{pmatrix} \Psi^{L,\alpha} \\ \Psi^{L,\beta} \end{pmatrix}, \quad (2.37)$$

$$\Psi^S = \begin{pmatrix} \Psi^{S,\alpha} \\ \Psi^{S,\beta} \end{pmatrix}, \quad (2.38)$$

where  $\alpha$  corresponds to  $s_z = +\frac{\hbar}{2}$  and  $\beta$  corresponds to  $s_z = -\frac{\hbar}{2}$ . The term in the brackets in Equation (2.29) is often written as  $\hat{h}_D$ , resulting in the Dirac Hamiltonian [22],

$$\hat{h}_D \Psi_{\text{Dirac}} = E \Psi_{\text{Dirac}}. \quad (2.39)$$

For a many-electron system, the interaction between the electrons has to be corrected due to relativistic effects as well. In practice, the interaction of the electron  $i$  and  $j$  are often approximated as [21, 22]

$$\hat{V}_{ij} = e^2 \left[ \frac{1}{r_{ij}} - \frac{\boldsymbol{\alpha}_i \boldsymbol{\alpha}_j}{2r_{ij}} - \frac{(\boldsymbol{\alpha}_i \mathbf{r}_{ij})(\boldsymbol{\alpha}_j \mathbf{r}_{ij})}{2r_{ij}^3} \right]. \quad (2.40)$$

The first term is the unretarded Coulomb interaction, the second and third terms are the Breit interaction.  $r_{ij}$  is the distance of electron  $i$  and electron  $j$ . Adding  $\hat{h}_D$  of each electron to the Hamiltonian yields the Dirac–Coulomb–Breit Hamiltonian as [21, 22]

$$\hat{H}^{DCB} = \sum_i^N \hat{h}^D(i) + \sum_i^N \sum_{j>i}^N \frac{e^2}{r_{ij}} - \sum_i^N \sum_{j>i}^N \frac{e^2}{2} \left[ \frac{\boldsymbol{\alpha}_i \boldsymbol{\alpha}_j}{r_{ij}} + \frac{(\boldsymbol{\alpha}_i \mathbf{r}_{ij})(\boldsymbol{\alpha}_j \mathbf{r}_{ij})}{r_{ij}^3} \right], \quad (2.41)$$

where the first sum contains the Dirac single-electron operators, the second sum contains the electron–electron Coulomb interaction, and the last sum is the so-called Breit

operator. The Breit operator is often ignored because the Breit interactions are small for molecular systems [21, 22], leading to the Dirac–Coulomb Hamiltonian,

$$\hat{H}^{DC} = \sum_i^N \hat{h}^D(i) + \sum_i^N \sum_{j>i}^N \frac{e^2}{r_{ij}}. \quad (2.42)$$

In practice, these equation can be solved using the Dirac–Hartree–Fock method [21, 22], but this method is not discussed in detail, since KS-DFT was used throughout this work. Thus, the relativistic approach to DFT is focused on instead.

### 2.2.2. Current Density Functional Theory

The extension of DFT into a relativistic theory is based on the four-current  $j^\mu$  [21, 22], which is defined as  $(ic\rho(\mathbf{r}), j_x(\mathbf{r}), j_y(\mathbf{r}), j_z(\mathbf{r}))$ .  $\rho(\mathbf{r})$  again denotes the electron density, while  $(j_x(\mathbf{r}), j_y(\mathbf{r}), j_z(\mathbf{r}))$  is the current density  $\mathbf{j}(\mathbf{r})$ . Instead of expressing the energy as a functional of  $\rho(\mathbf{r})$  it is now expressed as a functional of  $j^\mu$  [22]. Similar to normal DFT, one can formulate theorems to prove the correspondence of  $j^\mu$  with an external potential, as well as the validity of a minimum principle, allowing to get  $j_0^\mu$ , leading to the current-density functional theory (cDFT) [22].

As for KS-DFT, a four-component Kohn–Sham model [22] can be formulated, now using a reference system of non-interacting fermions with the same  $j^\mu$  as the interacting system. The wave function of the non-interacting fermions can again be described using a single Slater determinant, allowing to calculate  $\rho(\mathbf{r})$  and  $\mathbf{j}(\mathbf{r})$  of the non-interacting system as

$$\rho(\mathbf{r}) = \sum_i^N (\psi_i^{\text{DKS}}(\mathbf{r}))^\dagger \cdot \psi_i^{\text{DKS}}(\mathbf{r}), \quad (2.43)$$

$$\mathbf{j}(\mathbf{r}) = c \sum_i^N (\psi_i^{\text{DKS}}(\mathbf{r}))^\dagger \cdot \boldsymbol{\alpha} \cdot \psi_i^{\text{DKS}}(\mathbf{r}), \quad (2.44)$$

using the four-component Kohn–Sham orbitals  $\psi^{\text{DKS}}(\mathbf{r})$ . Another important quantity is the magnetization,

$$\mathbf{m}(\mathbf{r}) = \sum_i^N (\psi_i^{\text{DKS}}(\mathbf{r}))^\dagger \cdot \boldsymbol{\beta} \cdot \left( \begin{pmatrix} \boldsymbol{\sigma}_x & \mathbf{0}_2 \\ \mathbf{0}_2 & \boldsymbol{\sigma}_x \end{pmatrix}, \begin{pmatrix} \boldsymbol{\sigma}_y & \mathbf{0}_2 \\ \mathbf{0}_2 & \boldsymbol{\sigma}_y \end{pmatrix}, \begin{pmatrix} \boldsymbol{\sigma}_z & \mathbf{0}_2 \\ \mathbf{0}_2 & \boldsymbol{\sigma}_z \end{pmatrix} \right) \cdot \psi_i^{\text{DKS}}(\mathbf{r}), \quad (2.45)$$

introducing a spin-degree of freedom into cDFT. The energy can then be calculated as

$$E[j^\mu] = T[j^\mu] + V_{NN}[j^\mu] + J[j^\mu] + E_{\text{XC}}[j^\mu], \quad (2.46)$$

and similar to KS-DFT, one arrives at the relativistic Kohn–Sham equations [21, 22]

$$\left[ c\boldsymbol{\alpha} \cdot \left( \mathbf{p} + \frac{e}{c}\mathbf{A}_{\text{eff}}(\mathbf{r}) \right) + \beta m_e c^2 - e v_{\text{eff}}(\mathbf{r}) \right] \psi^{\text{DKS}}(\mathbf{r}) = \epsilon_i \psi^{\text{DKS}}(\mathbf{r}) \quad (2.47)$$

where  $v_{\text{eff}}(\mathbf{r})$  is the effective scalar potential,

$$v_{\text{eff}}(\mathbf{r}) = v_{\text{ext}}(\mathbf{r}) - \frac{e}{c} \int d^3\mathbf{r}' \frac{\boldsymbol{\rho}(\mathbf{r}')}{|\mathbf{r} - \mathbf{r}'|} - \frac{c}{e} \frac{\delta E_{\text{XC}}[j^\mu]}{\delta \rho(\mathbf{r})}, \quad (2.48)$$

and  $\mathbf{A}_{\text{eff}}(\mathbf{r})$  is the effective vector potential,

$$\mathbf{A}_{\text{eff}}(\mathbf{r}) = \mathbf{A}_{\text{ext}}(\mathbf{r}) - \frac{e}{c} \int d^3\mathbf{r}' \frac{\mathbf{j}(\mathbf{r}')}{|\mathbf{r} - \mathbf{r}'|} - \frac{c}{e} \frac{\delta E_{\text{XC}}[j^\mu]}{\delta \dot{\mathbf{j}}(\mathbf{r})}. \quad (2.49)$$

In the absence of magnetic fields, the Dirac–Coulomb equivalent of the relativistic Kohn–Sham equations can be obtained as [21]

$$\begin{pmatrix} v^{\text{eff}}[\rho(\mathbf{r})] & c(\boldsymbol{\sigma} \cdot \mathbf{p}) \\ c(\boldsymbol{\sigma} \cdot \mathbf{p}) & v^{\text{eff}}[\rho(\mathbf{r})] - 2m_e c^2 \end{pmatrix} \psi^{\text{DKS}}(\mathbf{r}) = E \psi^{\text{DKS}}(\mathbf{r}), \quad (2.50)$$

and the energy again depends on  $\rho(\mathbf{r})$  only. This allows using the density-only exchange–correlation functionals [21]. Despite a density-only formulation, one can also arrive at an expression where the functionals in addition depend on  $\mathbf{m}(\mathbf{r})$ . This also leads to a non-relativistic treatment of the spin-degree of freedom in DFT. Without spin-dependent relativistic effects and if the  $z$  component of  $\mathbf{m}(\mathbf{r})$  is considered only, the magnetization reduces to the difference of the density formed by electrons with a spin  $\alpha$  and the density formed by electrons with a spin  $\beta$  [22].

Solving the Dirac–Kohn–Sham equations offers a possibility to calculate the electronic structure with a relativistic treatment. However, the positronic structure are obtained as well. A Hamiltonian which can be used to calculate the electronic states independently of the positronic states would lead to a less computational effort, since the unneeded degrees of freedom of the positrons can be neglected [22]. Such Hamiltonians are called quasirelativistic or two-component Hamiltonians.

### 2.2.3. Quasirelativistic Hamiltonians

If electronic and positronic states were decoupled, it would be sufficient to solve the Dirac equation for the large component only, to get the electronic states. The wave function would reduce from a four-component to a two-component wave function. Such methods are called two-component calculations [22]. A further reduction of the dimension of the wave functions leads to one-component (scalar-relativistic) calculations by assuming the coupling of the  $\alpha$  and  $\beta$  orbitals to be zero [29]. Several methods to decouple the electronic and positronic states exist, and a few of them are discussed now.

#### Decoupling of Positronic and Electronic States using a Unitary Transformation

A possible approach for the decoupling of electronic and positronic states is a block diagonalization of the relativistic Hamiltonian by applying a unitary transformation [21, 22].  $\hat{h}^D$  can be written as

$$\hat{h}^D = \begin{pmatrix} \mathcal{E}^{LL} & \mathcal{O}^{LS} \\ \mathcal{O}^{SL} & \mathcal{E}^{SS} \end{pmatrix}, \quad (2.51)$$

where  $\mathcal{E}$  are the block-diagonal elements which do not contain coupling of electronic and positronic states, and  $\mathcal{O}$  are the off-diagonal elements which describe the coupling of electronic and positronic states [22].  $\hat{h}^D$  can be block-diagonalized using a unitary transformation,

$$\mathbf{U}\hat{h}^D\mathbf{U}^\dagger = \begin{pmatrix} \mathcal{E}^{LL'} & 0 \\ 0 & \mathcal{E}^{SS'} \end{pmatrix}, \quad (2.52)$$

leading to a formulation where electronic states are decoupled from the positronic ones and can thus be calculated separately [21,22]. The unitary transformation is not uniquely defined, which give rise for several different decoupling methods [22]. Popular decoupling schemes are the Douglas–Kroll–Hess method and the exact two-component (X2C) approach. While the Douglas–Kroll–Hess method decouples the Dirac Hamiltonian sequentially, the X2C method does so in one step [29].

## Decoupling of Positronic and Electronic States by Elimination of the Small Component

A different approach for the formulation of a quasirelativistic Hamiltonian is based on eliminating the small component [21]. Starting from the Dirac equation written as

$$(V - E)\Psi^L + c(\boldsymbol{\sigma} \cdot \mathbf{p})\Psi^S = 0 \quad (2.53a)$$

$$c(\boldsymbol{\sigma} \cdot \mathbf{p})\Psi^L + (V - E - 2m_e c^2)\Psi^S = 0, \quad (2.53b)$$

one can eliminate  $\Psi^S$  from Equation (2.53a) by replacing it with the expression

$$c(\boldsymbol{\sigma} \cdot \mathbf{p})\Psi^L(2m_e c^2 - V + E)^{-1} = \Psi^S, \quad (2.54)$$

derived from Equation (2.53b). Having replaced  $\Psi^S$ , a possible formulation of the resulting equation is

$$(V - E)\psi^L + \frac{1}{2m_e}(\boldsymbol{\sigma} \cdot \mathbf{p})\frac{2m_e c^2}{2m_e c^2 - V} \left[1 + \frac{E}{2m_e c^2 - V}\right]^{-1} (\boldsymbol{\sigma} \cdot \mathbf{p})\psi^L = 0. \quad (2.55)$$

Expanding  $\left[1 + \frac{E}{2m_e c^2 - V}\right]^{-1}$  as a power series, and terminating at zeroth-order, one arrives at the zeroth-order regular approximation (ZORA)-Hamiltonian [21, 30],

$$\hat{H}^{\text{ZORA}} = V + (\boldsymbol{\sigma} \cdot \mathbf{p})\frac{c^2}{2m_e c^2 - V} (\boldsymbol{\sigma} \cdot \mathbf{p}). \quad (2.56)$$

The eigenvalues of  $\hat{H}^{\text{ZORA}}$ ,

$$\hat{H}^{\text{ZORA}}\psi_i^{\text{ZORA}} = E_i^{\text{ZORA}}\psi_i^{\text{ZORA}}, \quad (2.57)$$

suffer from several problems. On the one hand, they strongly deviate from the Dirac eigenvalues, on the other hand, they are electric-gauge dependent [21]. Different approaches to solve this problem were proposed, like using a frozen potential in the denominator [31] or using scaled ZORA energies [32].

In addition to  $\hat{H}^{\text{ZORA}}$ , the Breit–Pauli Hamiltonian  $\hat{H}^{\text{BP}}$  can be derived from a different formulation of Equation (2.55) [21].  $\hat{H}^{\text{BP}}$  is variationally unstable, does not include relativistic effects in zeroth order, and is ill-defined in some points at space, which makes the usage of  $\hat{H}^{\text{ZORA}}$  preferable.

### 2.2.4. Spin–Orbit Coupling as a Relativistic Effect

The Dirac equation contains several relativistic corrections to the electronic energy [21, 22], which include several spin-independent or scalar-relativistic effects (*e.g.* the mass-velocity term and the Darwin term), which are not discussed in detail, and spin-dependent effects like SOC. SOC describes the interaction of the electron’s spin with the orbital angular momentum of itself, or of other electrons in an electric field<sup>4</sup>.

The presence of SOC can be revealed by reformulating the two-spinor form of the Dirac equation [21, 22],

$$[V(\mathbf{r}) - E] \Psi^L + [c(\boldsymbol{\sigma} \cdot \mathbf{p})] \Psi^S = 0 \quad (2.58a)$$

$$[c(\boldsymbol{\sigma} \cdot \mathbf{p})] \Psi^L + [-2m_e c^2 - E + V(\mathbf{r})] \Psi^S = 0. \quad (2.58b)$$

Replacing  $\Psi^S$  with

$$\Psi^S = \frac{(\boldsymbol{\sigma} \cdot \mathbf{r})}{2m_e c} \phi^L, \quad (2.59)$$

where  $\phi^L$  is a pseudo-large component, and multiplying Equation (2.58b) with  $\frac{(\boldsymbol{\sigma} \cdot \mathbf{p})}{2m_e c}$  leads to

$$[V(\mathbf{r}) - E] \Psi^L + [c(\boldsymbol{\sigma} \cdot \mathbf{p})] \frac{(\boldsymbol{\sigma} \cdot \mathbf{p})}{2m_e c} \phi^L = 0 \quad (2.60a)$$

$$\left[ \frac{(\boldsymbol{\sigma} \cdot \mathbf{p})}{2m_e c} c(\boldsymbol{\sigma} \cdot \mathbf{p}) \right] \Psi^L + \frac{(\boldsymbol{\sigma} \cdot \mathbf{p})}{2m_e c} [-2m_e c^2 - E + V(\mathbf{r})] \frac{(\boldsymbol{\sigma} \cdot \mathbf{p})}{2m_e c} \phi^L = 0. \quad (2.60b)$$

Applying Dirac’s relation [21],

$$(\boldsymbol{\sigma} \cdot \mathbf{u}) V(\mathbf{r}) (\boldsymbol{\sigma} \cdot \mathbf{v}) = \mathbf{u} V(\mathbf{r}) \mathbf{v} + i \boldsymbol{\sigma} \cdot (\mathbf{u} V(\mathbf{r}) \times \mathbf{v}), \quad (2.61)$$

leads to the modified Dirac equation,

$$[V(\mathbf{r}) - E] \Psi^L + \hat{T} \phi^L = 0 \quad (2.62)$$

$$\hat{T} \Psi^L - \left[ -\hat{T} - \frac{E}{2m_e c^2} \hat{T} + \frac{\mathbf{p} V(\mathbf{r}) \mathbf{p}}{4m_e^2 c^2} + \frac{i \boldsymbol{\sigma} \cdot (\mathbf{p} V(\mathbf{r}) \times \mathbf{p})}{4m_e^2 c^2} \right] \phi^L = 0. \quad (2.63)$$

---

<sup>4</sup> For instance the field of the nuclei or the field of the other electrons.

The term containing the cross product can be written as

$$\mathbf{i}\boldsymbol{\sigma} \cdot (\mathbf{p}V(\mathbf{r}) \times \mathbf{p}) = \hbar\boldsymbol{\sigma} \cdot (\nabla V(\mathbf{r}) \times \mathbf{p}). \quad (2.64)$$

Assuming a spherical potential [21],

$$\nabla V(\mathbf{r}) = \frac{1}{r} \frac{\partial V(r)}{\partial r} \mathbf{r}, \quad (2.65)$$

using the fact that the orbital angular momentum is defined as [22]

$$\mathbf{l} = (\mathbf{r} \times \mathbf{p}), \quad (2.66)$$

and the definition of the spin [22],

$$\mathbf{s} = \frac{\hbar}{2} \boldsymbol{\sigma}, \quad (2.67)$$

allows to rewrite Equation (2.64) as

$$\hbar\boldsymbol{\sigma} \cdot (\nabla V(\mathbf{r}) \times \mathbf{p}) = \frac{1}{r} \frac{\partial V(r)}{\partial r} \hbar\boldsymbol{\sigma} \cdot (\mathbf{r} \times \mathbf{p}) = \frac{2}{r} \frac{\partial V(r)}{\partial r} \mathbf{s} \cdot \mathbf{l}. \quad (2.68)$$

This describes an interaction of the electron's spin with its orbital angular momentum, which is also called SOC [22].

SOC is also contained in two-component Hamiltonians, which can, *e.g.* be seen in the Breit–Pauli Hamiltonian.  $\hat{H}^{\text{BP}}$  contains three different types of SOC. The first is the SOC due to the interaction of the electron's spin with its orbital angular momentum resulting from its motion around the nuclei [22],

$$\hat{H}^{\text{BP, so}} = \frac{1}{2m_e^2 c^2} \sum_i \sum_I \frac{Z_I (\mathbf{r}_{iI} \times \hat{\mathbf{p}}_i) \cdot \hat{\mathbf{s}}_i}{r_{iI}^3}, \quad (2.69)$$

where  $\mathbf{r}_{iI}$  is the relative position of electron  $i$  to nucleus  $I$ . The second one is the SOC due to the interaction of its spin with its orbital angular momentum resulting from its motion around the other electrons, also called spin–same orbit coupling [22],

$$\hat{H}^{\text{BP, sso}} = -\frac{1}{2m_e^2 c^2} \sum_{i,j \neq i} \frac{(\mathbf{r}_{ij} \times \hat{\mathbf{p}}_i) \cdot \hat{\mathbf{s}}_i}{r_{ij}^3}, \quad (2.70)$$

where  $\mathbf{r}_{ij}$  is the relative position of electron  $i$  to electron  $j$ . The third one is the SOC due to the interaction of electron's spin with the orbital angular momentum of the other electrons resulting from their motion around the electrons, also called spin–other orbit coupling [22]

$$\hat{H}^{\text{BP, soo}} = -\frac{1}{m_e^2 c^2} \sum_{i,j \neq i} \frac{(\mathbf{r}_{ij} \times \hat{\mathbf{p}}_i) \cdot \hat{\mathbf{s}}_j}{r_{ij}^3}. \quad (2.71)$$

SOC is also contained in  $\hat{H}^{\text{ZORA}}$ . This can be shown by rewriting Equation (2.56) as [21]

$$\hat{H}^{\text{ZORA}} = V + \frac{m_e c^2 \hat{T}}{2m_e c^2 - V} + \frac{c^2}{(2m_e c^2 - V)^2} \left[ (\mathbf{p}V(\mathbf{r})) \cdot \mathbf{p} - \hbar \boldsymbol{\sigma} \cdot (\nabla V(\mathbf{r}) \times \mathbf{p}) \right]. \quad (2.72)$$

The term with the cross product again contains SOC. For the scaled-ZORA approach, the effective DFT potential  $v^{\text{eff}}$  is used as a potential to build  $\hat{H}^{\text{ZORA}}$  in DFT [33], and thus contains parts of the electron–electron SOC [34] (the missing part is the spin–other orbit coupling).

Two-component DFT calculations are useful to investigate SOC effects in molecular systems because SOC is described by quasirelativistic Hamiltonians like  $\hat{H}^{\text{ZORA}}$ . Since properties of molecular systems were extracted from the effective single-particle Hamiltonian matrix and overlap matrix during this work, the shape of those matrices resulting from a two-component calculation including SOC is explained in the following.

### 2.2.5. Effective Single-Particle Hamiltonian Matrix and Overlap Matrix in Two-Component Electronic Structure Calculations

In two-component HF and DFT calculations, a molecular orbital can be represented as a two-component complex molecular spinor [35],

$$\psi_i = \begin{pmatrix} \psi_i^{(\alpha)} \\ \psi_i^{(\beta)} \end{pmatrix}, \quad (2.73)$$

where  $\psi_i^{(\alpha)}$  and  $\psi_i^{(\beta)}$  are scalar functions describing the  $\alpha$  and  $\beta$  part of the molecular spinor.  $\psi_i^{(\alpha)}$  and  $\psi_i^{(\beta)}$  can be expanded using two-component atomic-centered basis

functions, resulting in complex two-component molecular spinors of the form [35–37]

$$\psi_i = \sum_{\mu} c_{\mu i}^{\alpha} \begin{pmatrix} \phi_{\mu} \\ 0 \end{pmatrix} + c_{\mu i}^{\beta} \begin{pmatrix} 0 \\ \phi_{\mu} \end{pmatrix} = \sum_{\mu} \phi_{\mu} \left[ \text{Re} \begin{pmatrix} c_{\mu i}^{\alpha} \\ c_{\mu i}^{\beta} \end{pmatrix} + i \text{Im} \begin{pmatrix} c_{\mu i}^{\alpha} \\ c_{\mu i}^{\beta} \end{pmatrix} \right], \quad (2.74)$$

where  $\phi_{\mu}$  is an atom-centered basis function. The resulting effective single-particle Hamiltonian matrix and overlap matrix in the atomic orbital basis are  $2 \times 2$  block matrices,

$$\mathbf{H} = \begin{pmatrix} \mathbf{H}^{\alpha\alpha} & \mathbf{H}^{\alpha\beta} \\ \mathbf{H}^{\beta\alpha} & \mathbf{H}^{\beta\beta} \end{pmatrix}, \quad (2.75)$$

$$\mathbf{S} = \begin{pmatrix} \mathbf{S}^{\alpha\alpha} & \mathbf{0} \\ \mathbf{0} & \mathbf{S}^{\beta\beta} \end{pmatrix}. \quad (2.76)$$

An element of the spin-conserving block  $\mathbf{H}^{\alpha\alpha}$  and spin-flip blocks  $\mathbf{H}^{\alpha\beta}$  can be written as

$$\mathbf{H}_{\mu\nu}^{\alpha\alpha} = \left\langle \begin{pmatrix} \phi_{\mu} \\ 0 \end{pmatrix} \left| \hat{h} \right| \begin{pmatrix} \phi_{\nu} \\ 0 \end{pmatrix} \right\rangle \quad (2.77)$$

$$\mathbf{H}_{\mu\nu}^{\alpha\beta} = \left\langle \begin{pmatrix} \phi_{\mu} \\ 0 \end{pmatrix} \left| \hat{h} \right| \begin{pmatrix} 0 \\ \phi_{\nu} \end{pmatrix} \right\rangle, \quad (2.78)$$

where  $\hat{h}$  can be the Fock operator or the Kohn–Sham Hamiltonian in a two-component form [35, 36].

For a closed-shell system without SOC, the matrix elements of  $\mathbf{H}^{\sigma\sigma'}$  are zero and the matrix elements of  $\mathbf{H}^{\sigma\sigma}$  are real [20]. The effect of SOC on the elements of an effective single-particle Hamiltonian matrix in an atomic-orbital basis can be shown by formulating a simplified single-electron SOC Hamiltonian matrix element as [38, 39]

$$\langle \psi_j | \hat{H}_{\text{SOC}} | \psi_j \rangle = \xi_j \langle \psi_j | \hat{\mathbf{l}} \cdot \hat{\mathbf{s}} | \psi_j \rangle, \quad (2.79)$$

where  $\xi_j$  is a single-electron SOC constant<sup>5</sup>. The angular-momentum operator  $\hat{\mathbf{l}}$  is a vector  $(\hat{l}_x, \hat{l}_y, \hat{l}_z)$  as well as the spin-momentum operator  $\hat{\mathbf{s}} (\hat{s}_x, \hat{s}_y, \hat{s}_z)$ . In the following,

---

<sup>5</sup> The constant is about  $460 \text{ cm}^{-1}$  for the  $3d$ -orbitals of an iron(III) ion [38].

the effect of  $\hat{H}_{\text{SOC}}$  on two-component basis functions located on a single atom are shown, represented by atom-centered  $p$ -type GTOs.

$\hat{\mathbf{l}}$  is defined as in Equation (2.66) and can be written as [22]

$$\hat{\mathbf{l}} = \mathbf{r} \times \mathbf{p} = \begin{pmatrix} y\hat{p}_z - z\hat{p}_y \\ z\hat{p}_x - x\hat{p}_z \\ x\hat{p}_y - y\hat{p}_x \end{pmatrix} = -i\hbar \begin{pmatrix} y\frac{\partial}{\partial z} - z\frac{\partial}{\partial y} \\ z\frac{\partial}{\partial x} - x\frac{\partial}{\partial z} \\ x\frac{\partial}{\partial y} - y\frac{\partial}{\partial x} \end{pmatrix} = \begin{pmatrix} \hat{l}_x \\ \hat{l}_y \\ \hat{l}_z \end{pmatrix}. \quad (2.80)$$

Setting the position of the atomic nucleus on which the GTO is centered to zero, the real solid harmonics  $p$ -type GTO ( $p_x, p_y, p_z$ ) has the form [40]

$$p_j(\mathbf{r}) = j \cdot e^{-A(x^2+y^2+z^2)} = j \cdot R(\mathbf{r}), \quad (2.81)$$

where  $j$  denotes the  $x, y$ , or  $z$  coordinate and  $A$  is the exponent of the radial part  $R(\mathbf{r})$ . The derivatives with respect to the spatial coordinate  $k$  of the  $p$ -type GTOs,

$$\frac{\partial p_j(\mathbf{r})}{\partial k} = \begin{cases} -2A \cdot j \cdot k \cdot R(\mathbf{r}), & \text{if } (j \neq k) \wedge (j \in (x, y, z)) \\ R(\mathbf{r}) - 2A \cdot j^2 \cdot R(\mathbf{r}), & \text{if } (j = k) \wedge (j \in (x, y, z)) \end{cases}, \quad (2.82)$$

are needed to evaluate the matrix elements. Combining Equations (2.80), (2.81), and (2.82), the expressions

$$\hat{\mathbf{l}}|p_x\rangle = \hbar \begin{pmatrix} 0 \\ -i|p_z\rangle \\ i|p_y\rangle \end{pmatrix} \quad (2.83)$$

for the  $p_x$ -type GTOs,

$$\hat{\mathbf{l}}|p_y\rangle = \hbar \begin{pmatrix} i|p_z\rangle \\ 0 \\ -i|p_x\rangle \end{pmatrix} \quad (2.84)$$

for the  $p_y$ -type GTOs, and

$$\hat{\mathbf{l}}|p_z\rangle = \hbar \begin{pmatrix} -i|p_y\rangle \\ i|p_x\rangle \\ 0 \end{pmatrix} \quad (2.85)$$

for the  $p_z$ -type GTOs can be formulated. The effect of a component of  $\hat{\mathbf{l}}$  can be described as a  $90^\circ$  rotation of one  $p$ -basis function around a single Cartesian axes a multiplication with  $i$ .

Similar to  $\hat{\mathbf{l}}$ ,  $\hat{\mathbf{s}}$  can be reformulated using Equation (2.67) as [22]

$$\hat{\mathbf{s}} = \frac{\hbar}{2} \begin{pmatrix} \boldsymbol{\sigma}_x \\ \boldsymbol{\sigma}_y \\ \boldsymbol{\sigma}_z \end{pmatrix} = \begin{pmatrix} \hat{s}_x \\ \hat{s}_y \\ \hat{s}_z \end{pmatrix}. \quad (2.86)$$

This operator can act on two-component basis functions, which can be written for  $p$ -type GTOs as

$$|p_j\rangle^\sigma = \begin{cases} \begin{pmatrix} |p_j\rangle \\ 0 \end{pmatrix}, & \text{if } (\sigma = \alpha) \\ \begin{pmatrix} 0 \\ |p_j\rangle \end{pmatrix}, & \text{if } (\sigma = \beta) \end{cases}. \quad (2.87)$$

The action of  $\hat{\mathbf{s}}$  on the  $\alpha$   $p$ -type two-component basis functions can be written as

$$\hat{\mathbf{s}} |p_j\rangle^\alpha = \frac{\hbar}{2} \begin{pmatrix} |p_j\rangle^\beta \\ i |p_j\rangle^\beta \\ |p_j\rangle^\alpha \end{pmatrix}, \quad (2.88)$$

and the action on the  $\beta$   $p$ -type basis functions as

$$\hat{\mathbf{s}} |p_j\rangle^\beta = \frac{\hbar}{2} \begin{pmatrix} |p_j\rangle^\alpha \\ -i |p_j\rangle^\alpha \\ -|p_j\rangle^\beta \end{pmatrix}, \quad (2.89)$$

leading to a spin-conserving<sup>6</sup> effect of the  $\hat{s}_z$  operator and spin-flip effect<sup>7</sup> of the  $\hat{s}_y$  and  $\hat{s}_x$  operators.

---

<sup>6</sup>  $\boldsymbol{\sigma}_z \cdot |p_j\rangle^\alpha = \begin{pmatrix} 1 & 0 \\ 0 & -1 \end{pmatrix} \cdot \begin{pmatrix} |p_j\rangle \\ 0 \end{pmatrix} = \begin{pmatrix} |p_j\rangle \\ 0 \end{pmatrix} = |p_j\rangle^\alpha.$

<sup>7</sup>  $\boldsymbol{\sigma}_x \cdot |p_j\rangle^\alpha = \begin{pmatrix} 0 & 1 \\ 1 & 0 \end{pmatrix} \cdot \begin{pmatrix} |p_j\rangle \\ 0 \end{pmatrix} = \begin{pmatrix} 0 \\ |p_j\rangle \end{pmatrix} = |p_j\rangle^\beta, \boldsymbol{\sigma}_y \cdot |p_j\rangle^\alpha = \begin{pmatrix} 0 & -i \\ i & 0 \end{pmatrix} \cdot \begin{pmatrix} |p_j\rangle \\ 0 \end{pmatrix} = i \begin{pmatrix} 0 \\ |p_j\rangle \end{pmatrix} = i |p_j\rangle^\beta.$

Any matrix element of  $\hat{H}^{\text{SOC}}$  in the chosen GTO basis ( $p$ -type) can be written as (see Equation (2.79))

$$\xi_j \langle p_k^\sigma | \hat{\mathbf{l}} \cdot \hat{\mathbf{s}} | p_l^{\sigma'} \rangle = \xi_j \left( \langle p_k^\sigma | \hat{l}_x \cdot \hat{s}_x | p_l^{\sigma'} \rangle + \langle p_k^\sigma | \hat{l}_y \cdot \hat{s}_y | p_l^{\sigma'} \rangle + \langle p_k^\sigma | \hat{l}_z \cdot \hat{s}_z | p_l^{\sigma'} \rangle \right) \quad (2.90)$$

Since  $\langle p_i^\sigma | p_j^{\sigma'} \rangle$  is zero if  $i \neq j$  (assuming both orbitals to be located on the same atom) or  $\sigma \neq \sigma'$ , the non-zero SOC elements between the two-component  $p$  basis functions for a single atom are

$$\langle p_y^\alpha | \hat{l}_x \hat{s}_x | p_z^\beta \rangle = \langle p_y^\beta | \hat{l}_x \hat{s}_x | p_z^\alpha \rangle = -\langle p_z^\beta | \hat{l}_x \hat{s}_x | p_y^\alpha \rangle = -\langle p_z^\alpha | \hat{l}_x \hat{s}_x | p_y^\beta \rangle = \frac{-i\hbar^2}{2} \quad (2.91)$$

$$\langle p_x^\alpha | \hat{l}_y \hat{s}_y | p_z^\beta \rangle = -\langle p_x^\beta | \hat{l}_y \hat{s}_y | p_z^\alpha \rangle = \langle p_z^\beta | \hat{l}_y \hat{s}_y | p_x^\alpha \rangle = -\langle p_z^\alpha | \hat{l}_y \hat{s}_y | p_x^\beta \rangle = \frac{\hbar^2}{2} \quad (2.92)$$

$$\langle p_x^\alpha | \hat{l}_z \hat{s}_z | p_y^\beta \rangle = -\langle p_x^\beta | \hat{l}_z \hat{s}_z | p_y^\alpha \rangle = \langle p_y^\beta | \hat{l}_z \hat{s}_z | p_x^\alpha \rangle = -\langle p_y^\alpha | \hat{l}_z \hat{s}_z | p_x^\beta \rangle = \frac{-i\hbar^2}{2} \quad (2.93)$$

Thus, as a consequence of SOC, some matrix elements of  $\mathbf{H}$  become complex and some matrix elements of  $\mathbf{H}^{\sigma\sigma'}$  become non-zero.

## 2.3. Electron Transport Properties of Nanoscale Structures

Methods like DFT can be used to investigate electron transport properties of nanojunctions theoretically. A very popular method for doing so is the so-called Landauer–Büttiker–Imry approach [41, 42] or in short the Landauer approach. In this approach, electron transport is described as the elastic scattering of electrons from one lead to another lead through a scattering region connecting both leads (see Figure ) [24].

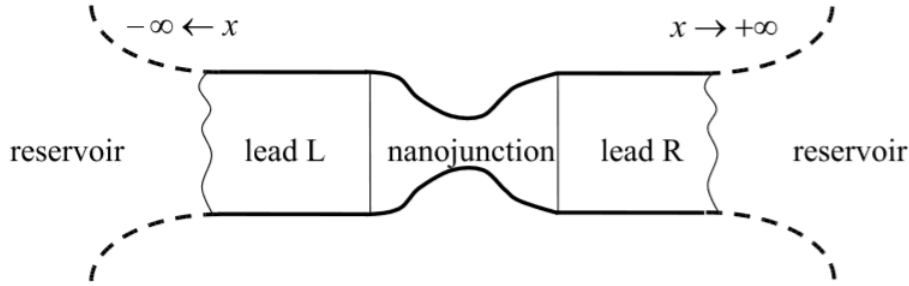


Figure 1: Within the Landauer approach the quantum mechanical system is divided into three regions: a left lead (lead L), a right lead (lead R), and the central/scattering region (nanojunction). The leads are assumed to be connected to electronic reservoirs from which electrons can enter or leave the system. The reservoirs are considered as infinite systems. Having entered the leads, electrons move from the leads to the central region from which they are either reflected or transmitted. After the scattering event, they move back to the electronic reservoirs. The depiction was taken from Reference [24].

### 2.3.1. Landauer Approach

In the Landauer approach, several approximations are made to describe electron transport [24]. A mean-field electronic structure method is employed, *i.e.*, an effective single-particle Hamiltonian is used to describe the quantum mechanical system under investigation. The quantum mechanical system is split into three parts, namely a left lead, a right lead, and a central/scattering region, and is assumed to be in a steady state. In addition, the system is considered to be an open quantum system, where electrons can

enter or leave the system due to the connection of an electronic reservoir to each of the leads. The reservoirs are described as infinite systems from which the electrons originate as a wave packet moving along the leads to the central region, and are either reflected or transmitted. The electrons enter the lead from the reservoirs with the equilibrium distribution [24],

$$f_X(E) = \frac{1}{e^{\frac{E-\mu_x}{k_B T}} + 1}. \quad (2.94)$$

The electron transport is therefore reduced to a scattering problem, *i.e.*, is described as a coherent tunneling process. This description of the electron transport holds for low temperatures, short molecules, and if no energy levels of the nanojunction are close to the Fermi energy.

The total electron current within the Landauer approach can be described as [24]

$$I = \frac{e}{\pi\hbar} \int dE [f_L(E)\mathcal{T}_{LR}(E) - f_R(E)\mathcal{T}_{RL}(E)], \quad (2.95)$$

where  $\mathcal{T}_{XY}(E)$  is the total transmission function which is connected to the probability of an electron coming from the lead  $X$  to be transmitted through the central region to the lead  $Y$ . Due to flux conservation,  $\mathcal{T}_{RL}(E) = \mathcal{T}_{LR}(E) = \mathcal{T}(E)$ , and Equation (2.95) becomes [24]

$$I = \frac{e}{\pi\hbar} \int dE [f_L(E) - f_R(E)] \mathcal{T}(E). \quad (2.96)$$

In principle,  $\mathcal{T}$  depends on the applied voltage. It is often sufficient to evaluate the transport properties within the linear regime at the zero-bias limit as [24]

$$I = \frac{2e^2}{h} \mathcal{T}(E_F)V, \quad (2.97)$$

with  $V$  as the applied voltage, and  $\mathcal{T}(E_F)$  as the transmission function at the Fermi energy<sup>8</sup>, calculated at  $V = 0$ .  $\mathcal{T}_{XY}$  can be calculated using DFT or any mean-field based method as [24]

$$\mathcal{T} = \text{Tr} [\hat{\Gamma}_R \hat{\mathbf{G}}^r \hat{\Gamma}_L \hat{\mathbf{G}}^a], \quad (2.98)$$

---

<sup>8</sup> In a ground-state system,  $E_F$  describes the highest energy an electron can have [24].

where  $\hat{\Gamma}_R$  describes the coupling of the central region with the right electrode,  $\hat{\Gamma}_L$  describes the coupling of the central region with the left electrode, and  $\hat{\mathbf{G}}^{r/a}$  are the retarded and advanced Green's function of the central region in the presence of the left and right leads [24].

For any effective single-particle Hamiltonian, a corresponding Green's function can be defined as [24]

$$\hat{\mathbf{G}}(z) = \frac{\hat{\mathbf{1}}}{z - \hat{\mathbf{H}}}, \quad (2.99)$$

with  $z = E \pm i\epsilon^9$ , where  $\pm$  defines the retarded and advanced Green's function as [24]

$$\hat{\mathbf{G}}^r(E) = \frac{\hat{\mathbf{1}}}{(E + i\epsilon) - \hat{\mathbf{H}}}, \quad (2.100)$$

$$\hat{\mathbf{G}}^a(E) = \frac{\hat{\mathbf{1}}}{(E - i\epsilon) - \hat{\mathbf{H}}}. \quad (2.101)$$

An ansatz for the calculation of the central region's retarded and advanced Green's function in the presence of the leads can be derived using the Löwdin partitioning scheme [43].

The Hamiltonian of the junction can be written as

$$\hat{\mathbf{H}}_J = \begin{pmatrix} \hat{\mathbf{H}}_L & \hat{\mathbf{V}}_{LC} & \mathbf{0} \\ \hat{\mathbf{V}}_{LC}^\dagger & \hat{\mathbf{H}}_C & \hat{\mathbf{V}}_{CR} \\ \mathbf{0} & \hat{\mathbf{V}}_{CR}^\dagger & \hat{\mathbf{H}}_R \end{pmatrix}, \quad (2.102)$$

assuming the coupling between the left and right electrode to be zero. Using such a partitioning, an effective Hamiltonian  $\hat{\mathbf{H}}_C^{\text{eff}}$  for the central subsystem, which includes the effect of the left and right lead, can be written as [43]

$$\hat{\mathbf{H}}_C^{\text{eff}} = \hat{\mathbf{H}}_C - \begin{pmatrix} \hat{\mathbf{V}}_{LC}^\dagger & \hat{\mathbf{V}}_{RC}^\dagger \end{pmatrix} \left[ \begin{pmatrix} z - \hat{\mathbf{H}}_L & \mathbf{0} \\ \mathbf{0} & z - \hat{\mathbf{H}}_R \end{pmatrix} \right]^{-1} \begin{pmatrix} \hat{\mathbf{V}}_{LC} \\ \hat{\mathbf{V}}_{RC} \end{pmatrix}. \quad (2.103)$$

Using the relation  $[z - \hat{\mathbf{H}}_{L/R}]^{-1} = \hat{\mathbf{G}}_{L/R}(z)$ , Equation (2.103) can be rewritten as [24]

$$\hat{\mathbf{H}}_C^{\text{eff}} = \hat{\mathbf{H}}_C - \hat{\mathbf{V}}_{LC}^\dagger \hat{\mathbf{G}}_L(z) \hat{\mathbf{V}}_{LC} - \hat{\mathbf{V}}_{RC}^\dagger \hat{\mathbf{G}}_R(z) \hat{\mathbf{V}}_{RC} = \hat{\mathbf{H}}_C - \hat{\Sigma}_L(z) - \hat{\Sigma}_R(z). \quad (2.104)$$

---

<sup>9</sup>  $E$  is the energy, and  $\epsilon$  is an infinitesimally small imaginary offset, which prevents a division by zero.

$\hat{\Sigma}_{L/R}(z)$  are the so-called self energies of the left and right electrode which contain the effect of both electrodes on the central system. As for the Green's function, the self-energy corresponds to a retarded and an advanced self-energy [24],

$$\hat{\Sigma}_{L/R}^r(E) = \hat{\Sigma}_{L/R}(E + i\epsilon), \quad (2.105)$$

$$\hat{\Sigma}_{L/R}^a(E) = \hat{\Sigma}_{L/R}(E - i\epsilon). \quad (2.106)$$

The advanced and retarded Green's function of the central subsystem can be written as

$$\hat{\mathbf{G}}^{r/a}(E) = \left[ E - \hat{\mathbf{H}}_C - \hat{\Sigma}_L^{r/a}(E) - \hat{\Sigma}_R^{r/a}(E) \right]^{-1}. \quad (2.107)$$

$\hat{\Sigma}_{L/R}^{r/a}(E)$  are related to the coupling operators  $\hat{\mathbf{\Gamma}}_{L/R}$  as [24]

$$\hat{\mathbf{\Gamma}}_{L/R}(E) = i \left[ \hat{\Sigma}_{L/R}^r(E) - \hat{\Sigma}_{L/R}^a(E) \right]. \quad (2.108)$$

The Landauer approach does not include any many-body interactions because it is based on an effective single-particle Hamiltonian. Electron transport is described as coherent tunneling with elastic scattering events. For molecular spin- and electronics, the electron-phonon interaction can be named as an important effect beyond the scope of the Landauer approach. Electron-phonon interactions can induce inelastic scattering events, where tunneling electrons excite or de-excite vibrations in the molecule. The vibration excited by the tunneling electrons can be investigated with the inelastic electron tunneling spectroscopy (IETS), which is an important tool for the structural investigation of nanojunctions [24, 44]. The inclusion of electron-phonon interactions is possible with the more general non-equilibrium Green's function (NEGF) approach, which is discussed in the following section.

### 2.3.2. Electron-Phonon Interactions in Electron Transport Calculations

The NEGF approach [24] describes the electron transport again by using  $\hat{\mathbf{H}}_J$  (see Equation (2.102)) to describe the junction. The same partitioning scheme as for the Landauer approach is used. While within the Landauer approach, the full Hamiltonian is considered to be at the mean-field level, within the NEGF approach  $\hat{\mathbf{H}}_C$ ,  $\hat{\mathbf{V}}_{LC}$  and  $\hat{\mathbf{V}}_{RC}$  may

contain any form of many-body interactions<sup>10</sup>. The total current is then calculated as (assuming the electrodes to be at equilibrium) [24]

$$I = \frac{ie}{\hbar} \int \frac{dE}{2\pi} \text{Tr} \left\{ \left[ \hat{\Gamma}_L(E) - \hat{\Gamma}_R(E) \right] \hat{\mathbf{G}}^<(E) + \left[ f_L(E) \hat{\Gamma}_L(E) - f_R(E) \hat{\Gamma}_R(E) \right] \left[ \hat{\mathbf{G}}^r(E) - \hat{\mathbf{G}}^a(E) \right] \right\}, \quad (2.109)$$

where  $\hat{\mathbf{G}}^<(E)$  is the lesser Green's function defined as

$$\hat{\mathbf{G}}^<(E) = \left( \hat{1} + \hat{\mathbf{G}}^r(E) \hat{\Sigma}^r(E) \right) \hat{\mathbf{G}}_0^<(E) \left( \hat{1} + \hat{\Sigma}^a(E) \hat{\mathbf{G}}^a(E) \right) + \hat{\mathbf{G}}^r(E) \hat{\Sigma}^<(E) \hat{\mathbf{G}}^a(E). \quad (2.110)$$

$\hat{\mathbf{G}}_0^<$  is the lesser Green's function without many-body interactions, and  $\Sigma^<(E)$  is the lesser self energy, which contains the lesser self energies of the left and right electrodes,

$$\hat{\Sigma}^<(E) = \hat{\Sigma}_L^<(E) + \hat{\Sigma}_R^<(E). \quad (2.111)$$

If the leads are at equilibrium,  $\hat{\Sigma}_{L/R}^<(E)$  becomes [24]

$$\hat{\Sigma}_{L/R}^< = i f_{L/R}(E) \hat{\Gamma}_{L/R}. \quad (2.112)$$

To include the effect of electron–phonon interactions, it is convenient to use an effective single-particle Hamiltonian for the calculation of  $\hat{\mathbf{H}}_J$  within the Born–Oppenheimer approximation, and to include electron–phonon coupling through additional self energies  $\hat{\Sigma}_{\text{elph}}^{</r/a}$  [24]. Assuming the coupling to the electrodes being unaffected by the electron–phonon interaction, the self energies become [24]

$$\hat{\Sigma}^{</r/a}(E) = \hat{\Sigma}_L^{</r/a}(E) + \hat{\Sigma}_R^{</r/a}(E) + \hat{\Sigma}_{\text{elph}}^{</r/a}(E), \quad (2.113)$$

and the retarded and advanced Green's functions can be evaluated as

$$\hat{\mathbf{G}}^{r/a}(E) = \left[ E - \hat{\mathbf{H}}_C - \hat{\Sigma}_L^{r/a}(E) - \hat{\Sigma}_R^{r/a}(E) - \hat{\Sigma}_{\text{elph}}^{r/a} \right]^{-1}. \quad (2.114)$$

Since  $\hat{\mathbf{H}}_J$  is calculated using an effective single-particle Hamiltonian,  $\hat{\mathbf{G}}^<(E)$  becomes [24]

$$\hat{\mathbf{G}}^<(E) = \hat{\mathbf{G}}^r(E) \hat{\Sigma}^<(E) \hat{\mathbf{G}}^a(E). \quad (2.115)$$

---

<sup>10</sup> For example electron–electron or electron–ion interactions beyond the mean-field level.

By inserting Equation (2.115) and Equation (2.113) into Equation (2.109), and by defining the the spectral function as [24]

$$\hat{\mathbf{A}}(E) = i \left[ \hat{\mathbf{G}}^r(E) - \hat{\mathbf{G}}^a(E) \right] = \hat{\mathbf{G}}^r(E) \left[ \hat{\mathbf{\Gamma}}_L(E) + \hat{\mathbf{\Gamma}}_R(E) + \hat{\mathbf{\Gamma}}_{\text{elph}}(E) \right] \hat{\mathbf{G}}^a(E), \quad (2.116)$$

where  $\hat{\mathbf{\Gamma}}_{\text{elph}}(E)$  is the coupling of the central region with the phonons, the following expression for the current is obtained [24],

$$I = I_{\text{el}} + I_{\text{inel}}. \quad (2.117)$$

Here  $I_{\text{el}}$  is the elastic part of the current and  $I_{\text{inel}}$  the inelastic one. They can be written explicitly as

$$I_{\text{el}} = \frac{e}{\pi\hbar} \int dE [f_L(E) - f_R(E)] \text{Tr} \left\{ \hat{\mathbf{\Gamma}}_R(E) \hat{\mathbf{G}}^r(E) \hat{\mathbf{\Gamma}}_L(E) \hat{\mathbf{G}}^a(E) \right\}, \quad (2.118)$$

$$I_{\text{inel}} = \frac{ie}{2\hbar} \int \frac{dE}{2\pi} \text{Tr} \left\{ \left[ \hat{\mathbf{\Gamma}}_L(E) - \hat{\mathbf{\Gamma}}_R(E) \right] \hat{\mathbf{G}}^r(E) \hat{\mathbf{\Sigma}}_{\text{elph}}^<(E) \hat{\mathbf{G}}^a(E) \right. \\ \left. - i \left[ f_L(E) \hat{\mathbf{\Gamma}}_L(E) - f_R(E) \hat{\mathbf{\Gamma}}_R(E) \right] \hat{\mathbf{G}}^r(E) \hat{\mathbf{\Gamma}}_{\text{elph}}(E) \hat{\mathbf{G}}^a(E) \right\}. \quad (2.119)$$

Having introduced the theoretical background, the investigation of spin-dependent electron transport phenomena done in this thesis as well as their results are discussed. Throughout the rest of this thesis, the term DFT is used equivalently to KS-DFT.

### 3. Large Magnetoresistance in TEMPO-OPE Single-Molecule Junctions

This thesis deals with the investigation of spin-dependent phenomena, both in molecules and nanostructured devices. In this part the focus lies on molecular systems with unpaired electrons and on magnetoresistance<sup>11</sup>. The underlying experiments were done by Scheer *et al.* and are documented in a joint publication [16]. The goal was to find an explanation for the experimental observations, *i.e.*, the large magnetoresistance in a molecular junction of an organic radical.

#### 3.1. Introduction

Commonly used spintronic devices such as spin valves are based on inorganic materials [45]. In fact, organic materials show some advantages over inorganic materials with respect to their application in the field of spintronics because they consist of light elements, and therefore only have low SOC and hyperfine interactions compared to inorganic materials [46]. Spin-relaxation times, therefore, are much higher for organic materials, which would lead to a longer preservation of the spin during the transport [45,46]. However, a challenge for organic materials is the low mobility of charge carriers, which leads to shorter spin-diffusion lengths than for inorganic materials [47]. Furthermore, organic molecules can be multiply functionalized, which leads to very flexible possibilities in designing molecular-spintronic devices [45].

Several experimental and theoretical studies on organic molecules in the field of spintronics have been reported in the literature. The possibility of large magnetoresistance for organic materials without unpaired electrons was shown for single-molecular junctions based on DFT [49] and experimentally for organic semiconductors [50]. The latter is also known as organic magnetoresistance [50].

Organic radicals are also interesting candidates in the field of spintronics [48]. Several

---

<sup>11</sup> Magnetoresistance describes the dependence of the electrical resistance on an external magnetic field.

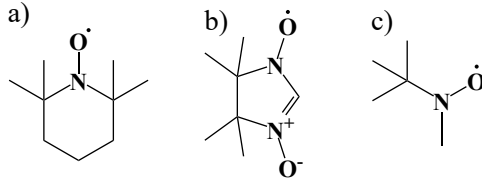


Figure 2: Several stable radicals for hypothetical organic magnetic materials. **a)** (2,2,6,6-Tetramethylpiperidin-1-yl)oxyl (TEMPO) radical **b)** *tert*-butylnitroxide radical **c)**  $\alpha$ -nitronyl nitroxide radical [48].

stable radicals (see Figure 2) based on the nitroxide radical are known to show magnetoresistance in single crystals or as a wire molecule in gold nanoparticle networks [51–53]. 2-[2-(4,5-dibromo-[1,3]dithiol-2-ylidene)-1,3-benzodithiol-5-yl]-4,4,5,5-tetramethylimidazoline-3-oxide-1-oxyl and similar molecules were shown to exhibit large magnetoresistance in single crystals of organic radicals [52–54]. In gold-nanoparticle arrays, thiophene-based wires functionalized with  $\alpha$ -nitronyl nitroxide radicals also exhibited negative magnetoresistance [51]. Several other organic radicals were predicted to be organic spin filters in several theoretical studies [55–57], and polymers based on the nitronyl nitroxide and the 2,2,6,6-tetramethylpiperidine-1-oxyl (TEMPO) radical were proven to be potential candidates for organic memory devices [58–60].

The motivation for this chapter was given by Scheer *et al.* [16], who measured magnetic-field dependent  $I$ - $V$  curves for several oligo(*p*-phenyleneethynylene) (OPE)-based molecules at 4.2 K (see Figure 3) in mechanically-controlled break junctions. While non-radical OPE molecules only showed a small positive magnetoresistance (2 % to 4 %), a TEMPO functionalized OPE molecule (TEMPO-OPE) exhibited a much larger positive magnetoresistance (16 % to 287 %, showing a strong variation from device to device). The magnetic field was applied perpendicular to the transport direction and the magnetoresistance increased up to fields of 4 T [16].

In the following, attempts to explain the large magnetoresistance in TEMPO-OPE single-molecule junctions are presented. First, an overview of the used methods is given.

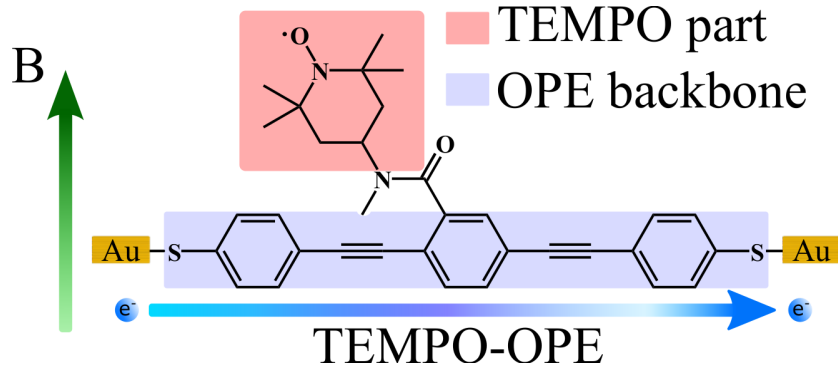


Figure 3: Schematic illustration of the experimental setup for the measurement of the  $I$ - $V$  curves for the TEMPO-OPE molecule [16]. The TEMPO-OPE molecule consists of an OPE backbone and a TEMPO radical. The magnetic field was applied perpendicular to the transport direction.

### 3.2. Theoretical Methods to Investigate Magnetoresistance in Single-Molecule Junctions of TEMPO-OPE

The Landauer approach [41, 42] was employed to investigate the magnetoresistance of the TEMPO-OPE single-molecule junctions, based on DFT calculations at zero bias voltage with atom-centered basis functions (for details of the applied computational methodology, see Appendix A). This approach was already used to investigate spin-dependent transport phenomena like spin-filter properties of several organic radicals [55–57]. Theoretical background on the Landauer approach is given in Section 2.3.

To get first insights into possible origins of the magnetoresistance in TEMPO-OPE single-molecule junctions, several properties for a single-molecule junction of a TEMPO-OPE molecule were calculated:

- The spin density and atomic transport path of conducted electrons: since the spin-filter capability of a radical correlates with the amount of spin density on the transport path [55, 56], the amount of spin density on the transport path may represent the direct interaction of the radical on the conducted electrons.

- Transmission function: a difference in the transmission of the  $\alpha$  and  $\beta$  electrons ( $T^{\alpha\alpha}/T^{\beta\beta}$ ) in the vicinity of the Fermi energy indicates an influence of the spin density on the conducted electrons accessible in the experiment.
- Subsystem molecular orbitals: the highest occupied molecular orbital (HOMO), lowest unoccupied molecular orbital (LUMO), and singly occupied molecular orbital (SOMO) of the central region are of interest here<sup>12</sup>. A participation of the SOMO of the central subsystem in the transport might give insights into the influence of the unpaired electron on the electron transport. This can either be directly, if the SOMO of the central subsystem directly couples electronically to the left and right electrode, or indirectly, if it only couples electronically with the HOMO or the LUMO of the central subsystem, which by themselves couple to the left and right electrode [55, 56]. The latter could for instance result in a quantum interference (QI) feature like a Fano resonance [55, 56, 62, 63].

All calculated properties are based on DFT calculations without a magnetic field. Transport calculations with a simulated external magnetic field could give important insights into the mechanism of the large magnetoresistance. However, quantum chemistry codes being able to do so, like BAGEL [64, 65] or the LONDON program [66], were either not compilable or accessible during this work.

In single-molecule experiments, the electrodes are not only connected by a single molecule, but completely covered with adsorbed molecules [67]. Thus, besides the TEMPO-OPE molecule forming the contact between the two electrodes, the TEMPO-OPE molecules covering the gold electrodes could be responsible for the large magnetoresistance. If the radical part of these TEMPO-OPE molecules interacted with the electrode, this interaction could be sensitive to an external magnetic field, and therefore could influence the electronic structure of the gold electrode. Thus, in addition to the transport properties

---

<sup>12</sup> Central subsystem molecular orbitals are obtained by solving the secular equation of the central subsystem ( $\mathbf{H}_C \mathbf{C}_C = \mathbf{S}_C \mathbf{C}_C \epsilon_C$ ) [61].

of a single TEMPO-OPE molecule connecting the electrodes, first calculations concerning such interactions were done, based on DFT calculations under periodic-boundary conditions (for details of the used methodology, see Appendix A.).

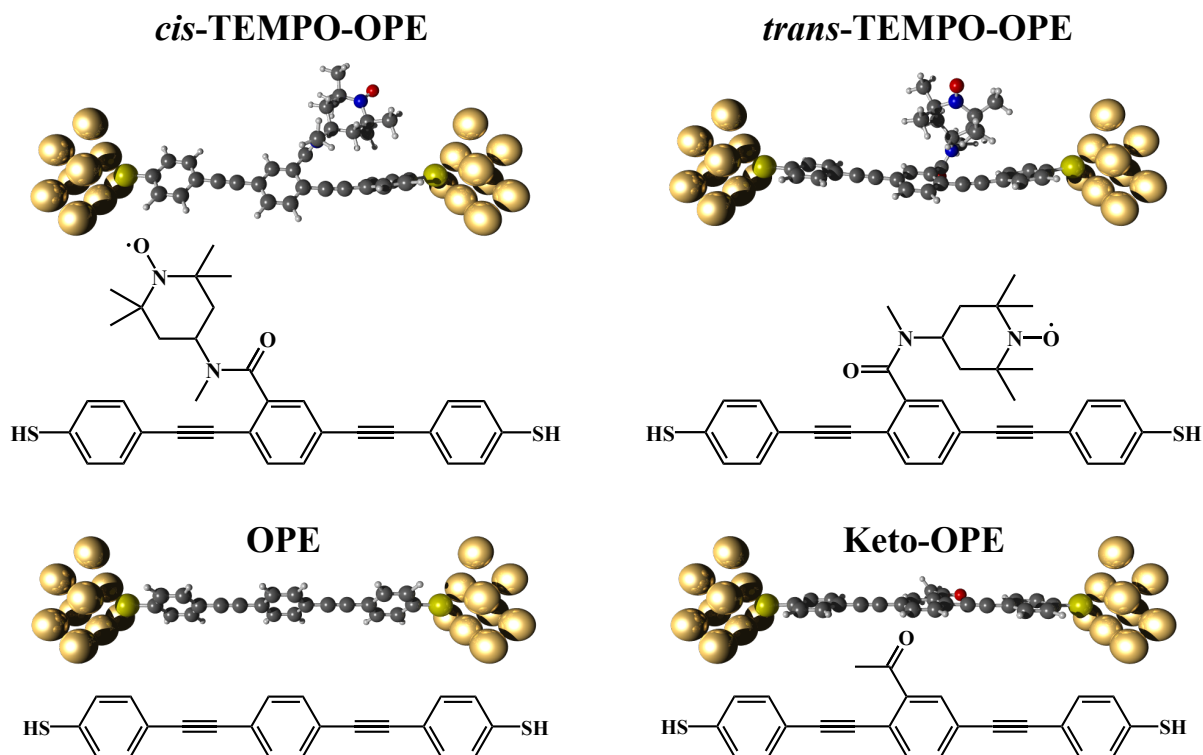


Figure 4: Lewis structures of the OPE, Keto-OPE, *cis*-TEMPO-OPE, and *trans*-TEMPO-OPE molecules and their optimized structures contacted to two nine-atomic gold clusters. The structures were optimized as isolated molecules (BP86-D3/def2-TZVP). For the *cis*-TEMPO-OPE, the conjugation of the OPE backbone is partially broken, due to a tilting of one of the outer benzene ring, while for the *trans*-TEMPO-OPE, the OPE backbone is nearly planar. The OPE and Keto-OPE molecules show a complete planar geometry.

### 3.3. Attempt to Identify Possible Origins of Magnetoresistance in TEMPO-OPE Single-Molecule Junctions

To find an explanation for the magnetoresistance in TEMPO-OPE single-molecule junctions, the transmission functions of two possible isomers of the TEMPO-OPE radical (*cis* and *trans* with respect to the amid bond, see Figure 4) were calculated. Both isomers were found to be very close in energy (see Appendix B). The potential participation of the SOMO in the electron transport and the presence of spin density within the electron transport pathway were the focus of this investigation, since both could offer first indications for an explanation for the magnetoresistance. For comparison, the transmission functions of an OPE and a phenyl-ketone derivatized OPE molecule (Keto-OPE, see Figure 4) were calculated as well. Both molecules were also measured in the experiments done by Scheer *et.al* [16].

To build the gold–molecule–gold junctions, the thiol groups’ hydrogen atoms of the optimized isolated molecules<sup>13</sup> were removed and the resulting structures were placed between two nine-atomic gold clusters (fcc-position,  $d_{\text{Au–Au}} = 2.88 \text{ \AA}$  as in crystalline gold [61], and  $d_{\text{S–Au}} = 2.48 \text{ \AA}$ , based on calculations for phenylthiol from the literature [68]). Afterwards, the electron transport properties were calculated with ARTAIOS based on a DFT single-point calculation<sup>14</sup>. The central region was chosen to be the molecules only. Herrmann *et al.* used the same procedure to calculate electron transport properties for several organic radicals [55, 56]. Since the exact value of  $E_F$  is unknown, if the electron transport properties are calculated with ARTAIOS, it was estimated ( $-5 \text{ eV}$  [69]).

In the following discussion of the electron transport properties of the investigated molecules, the terms HOMO, SOMO, or LUMO refer to the orbitals of the central subsystem (molecule only), the atomic transport path of the conducted electrons is called local transmission (describing the magnitude of the current between pairs of atoms).

---

<sup>13</sup> BP86-D3/def2-TZVP. For details see Appendix A.

<sup>14</sup> B3LYP-def2-SVP. For details see Appendix A.

### 3.3.1. Influence of the Radical Part of the TEMPO-OPE Molecule on Electron Transport Properties

The optimized OPE and Keto-OPE molecules both show a planar structure (see Figure 4), and the transport properties for both molecules are very similar. The calculated transmission functions, subsystem-molecular orbitals, and local transmissions are depicted in Figure 5. The two peaks in the transmission function closest to  $E_F$  can be assigned to the transport through the HOMO (at lower energies, hole transport) and the transport through the LUMO (at higher energies, electron transport). The transmission function for the OPE molecule is in agreement with other calculated transmission functions from the literature [70–72]. The local transmissions indicate the path of the conducted electrons at  $E_F$  to be along the OPE backbone, which is not strongly influenced by the phenyl-ketone group.

For the *cis*-TEMPO-OPE, the proximity of the TEMPO radical to one of the outer rings leads to a distortion of the formerly planar OPE structure, inducing a twist of one of the outer rings. This is mainly induced by dispersion interactions, which is indicated by the fact that omitting dispersion interactions in the structure optimization again leads to a planar structure (see Appendix B). This should reduce the transmission compared to the OPE molecule. For the *trans*-isomer, the OPE-backbone is almost planar, which is why the *cis*-isomer should also be less conducting than the *trans*-isomer. Both is also confirmed by the calculated transmission functions.

The calculated transmission functions, subsystem-molecular orbitals, and local transmissions for the *cis*- and *trans*-TEMPO-OPE are depicted in Figure 6, the calculated spin densities are shown in Figure 7. Qualitatively, the transmission function for the *cis*- and *trans*-isomer are very similar compared to the transmission function of the OPE molecule. The closest peak in the transmission function below  $E_F$  corresponds to the HOMO (hole transport), and the closest peak at higher energies corresponds to the LUMO (electron transport). The low transmission of the *cis*-isomer compared to the *trans*-isomer can be explained by looking at the HOMO and LUMO (Figure 6, part b).

While for the *trans*-isomer, atomic orbitals on all carbon atoms of the OPE backbone evenly contribute to both orbitals, the contribution of the carbon atoms of the twisted ring is much smaller for the *cis*-isomer. Therefore, the coupling to the electrodes should be asymmetric for the *cis*-isomer, while it should be symmetric for the *trans*-isomer. This can be confirmed by a Breit–Wigner fit<sup>15</sup>, assuming the transport being dominated by a single level (here the HOMO, see Appendix B). Since the Breit–Wigner fit in the experiments are nearly symmetric with respect to the coupling to the left and right electrode, the structure of the *trans*-isomer can be assumed to be closer to the structure in the experiment, or the tilting of the ring is overestimated by the employed dispersion interaction.

For the whole range of energy,  $\mathcal{T}^{\alpha\alpha}(E)$  and  $\mathcal{T}^{\beta\beta}(E)$  are almost the same (see Figure 6, part a). This indicates that no spin density is located on the transport path of the current, which is confirmed by the spin densities in combination with the local transmissions (see Figure 6, part c, and Figure 7). A small feature in  $\mathcal{T}^{\alpha\alpha}(E)$  is located at the energy of the SOMO ( $E - E_F = -0.15$  eV) for the *cis*-isomer, but the feature is negligible due to its small size. This behavior can be explained by the localization of the SOMO on the TEMPO part of the TEMPO-OPE molecule, and its vanishing expansion onto the OPE backbone (where the current goes through). Since the HOMO and LUMO are completely localized on the OPE backbone, they do not couple electronically with the SOMO (see Figure 6, part b). This leads to an absence of a Fano resonance at the energy of the SOMO.

Thus, no insight into the magnetoresistance of the TEMPO-OPE molecular junction can be gained because the electron transport seems to be unaffected by the SOMO and no spin density is located on the transport pathway of the conducted electrons.

---

<sup>15</sup> A Breit–Wigner fit assumes a single-level dominated transport and is fitted against the calculated transmission function. Experimentally, the Breit–Wigner fit can be done using the measured  $I$ - $V$  curves and using the Landauer formula [16].

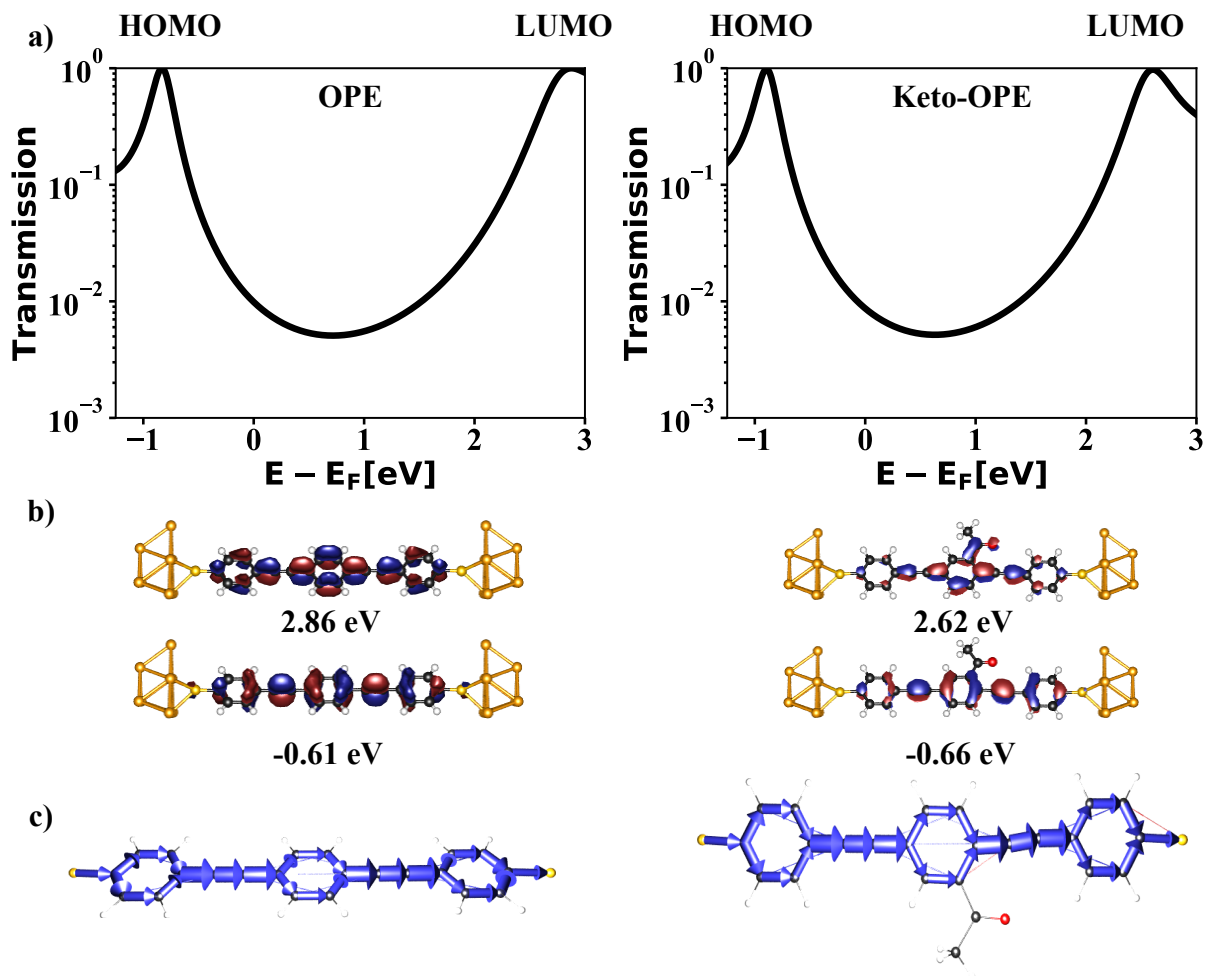


Figure 5: Electron transport properties of the OPE and Keto-OPE molecule using B3LYP/def2-SVP. The calculated transmission functions (a), subsystem-molecular orbitals of the molecule-only central region (b) and local transmissions at the estimated  $E_F$  (c) are shown. All energies are shifted with respect to the estimated  $E_F$  of -5 eV. Both molecules show a peak close to the energy of the HOMO and LUMO. The local transmissions indicate that for both molecules, the current is mainly moving along the OPE backbone.

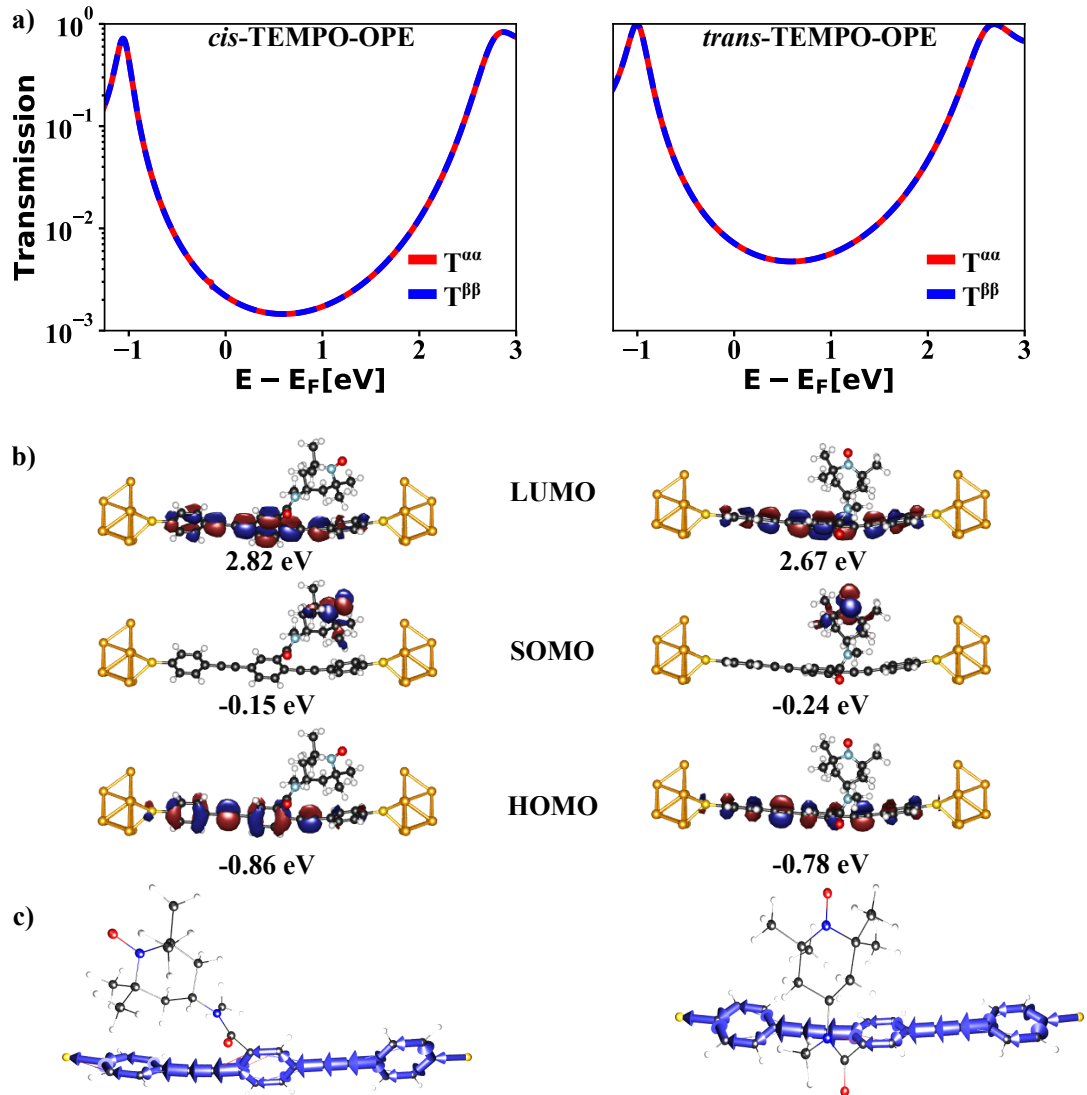


Figure 6: Transport properties of the *cis*- and *trans*-TEMPO-OPE molecule using B3LYP/def2-SVP. The calculated transmission functions (a), subsystem-molecular orbitals of the molecule-only central region (b), and local transmissions at the estimated  $E_F$  (c) are shown. All energies are shifted with respect to the estimated  $E_F$  of -5 eV. Since the energies and shapes for the  $\alpha$  and  $\beta$  parts of the HOMO and LUMO are the same, only one spin part is shown. Both molecules show a peak close to the energy of the HOMO and LUMO. No significant feature can be observed at the energy of the SOMO.  $T^{\alpha\alpha}$  and  $T^{\beta\beta}$  are nearly the same for the whole energy range depicted. The local transmissions indicate that the current is not passing the radical and only moves through the OPE backbone.

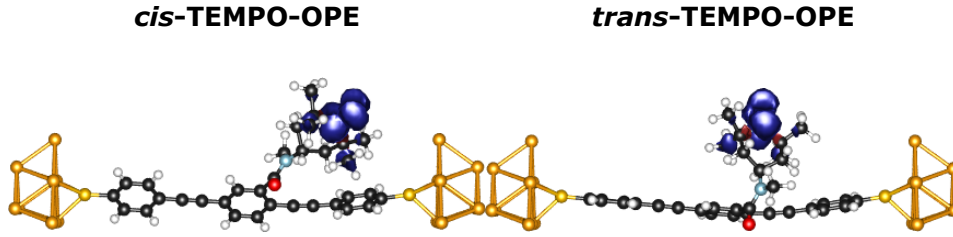


Figure 7: Calculated spin densities for the *cis*- and *trans*-TEMPO-OPE molecules (isosurface value: 0.001). For both isomers, the spin density does not extend onto the OPE backbone. Therefore, the spin density does not seem to influence the electron transport.

As a conclusion, the results suggest that the SOMO does not contribute to the electron transport. This is in agreement with the absence of a Kondo resonance in the experiment [16] because the current neither passes the radical nor any spin density. Thus, the transport calculations cannot give any hint for an explanation of the observed large magnetoresistance in TEMPO-OPE single-molecule junctions. The validity of the electron transport calculations done for the TEMPO-OPE molecule are supported by the fact that the transmission function for the *trans*-TEMPO-OPE molecule is of the same order of magnitude as for the OPE molecule, which is in agreement with the experimental results [16].

Besides the molecule forming the contact, many additional molecules likely cover the electrode in the experimental setup [67]. Those molecules may also react to an external magnetic field, influence the transport, and may be the origin of the large magnetoresistance. To obtain insight into the interaction between the TEMPO-OPE molecules and the gold electrodes, a TEMPO-OPE molecule was optimized<sup>16</sup> on a gold surface and the results of this investigation are discussed next.

---

<sup>16</sup> PBE with periodic-boundary conditions and a modified  $C_6$  parameter for gold in the DFT-D2 method. See Appendix B for details.

### 3.3.2. Possible Interaction between TEMPO Radical and Gold Electrodes

A potential interaction of the adsorbed TEMPO-OPE molecules with the gold electrodes was investigated by optimizing the TEMPO-OPE molecule on a gold-(111)-surface. Two different unit cells ( $d_{\text{Au-Au}} = 2.884 \text{ \AA}$ ) were used: a smaller one ( $4 \times 4$  surface, slab consisting of four atomic layers of gold) where the neighboring TEMPO-OPE molecules could interact with each other, and a larger one ( $7 \times 7$  surface, slab consisting of three atomic layers) where the TEMPO-OPE molecule was nearly isolated<sup>17</sup>.

The optimized structures indicate that the TEMPO radical part of the molecule is getting close to the gold surface (see Figure 8). If the interaction of the TEMPO radical with the surface depended on an external magnetic field, the electronic structure of the electrode/interface could be affected by this field. This could affect the electronic coupling of the electrode with the molecule, and therefore the electron transport. A change of coupling due to the magnetic field would be consistent with the experimental Breit-Wigner fit, which indicates the coupling of the molecule to the left and right electrode to decrease with the magnetic field [16]. A more detailed analysis of the bonding situation of the radical part of the TEMPO-OPE molecule and the gold electrode, as well as the reaction to an external magnetic field could give helpful insights into the origin of the magnetoresistance. However, due to reasons of time this task is not part of thesis anymore.

In addition to the TEMPO-OPE molecule, the transport properties of four other organic radicals were calculated. Due to a similar structural motif as the TEMPO-OPE molecule (radical which is attached to a conducting conjugated backbone), first-principles electron transport properties of these four radicals might be the basis of structure-property relationship investigations of magnetoresistance and electron transport for such systems.

---

<sup>17</sup> Since the optimization moved both thiol groups close to the surface, the hydrogen atoms of both thiol groups were removed. This allowed both thiolates to form bonding interactions with the gold.

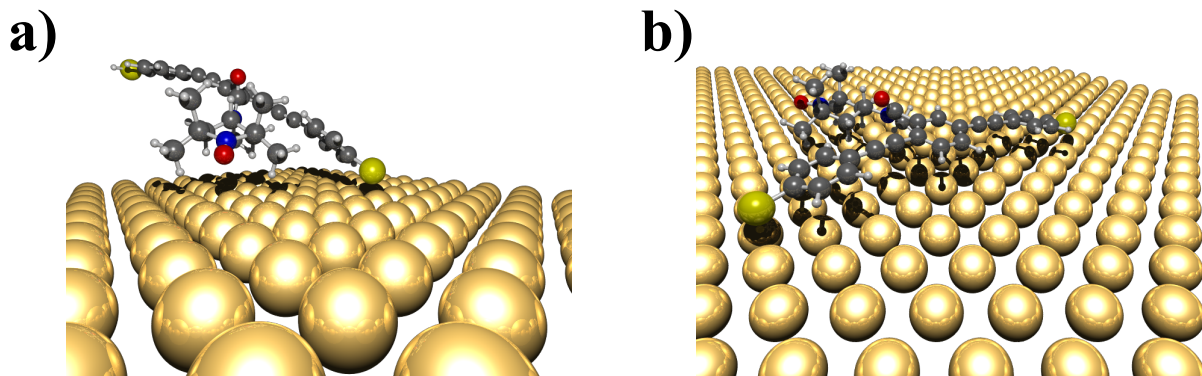


Figure 8: Optimized structures of the TEMPO-OPE molecule on a gold surface using periodic-boundary conditions, PBE, and a modified  $C_6$  parameter of gold for the DFT-D2 method. Tonigold *et al.* [73] showed that the dispersion interaction of gold and aromatic molecules is better described by changing the default  $C_6$  parameter of gold (DFT-D2). Only a single molecule is depicted (see Appendix B for a picture with neighboring TEMPO-OPE molecules). **a)** Illustration of a TEMPO-OPE molecule on a Au(111)-surface ( $4 \times 4$  surface cell). The interaction of the TEMPO-OPE molecule with its periodic images prevents the TEMPO-OPE from completely flat adsorbing on the gold surface with the OPE backbone. The TEMPO radical is close to the surface ( $d_{\text{O}-\text{Au}} = 3.13 \text{ \AA}$ ). **b)** Illustration of the nearly isolated TEMPO-OPE molecule adsorbed on a Au(111)-surface ( $7 \times 7$  surface cell). The molecule is lying on the surface and the OPE backbone is nearly planar and nearly parallel to the surface. The TEMPO part is again close to the gold surface ( $d_{\text{O}-\text{Au}} = 4.39 \text{ \AA}$ ).

### 3.4. Effect of Structural Changes on Electron Transport Properties at the example of Organic Radicals Similar to TEMPO-OPE

To investigate the electron transport properties of four organic radicals which all share the same structural motif, a conducting diamagnetic backbone being functionalized with a radical group (see Figure 9), the exact same methodology used for the calculation of electron transport properties for TEMPO-OPE single-molecule junctions was employed. Radicals 1 and 2 consist of an imidazole-based radical linked to a 1,4-(biphenyl)-benzene backbone. While for radical 1 the thiol-anchoring groups are directly attached to the 1,4-(biphenyl)-benzene backbone, for radical 2 benzenethiol is attached to the 1,4-(biphenyl)-benzene backbone with an ethynyl linker. The molecules 3 and 4 are based on the TEMPO-OPE molecule, replacing the TEMPO radical and its linker with an imidazole and a tert-butyl nitroxide based radical, respectively (see Figure 9). The direct connection of the radicals to the backbone may induce a stronger electronical coupling of the SOMO with the HOMO/LUMO, a direct participation of the SOMO in the electron transport, or a removal of the degeneracy of the  $\alpha$  and  $\beta$  part of the HOMO/LUMO. The gold–molecule–gold junctions of the radicals were prepared in the same way as for the OPE, Keto-OPE, and TEMPO-OPE molecules. Radical 3 adsorbed on a Au(111) surface was already shown to exhibit the Kondo effect [74] and it is actually investigated experimentally by Scheer *et al.* for molecular junctions. Radical 3 and the other radicals represent molecules which might be interesting for the investigation of structure-property relations of magnetoresistance and electron transport (the structural changes might lead to a direct interaction of the radical with the conducted electrons) in molecules with a similar general structural motif as the TEMPO-OPE molecule.

For radical 1 and 2 (see Figure 10 for radical 1 and Figure 11 for radical 2), the peaks in the transmission function closest to  $E_F$  can be assigned to the transport through the HOMO (at lower energies) and the transport through the LUMO (at higher energies). For radical 1, the  $\alpha$  and  $\beta$  parts of the HOMO and LUMO are nearly degenerate, and the SOMO does not induce a Fano resonance. For radical 2, a Fano resonance occurs in

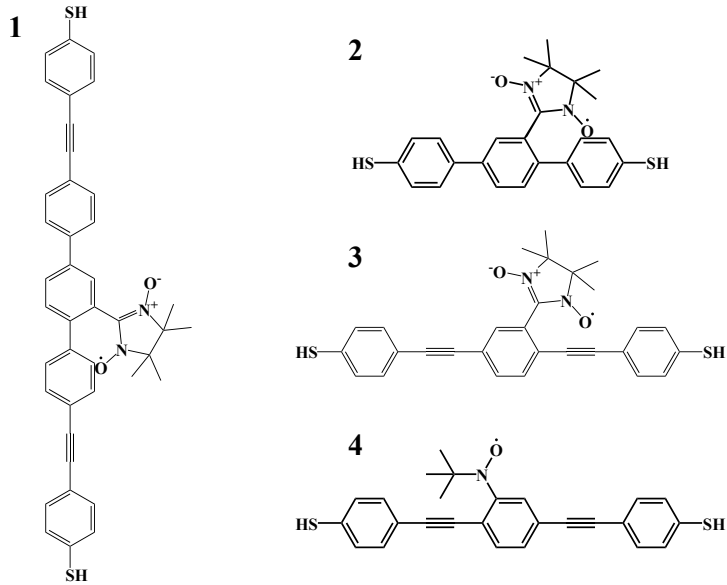


Figure 9: Lewis structure of additionally investigated organic radicals for a potential investigation of property-structure relationships of the spin dependent transport. The radicals differ in the type of radicals attached to the conducting backbone as well as in the type of conducting backbone.

$\mathcal{T}^{\beta\beta}(E)$  located at the energy of the  $\beta$  part of the SOMO. The  $\alpha$  part of the SOMO does not induce a feature in  $\mathcal{T}^{\alpha\alpha}(E)$ , which may originate from its energy being far away from the HOMO/LUMO (about 1 eV/3 eV). The  $\alpha$  and  $\beta$  parts of the HOMO and LUMO are nearly degenerate. Besides the Fano resonance, no significant difference in  $\mathcal{T}^{\alpha\alpha}(E)$  and in  $\mathcal{T}^{\beta\beta}(E)$  occurs and the difference is negligible at the estimated  $E_F$ . For molecules 3 and 4 (see Figure 12 for radical 3 and Figure 13 for radical 4), the closest peaks to  $E_F$  in the transmission function can again be assigned to the transport through the HOMO (at lower energies) and the transport through the LUMO (at higher energies). As for the TEMPO-OPE molecule, the  $\alpha$  and  $\beta$  parts of the HOMO and LUMO are nearly degenerate. For both molecules, a Fano resonance occurs in  $\mathcal{T}^{\alpha\alpha}(E)$  at the energies of the SOMO. This results in a slightly different transmission for  $\alpha$  and  $\beta$  electrons in the vicinity of  $E_F$ . The feature is much more pronounced for radical 4 than for radical 3, implying a stronger coupling of the SOMO with the HOMO/LUMO.

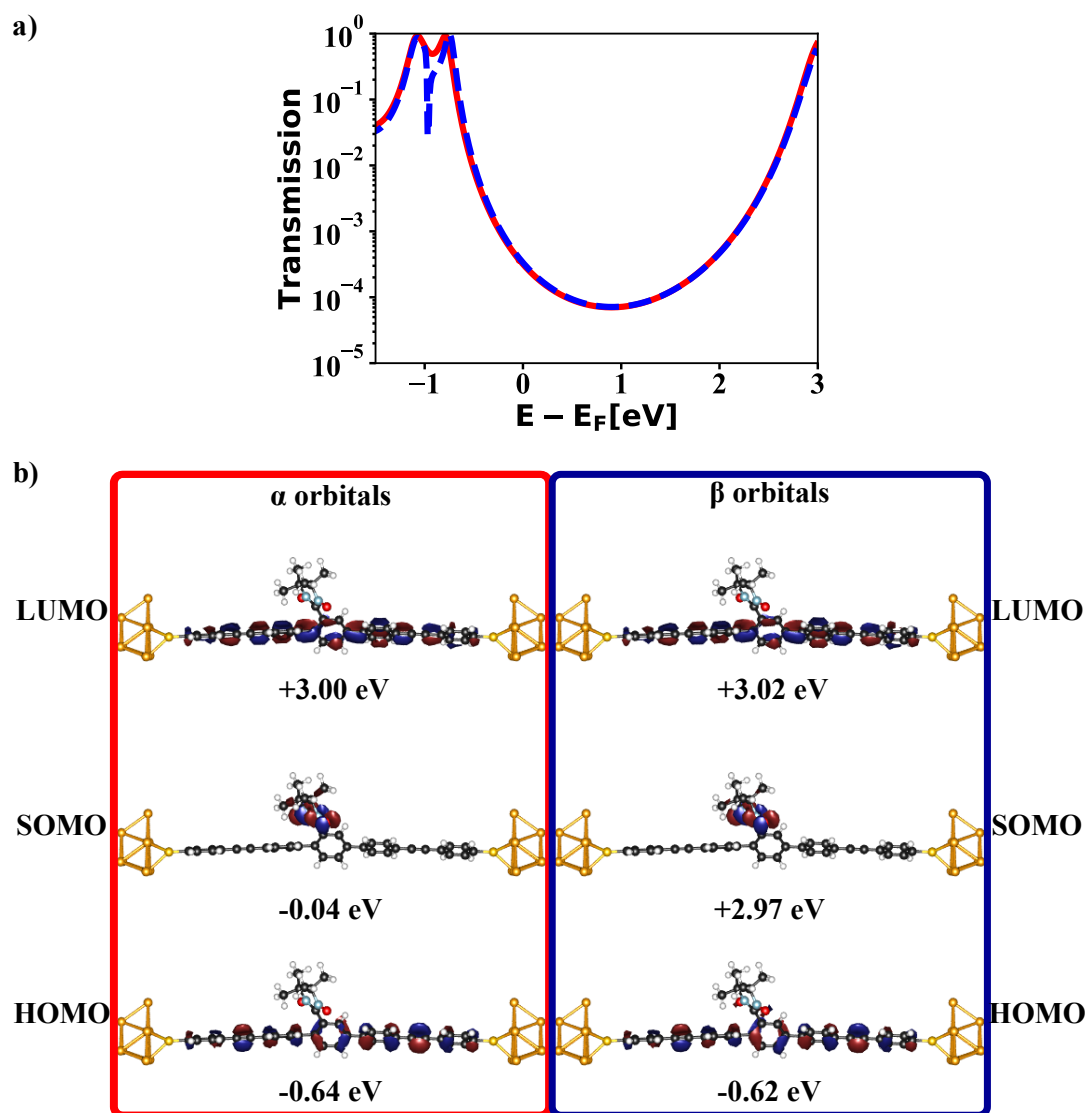


Figure 10: Calculated transmission functions (a) and subsystem molecular orbitals of the molecule-only central region (b) for  $\alpha$  and  $\beta$  electrons for radical 1. The HOMO and LUMO are nearly degenerate with respect to the spin, and the SOMO does not induce spin-dependent features in  $\mathcal{T}(E)$ . All energies are shifted with respect to the estimated  $E_F$  of -5 eV. The molecular orbitals were assigned by comparison with the molecular orbitals of the isolated molecule.

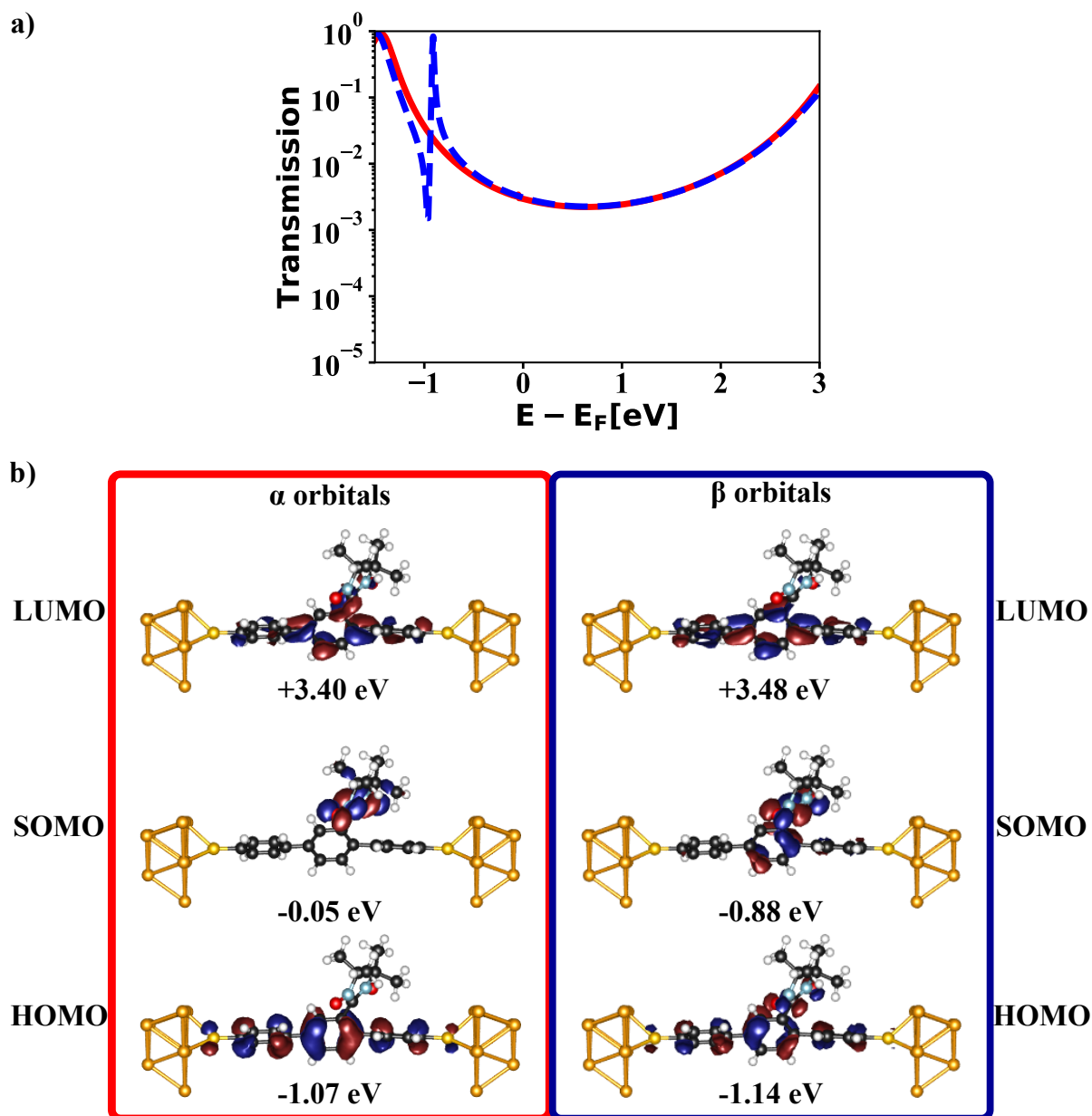


Figure 11: Calculated transmission functions (a) and subsystem-molecular orbitals of the molecule-only central region (b) for  $\alpha$  and  $\beta$  electrons for radical 2. While the HOMO and LUMO are nearly degenerate with respect to the spin, the  $\beta$  SOMO induces a Fano resonance at about -0.88 eV. This resonance leads a different transmission of  $\alpha$  and  $\beta$  electrons. However, both transmissions are nearly the same at  $E_F$ . All energies are shifted with respect to the estimated  $E_F$  of -5 eV. The molecular orbitals were assigned by comparison with the molecular orbitals of the isolated molecule.

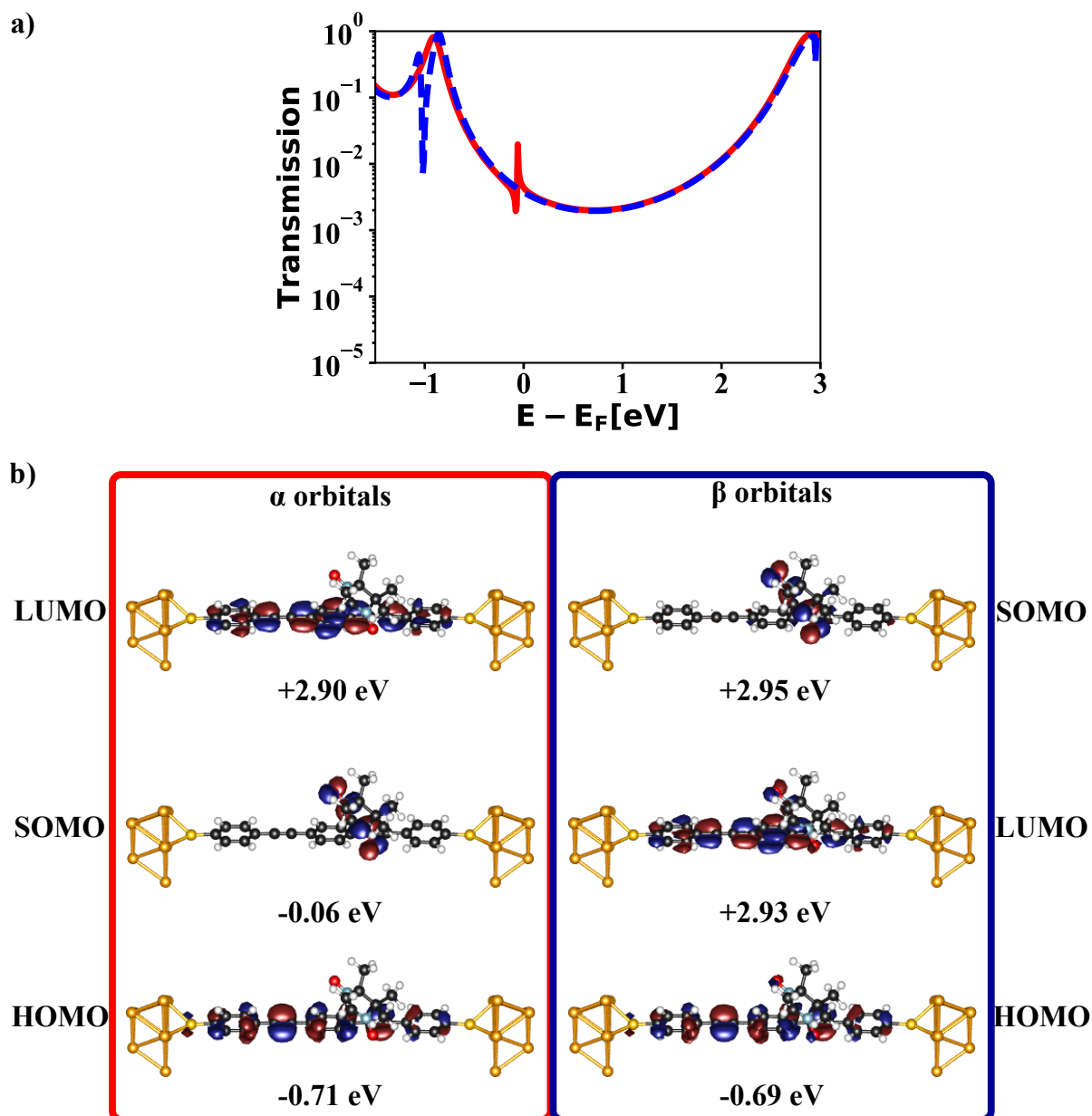


Figure 12: Calculated transmission functions (a) and subsystem-molecular orbitals of the molecule-only central region (b) for  $\alpha$  and  $\beta$  electrons for radical 3. While the HOMO and LUMO are nearly degenerate with respect to the spin, the  $\alpha$  SOMO induces a Fano resonance at about -0.06 eV. This resonance induces a different transmission of  $\alpha$  and  $\beta$  electrons, which is very small at the vicinity of  $E_F$ . All energies are shifted with respect to the estimated  $E_F$  of -5 eV. The molecular orbitals were assigned by comparison with the molecular orbitals of the isolated molecule.

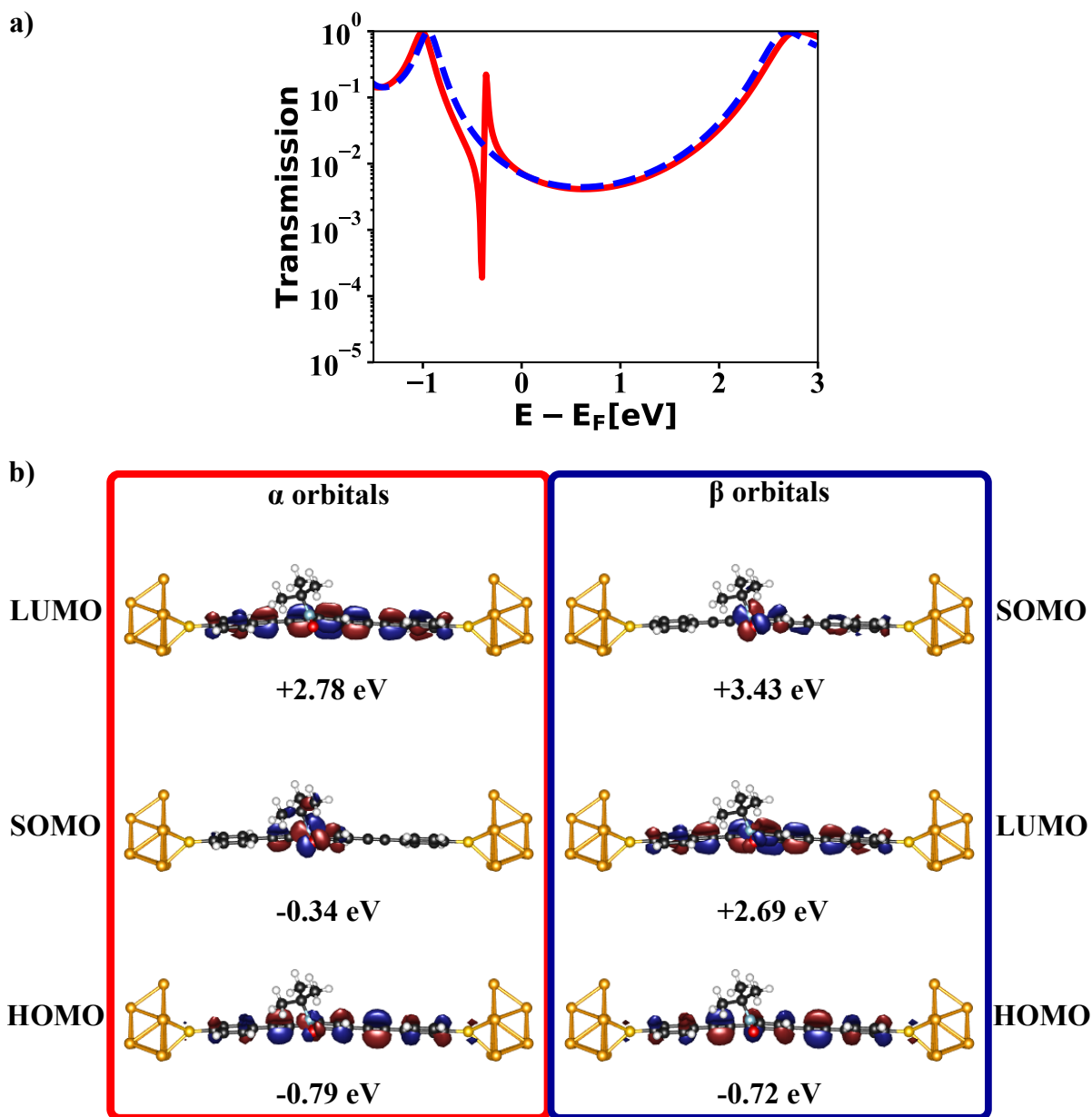


Figure 13: Calculated transmission functions (a) and subsystem-molecular orbitals of the molecule-only central region (b) for  $\alpha$  and  $\beta$  electrons for radical 4. While the HOMO and LUMO are nearly degenerate with respect to the spin, the  $\alpha$  SOMO induces a Fano resonance at about -0.34 eV. This resonance induces a different transmission of  $\alpha$  and  $\beta$  electrons, which is rather small at  $E_F$ . All energies are shifted with respect to the estimated  $E_F$  of -5 eV. The molecular orbitals were assigned by comparison with the molecular orbitals of the isolated molecule.

The results of the electron transport calculations for the four investigated radicals may provide the basis of further investigations regarding spin-dependent electron transport in similar organic radicals or regarding structure-property relations of magnetoresistance in organic radicals with the same structural motif. The calculations indicate that some of these radicals may exhibit interesting spin-dependent transport phenomena due to an indirect participation of the SOMO in the transport. The calculations show that changing the radical part or the conducting backbone of the TEMPO-OPE molecule might lead to a direct influence of the radical on the electron transport.

### 3.5. Conclusion

In this part of the thesis, spin-dependent transport properties of several organic radicals have been investigated based on the Landauer approach in combination with DFT, focusing on finding an explanation for the experimentally observed magnetoresistance in a TEMPO-OPE molecular junction.

The transport calculations indicate that the unpaired electron does not influence the transport significantly. The SOMO does not contribute to the transport, and  $\mathcal{T}^{\alpha\alpha}(E)$  and  $\mathcal{T}^{\beta\beta}(E)$  in the vicinity of  $E_F$  are nearly the same. This originates from the localization of the SOMO on the TEMPO-radical part of the molecule. The transport calculations do not give any insight into the experimentally observed large magnetoresistance of the TEMPO-OPE molecule, and indicate that the TEMPO-OPE molecule forming the contact is not responsible for this phenomenon. Structure optimizations regarding the non-bridging TEMPO-OPE molecules covering the electrodes indicate a possible radical–electrode interaction. Such an interaction may depend on an external magnetic field and therefore may influence the coupling of the electrode with the molecule indirectly.

## 4. Circular Photogalvanic Effect in Lead-(II)-Sulfide Nano-sheets

Besides unpaired electrons, this work deals with SOC as an origin of spin-dependent electron transport properties, focusing on the Rashba effect in nanostructured materials and the Rashba-like CISS effect. In this part of the work, results of an investigation concerning the Rashba effect in nanostructured materials are presented.

The investigation in this part was aimed to identify the origin of the CPGE induced current observed for lead-(II)-sulfide nanosheets. All experiments were done by Klinker *et al.* and are documented in a joint publication [17].

### 4.1. Introduction

Semiconducting materials in combination with strong SOC are of great importance in the field of spin-orbitronics. In this field, effects based on SOC are used to manipulate the spin [75]. Spin-orbitronic materials allow to control the electron's spin-degree of freedom with electric fields [75] and show magnetoresistance [76], making them promising for the development of new spintronic devices [75,77].

An important spin-orbitronics effect is the Rashba effect [75,78]. It originates from a combination of SOC and structure inversion asymmetry<sup>18</sup>. Devices based on this effects were suggested for spin field-effect transistors [80,81], spin-charge converters [77,82,83] and charge-spin converters [77]. The effect is also interesting from a chemical point of view, since the Rashba effect can be chemically controlled by using different adsorbates or by chemical modification [82,84].

The strength of the Rashba effect in a system can be estimated by making use of the CPGE, which manifests as a current induced by the illumination of those materials with

---

<sup>18</sup> Such materials are symmetric under spatial inversion in bulk, but inversion symmetry is broken, *e.g.* due to interfaces like in quantum wells. A familiar effect is the Dresselhaus effect, which occurs in materials with bulk inversion asymmetry [79].

circularly polarized light [85–88]. Although such a current is not expected for highly symmetric systems [17], Klinke *et al.* observed a CPGE-induced current in (001)-lead-(II)-sulfide nanosheets, which are symmetric under inversion ( $D_{4h}$  symmetry) [17]. In their experimental setup (see Figure 14), the nanosheets were placed on a silicon/silicondioxide substrate, contacted with gold electrodes, and a gate voltage was applied perpendicularly to the nanosheet. The asymmetric interface (silicon/silicondioxide substrate and vacuum) as well as the electric field of the gate were assumed to break inversion symmetry (Symmetry:  $D_{4h}$  to  $C_{4v}$ ), which in combination with the strong SOC of the lead were assumed to induce a Rashba effect. This finding was promising, because the preparation of lead-(II)-sulfide nanosheets is inexpensive in comparison to other Rashba nanostructures [17], *e.g.* based on indium-(III)-nitride [87] or zinc-(II)-oxide [89].

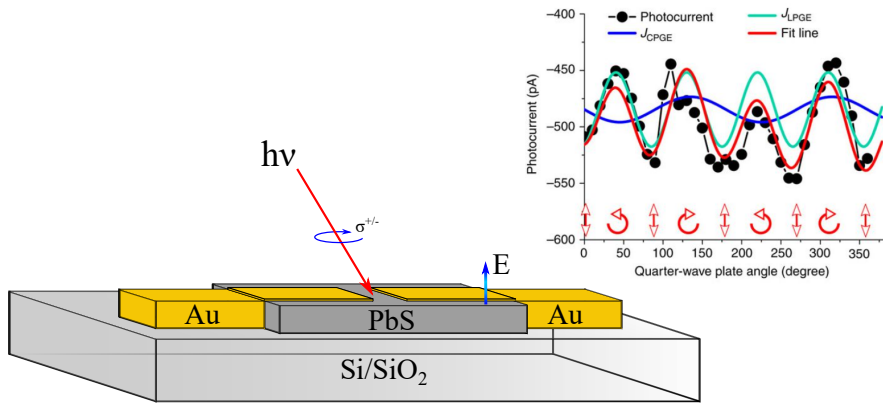


Figure 14: Experimental setup and measured photocurrent by Klinke *et al.*. The (001)-lead-(II)-sulfide nanosheets were placed on a silicon/silicondioxide substrate and contacted with gold electrodes. After illuminating the nanosheet with red light, a photocurrent was detected. The photocurrent at zero bias depends on the quarter-wave plate angle, *i.e.*, on the polarization of the light. A fit of the photocurrent shows, besides a linear photogalvanic effect, a non-zero circular photogalvanic effect. The magnitude of the photocurrent which is induced by the CPGE is controllable by the angle-of illumination and an electrical field from the gate [17].

The goal of the theoretical investigation concerning lead-(II)-sulfide was to verify the presence of a Rashba effect in lead-(II)-sulfide nanosheets and, thus, to give a first-principles based explanation of the observed CISS effect. Before discussing the theoretical study, additional theoretical background is given to understand the results of the calculations. Although it was assumed that the CPGE in lead-(II)-sulfide nanosheets originated from the Rashba effect, other plausible explanations were possible and investigated, like lead-(II)-sulfide sheets being topological insulators [75, 90] or exhibiting spin–valley coupling [91–94]. Thus, besides the Rashba effect, topological insulators and spin–valley systems are also subject of the additional theoretical background.

### **P- and T-Symmetry in Periodic Systems**

The solutions of the Schrödinger equation under periodic-boundary conditions have the form [95]

$$\Omega_j(\mathbf{r}, \mathbf{k}) = u_j(\mathbf{r}, \mathbf{k}) \cdot e^{i\mathbf{k}\cdot\mathbf{r}}, \quad (4.1)$$

where  $\mathbf{k}$  is a wave vector, describing the quasimomentum of the electron in the crystal and  $u_j(\mathbf{r}, \mathbf{k})$  is a Bloch function, reflecting the periodicity of the crystal lattice. The states described with the same index  $j$  form a band. Therefore, the electronic structure of a solid can be described with a band structure, in which the energies of the bands' states are plotted against  $\mathbf{k}$ .

Bands where all states are occupied are called valence bands and bands which are completely unoccupied or partly occupied are called conduction bands [95]. Solids can be classified as insulators, semiconductors or metals [95]. In insulators and semiconductors, all valence bands are fully occupied and all conduction bands are empty. The highest valence band and the lowest conduction band are separated in energy by the band gap, which is small compared to  $k_B T$  for semiconductors. Metals are defined as systems with partially filled conduction bands and do not have a band gap.

Two important symmetries can be defined in band structures, namely P-symmetry (space-inversion symmetry) and T-symmetry (time-reversal symmetry) [79]. P-symme-

try describes the invariance under space inversion and T-symmetry the invariance under time reversal<sup>19</sup>. Both symmetries lead to certain relations within the band structure, which are mathematically defined for P-symmetry as

$$E^\uparrow(\mathbf{k}) = E^\uparrow(-\mathbf{k}), \quad (4.2)$$

and for T-symmetry as

$$E^\uparrow(\mathbf{k}) = E^\downarrow(-\mathbf{k}). \quad (4.3)$$

$E^\uparrow(\mathbf{k})$  describes the energy of a band at  $\mathbf{k}$  for one spin orientation, and  $E(\mathbf{k})^\downarrow$  the energy of a band at  $\mathbf{k}$  for the opposite one. If both symmetries are present, the relation

$$E^\uparrow(\mathbf{k}) = E^\downarrow(\mathbf{k}) \quad (4.4)$$

is valid, *i.e.*, no spin splitting of the band structure is possible. A removal of structural inversion-symmetry in combination with strong SOC can lead to a removal of P-symmetry in the band structure [79], which allows for spin splitting in the band structure.

### **Materials with a Band Structure without P-Symmetry**

The CPGE is closely connected to the removal of the P-symmetry in the band structure and, *e.g.* can be observed in Rashba systems, topological insulators, and spin–valley materials [93, 94, 96–101]. In the following, those systems are explained.

#### Rashba effect

The Rashba effect occurs for systems with structure inversion asymmetry [79]. Those systems are symmetric under inversion in bulk, but inversion symmetry is broken, *e.g.* due to an interface (like in quantum wells) [75], at metallic surfaces [102], or due to

---

<sup>19</sup> Space inversion inverts the momentum of the electron, time reversal inverts the momentum and flips the spin.

distortions [103]. The effect was originally described for a two-dimensional electron gas [78] defined by the Hamiltonian

$$\hat{H} = \frac{\hbar^2}{2m^*} \mathbf{k}_{\parallel}^2, \quad (4.5)$$

where  $\mathbf{k}_{\parallel}$  is the two-dimensional quasimomentum and  $m^*$  is the effective mass of the electron [78]. The resulting bands have a parabolic shape and are centered at  $\mathbf{k}_{\parallel} = (0, 0)$ . Each band consists of two spin sub bands, describing the two different degenerate spin projections (see Figure 15, part a). If an electric field is applied perpendicularly to the two-dimensional electron gas, an effective magnetic field is induced by the momentum  $\mathbf{k}_{\parallel}$  of the electron. This allows the spin to couple with the quasimomentum, due to SOC [75]. Since the orientation of the magnetic field is depending on the direction of the electron's momentum, the degeneracy of the spin states for the same non-zero  $\mathbf{k}_{\parallel}$  is removed (see Figure 15, part b) [75]. One spin sub band shifts towards higher values of  $\mathbf{k}_{\parallel}$ , and the other one towards lower values of  $\mathbf{k}_{\parallel}$ . P-symmetry of the band structure is removed. This band splitting is also called Rashba spin splitting or Rashba effect [75, 78, 104, 105].

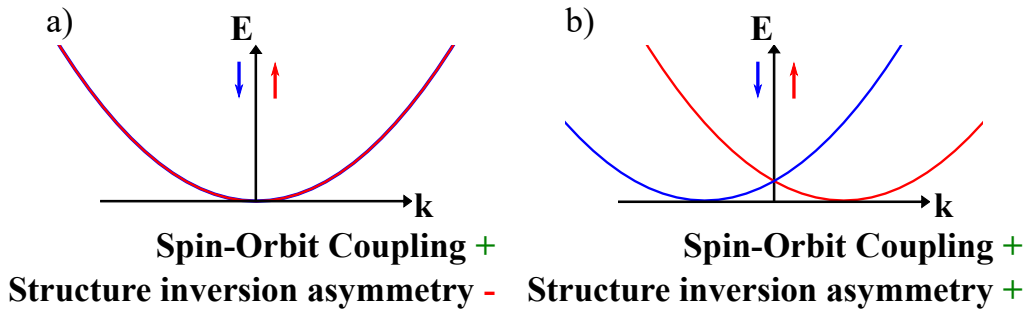


Figure 15: Removal of P-symmetry due to a combination of SOC and structure inversion asymmetry [79]. **a)** SOC does not remove the P-symmetry in the band structure for systems which are symmetric under spacial inversion in bulk. **b)** The combination of structure inversion asymmetry with SOC leads to a splitting of the bands, shifting bands with one spin to values of higher  $\mathbf{k}$  and bands with the opposite spin to values of lower  $\mathbf{k}$ .

Phenomenologically, the effect is described by the Rashba-SOC Hamiltonian [78, 79]

$$\hat{H}_R = \left( \frac{\alpha_R}{\hbar} \right) (\mathbf{e}_z \times \mathbf{k}) \cdot \boldsymbol{\sigma}. \quad (4.6)$$

$\alpha_R$  is the Rashba parameter depending on the strength of the electric field [106] and  $\mathbf{z}$  is the direction of the electric field, which is oriented perpendicular to the two-dimensional electron gas [75]. The electric field can be an external electric field or internal electric fields originating from structure inversion asymmetries [75, 79]. The Rashba effect can thus be modified by an external electrical field, which opens the possibility to manipulate the spin with such a field [75, 80, 81].

### Topological Insulators

Normal insulators are defined by a large band gap compared to  $k_B T$  [95] separating the highest valence and the lowest conduction band (see Figure 16, part a). Such materials have bad conducting properties compared to metals due to the high-energy cost of creating mobile charge carriers [95]. For topological insulators the valence and conduction bands intersect with each other, which would in principle lead to metallic behavior and is called band inversion because the orbital character of the valence and conduction band changes for some values of  $\mathbf{k}$  (see Figure 16, part b) [107]. Both bands are coupled by SOC, which leads to an opening of a band gap and transforms the metallic system into an insulator (see Figure 16, part c) [107]. Such systems can possess metallic surface states<sup>20</sup> or metallic edge states<sup>21</sup> within the bulk band gap [75, 107, 108]. Those surface states have a special spin texture with broken P-symmetry, a linear band dispersion [98], and can be manipulated with electric fields [109, 110].

A transition from a normal insulator to a topological insulator was observed for, *e.g.*  $\text{Pb}_x\text{Sn}_{1-x}\text{Te}$  materials [111].

---

<sup>20</sup> Three-dimensional topological insulator

<sup>21</sup> Two-dimensional topological insulator

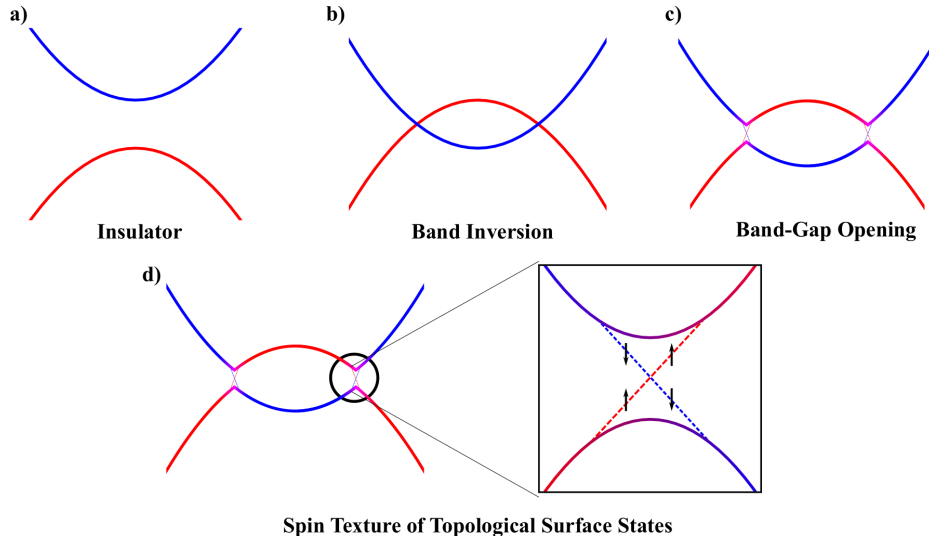


Figure 16: Illustration of a transition from a trivial insulator to a topological insulator [107]. The energy-axis and  $\mathbf{k}$ -axis are not written sake of clarity. **a)** For normal insulators the highest valence band (red) and lowest conduction band (blue) are separated by the band gap. **b)** If SOC was neglected, a system with intersecting bands would show metallic behavior. **c)** Since both bands are coupled due to SOC, a band gap opens and the bulk system behaves as an insulator. **d)** Possible band dispersion of metallic surface or edge states (dotted lines), which are characteristic for topological insulators.

### Spin-Valley Coupling

Besides spin and charge, the electron can have an additional degree of freedom which is called valley-pseudospin [112]. This variable describes which valley of the band structure the electron occupies. A valley is the designation for a local maximum in the valence band or a local minimum in the conduction band. Due to strong SOC and if inversion symmetry is broken, the electron's spin can couple with the valley-pseudospin, leading to a Zeemann-like spin-splitting at the valleys [92,113] (see Figure 17). This behavior can be explained for monolayers of  $\text{MoS}_2$  possessing a hexagonal Brillouine zone with two different valleys at the K- and K'-points [92,112]. In the absence of SOC, the valleys are degenerate with respect to the spin but can be distinguished by their valley-pseudospin (-K and +K). If SOC is considered, the valley-pseudospin and the spin can couple and

the spin bands are split at the valleys (see Figure 17). T-symmetry is not broken due to SOC, and the spin-splitting is opposite if comparing the -K with the +K valley.

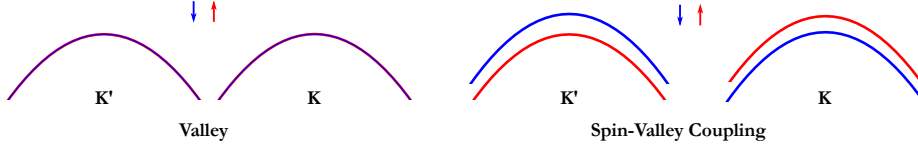


Figure 17: Schematic band structure describing spin–valley coupling [92]. **a)** In MoS<sub>2</sub> monolayers two valleys can be distinguished with respect to their valley pseudospin, located at the K and K' point. **b)** Due to SOC the valley pseudospin and the spin of the electron can couple leading to a Zeeman-like splitting of the spin bands. The splitting is different at the K and K' point.

### Circular Photogalvanic Effect

Due to the absence of P-symmetry in the band structures of the systems discussed above, an observation of a CPGE-induced current in such systems is possible and can be explained by the selection rules for optical excitations, focusing on the total angular momentum  $j$  and the projection of the total angular momentum onto the quantization axis  $m_j$ .

If SOC is considered, excitations of electrons from one band into another must follow the selection rule  $\Delta m_j = 0, \pm 1$ . This is the case because the photon has a spin-angular momentum of  $\sigma_p = \pm 1$  oriented along its line-of flight. This selection rule depends on the orientation of the axis for which  $\Delta m_j$  defines the change of total-angular momentum relative to the orientation of  $\sigma_p$ , *i.e.*, to the line-of flight of the photon: if both are aligned parallel,  $m_j$  has to change by  $\pm 1$ . Otherwise, transitions with  $\Delta m_j = 0$  are also allowed [95, 114].

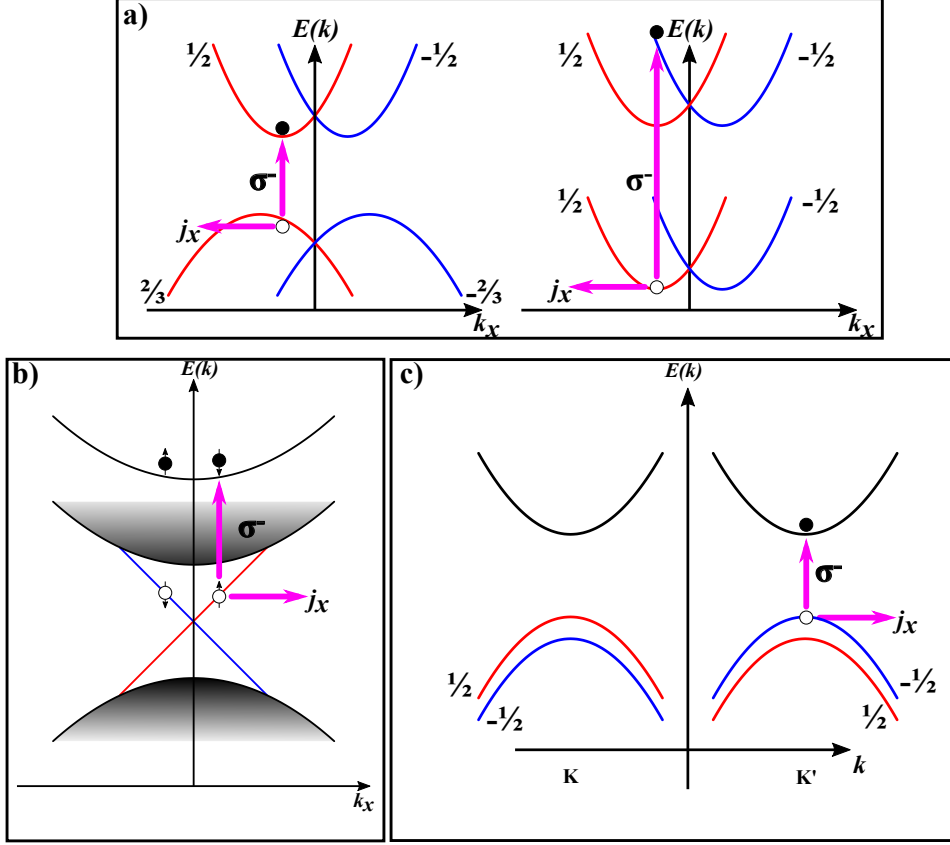


Figure 18: Possible mechanisms of CPGE in Rashba systems, topological insulators, and spin-valley systems. **a)** For Rashba systems, two different selection mechanisms are given, which depend on the character of the valence and conduction bands. This are either excitations from a  $j = \frac{3}{2} / m_j = \pm \frac{3}{2}$  valence band in a  $j = \frac{1}{2} / m_j = \pm \frac{1}{2}$  conduction band or excitations from a  $j = \frac{1}{2} / m_j = \pm \frac{1}{2}$  valence band in a  $j = \frac{1}{2} / m_j = \pm \frac{1}{2}$  conduction band. In both cases, illumination with circularly polarized light leads to an asymmetric charge carrier distribution resulting in a current  $j_x$  [96, 97]. **b)** For topological insulators, an asymmetric charge carrier distribution can be created by selectively exciting electrons with a certain spin orientation of the surface/edge states into conduction bands with circularly polarized light, resulting in a current  $j_x$  [98–100]. **c)** In spin-valley systems with a hexagonal Brillouin zone, electrons in certain valleys (K/K') are selectively excited with circularly polarized light. This results in an asymmetric charge carrier distribution and leads to a current  $j_x$  [93, 101].

An excitation from a  $j = \frac{1}{2}$  band into another  $j = \frac{1}{2}$  band due to photons with  $\sigma_p = +1$  would induce transitions of  $m_j = -\frac{1}{2} \rightarrow m_j = \frac{1}{2}$ . If P- and T-symmetry hold, the amount of excited charge carriers at  $\mathbf{k}$  is the same as at  $-\mathbf{k}$  (see Equation (4.2)), and no current would occur. If the P-symmetry of the band structure is broken, the amount of excited charge carriers can be different when comparing  $\mathbf{k}$  and  $-\mathbf{k}$ , which would result in an asymmetric charge-carrier distribution in  $\mathbf{k}$ -space and a current. This phenomenon is called CPGE [86, 88].

Due to the absence of P-symmetry in the band structure, different mechanisms for the CPGE, based on optical selection rules, can be formulated for the Rashba effect [96, 97](see Figure 18, part a), for topological insulators [98–100](see Figure 18, part b) and for spin–valley systems [93, 101](see Figure 18, part c).

To cover all possible underlying mechanisms of the CPGE in lead-(II)-sulfide nanosheets, a suitable method has to be chosen. Thus, the applicability of available methods to describe these effects with DFT is discussed next.

## 4.2. Theoretical Methods to Investigate the Circular Photogalvanic Effect in Lead-(II)-Sulfide Nanosheets

Since this work deals with a first-principles investigation of spin-dependent transport phenomena, the applicability of DFT to the previously described P-symmetry related effects is discussed now.

DFT under periodic-boundary conditions is a well-established method for the qualitative investigation of semiconductors, although it has been shown that DFT-based calculations for semiconductors tend to underestimate the band gap when using LDA and GGA functionals [115, 116]. Previous calculations for lead-(II)-sulfide, lead-(II)-selenide, and lead-(II)-telluride by Svane *et al.* [117] and by Hummer *et al.* [118] showed the occurrence of a band inversion when using LDA or GGA functionals in combination with SOC. This band inversion occurred due to an underestimation of the band gap in com-

parison to the experimental one and vanished for methods which predict band gaps in good agreement with the experiment (hybrid functionals and methods based on the *GW* approximation [117, 118]). Therefore, the band inversion was artificial. This problem could lead to a false-positive identification of lead-(II)-sulfide nanosheets as topological insulators and thus to a false origin of the CPGE effect. False-positive as well as false-negative identifications of materials as topological insulators were reported for instance in Reference [119]. For (111)-lead-(II)-chalcogenide surfaces, stress-induced topological phases were predicted using a hybrid functional [120]. For (001)-lead-(II)-selenide monolayers, topological states were predicted using pure functionals [121].

The Rashba splitting and its manipulation with an electric field were discussed in several theoretical studies for gold surface states [122, 123], as well as for semiconductors like perovskites [106, 124, 125], germanium-based systems [126, 127], and bismuth-based structures [128]. The results were consistent with experimental results, if available, and thus showed that DFT is a reliable tool for the investigation of the Rashba effect.

Spin–valley coupling was also successfully investigated using DFT, especially for layers of transition metal dichalcogenides like MoS<sub>2</sub> [129, 130] and WSe<sub>2</sub> [94, 130].

Overall, DFT has been employed to investigate the Rashba effect, topological insulators and spin–valley system, but semiconductors such as (001)-lead-(II)-sulfide nanosheets have been shown to be problematic systems using DFT in combination with pure functionals and SOC. To investigate the CPGE in lead-(II)-sulfide nanosheets, (001)-nanosheets (modeled by 15 atomic layers) and bulk lead-(II)-sulfide were simulated using DFT under periodic-boundary conditions (for details see Appendix A). SOC and an external electric field was considered in combination with a GGA functional, due to the high computational cost of hybrid functionals and approaches based on the *GW* approximation. To circumvent the problem of artificial topological states, the lattice constant as well as the atomic positions within the nanosheets were optimized (a dependence of the band gap on the lattice constant was shown, *e.g.* in Reference [131] for lead-(II)-telluride). Non-primitive unit cells were used for the calculation of the bulk and the

nanosheets (see Figure 19). The asymmetric interface in the experiment as well as the linker-molecules bound to the lead-(II)-sulfide nanosheet surface were not simulated. The used methodology (GGA functional) and the approximations to the structure (neglecting the linker and the asymmetric interface) were assumed to be sufficient, since the focus was to get only a qualitative understanding of the CPGE effect in lead-(II)-sulfide nanosheets. For further details of the used methodology see Appendix A.

Having introduced the used methodology and having shown potential problematic issues concerning DFT and lead-(II)-sulfide, the results of the first-principles investigation for lead-(II)-sulfide are presented and discussed next.

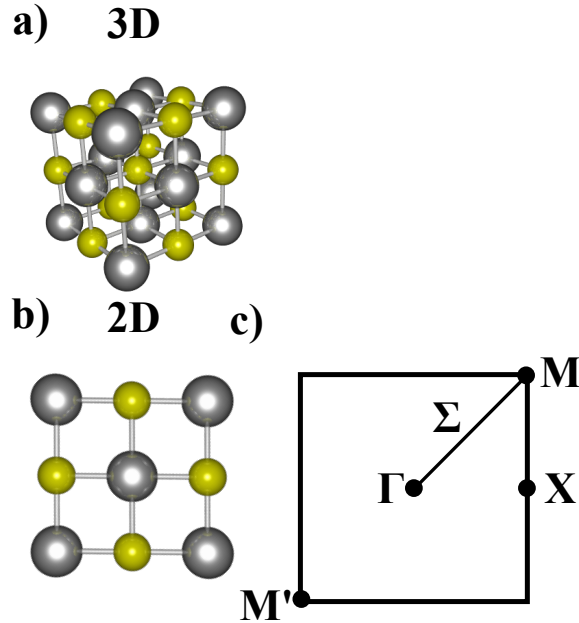


Figure 19: Illustration of the employed unit cells during this work for lead-(II)-sulfide in bulk (a) and for the (001)-lead-(II)-sulfide nanosheet (b), as well as the two-dimensional Brillouine zone of the (001)-lead-(II)-sulfide nanosheet (c). The band gap of the (001)-lead-(II)-sulfide nanosheet is located at the M-point. The path connecting the  $\Gamma$  and the M-point is referred to as  $\Sigma$  path.

### 4.3. Band Structures and Origin of the Circular Photogalvanic Effect in (001)-Lead-(II)-Sulfide Nanosheets

To investigate the CPGE in lead-(II)-sulfide nanosheets, the chosen methodology was applied to bulk lead-(II)-sulfide as a benchmark, as well as to (001)-lead-(II)-sulfide nanosheets to find the underlying mechanism of the effect. The results for the bulk lead-(II)-sulfide are discussed first.

#### 4.3.1. Bulk Lead-(II)-Sulfide and Validation of the Methodology

To validate the methodology (*e.g.* testing the used pseudopotentials), the band structure of bulk lead-(II)-sulfide was calculated and compared to values from the literature, using either the experimental (5.909 Å [117]) or the optimized lattice constant (6.002 Å).

Table 1: Calculated values for the DFT band gaps of bulk lead-(II)-sulfide (experimental and optimized lattice constant). For comparison, calculated band gaps from previous studies [117, 118] are given as well. The variable  $a_0$  denotes the lattice constant and “scalar” scalar-relativistic. The absolute values are given, since band gaps in structures with a band inversion are normally given as negative values.

	$ E_{\text{gap}}^{\text{Bulk}} $ [eV]
This work	
Scalar( $a_0 = 5.909\text{Å}$ )	0.33
Scalar( $a_0 = 6.002\text{Å}$ )	0.49
SOC( $a_0 = 5.909\text{Å}$ )	0.13
SOC( $a_0 = 6.002\text{Å}$ )	0.02
Literature	
Scalar( $a_0 = 5.936\text{Å}$ )	0.37
SOC( $a_0 = 5.936\text{Å}$ )	0.01
SOC( $a_0 = 5.909\text{Å}$ )	0.17

Without considering SOC, the DFT band gaps are 0.33 eV (experimental lattice constant) and 0.49 eV (optimized lattice constant). Taking SOC into account decreases the DFT band gap to 0.13 eV (experimental lattice constant) and 0.02 eV (optimized lattice constant). The band gaps and band structures along the  $\Gamma \rightarrow L \rightarrow W$  path (see Figure 20) are in good agreement with previously calculated data of lead-(II)-sulfide (see Table 1) [117, 118].

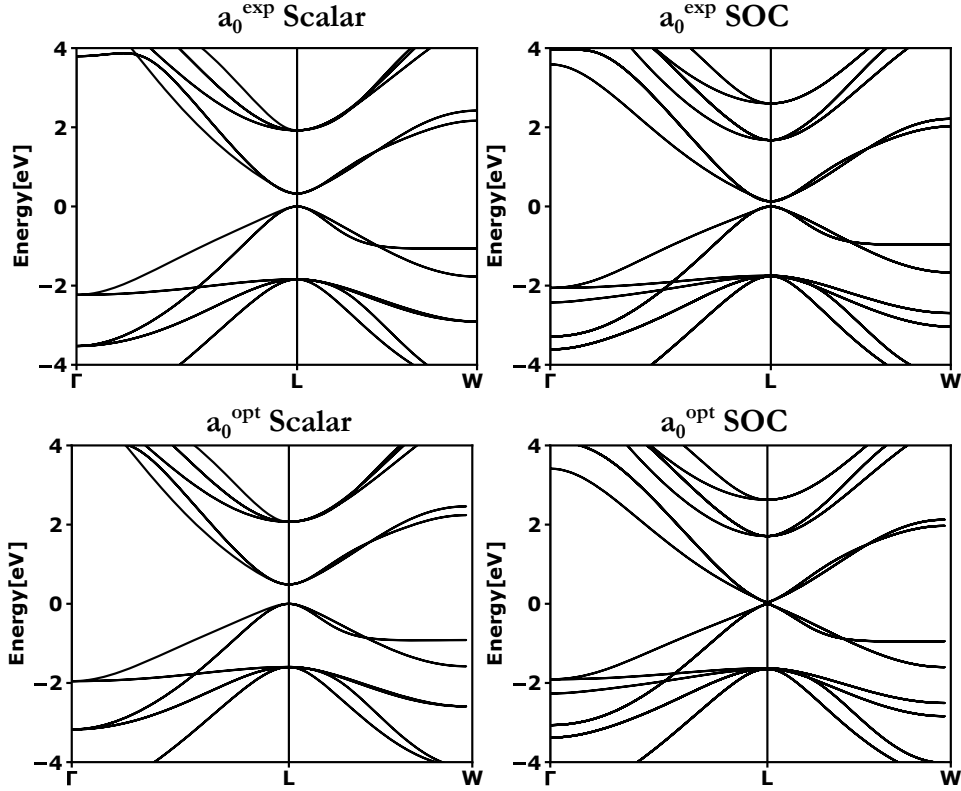


Figure 20: Calculated band structure of bulk lead-(II)-sulfide along the  $\Gamma \rightarrow L \rightarrow W$  path using PBE. The band gap (located at the L-point) decreases massively if SOC is considered, as known from the literature [117, 118]. Without considering SOC, the band gap increases when increasing the used lattice constant, while with SOC, the band gap decreases with the lattice constant. The experimental lattice constant is denoted as  $a_0^{\text{exp}}$ , the optimized one as  $a_0^{\text{opt}}$ , and “scalar” is an abbreviation for scalar-relativistic.

### 4.3.2. (001)-Lead-(II)-Sulfide Nanosheets and the Effect of Spin–Orbit Coupling and an External Electric Field

To explain the CPGE in lead-(II)-sulfide nanosheets, the band structures of two different slabs were calculated, using either the experimental lattice constant and keeping all atoms fixed at the bulk-like position, or the optimized lattice constant and with fully relaxed atoms. In comparison with the experimental observations, the following trends are expected:

- A removal of P-symmetry of the band structure, if SOC is combined with an external electric field applied perpendicularly to the surface.
- An increase of the asymmetry in the band structure with the strength of the electric field (the CPGE-current increases with the strength of the gate voltage in the experiment).
- An in-plane spin orientation of the bands (the CPGE-current increases with the angle-of illumination in the experiment, see explanation of the CPGE in Section 4.1).

The analysis of the band structure is focused on the vicinity of the band gap (M- and M'-point). The calculated band structures for the unrelaxed and the fully-relaxed slab (see Figure 21) show the importance of increasing the DFT band gap by fully optimizing the slab. For the non-optimized slab, SOC leads to an avoiding-crossing region at the band gap, probably induced by a band inversion in combination with SOC [107]. This feature in the band structure is probably artificial as indicated by the DFT investigations by Svane *et al.* [117] and Hummer *et al.* [118]. The full relaxation of the slab yields a parabolic shape of the bands at the M-point and increases DFT band gap. Therefore, further calculations including electric fields were only done for the fully-relaxed slab. The focus was to get only a qualitative explanation for the CISS effect. Thus, the remaining underestimation of the band gap was not considered to be of any problem.

To reveal the origin of the CPGE, the band structure of the fully-relaxed slab was calculated with an symmetry-breaking external electric field in combination with SOC. A splitting of the valence and conduction bands along  $\mathbf{k}$ -space occurs at the M-point (see Figure 22), indicating a Rashba effect. To further validate this assumption, the spin-projected band structure was calculated.

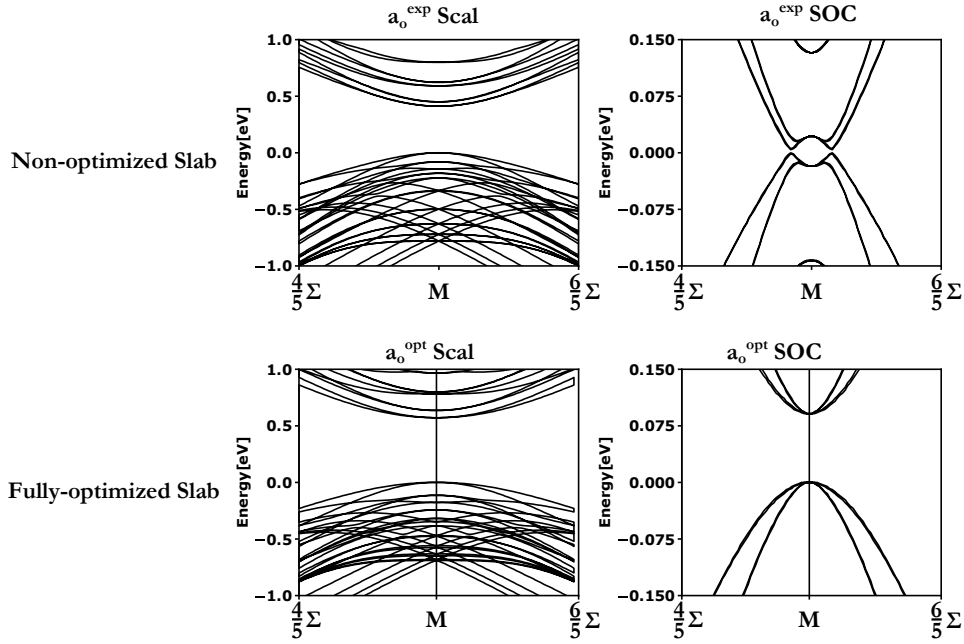


Figure 21: Calculated band structure of (001)-lead-(II)-sulfide nanosheets in the vicinity of the M-point using PBE. The band gap (located at the M-point) for the non-optimized slab is smaller than the one for the fully-optimized slab. If SOC is considered, the band gap of the non-optimized slab becomes nearly zero and an avoiding-crossing region occurs. In contrast, the bands of the fully-optimized slab remain parabolic in the vicinity of the M-point. The experimental lattice constant is denoted as  $a_0^{\text{exp}}$ , the optimized one as  $a_0^{\text{opt}}$ , and scalar-relativistic as “scal”.

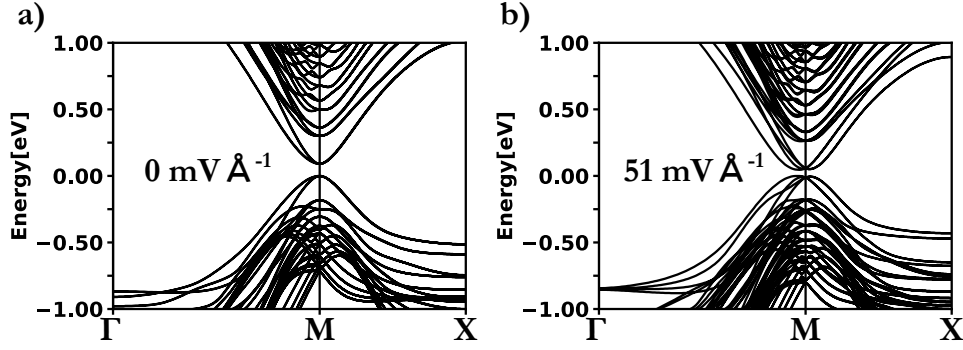


Figure 22: Calculated band structure of (001)-lead-(II)-sulfide nanosheets without (a) and with (b) electric field perpendicular to the surface, using a fully-optimized slab. The electric field in combination with SOC leads to a band splitting at the M-point.

A Rashba effect can be identified by the orientation of the spin vectors of the bands (see Figure 15). The calculated spin vectors of the highest valence and the lowest conduction band are oriented in the surface plane of the nanosheet ( $xy$ -plane). To obtain further insight, the spin vectors of the bands were analyzed in two different ways:

- In one dimension along the  $\Sigma$  path (see Figure 19). The spin vector was projected onto the axis being perpendicular to the  $\Sigma$  path and lying in the  $xy$ -plane.
- In two dimensions around the M- and M'-point. The spin vector was projected onto the  $xy$ -plane of the two-dimensional Brillouin zone.

The one-dimensional case shows a  $\mathbf{k}$ -dependent splitting of the spin bands for the highest valence and the lowest conduction band, as known from Rashba systems (see Figure 23). While one spin band shifts to lower values of  $\mathbf{k}$ , the spin band with the opposite spin orientation shifts to higher values of  $\mathbf{k}$ . The strength of the splitting increases with the strength of the simulated electric field. The two-dimensional plot shows a spiral-like spin structure centered around the M- and M'-points, typical for Rashba systems [79, 132] (see Figure 24). The P-symmetry of the band structure is removed, indicated by comparing the spin textures of the M- and M'-points.

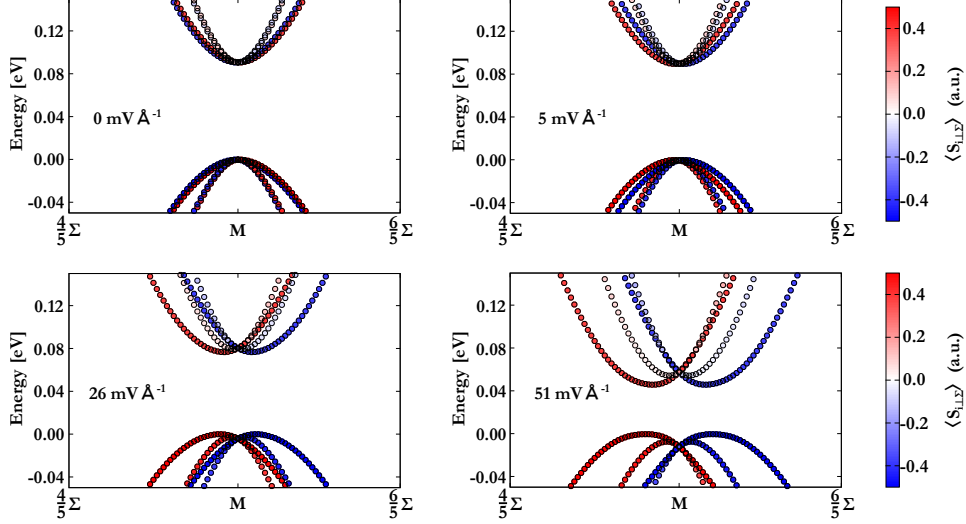


Figure 23: Spin-resolved band structure of (001)-lead-(II)-sulfide nanosheets in the vicinity of the M-point considering SOC and applying an external electric field. The spin is projected onto the in-plane axis, perpendicular to the  $\Sigma$  path. Red denotes a positive projection and blue a negative one. The electric field induces a  $\mathbf{k}$ -dependent band splitting of the spin bands, confirming a Rashba effect. The strength of the splitting increases with the electric field.

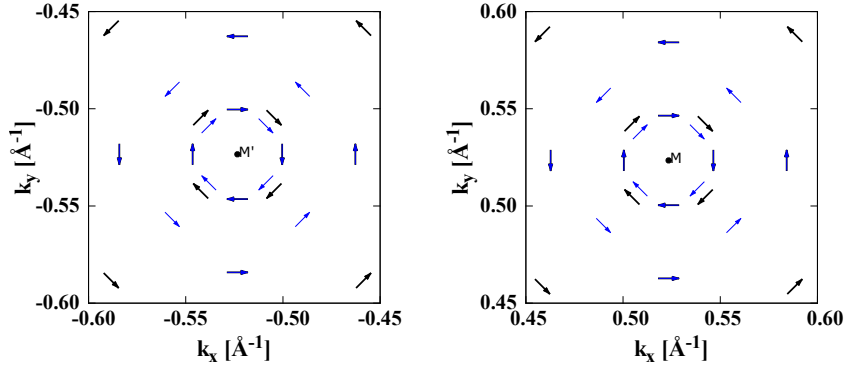


Figure 24: Two-dimensional representation of the spin vector for the two highest valence bands in the vicinity of the M- (a) and M'-point (b). The spin vectors show a typical spin texture for the Rashba effect [79], and the P-symmetry of the band structure is removed. The orientation of the spins are shown for the states of the valence bands at 0.044 eV below the valence-band maximum.

The band structure strongly indicates that the Rashba effect is responsible for the CPGE in (001)-lead-(II)-sulfide nanosheets, and the results are fully consistent with the experimental findings [17]. The increase of the CPGE with the electric field can be explained by an increase of the Rashba spin splitting with the field, and the increase of the CPGE with the angle-of-illumination can be explained by the in-plane spin structure (see explanation of CPGE in Section 4.1).

To finally validate that the Rashba effect is responsible for the observed CPGE, a selection mechanism for the excitation with circularly polarized light has to be formulated. To do so, the band structures were resolved by the projected density of states (pDOS). The results are discussed in the following.

### 4.3.3. Formulation of a Selection Mechanism for the Circular Photogalvanic Effect in (001)-Lead-(II)-Sulfide Sheets

The pDOS-resolved band structures give information about the orbital character of the bands with respect to the total angular momentum  $j$ , which can give insight into the CPGE by identifying allowed excitations. The sum of the pDOS-resolved band structures for all atoms indicates that the highest valence band is dominantly of sulfur  $p_{3/2}$ -orbital character and the lowest conduction band is dominantly of lead  $p_{1/2}$ -orbital character (see Figure 25). A selection rule for the absorption of circularly polarized light, and consequently the origin of the CPGE, can be formulated. The pDOS-resolved band structure indicates possible excitations upon absorbing a circularly polarized photon to be<sup>22</sup>;  $|\frac{3}{2}, +\frac{3}{2}\rangle \rightarrow |\frac{1}{2}, +\frac{1}{2}\rangle$ ;  $|\frac{3}{2}, +\frac{1}{2}\rangle \rightarrow |\frac{1}{2}, -\frac{1}{2}\rangle$ ;  $|\frac{3}{2}, -\frac{1}{2}\rangle \rightarrow |\frac{1}{2}, +\frac{1}{2}\rangle$ ;  $|\frac{3}{2}, -\frac{3}{2}\rangle \rightarrow |\frac{1}{2}, -\frac{1}{2}\rangle$  (see Figure 26). Assuming circularly polarized light with  $\sigma_p = +1$ , an allowed excitation would be  $|\frac{3}{2}, -\frac{3}{2}\rangle \rightarrow |\frac{1}{2}, -\frac{1}{2}\rangle$ . Due to the Rashba-splitting the  $|\frac{3}{2}, -\frac{3}{2}\rangle$  band maximum shifts to higher values of  $\mathbf{k}$  at the M- and M'-points. Excitations in the vicinity of the M- and M'-point would now induce an asymmetric distribution of charge carriers, which

---

<sup>22</sup> Bands are given in  $|j, m_j\rangle$ .

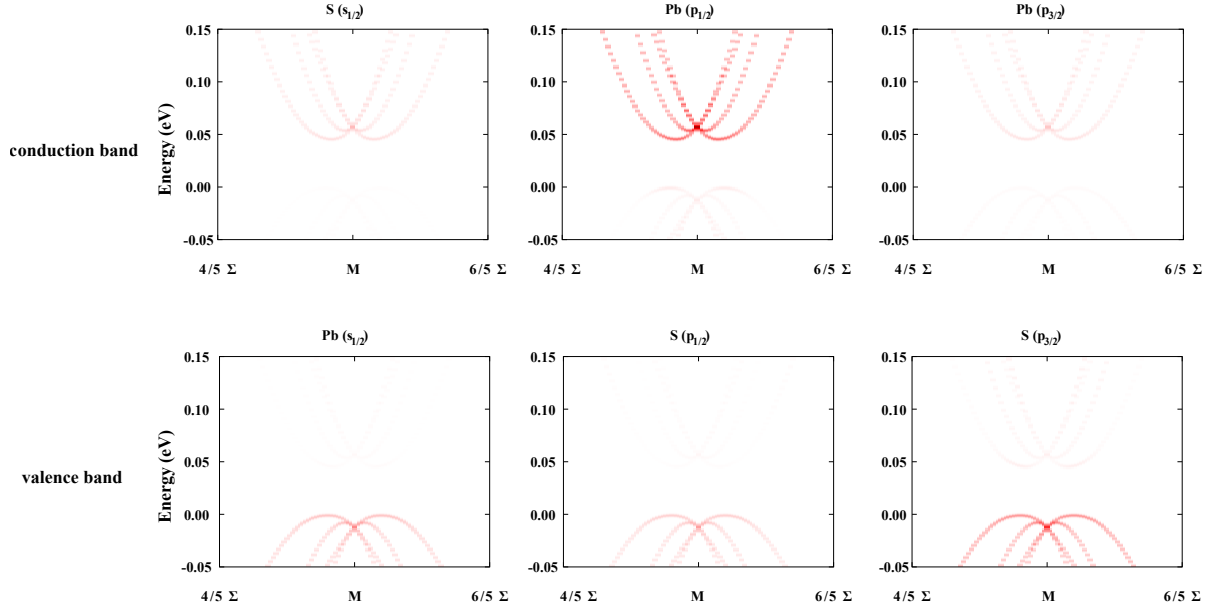


Figure 25: Calculated pDOS-resolved band structure for (001)-lead-(II)-sulfide nanosheets. The highest valence band has strong sulfur  $p_{3/2}$ -orbital character and the lowest conduction band has strong lead  $p_{1/2}$ -orbital character. The pDOS was summed over all atoms for the corresponding orbital at a field of  $51 \frac{\text{mV}}{\text{\AA}}$ . The intensity of the color corresponds to the size of the pDOS of the orbital for a certain energy and a certain point in k-space.

would result in an electric current (see Figure 26). The current would increase with the electric field because the splitting increases with the electric field, as well as with the angle-of-illumination because a larger illumination-angle leads to larger projection of the spin-angular momentum of the photon on the in-plane spin of the bands<sup>23</sup>.

---

<sup>23</sup> The amount of excitations where  $m_j$  has to change by  $\pm 1$  increases with the angle of illumination, see explanation of the CPGE in Section 4.1.

## 4.4. Conclusion

In this part, the origin of the CPGE current observed in (001)-lead-(II)-nanosheets has been investigated using first-principles methods. An induced Rashba effect due to an electric field with the strong SOC in lead-(II)-sulfide nanosheets offers a plausible mechanism for the effect. The Rashba spin splitting of the bands increases with the strength of the electric field and the spins of the bands are completely oriented within the surface plane of the nanosheet, both being consistent with the experimental observations. Selective excitations of  $|j = \frac{3}{2}, m_j = \pm\frac{3}{2}\rangle$  into  $|j = \frac{3}{2}, m_j = \pm\frac{1}{2}\rangle$  bands with circularly polarized light provide a reasonable answer for the CPGE in (001)-lead-(II)-sulfide nanosheets, since such excitations in combination with Rashba splitting would lead to an asymmetric charge-carrier distribution, and therefore to an electric photocurrent.

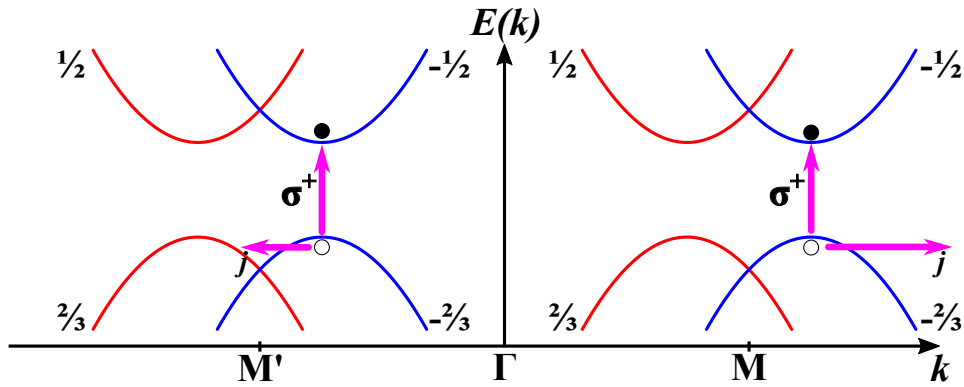


Figure 26: Suggested mechanism for the CPGE in (001)-lead-(II)-sulfide nanosheets. Excitations induced by circularly polarized light induces an asymmetric charge carrier distribution at the M- and M'-point. This induces an electric current and explains the observed CPGE. The bands are given by their quantum number  $m_j$ . Spin-up and spin-down bands are depicted in red and blue respectively.

## 5. Chiral-Induced Spin Selectivity in Helical Molecules

In the previous section, the focus has been on a first-principles investigation of the Rashba effect, which offers promising alternatives for electronic devices due to the ability to manipulate the spin degree of freedom with an electric field. While this effect can be observed in nanostructured systems with broken inversion symmetry, a similar Rashba-like effect can be observed in chiral molecules: the chiral-induced spin selectivity effect. This part of the thesis deals with, until now, rather little studied first-principles descriptions of this effect.

### 5.1. Introduction

Chirality describes a form of isomerism where two molecules (enantiomers) are related by mirror symmetry, but the two mirror images cannot be superimposed on one another [133]. The importance of chirality is manifold. In the field of pharmaceuticals, different chiralities can lead to different pharmacokinetics and pharmacodynamics of the two isomers (*e.g.* thalidomide) [134]. In the field of spectroscopy, optical activity and circular dichroism are important phenomena, related to chiral molecules. Optical activity describes the ability of chiral molecules to rotate the polarization plane of light which passes through the optically active medium, circular dichroism describes the different absorption of circularly polarized light by two enantiomers [135]. The effect of circular dichroism can be used to distinguish enantiomers by vibrational circular dichroism spectroscopy [136].

The concept of circular dichroism for light was extended theoretically to electron beams by Farago [137–139]. He suggested that electron scattering can be accompanied with spin polarization for chiral molecules, referred to as electron-optical activity. The theoretical work was confirmed by experimental studies [140,141], but these were showing only a very small amount of spin polarization. In the year 2011, a much stronger spin polarization was observed for two different types of experiments using deoxyribonucleic acid (DNA)

as a chiral molecule adsorbed on metal surfaces [142,143]. In one experiment, photoelectrons were emitted from a gold surface on which a monolayer of double-stranded DNA was adsorbed [143]. The photoelectrons were created using either circularly or linearly polarized light. For plain gold, linearly polarized light is expected to induce emission of non-polarized electrons, while circularly polarized light is expected to induce emission of polarized electrons, where the sign of polarization depends on the handedness of the circularly polarized light. With an added monolayer of double-stranded DNA, even the electrons emitted by linearly polarized light were polarized, and the sign of polarization for the electrons emitted by using circularly polarized light was independent of the handedness of the polarization of the light (but different absolute values). This indicated that the helical DNA acts as a spin filter, polarizing the photoemission electron beam. In another experiment, the current through a double-stranded DNA molecule in dependence of the magnetization of a nickel layer on which the DNA molecule was adsorbed was measured [142]. The current for one direction of out-of-plane magnetization was much larger than for the other direction of out-of-plane magnetization, indicating that the conductance of electrons of a certain spin polarization is larger than for electrons with the other spin polarization. This result again indicated that DNA molecules act as spin filters. In both experiments, the amount of polarization was increasing with the length of the DNA molecule, and other experiments also showed that the sign of spin polarization changes with the handedness of the helical molecule [144,145]. This phenomenon was called chiral-induced spin selectivity (CISS) or CISS effect. The CISS effect is not restricted to DNA, but can be found for several other molecules such as oligopeptides [146,147], entire proteins [148], helicene [149] and helical polymers [150]. While most experiments were done on monolayers, it was also shown by Mujica *et al.* that the effect can also be observed for single-molecule junctions [147]. It was also shown, that the CISS effect in photoemission experiments can be found on several substrates such as copper [151], silver [151], and aluminum [148], *i.e.*, it is not relying on the strong SOC in the substrate. The CISS effect also manifests in electron-transfer rates using spin-dependent electrochemical cyclic voltammetry [152], photoluminescence [153],

nuclear-magnetic resonance spectroscopy [154], and other experimental setups [155]. The amount of spin polarization achieved in conduction experiments varies depending on the system. For single-molecule junctions of a 22-amino-acid oligopeptide (Lys-Ala-Ala-Ala-Glu-based sequence), the spin polarization reached a value of about 60 % [147]. Monolayers of helicene molecules reached values of about 50 % [149], and monolayers of peptides reached roughly 8 % to 45 %, depending on the applied pressure to the molecule and on the length of the molecules (Ala-AIB peptide sequence) [156].

The CISS effect has several promising applications in the field of spintronics, analytical chemistry and electrochemistry. In the field of spintronics, memory devices were suggested [157–159], as well as a memresistor [160] without using external magnetic fields. In analytical chemistry, the effect was employed to monitor spin-dependent processes [161] as well as for a potential separation of a mixture of two enantiomers [162]. In the field of electrochemistry, it was shown that the electrochemical splitting of water into oxygen and hydrogen is enhanced by using chiral-CuO coated electrodes [163] or chiral-molecule coated nanoparticles [164]. In addition to technological applications, the CISS effect may also be important for the efficient electron transfer in biological systems and for biorecognition [165].

While experimentally the CISS effect is well studied, a theoretical description appears to be quite difficult. It is well established that CISS can be explained by spin–orbit coupling in analogy to the Rashba effect [144, 145]. Several theoretical approaches were developed to describe the CISS effect, but all fail to account for the magnitude of the spin polarization [4] without assuming unrealistically large atomic SOC for carbon atoms; for helical structures, the effective SOC appears to be enhanced compared to the bare atomic SOC of light atoms [145, 166].<sup>24</sup>

Mujica *et al.* described the photoemission experiment theoretically using scattering the-

---

<sup>24</sup> The photoemission experiments using copper, silver and aluminum surfaces excluded the possibility of an inherited SOC by the substrate.

ory [167–170]. In their first model [167], SOC was enhanced by modifying the effective mass of the electron to get non-negligible results for the spin polarization. In their second model [168, 169], effective SOC parameters were not modified but the consideration of multiple-scattering events was necessary to achieve a non-zero spin polarization. Conductance experiments were also the focus of several theoretical studies. The first studies used tight-binding models to derive symmetry-adapted Hamiltonians for the calculation of transport properties. The effective parameters describing the Hamiltonian were not derived but only screened/selected to identify the effect of the parameters on the spin filtering. To reproduce the magnitude of the CISS, much larger values for the effective SOC than expected from experimental values for light atoms were needed. Such investigations were done by Cuniberti *et al.* [171, 172] for electron transport in the presence of a helical potential, by Guo and Sun for DNA [173–176], proteins [177], and helicene molecules [178] including dephasing, and by Matityahu *et al.* [179] taking nonunitary effects into account by introducing the possibility of leakage of the transmitted electrons. Later, Mujica *et al.* and Medina *et al.* developed an analytical continuum model to describe the CISS effect, and derived the electron transport properties for biomolecules [180–182]. They were the first to use a semi-empirical method to derive a spin-dependent Hamiltonian for DNA and to estimate its parameters. To do so, they used an empirical expression for Slater-Koster overlaps, including kinetic terms, intrinsic SOC, Rashba SOC, Stark couplings, internal electric fields, and an external electric field. No transport properties were extracted from this model, but an enhancement of the SOC for helical structures compared to planar structures was found, in analogy to carbon nanotubes compared to graphene. Just recently, a first-principles based investigation of the CISS effect including SOC within a Landauer transport calculation was done by Cuniberti *et al.* [166]. They showed for the first time that DFT-based electron transport calculations can describe both the enhanced spin polarization for helical peptides compared to linear peptides and the helicity dependence of the spin polarization. Nevertheless, the spin polarization was strongly underestimated and only appeared far from the Fermi energy.

The strong SOC in helical structures was also discussed by Naaman *et al.* [183] and Nitzan *et al.* [184]. Naaman *et al.* stated that SOC is enhanced by a combination of SOC and the dipolar potential of the helical molecule. Nitzan *et al.* suggested that the strong SOC does not originate from the molecule itself but from the gold substrate, which was falsified by experiments showing the CISS effect on an aluminum surface for the photoemission experiment [148].

In this part of this thesis, attempts to understand the origin of the CISS effect in DFT based transport calculations are presented. While Cuniberti *et al.* [166] already showed that the CISS effect is described with DFT electron transport calculations qualitatively, a detailed insight into its origin was missing. Such an insight is the focus of this part, based on an analytical derivation of necessary conditions to describe the CISS effect within DFT and a detailed analysis of the Hamiltonian matrix elements. The latter is close to the semi-empirical coupling analysis done by Mujica and Medina *et al.* [180–182], but is based on a first-principles method and is directly connected to the spin filtering in Landauer transport calculations.

First, details on the implementations into ARTAIOS, a postprocessing tool of quantum chemistry results, done for the investigation of the CISS effect are explained. This includes extensions of the Landauer approach to consider SOC and dephasing as well as the calculation of the matrices required for the transport calculations. Afterwards, the origin of the CISS effect within the implemented Landauer approach is discussed and verified using model systems. Finally, the application of the implemented methodology to experimental relevant systems, to check the ability to predict the correct order of magnitude of the CISS effect, is discussed.

## 5.2. Theoretical Methods to Investigate Chiral-Induced Spin Selectivity

In this work, the first-principles description of the CISS effect in electron-transport experiments is based on Green's functions and the Landauer approach using DFT. The plane-wave electronic-structure codes TRANSIESTA [185], QUANTUM ESPRESSO [186,187], and OPENMX [188] can include SOC in transport calculations. However, either the lack of hybrid functionals or the long computational times of both hybrid DFT calculations and SOC including transport calculations led to the choice of extending the program ARTAIOS, which can postprocess different electronic-structure codes, in particular those which have more efficient implementations of SOC combined with hybrid functionals. Methods to consider SOC in the Landauer approach were already presented in the literature, *i.e.*, in References [189,190]. Evers *et al.* introduced a Landauer-transport based approach [190], which can be used to calculate spin-dependent transmission functions including SOC as

$$\mathcal{T}(E)^{\sigma\sigma'} = \text{Tr} \left[ \mathbf{\Gamma}_R^{\sigma'\sigma'}(E) \mathbf{G}^{\sigma'\sigma}(E) \mathbf{\Gamma}_L^{\sigma\sigma}(E) (\mathbf{G}^{\sigma'\sigma})^\dagger(E) \right], \quad (5.1)$$

where  $\mathbf{\Gamma}_{\sigma'\sigma}^X(E)$  are spin-dependent coupling matrices to the right and left electrode, and  $\mathbf{G}^{\sigma\sigma'}(E)$  are spin-dependent Green's function matrices. The equation differs by a spin-index  $\sigma$  from the equation in Reference [190]. It is derived later. These spin-dependent transmission functions can then be used to calculate the spin polarization of the transmitted electrons (in the following just called spin polarization),

$$SP = \frac{T^{\alpha\alpha} + T^{\beta\alpha} - T^{\alpha\beta} - T^{\beta\beta}}{T^{\alpha\alpha} + T^{\beta\alpha} + T^{\alpha\beta} + T^{\beta\beta}}. \quad (5.2)$$

This methodology can be used in combination with electronic-structure programs like NWCHEM, TURBOMOLE, or ADF. For this work, TURBOMOLE and ADF were chosen. ADF has the advantages of using STOs instead of GTOs single-particle basis functions, the very efficient ZORA Hamiltonian for the inclusion of scalar-relativistic effects and SOC, and the ability of applying an external electric field. The ZORA Hamiltonian is well suited for the description of SOC [21] and does include the nuclear and the electronic

potential for its evaluation [33]. Since it was not possible to do all calculations with ADF due to convergence problems using pure functionals and problems in constructing the matrices needed for the transport calculations for some systems, TURBOMOLE was used as well.

In addition to SOC, dephasing may be important for the CISS effect, as suggested by Guo and Sun [173] and by Mujica *et al.* [191]. Therefore, Equation (5.1) was extended here by an approach to include dephasing phenomenologically, developed by Frauenheim *et al.* [192]. In this approach, the self energy of the electron–phonon interaction is chosen in such a way that an effective transmission function can be calculated as

$$\mathcal{T}^{\text{eff}} = \text{Tr} \left[ \mathbf{\Gamma}_L \mathbf{G}^{r,n} \left( \mathbf{\Gamma}_R + \mathbf{\Gamma}_{R,\text{elph}}^{n-1} \right) \mathbf{G}^{a,n} \right]. \quad (5.3)$$

Although dephasing can be considered in this way, the normal modes of the molecules are not treated explicitly in this approach. However, it offers a fast and simple implementation for investigating the effect of dephasing on the CISS effect.

### 5.3. Derivations and Implementations of a Two-Component Landauer Approach and an effective Dephasing Model

To investigate the CISS effect based on first-principles calculations, methods to calculate electron transport based on two-component DFT were implemented. In the following, these implementations and the derivations of the used approaches to calculate the electron transport properties are explained. This includes the following implementations:

- The calculation of the effective single-particle Hamiltonian matrix (Fock matrix)  $\mathbf{H}$  and of the overlap matrix  $\mathbf{S}$  using the output of TURBOMOLE and ADF. These quantities are the basis for the electron transport calculations.
- The calculation of  $\mathcal{T}^{\sigma\sigma'}$ . This allows to include SOC into electron transport calculations.
- The calculation of  $\mathcal{T}^{\text{eff}}$ . This allows to additionally include dephasing into the electron transport calculations, which might be important for the CISS effect.

First, how to calculate  $\mathbf{H}$  and  $\mathbf{S}$  using TURBOMOLE or ADF is presented.

### 5.3.1. Fock and Overlap Matrices from Two-Component DFT Calculations

To obtain electron transport properties using the Landauer approach in combination with SOC,  $\mathbf{H}$  and  $\mathbf{S}$  from a two-component DFT calculation have to be computed. For one-component calculations, both matrices often are part of the output. However, for two-component calculations, this is not the case (at least not for TURBOMOLE and ADF). Thus, a tool, based on the programming language FORTRAN90, to calculate both matrices was created to get  $\mathbf{H}$  and  $\mathbf{S}$  in the form as given in Equations (2.75) and (2.76). The tool was designed to create the needed matrices using the output of ADF or TURBOMOLE.

In principle,  $\mathbf{S}$  could be extracted from a one-component calculation and be used to construct the two-component  $\mathbf{S}$ , since the overlap matrix only depends on the used basis functions and their positions (see Section 2.1). However,  $\mathbf{S}$  can also be calculated on-the-fly by using the relation [20]

$$\mathbf{C}^\dagger \mathbf{S} \mathbf{C} = \mathbf{1} \quad (5.4)$$

to yield  $\mathbf{S}$  as

$$\mathbf{S} = (\mathbf{C}^\dagger)^{-1} (\mathbf{C})^{-1}. \quad (5.5)$$

$\mathbf{S}$  can then be used to evaluate  $\mathbf{H}$  based on Equation (2.15) as

$$\mathbf{H} = \mathbf{S} \mathbf{C} \boldsymbol{\epsilon} (\mathbf{C})^{-1}. \quad (5.6)$$

Therefore,  $\mathbf{S}$  and  $\mathbf{H}$  can be calculated using the eigenvalue matrix  $\boldsymbol{\epsilon}$  and coefficient matrix  $\mathbf{C}$  only, which are part of the TURBOMOLE and ADF output.

#### Details on the Calculation of $\mathbf{S}$ and $\mathbf{H}$ for Turbomole

TURBOMOLE gives  $\boldsymbol{\epsilon}$  and  $\mathbf{C}$  as a standard output. For a closed-shell calculation, they are contained in the file MOS, for open-shell calculations the spin-up ( $\alpha$ ) molecular orbital

coefficients and eigenvalues are contained in the file ALPHA, while the spin-down ( $\beta$ ) molecular orbital coefficients and eigenvalues are contained in the file BETA. For two-component calculations,  $\epsilon$  is contained in the SPINOR.R or SPINOR.I file. The SPINOR.R file also contains the real part of  $\mathbf{C}$ , while the SPINOR.I file contains the complex part of  $\mathbf{C}$ .

### Details on the Calculation of $\mathbf{S}$ and $\mathbf{H}$ for ADF

For ADF, to extract  $\mathbf{H}$  and  $\mathbf{S}$ , the tool DMPKF can be used to translate the binary-format TAPE21 file, produced during the SCF calculation, into an ASCII format. For the one-component DFT calculations, the scaled ZORA  $\epsilon$  is stored under the keyword ESCALE\_A for the  $\alpha$  and under ESCALE\_B for the  $\beta$  orbitals, while  $\mathbf{C}$  is stored under the keyword EIG-CORESFO\_A for the  $\alpha$  and under EIG-CORESFO\_B for the  $\beta$  orbitals. For the two-component DFT calculation, having used the TAPE21 file from a scalar-relativistic calculation as a fragment,  $\epsilon$  for the scaled ZORA energies is stored under the keyword ESCALE\_A A1/2, the real part of  $\mathbf{C}$  is stored under FRAGBAS-R\_A, and the imaginary part under FRAGBAS-I\_A.

For one-component calculations,  $\mathbf{C}$  and  $\epsilon$  can be used to obtain  $\mathbf{H}$  and  $\mathbf{S}$  in the spin-block form (see Equation (2.75) for spin-block form of  $\mathbf{H}$ ) where the spin-flip blocks are consequently zero. In a two-component calculation, ADF uses a double-group symmetry-adapted basis [21,33], which prevents a direct computation of  $\mathbf{H}$  and  $\mathbf{S}$  in the spin-block form. To circumvent this problem, one can use a so-called fragment basis in ADF: a basis function used in ADF, also called symmetrized fragment orbital (SFO), is a linear combination of STOs (see Equation (2.14) for linear combination of atomic orbitals),

$$\phi_i^{SFO} = \sum_j c_{ji}^{STO} \phi_j^{STO}. \quad (5.7)$$

The SFOs remain centered on atoms. The molecular orbitals are then expanded by

combining the SFOs,

$$\psi_i^{KS} = \sum_j c_j^{SFO} \phi_j^{SFO}. \quad (5.8)$$

For a one-component calculation, the SFOs can be described with the quantum number  $l$ <sup>25</sup>, while for a two-component calculation, the SFOs are described with the quantum number  $j$ <sup>26</sup>. If the molecular orbitals of a one-component calculation are used as a basis, which is referred to as fragment basis, for a subsequent two-component calculation, the new molecular orbitals are expanded using the old molecular orbitals as (see Equation (2.74))

$$\psi_i^{KS,SOC} = \sum_{\mu} \psi_{\mu}^{KS} \left[ \text{Re} \begin{pmatrix} c_{\mu i}^{\alpha} \\ c_{\mu i}^{\beta} \end{pmatrix} + i \text{Im} \begin{pmatrix} c_{\mu i}^{\alpha} \\ c_{\mu i}^{\beta} \end{pmatrix} \right]. \quad (5.9)$$

In this representation, it is possible to calculate the two-component matrices  $\mathbf{H}$  and  $\mathbf{S}$  in their spin-block form. However, since this basis is not atom-centered anymore, the partitioning for the Landauer approach (see Section 2.3) cannot be done atomwise, which makes a partitioning hard at all. To make an atomic-partitioning scheme possible, Equations (5.8) and (5.9) can be combined to yield  $\psi_i^{KS,SOC}$  expanded in the atom-centered SFO basis as

$$\psi_i^{KS,SOC} = \sum_j \phi_j^{SFO} \left[ \text{Re} \begin{pmatrix} \sum_{\mu} (c_{j\mu}^{SFO} \cdot c_{\mu i}^{\alpha}) \\ \sum_{\mu} (c_{j\mu}^{SFO} \cdot c_{\mu i}^{\beta}) \end{pmatrix} + i \text{Im} \begin{pmatrix} \sum_{\mu} (c_{j\mu}^{SFO} \cdot c_{\mu i}^{\alpha}) \\ \sum_{\mu} (c_{j\mu}^{SFO} \cdot c_{\mu i}^{\beta}) \end{pmatrix} \right]. \quad (5.10)$$

The resulting  $\mathbf{C}$  can be used to get  $\mathbf{S}$  and  $\mathbf{H}$  in the SFO basis.

Having introduced the computation of the needed two-component matrices for electron transport calculations, the implementation of the Landauer approach including SOC is described. The inclusion of SOC into the electron transport calculations is important to describe the CISS effect with first-principles methods.

---

<sup>25</sup> The used  $p$ -orbital for instance are the  $p_x$ ,  $p_y$  and  $p_z$  orbitals.

<sup>26</sup> The used  $p$ -orbital for instance are the  $p_{1/2}$  and  $p_{3/2}$  orbitals.

### 5.3.2. Two-Component Landauer Approach to include Spin–Orbit Coupling

The two-component  $\mathbf{H}$  and  $\mathbf{S}$  can be used to evaluate the electron transport properties by employing the Landauer approach, which then may incorporate SOC. An approach to do so, introduced by Evers *et al.* [190], was adopted and implemented into ARTAIOS. This implementation was the basis of the first-principles investigation of CISS done during this work. The theoretical background for the Landauer approach can be found in Section 2.3. Instead of writing the Green’s function matrices as  $\mathbf{G}^r$  and  $\mathbf{G}^a$ , the terminology as employed in Reference [190] is used ( $\mathbf{G}$  and  $\mathbf{G}^\dagger$ ).

#### Spin-Dependent Transmission Functions within the Landauer Approach

As mentioned in Section 2.2.5,  $\mathbf{H}$  becomes a block matrix upon including SOC. In the same manner, the Green’s function matrix<sup>27</sup> becomes a block matrix of the form [190]

$$\mathbf{G} = \begin{pmatrix} \mathbf{G}^{\alpha\alpha} & \mathbf{G}^{\alpha\beta} \\ \mathbf{G}^{\beta\alpha} & \mathbf{G}^{\beta\beta} \end{pmatrix}. \quad (5.11)$$

In principle, the self-energy matrices  $\mathbf{\Sigma}_L$  and  $\mathbf{\Sigma}_R$  as well as the coupling matrices  $\mathbf{\Gamma}_L$  and  $\mathbf{\Gamma}_R$  also have the same form. If a collinear orientation of the spin within the electrodes is assumed, *i.e.*, SOC is only considered in the central region,  $\mathbf{\Sigma}_L$  and  $\mathbf{\Sigma}_R$  as well as  $\mathbf{\Gamma}_L$  and  $\mathbf{\Gamma}_R$  become block-diagonal matrices,

$$\mathbf{\Gamma} = \begin{pmatrix} \mathbf{\Gamma}^{\alpha\alpha} & 0 \\ 0 & \mathbf{\Gamma}^{\beta\beta} \end{pmatrix}, \quad (5.12)$$

$$\mathbf{\Sigma} = \begin{pmatrix} \mathbf{\Sigma}^{\alpha\alpha} & 0 \\ 0 & \mathbf{\Sigma}^{\beta\beta} \end{pmatrix}. \quad (5.13)$$

This approach was introduced by Evers *et al.* [190]. The advantage of this approach is the clear separation of the transmission function into two spin-conserving and two spin-flip contributions, allowing for a calculation of the spin polarization of the transmitted electrons. The spin-conserving and spin-flip transmissions emerge by inserting these

---

<sup>27</sup> The energy dependence is not written in this derivation for sake of clarity.

equations into Equation (2.98)

$$\mathcal{T}(E)_{LR} = \text{Tr} \left[ \begin{pmatrix} \mathbf{\Gamma}_R^{\alpha\alpha} & 0 \\ 0 & \mathbf{\Gamma}_R^{\beta\beta} \end{pmatrix} \begin{pmatrix} \mathbf{G}^{\alpha\alpha} & \mathbf{G}^{\alpha\beta} \\ \mathbf{G}^{\beta\alpha} & \mathbf{G}^{\beta\beta} \end{pmatrix} \begin{pmatrix} \mathbf{\Gamma}_L^{\alpha\alpha} & 0 \\ 0 & \mathbf{\Gamma}_L^{\beta\beta} \end{pmatrix} \begin{pmatrix} (\mathbf{G}^{\alpha\alpha})^\dagger & (\mathbf{G}^{\beta\alpha})^\dagger \\ (\mathbf{G}^{\alpha\beta})^\dagger & (\mathbf{G}^{\beta\beta})^\dagger \end{pmatrix} \right]. \quad (5.14)$$

$$= \text{Tr} \left[ \mathbf{\Gamma}_R^{\alpha\alpha} \mathbf{G}^{\alpha\alpha} \mathbf{\Gamma}_L^{\alpha\alpha} (\mathbf{G}^{\alpha\alpha})^\dagger + \mathbf{\Gamma}_R^{\alpha\alpha} \mathbf{G}^{\alpha\beta} \mathbf{\Gamma}_L^{\beta\beta} (\mathbf{G}^{\alpha\beta})^\dagger \right. \\ \left. + \mathbf{\Gamma}_R^{\beta\beta} \mathbf{G}^{\beta\alpha} \mathbf{\Gamma}_L^{\alpha\alpha} (\mathbf{G}^{\beta\alpha})^\dagger + \mathbf{\Gamma}_R^{\beta\beta} \mathbf{G}^{\beta\beta} \mathbf{\Gamma}_L^{\beta\beta} (\mathbf{G}^{\beta\beta})^\dagger \right]. \quad (5.15)$$

$$= \text{Tr} \left[ \mathbf{\Gamma}_R^{\alpha\alpha} \mathbf{G}^{\alpha\alpha} \mathbf{\Gamma}_L^{\alpha\alpha} (\mathbf{G}^{\alpha\alpha})^\dagger \right] \\ + \text{Tr} \left[ \mathbf{\Gamma}_R^{\alpha\alpha} \mathbf{G}^{\alpha\beta} \mathbf{\Gamma}_L^{\beta\beta} (\mathbf{G}^{\alpha\beta})^\dagger \right] \\ + \text{Tr} \left[ \mathbf{\Gamma}_R^{\beta\beta} \mathbf{G}^{\beta\alpha} \mathbf{\Gamma}_L^{\alpha\alpha} (\mathbf{G}^{\beta\alpha})^\dagger \right] \\ + \text{Tr} \left[ \mathbf{\Gamma}_R^{\beta\beta} \mathbf{G}^{\beta\beta} \mathbf{\Gamma}_L^{\beta\beta} (\mathbf{G}^{\beta\beta})^\dagger \right]. \quad (5.16)$$

The total transmission function can be written as the sum of four contributions.

$$\mathcal{T}_{LR} = \mathcal{T}_{LR}^{\alpha\alpha} + \mathcal{T}_{LR}^{\beta\alpha} + \mathcal{T}_{LR}^{\alpha\beta} + \mathcal{T}_{LR}^{\beta\beta}, \quad (5.17)$$

$\mathcal{T}_{RL}^{\alpha\alpha}$  and  $\mathcal{T}_{RL}^{\beta\beta}$  are the spin-conserving transmission functions (electrons enter and leave the scattering region with the same spin), where  $\mathbf{\Gamma}_L$  and  $\mathbf{\Gamma}_R$  are emerging from the same spin block, and  $\mathcal{T}_{RL}^{\alpha\beta}$  and  $\mathcal{T}_{RL}^{\beta\alpha}$  are the spin-flip transmission functions (electrons enter and leave the scattering region with different spin) where  $\mathbf{\Gamma}_L$  and  $\mathbf{\Gamma}_R$  are emerging from different spin blocks.

### Details on the Implementation of the Two-Component Landauer Approach

The formerly elaborated approach for the calculation of spin-dependent transmission functions was implemented into ARTAIOS to consider SOC in electron transport calculations. The FORTRAN90 programming language was used and optimized linear algebra libraries, namely BLAS [193] and LAPACK [194] were employed. The principle methods to calculate the needed matrices were adopted from ARTAIOS [195].

In the program,  $\mathbf{G}$ ,  $\mathbf{\Sigma}_L$ ,  $\mathbf{\Sigma}_R$ ,  $\mathbf{\Gamma}_L$ , and  $\mathbf{\Gamma}_R$  are constructed as discussed in Reference [61].  $\mathbf{S}$  and  $\mathbf{H}$  are used as an input, obtained from a HF or DFT calculation as explained as in Section 5.3.1. The left electrode, right electrode, and the central region (see Section 2.3) are defined by a list of atoms or basis functions, given as an input.  $\mathbf{H}$  and  $\mathbf{S}$  are then

partitioned as

$$\mathbf{H} = \left[ \begin{array}{c|c} \mathbf{H}^{\alpha\alpha} & \mathbf{H}^{\alpha\beta} \\ \hline \mathbf{H}^{\beta\alpha} & \mathbf{H}^{\beta\beta} \end{array} \right] = \left[ \begin{array}{ccc|ccc} \mathbf{H}_L^{\alpha\alpha} & \mathbf{H}_{LC}^{\alpha\alpha} & \mathbf{0} & \mathbf{H}_L^{\alpha\beta} & \mathbf{H}_{LC}^{\alpha\beta} & \mathbf{0} \\ \mathbf{H}_{CL}^{\alpha\alpha} & \mathbf{H}_C^{\alpha\alpha} & \mathbf{H}_{CR}^{\alpha\alpha} & \mathbf{H}_{CL}^{\alpha\beta} & \mathbf{H}_C^{\alpha\beta} & \mathbf{H}_{CR}^{\alpha\beta} \\ \mathbf{0} & \mathbf{H}_{RC}^{\alpha\alpha} & \mathbf{H}_R^{\alpha\alpha} & \mathbf{0} & \mathbf{H}_{RC}^{\alpha\beta} & \mathbf{H}_R^{\alpha\beta} \\ \hline \mathbf{H}_L^{\beta\alpha} & \mathbf{H}_{LC}^{\beta\alpha} & \mathbf{0} & \mathbf{H}_L^{\beta\beta} & \mathbf{H}_{LC}^{\beta\beta} & \mathbf{0} \\ \mathbf{H}_{CL}^{\beta\alpha} & \mathbf{H}_C^{\beta\alpha} & \mathbf{H}_{CR}^{\beta\alpha} & \mathbf{H}_{CL}^{\beta\beta} & \mathbf{H}_C^{\beta\beta} & \mathbf{H}_{CR}^{\beta\beta} \\ \mathbf{0} & \mathbf{H}_{RC}^{\beta\alpha} & \mathbf{H}_R^{\beta\alpha} & \mathbf{0} & \mathbf{H}_{RC}^{\beta\beta} & \mathbf{H}_R^{\beta\beta} \end{array} \right]. \quad (5.18)$$

The resulting blocks from the partitioning scheme are then used to build the central-region effective single-particle Hamiltonian matrix  $\mathbf{H}_C$  as

$$\mathbf{H}_C = \left[ \begin{array}{c|c} \mathbf{H}_C^{\alpha\alpha} & \mathbf{H}_C^{\alpha\beta} \\ \hline \mathbf{H}_C^{\beta\alpha} & \mathbf{H}_C^{\beta\beta} \end{array} \right], \quad (5.19)$$

and the central-region overlap matrix  $\mathbf{S}_C$  as

$$\mathbf{S}_C = \left[ \begin{array}{c|c} \mathbf{S}_C^{\alpha\alpha} & \mathbf{0} \\ \hline \mathbf{0} & \mathbf{S}_C^{\beta\beta} \end{array} \right]. \quad (5.20)$$

$\Sigma_L$  is then obtained as

$$\begin{aligned} \Sigma_L &= \left[ \begin{array}{c|c} E\mathbf{S}_{LC}^{\alpha\alpha} - \mathbf{H}_{LC}^{\alpha\alpha} & \mathbf{0} \\ \hline \mathbf{0} & E\mathbf{S}_{LC}^{\beta\beta} - \mathbf{H}_{LC}^{\beta\beta} \end{array} \right]^\dagger \mathbf{g}_L \left[ \begin{array}{c|c} E\mathbf{S}_{LC}^{\alpha\alpha} - \mathbf{H}_{LC}^{\alpha\alpha} & \mathbf{0} \\ \hline \mathbf{0} & E\mathbf{S}_{LC}^{\beta\beta} - \mathbf{H}_{LC}^{\beta\beta} \end{array} \right] \\ &= \left[ \begin{array}{c|c} \Sigma_L^{\alpha\alpha} & \mathbf{0} \\ \hline \mathbf{0} & \Sigma_L^{\beta\beta} \end{array} \right] \end{aligned} \quad (5.21)$$

and  $\Sigma_R$  is built analogously using the coupling blocks between the right electrode and the central region.  $\mathbf{g}_X$  is the Green's function matrix of the left or right electrode, for which each element is obtained within the wide band limit (WBL) approximation<sup>28</sup> [196] as

$$(\mathbf{g}_X)_{ij} = -i\pi \text{LDOS}^{\text{const}} \delta_{ij}. \quad (5.22)$$

---

<sup>28</sup> The WBL approximation was shown to give reasonable results for molecular junctions using gold electrodes [196].

LDOS is the local density of states, which is assumed to be constant. In this work, the value  $0.036 \text{ eV}^{-1}$  was used [61].

It is important to note that  $\mathbf{H}_C$  is obtained by partitioning  $\mathbf{H}$  from a two-component DFT calculation, and therefore can include SOC.  $\mathbf{\Sigma}_L$  and  $\mathbf{\Sigma}_R$  in contrast are computed from  $\mathbf{H}$  of a one-component calculation as

$$\mathbf{H} = \left[ \begin{array}{c|c} \mathbf{H}^{\alpha\alpha} & \mathbf{0} \\ \hline \mathbf{0} & \mathbf{H}^{\beta\beta} \end{array} \right], \quad (5.23)$$

where  $\mathbf{H}^{\alpha\alpha} = \mathbf{H}^{\beta\beta}$  for a closed-shell system. All matrices are then used to calculate  $\mathbf{G}$  as

$$\mathbf{G} = \left[ \begin{array}{c|c} E\mathbf{S}_C^{\alpha\alpha} - \mathbf{H}_C^{\alpha\alpha} - \mathbf{\Sigma}_L^{\alpha\alpha} - \mathbf{\Sigma}_R^{\alpha\alpha} & -\mathbf{H}_C^{\alpha\beta} \\ \hline -\mathbf{H}_C^{\beta\alpha} & E\mathbf{S}_C^{\beta\beta} - \mathbf{H}_C^{\beta\beta} - \mathbf{\Sigma}_L^{\beta\beta} - \mathbf{\Sigma}_R^{\beta\beta} \end{array} \right]^{-1}. \quad (5.24)$$

$\mathbf{G}$ ,  $\mathbf{\Sigma}_L$ , and  $\mathbf{\Sigma}_R$  have to be calculated at every  $E$ . Both matrices can then be used to obtain  $\mathcal{T}^{\sigma\sigma'}(E)$  by partitioning  $\mathbf{G}$  as

$$\mathbf{G} = \left[ \begin{array}{c|c} \mathbf{G}^{\alpha\alpha} & \mathbf{G}^{\alpha\beta} \\ \hline \mathbf{G}^{\beta\alpha} & \mathbf{G}^{\beta\beta} \end{array} \right], \quad (5.25)$$

as well as  $\mathbf{\Gamma}_L$  and  $\mathbf{\Gamma}_R$  as

$$\mathbf{\Gamma}_X = \left[ \begin{array}{c|c} -2\text{Im}(\mathbf{\Sigma}_X^{\alpha\alpha}) & \mathbf{0} \\ \hline \mathbf{0} & -2\text{Im}(\mathbf{\Sigma}_X^{\beta\beta}) \end{array} \right] = \left[ \begin{array}{c|c} \mathbf{\Gamma}_X^{\alpha\alpha} & \mathbf{0} \\ \hline \mathbf{0} & \mathbf{\Gamma}_X^{\beta\beta} \end{array} \right]. \quad (5.26)$$

$\mathcal{T}^{\sigma\sigma'}(E)$  is then obtained by using Equation (5.1).

## Validation of the Implementation

To test the implementation for the calculation of the spin-dependent transmission functions,  $\mathcal{T}^{\sigma\sigma'}(E)$  was computed for *m*-diethynethiolbenzene (closed-shell) and 1,4-diethynethiol-2-methylbenzene (open-shell) gold–molecule–gold junctions (BP86/ZORA-DZ, for details see Appendix A). The results were compared to results obtained with the standard implementation in ARTAIOS, based on the output of ADF. The structures of the gold–molecule–gold junctions were taken from the examples within the ARTAIOS

package [195]. The energies of the transmission functions are shifted by the estimated  $E_F$  (-5 eV [69]).

The one-component calculations for  $\mathcal{T}^{\alpha\alpha}(E)$  and  $\mathcal{T}^{\beta\beta}(E)$  with the new implementation were done by building a “fake” two-component  $\mathbf{H}$  and  $\mathbf{S}$  using the one-component matrices. The results for the closed- and open-shell system for both programs are in very good agreement (see Figure 27 and Figure 28, part a). If SOC is added to the DFT calculation, four non-zero transmission functions contribute to  $\mathcal{T}$  (see Figure 27 and Figure 28, part b). For the closed-shell system both spin-conserving transmissions are the same, while for the open-shell systems, they are different. In both cases,  $\mathcal{T}^{\alpha\alpha}(E)$  and  $\mathcal{T}^{\beta\beta}(E)$  computed with SOC are in qualitative agreement with  $\mathcal{T}^{\alpha\alpha}(E)$  and  $\mathcal{T}^{\beta\beta}(E)$  obtained without SOC. The spin-flip transmission functions are several magnitudes smaller than the spin-conserving transmission functions, as to be expected due to the small SOC.

In addition, the effect of rotating the spin of the unpaired electron from the  $z$ -axis (collinear with respect to the spin of the electrode) into the  $xy$ -plane (non-collinear with respect to the spin of the electrode) was calculated for the open-shell system. The results obtained for the different orientations of the spin were used to validate the implementation, by comparing them to results from Evers *et al.* [190]. The authors used a different system, namely hydrogenated graphene, which is badly described within the WBL-approximation, and was therefore not used. TURBOMOLE (BP86/def2-SVP, for details see Appendix A) was used instead of ADF because a tool to rotate the spin of a system based on the molecular orbital coefficient matrix  $\mathbf{C}$  was available from the author’s master’s thesis<sup>29</sup>.

$\mathcal{T}^{\sigma\sigma'}(E)$  calculated with TURBOMOLE without including SOC and employing a collinear spin orientation with respect to the electrode’s spin is in qualitative agreement with the results of ADF (see Figures 28 and 29). If the spin of the unpaired electron is non-collinear with respect to the electrode’s spin, all transmission functions change with respect to the collinear orientation (see Figure 29). If the spin is in a collinear alignment, the spin-conserving transmission functions differ; both are the same, if the spin is non-

---

<sup>29</sup> Martin Sebastian Zöllner, *Magnetic anisotropy in nanoscopic systems*, 2015 University of Hamburg.

collinear. Non-zero spin-flip transmission occur for the non-collinear spin orientation, despite the absence of SOC. The spin-flip transmissions show maxima at the dips of the spin-conserving transmission functions. The results are consistent with the results of Evers *et al.* [190].

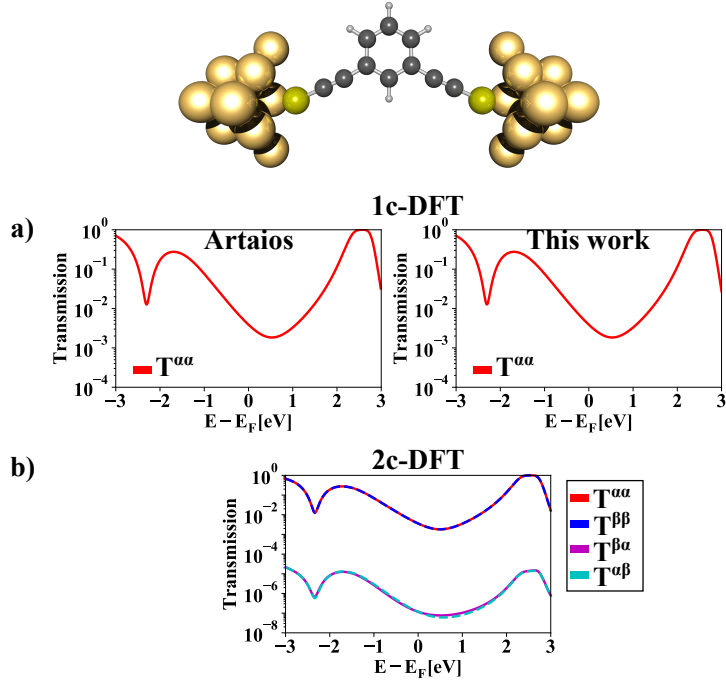


Figure 27: Comparison of ARTAIOS with the new program written during this work for a closed-shell system. All energies are shifted against the estimated  $E_F$  of -5 eV. **a)** For the DFT calculation without SOC, the results obtained with the new implementation are in good agreement with the results computed with ARTAIOS. **b)** If SOC is activated, four transmission functions contribute to the transmission. All spin-dependent transmission functions have the same shape as  $\mathcal{T}^{\alpha\alpha}(E)$  calculated without SOC. The spin-flip transmission functions are several magnitudes smaller than the spin-conserving transmission functions.

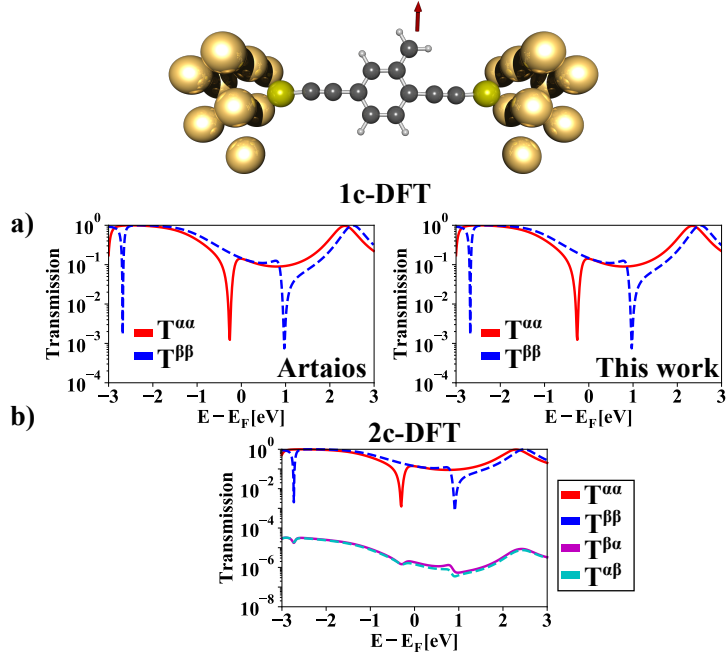


Figure 28: Comparison of ARTAIOS with the program written during this work, for an open-shell system. All energies are shifted against the estimated  $E_F$  of  $-5$  eV. **a)** For the DFT calculation without SOC the results obtained with the new implementation are in good agreement with the results computed with ARTAIOS. The results are consistent with Reference [55]. **b)** If SOC is activated, four transmission functions contribute to the transmission. The spin-conserving transmission functions have the same form as  $\mathcal{T}^{\alpha\alpha}(E)/\mathcal{T}^{\beta\beta}(E)$  calculated without SOC. The spin-flip transmission functions are several magnitudes smaller than the spin-conserving transmission functions, and are shaped like the mean of  $\mathcal{T}^{\alpha\alpha}(E)$  and  $\mathcal{T}^{\beta\beta}(E)$ .

Overall, the results confirm a successful implementation of the chosen methodology. However, although the implementation which has been described throughout Section 5.3.2 allows for a first-principles investigation of the CISS effect in conductance experiments, considering SOC alone might not be sufficient enough to describe the correct order of magnitude of the effect. Thus, the implementation of a method to include another potential important phenomenon for the description of CISS is presented next.

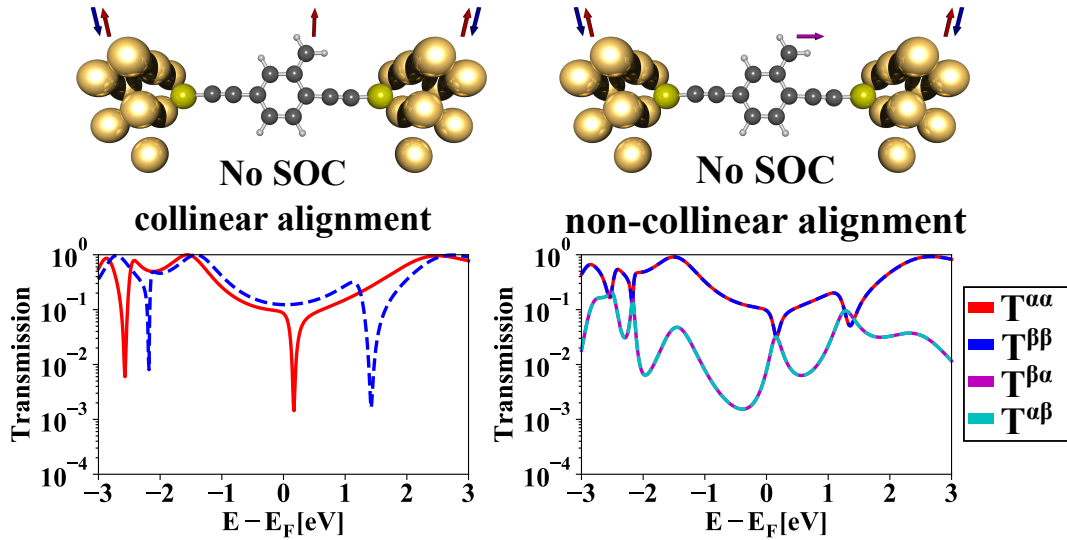


Figure 29: Effect of rotating the radical’s spin from a collinear to a non-collinear alignment (regarding the spin of the electrodes). All energies are shifted against the estimated  $E_F$  of -5 eV. If the spin is non-collinear, the spin-conserving transmission functions become equal. The spin-flip transmission functions now show maxima at the energies where the spin-conserving transmission functions have dips (resulting from destructive quantum interference).

### 5.3.3. Effective Dephasing Model to include Electron–Phonon Coupling

A method to calculate the effect of electron–phonon coupling for electron transport was implemented into ARTAIOS during this work, since electron–phonon coupling is under consideration to be important for the description of the CISS effect (see References [173] and [191]). To consider electron–phonon coupling within electron transport calculations, one in principle has to go beyond the Landauer-transport equation, and the electron–phonon coupling has to be computed. To circumvent this calculation, it is possible to introduce electron–phonon coupling using an effective parameter. One approach in doing so was introduced by Frauenheim *et al.* [192], leading to a Landauer-like formulation of the transport properties including electron–phonon coupling.

## Effective Transmission Function to include Electron–Phonon Coupling

In the following, the approach introduced by Frauenheim *et al.* is derived, starting from the NEGF approach (see Section 2.3.2). The matrix representation of the operators are used and the energy dependence of the used matrices is not written explicitly.

As explained in Section 2.3, electron–phonon interaction can be considered within the NEGF approach. The current from the left to the right electrode can be obtained as [192]

$$I_{LR} = i\frac{2e}{h} \int dE \text{Tr} [\mathbf{\Gamma}_L \mathbf{G}^< - \mathbf{\Sigma}_L^< \mathbf{A}]. \quad (5.27)$$

Inserting the definitions for  $\mathbf{G}^<$  (Equation (2.115)),  $\mathbf{A}$  (Equation (2.116)) and  $\mathbf{\Sigma}_L^<$  (Equation (2.112)) into Equation (5.27), the matrix over which the trace is taken becomes

$$\begin{aligned} [\mathbf{\Gamma}_L \mathbf{G}^< - \mathbf{\Sigma}_L^< \mathbf{A}] &= \mathbf{\Gamma}_L \mathbf{G}^r (\mathbf{\Sigma}_L^< + \mathbf{\Sigma}_R^< + \mathbf{\Sigma}_{\text{elph}}^<) \mathbf{G}^a \\ &\quad - i f_L \mathbf{\Gamma}_L \mathbf{G}^r (\mathbf{\Gamma}_L + \mathbf{\Gamma}_R + \mathbf{\Gamma}_{\text{elph}}) \mathbf{G}^a, \\ &= +i f_L \mathbf{\Gamma}_L \mathbf{G}^r \mathbf{\Gamma}_L \mathbf{G}^a \\ &\quad + i f_R \mathbf{\Gamma}_L \mathbf{G}^r \mathbf{\Gamma}_R \mathbf{G}^a \\ &\quad + \mathbf{\Gamma}_L \mathbf{G}^r \mathbf{\Sigma}_{\text{elph}}^< \mathbf{G}^a \\ &\quad - i f_L \mathbf{\Gamma}_L \mathbf{G}^r \mathbf{\Gamma}_L \mathbf{G}^a \\ &\quad - i f_L \mathbf{\Gamma}_L \mathbf{G}^r \mathbf{\Gamma}_R \mathbf{G}^a \\ &\quad - i f_L \mathbf{\Gamma}_L \mathbf{G}^r \mathbf{\Gamma}_{\text{elph}} \mathbf{G}^a. \end{aligned} \quad (5.28)$$

The first and the fourth term cancel each other, resulting in

$$\begin{aligned} i[\mathbf{\Gamma}_L \mathbf{G}^< - \mathbf{\Sigma}_L^< \mathbf{A}] &= (f_L - f_R) \mathbf{\Gamma}_L \mathbf{G}^r \mathbf{\Gamma}_R \mathbf{G}^a \\ &\quad + i \mathbf{\Gamma}_L \mathbf{G}^r \mathbf{\Sigma}_{\text{elph}}^< \mathbf{G}^a \\ &\quad + f_L \mathbf{\Gamma}_L \mathbf{G}^r \mathbf{\Gamma}_{\text{elph}} \mathbf{G}^a \end{aligned} \quad (5.30)$$

To continue, specific formulations for  $\mathbf{\Sigma}_{\text{elph}}^<$  and  $\mathbf{\Gamma}_{\text{elph}}$  are needed. Assuming strongly localized phonons as well as  $\mathbf{G}^{r/a/<}$  to be constant within reasonable ranges of phonon energies,  $\mathbf{\Gamma}_{\text{elph}}$  can be written as [192]

$$\mathbf{\Gamma}_{\text{elph}} \approx \gamma \mathbf{A} \gamma. \quad (5.31)$$

$\gamma$  is a phenomenological parameter, scaling the strength of the dephasing. Equation (5.31) can be written as

$$\gamma \mathbf{A} \gamma = \gamma \mathbf{G}^r (\mathbf{\Gamma}_L + \mathbf{\Gamma}_R + \mathbf{\Gamma}_{\text{elph}}) \mathbf{G}^a \gamma. \quad (5.32)$$

To calculate  $\mathbf{\Gamma}_{\text{elph}}$  and  $\mathbf{\Sigma}_{\text{elph}}$ , the self-consistent Born approximation [192] can be used, in which  $\mathbf{\Gamma}_{\text{elph}}$  is obtained iteratively.  $\mathbf{G}^{r/a}$ ,  $\mathbf{G}^<$  and  $\mathbf{\Gamma}_{\text{elph}}$  of each cycle  $n$  in the Born approximation can be formulated as

$$\mathbf{G}^{r/a;n} = \frac{1}{E\mathbf{S} - \mathbf{H}_C - \mathbf{\Sigma}_L^{r/a} - \mathbf{\Sigma}_R^{r/a} - \mathbf{\Sigma}_{\text{elph}}^{r/a;n-1}}, \quad (5.33)$$

$$\mathbf{G}^{<;n} = \mathbf{G}^{r;n} \left[ i f_L \mathbf{\Gamma}_L + i f_R \mathbf{\Gamma}_R + \mathbf{\Sigma}_{\text{elph}}^{<;n-1} \right] \mathbf{G}^{a;n}, \quad (5.34)$$

$$\mathbf{\Gamma}_{\text{elph}}^n = \gamma \mathbf{G}^{r;n} (\mathbf{\Gamma}_L + \mathbf{\Gamma}_R + \mathbf{\Gamma}_{\text{elph}}^{n-1}) \mathbf{G}^{a;n} \gamma, \quad (5.35)$$

with  $\mathbf{\Sigma}_{\text{elph}}^{<;-1} = 0$ ,  $\mathbf{\Sigma}_{\text{elph}}^{r/a;-1} = 0$ , and  $\mathbf{\Gamma}_{\text{elph}}^{<;-1} = 0$  at “zeroth” order.  $\mathbf{\Gamma}_{\text{elph}}^n$  can be written as

$$\mathbf{\Gamma}_{\text{elph}}^n = \mathbf{\Gamma}_{L,\text{elph}}^n + \mathbf{\Gamma}_{R,\text{elph}}^n, \quad (5.36)$$

where  $\mathbf{\Gamma}_{L,\text{elph}}^n$  is the sum over all parts which contain  $\mathbf{\Gamma}_L$  and  $\mathbf{\Gamma}_{R,\text{elph}}^n$  is the sum over all parts which contain  $\mathbf{\Gamma}_R$ . As a consequence of the assumptions leading to Equation (5.31),  $\mathbf{\Sigma}_{\text{elph}}^{<;n}$  can be written as [192]

$$\mathbf{\Sigma}_{\text{elph}}^{<;n} = \gamma \mathbf{G}^{<;n} \gamma. \quad (5.37)$$

Using Equations (5.34), Equation (5.37) for any order  $n$  can be written as

$$\mathbf{\Sigma}_{\text{elph}}^{<;n} = \gamma \left( \mathbf{G}^{r;n} \left[ i f_L \mathbf{\Gamma}_L + i f_R \mathbf{\Gamma}_R + \mathbf{\Sigma}_{\text{elph}}^{<;n-1} \right] \mathbf{G}^{a;n} \right) \gamma. \quad (5.38)$$

Equation (5.38) can then be written as

$$\mathbf{\Sigma}_{\text{elph}}^{<;n} = \gamma \left( \mathbf{G}^{r;n} \left[ i f_L \mathbf{\Gamma}_L + i f_R \mathbf{\Gamma}_R \right. \right. \quad (5.39)$$

$$\left. \left. + \gamma \left( \mathbf{G}^{r;n-1} \left[ i f_L \mathbf{\Gamma}_L + i f_R \mathbf{\Gamma}_R + \mathbf{\Sigma}_{\text{elph}}^{<;n-2} \right] \mathbf{G}^{a;n-1} \right) \gamma \right] \mathbf{G}^{a;n} \right) \gamma, \quad (5.40)$$

which leads to

$$\begin{aligned} \mathbf{\Sigma}_{\text{elph}}^{<;n} = & i f_L \gamma \mathbf{G}^{r;n} \mathbf{\Gamma}_L \mathbf{G}^{a;n} \gamma + i f_L \gamma \mathbf{G}^{r;n} \gamma \mathbf{G}^{r;n-1} \mathbf{\Gamma}_L \mathbf{G}^{a;n-1} \gamma \mathbf{G}^{a;n} \gamma + \dots \\ & + i f_R \gamma \mathbf{G}^{r;n} \mathbf{\Gamma}_R \mathbf{G}^{a;n} \gamma + i f_R \gamma \mathbf{G}^{r;n} \gamma \mathbf{G}^{r;n-1} \mathbf{\Gamma}_R \mathbf{G}^{a;n-1} \gamma \mathbf{G}^{a;n} \gamma + \dots, \end{aligned} \quad (5.41)$$

after recursively inserting all self-energies down to the order  $n = 0$ . Combining Equations (5.35) and (5.36) with Equation (5.41), the lesser self energy can be written as

$$\Sigma_{\text{elph}}^{<,n} = if_L \Gamma_{L,\text{elph}}^n + if_R \Gamma_{R,\text{elph}}^n. \quad (5.42)$$

Inserting this expression for  $\Sigma_{\text{elph}}^{<,n}$  into Equation (5.30) leads to

$$\begin{aligned} i[\Gamma_L \mathbf{G}^< - \Sigma_L^< \mathbf{A}] &= (f_L - f_R) \Gamma_L \mathbf{G}^r \Gamma_R \mathbf{G}^a \\ &+ i\Gamma_L \mathbf{G}^r \left( if_L \Gamma_{L,\text{elph}}^{n-1} + if_R \Gamma_{R,\text{elph}}^{n-1} \right) \mathbf{G}^a \\ &+ f_L \Gamma_L \mathbf{G}^r \left( \Gamma_{L,\text{elph}}^{n-1} + \Gamma_{R,\text{elph}}^{n-1} \right) \mathbf{G}^a, \end{aligned} \quad (5.43)$$

which can be formulated as

$$\begin{aligned} i[\Gamma_L \mathbf{G}^< - \Sigma_L^< \mathbf{A}] &= (f_L - f_R) \Gamma_L \mathbf{G}^r \Gamma_R \mathbf{G}^a \\ &- f_L \Gamma_L \mathbf{G}^r \Gamma_{L,\text{elph}}^{n-1} \mathbf{G}^a - f_R \Gamma_L \mathbf{G}^r \Gamma_{R,\text{elph}}^{n-1} \mathbf{G}^a \\ &+ f_L \Gamma_L \mathbf{G}^r \Gamma_{L,\text{elph}}^{n-1} \mathbf{G}^a + f_L \Gamma_L \mathbf{G}^r \Gamma_{R,\text{elph}}^{n-1} \mathbf{G}^a, \end{aligned} \quad (5.44)$$

where term two and term four cancel each other, yielding

$$i\text{Tr} [\Gamma_L \mathbf{G}^< - \Sigma_L^< \mathbf{A}] = (f_L - f_R) \text{Tr} \left[ \Gamma_L \mathbf{G}^r \Gamma_R \mathbf{G}^a + \Gamma_L \mathbf{G}^r \Gamma_{R,\text{elph}}^{n-1} \mathbf{G}^a \right]. \quad (5.45)$$

If this equation is inserted into Equation (5.27), the current can be computed as

$$I_{LR} = \frac{2e}{h} \int dE (f_L - f_R) \text{Tr} \left[ \Gamma_L \mathbf{G}^r \Gamma_R \mathbf{G}^a + \Gamma_L \mathbf{G}^r \Gamma_{R,\text{elph}}^{n-1} \mathbf{G}^a \right], \quad (5.46)$$

which is the expression given by Frauenheim *et al.* [192]. The trace can be summarized as an effective transmission function,

$$\mathcal{T}^{\text{eff}} = \text{Tr} \left[ \Gamma_L \mathbf{G}^r \Gamma_R \mathbf{G}^a + \Gamma_L \mathbf{G}^r \Gamma_{R,\text{elph}}^{n-1} \mathbf{G}^a \right]. \quad (5.47)$$

For the calculation of  $\mathcal{T}^{\text{eff}}$  using DFT, several possible formulations of  $\gamma$  were introduced by Frauenheim *et al.* [192].  $\gamma$  can be chosen as a single parameter, leading to

$$\left( \Sigma_{\text{elph}}^{r,a,<,>} \right)_{i\mu,i\nu} = \gamma_i^2 \mathbf{G}_{i\mu,i\nu}^{r,a,<,>}. \quad (5.48)$$

This approach ignores the overlap of the atomic orbitals within the central region. To take into account the overlap, Frauenheim *et al.* suggested to use a matrix  $\tilde{\gamma}_I$  for each atom  $I$  in the scattering region [192],

$$\tilde{\gamma}_I = \frac{\mathbf{M}_I \mathbf{S}_C}{2} + \frac{\mathbf{S}_C \mathbf{M}_I}{2}. \quad (5.49)$$

$\mathbf{M}_I$  is a matrix with the dimension of the entire central region. The diagonal elements, which correspond to basis functions located on atom  $I$ , are set to the value of an effective parameter  $\gamma$ , while all other elements are set to zero,

$$(\mathbf{M}_I)_{ij} = \begin{cases} \gamma, & \text{if } (i = j) \wedge (i \in I) \\ 0, & \text{otherwise} \end{cases}. \quad (5.50)$$

$\Sigma_{\text{elph}}^{r,a,<, >}$  can now be computed as

$$\Sigma_{\text{elph}}^{r,a,<, >} = \sum_I^{N_I} \tilde{\gamma}_I \mathbf{G}^{r,a,<, >} \tilde{\gamma}_I \quad (5.51)$$

where  $I$  runs over all atoms  $N_I$  located in the central region. As a consequence,  $\mathbf{\Gamma}_{\text{R,elph}}^n$  is obtained as

$$\begin{aligned} \mathbf{\Gamma}_{\text{R,elph}}^n &= \sum_I^{N_I} \tilde{\gamma}_I \mathbf{G}^{r,n} \mathbf{\Gamma}_R \mathbf{G}^{a,n} \tilde{\gamma}_I \\ &+ \sum_I^{N_I} \tilde{\gamma}_I \mathbf{G}^{r,n} \left( \sum_J^{N_I} \tilde{\gamma}_J \mathbf{G}^{r,n-1} \mathbf{\Gamma}_R \mathbf{G}^{a,n-1} \tilde{\gamma}_J \right) \mathbf{G}^{a,n} \tilde{\gamma}_I + \dots \end{aligned} \quad (5.52)$$

The formulas in Equation (5.47) and (5.52) were implemented into ARTAIOS.

### Details on the Implementation of the Effective Dephasing Model

The implementation of the just derived methodology to include electron–phonon coupling into electron transport calculations into ARTAIOS is explained next. To do so, instead of writing the Green’s function matrices as  $\mathbf{G}^r$  and  $\mathbf{G}^a$ , the terminology as employed in Reference [190] is used again ( $\mathbf{G}$  and  $\mathbf{G}^\dagger$ ).

The methodology for the calculation of  $\mathcal{T}^{\text{eff}}$  was implemented into ARTAIOS, employing the FORTRAN90 programming language as

$$\mathcal{T}_{LR}^{\text{eff}} = \text{Tr} \left[ \mathbf{\Gamma}_L \mathbf{G}^{\dagger,n} \left( \mathbf{\Gamma}_R + \mathbf{\Gamma}_{\text{R,elph}}^{n-1} \right) \mathbf{G}^n \right], \quad (5.53)$$

using the optimized linear algebra libraries BLAS [193] and LAPACK [194]. The dephasing value  $\gamma$  is given as an input parameter and the  $\tilde{\gamma}_I$  matrices are calculated

automatically according to Equation (5.49). The zeroth-order Green's function matrix  $\mathbf{G}^0$  is computed as

$$\mathbf{G}^0 = \left[ \begin{array}{c|c} E\mathbf{S}_C^{\alpha\alpha} - \mathbf{H}_C^{\alpha\alpha} - \Sigma_L^{\alpha\alpha} - \Sigma_R^{\alpha\alpha} & -\mathbf{H}_C^{\alpha\beta} \\ \hline -\mathbf{H}_C^{\beta\alpha} & E\mathbf{S}_C^{\beta\beta} - \mathbf{H}_C^{\beta\beta} - \Sigma_L^{\beta\beta} - \Sigma_R^{\beta\beta} \end{array} \right]^{-1}. \quad (5.54)$$

For every subsequent self-consistent Born approximation cycle  $n$ , the following steps are taken:

1.  $\Sigma_{\text{elph}}^n$  is calculated from Equation 5.51.
2.  $\Sigma_{\text{elph}}^n$  is used to obtain  $\mathbf{G}^{n+1}$  from Equation (5.33).
3. Convergence for every element  $\mathbf{G}_{ij}^{n+1}$  is checked. Convergence is achieved if no element  $\mathbf{G}_{ij}^{n+1}$  deviates by more than  $10^{-6}$  eV $^{-1}$  from the corresponding element  $\mathbf{G}_{ij}^n$ .
4. If convergence is achieved,  $\mathbf{\Gamma}_{R,\text{elph}}^{n-1}$  is computed from Equation (5.52), otherwise step 1 is repeated.

To calculate the spin-dependent  $\mathcal{T}^{\text{eff}}$ , it is partitioned into two spin-flip and two spin-conserving transmission functions.

### Validation of the Implementation

The just described implementation was validated by calculating  $\mathcal{T}^{\text{eff}}$  for an anthrachinone-based molecular junction (see Figure 30). The results were compared to results of Frauenheim *et al.* [192]. The anthrachinone-based molecular junction exhibits a destructive QI feature within the HOMO–LUMO gap, manifesting as a dip in  $\mathcal{T}$  (see Figure 30). Since dephasing leads to a loss of coherence,  $\mathcal{T}^{\text{eff}}$  should show a less pronounced QI feature and the transmission maxima should be broadened upon including effective electron–phonon coupling [192].

The gold–anthrachinone–gold junction was built by placing an optimized anthrachinone molecule<sup>30</sup> between two three-atomic gold clusters ( $d_{\text{Au–Au}} = 2.88$  Å as in crystalline

---

<sup>30</sup> B3LYP/def2-TZVP, for details see Appendix A.

gold [61], and  $d_{S-Au} = 2.48 \text{ \AA}$ , based on calculations for phenylthiol from the literature [68]). Therefore, much smaller electrodes are used in this work to save computational time, but the qualitative trends of including electron-phonon interactions should be captured well enough.

$\mathcal{T}^{\text{eff}}$  calculated without dephasing ( $\gamma = 0$ ) shows the same features as obtained by Frauenheim *et al.* (see Figure 30). Upon activating dephasing by successively increasing  $\gamma$  from 0.05 eV to 2.0 eV,  $\mathcal{T}^{\text{eff}}$  increases at the QI feature, and the LUMO peak is broadened (see Figure 31). The HOMO peak is only slightly affected by the dephasing. All of these dephasing effects are in agreement with the results by Frauenheim *et al.* [192], which indicates a successful implementation of the methodology.

Several approaches for a first-principles investigation of the CISS effect and their implementations have been presented and validated throughout Section 5.3. Next, the implemented Landauer approach is analyzed in detail, focusing on its ability to describe the CISS effect.

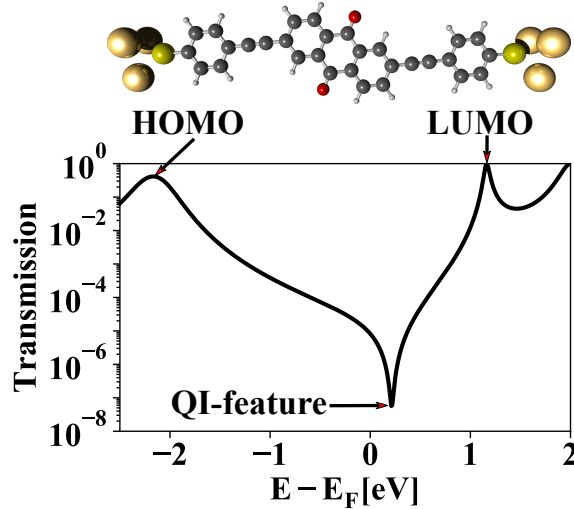


Figure 30: Transmission function for an anthracinone junction (B3LYP/ZORA-DZP).

Besides two transmission peaks, which can be assigned to the HOMO and LUMO, a dip close to  $E_F$  occurs. This feature results from destructive quantum interference. The energies are shifted by the estimated  $E_F$  of -5 eV.

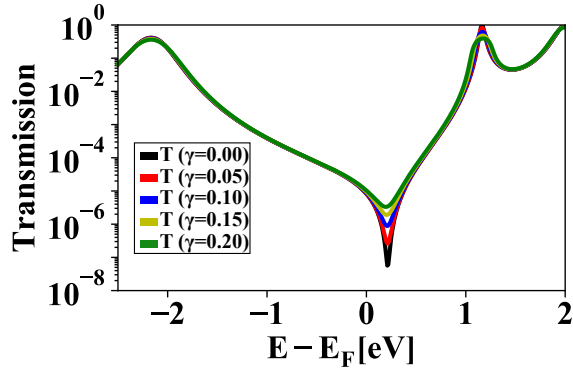


Figure 31: Effect of dephasing on the transmission function of an anthrachinone junction (B3LYP/ZORA-DZP). An increase of the effective dephasing parameter  $\gamma$  leads to an increase of the effective transmission at the QI feature, and the formerly sharp peak at the energy of the LUMO becomes broadened. Those observations are consistent with the results by Frauenheim *et al.* [192]. The energies are shifted by the estimated  $E_F$  of -5 eV.

#### 5.4. Possible Origins of Chiral-Induced Spin Selectivity with First-Principles Methods: Analytical Considerations for the Landauer Approach

To find a first-principles based explanation for the CISS effect, the Landauer approach was analyzed regarding its ability to describe the CISS effect using standard DFT methods (real basis functions). The knowledge of the origin of the effect in the Landauer approach is important, since it might give insight into dependencies of the effect on computational parameters and what kind of mechanisms might influence the effect in a first-principles description. To do so, the origin of a non-zero spin polarization of the transmitted electrons (which is called polarization, or  $SP$  as defined in Equation (5.2)) in closed-shell systems was investigated for the Landauer approach.

Starting point is the time-reversal (T) and space-inversion (P) symmetry of  $\mathcal{T}$ . This is similar to the T-symmetry and P-symmetry of the band structure for solids, as discussed in Section 4.1. Since space inversion inverts the momentum of an electron, and time re-

versal inverts the momentum and spin (described as a vector) of the electron [79], these symmetries are define in the following as

$$\mathcal{T}_{RL}^{\alpha\alpha} = \mathcal{T}_{LR}^{\alpha\alpha} \text{ and } \mathcal{T}_{RL}^{\alpha\beta} = \mathcal{T}_{LR}^{\beta\alpha} \quad (\text{P-symmetry})$$

$$\mathcal{T}_{RL}^{\alpha\alpha} = \mathcal{T}_{LR}^{\beta\beta} \text{ and } \mathcal{T}_{RL}^{\alpha\beta} = \mathcal{T}_{LR}^{\alpha\beta} \quad (\text{T-symmetry})$$

It is important to note that this definition for T-symmetry of  $\mathcal{T}$  is different from the commonly used mathematical definition [197]. However, since the focus of this part is the relation between the symmetry of the central region (defined by  $\mathbf{H}_C$ ) and  $SP$ , and the T-symmetry of  $\mathbf{H}_C$  directly defines the above defined T-Symmetry of  $\mathcal{T}$  (see Section 5.4.1), it is used throughout this work ( $T_{XY}^{\sigma\sigma'}$  denotes the transmission function of electrons from the  $\sigma$  spin channels of lead  $X$  to the  $\sigma'$  spin channels of lead  $Y$ ).

If P-symmetry and T-symmetry are present, the relations

$$\mathcal{T}_{RL}^{\alpha\alpha} = \mathcal{T}_{RL}^{\beta\beta} = \mathcal{T}_{LR}^{\beta\beta} = \mathcal{T}_{LR}^{\alpha\alpha}, \quad (5.55)$$

$$\mathcal{T}_{RL}^{\alpha\beta} = \mathcal{T}_{LR}^{\alpha\beta} = \mathcal{T}_{RL}^{\beta\alpha} = \mathcal{T}_{LR}^{\beta\alpha}, \quad (5.56)$$

are valid, and  $SP$  must be zero. The CISS effect within the Landauer approach is able to occur, if the P-symmetry of  $\mathcal{T}$  is broken by a combination of SOC and the molecule's symmetry. In the following, it is shown how the symmetry of  $\mathbf{G}$  can be directly translated into the symmetry of  $\mathcal{T}$ , and how the symmetry of  $\mathbf{G}$  is influenced by SOC and by the symmetry of the molecule. First, SOC as a necessary condition to achieve a non zero  $SP$  is derived. The derivation is based on the relations ( $X = L, R$ )

$$\mathbf{\Sigma}_X = i\text{Im}(\mathbf{\Sigma}_X) = [i\text{Im}(\mathbf{\Sigma}_X)]^T, \quad (5.57)$$

$$\mathbf{\Gamma}_X = (\mathbf{\Gamma}_X)^T, \quad (5.58)$$

$$\mathbf{\Gamma}_X^{\alpha\alpha} = \mathbf{\Gamma}_X^{\beta\beta}, \quad (5.59)$$

emerging from the assumption of a closed-shell system described within the implemented Landauer approach (for details of the implementation, see Section 5.3.2). Afterwards, a connection between the symmetry of a molecule and the absence of  $SP$  is done employing a model system. For the sake of clarity, the energy dependence of all used quantities is not written explicitly.

### 5.4.1. Conditions for P- and T-Symmetry of the Transmission Function

The symmetry of  $\mathbf{G}$  can be directly translated into the symmetry of  $\mathcal{T}$ . This can be shown by looking at the expressions for  $\mathcal{T}_{RL}^{\alpha\alpha}$ ,

$$\mathcal{T}_{RL}^{\alpha\alpha} = \text{Tr} \left[ \mathbf{\Gamma}_L^{\alpha\alpha} \mathbf{G}^{\alpha\alpha} \mathbf{\Gamma}_R^{\alpha\alpha} (\mathbf{G}^{\alpha\alpha})^\dagger \right], \quad (5.60)$$

and  $\mathcal{T}_{RL}^{\alpha\beta}$ ,

$$\mathcal{T}_{RL}^{\alpha\beta} = \text{Tr} \left[ \mathbf{\Gamma}_L^{\beta\beta} \mathbf{G}^{\beta\alpha} \mathbf{\Gamma}_R^{\alpha\alpha} (\mathbf{G}^{\beta\alpha})^\dagger \right]. \quad (5.61)$$

The same argument also holds for  $\mathcal{T}_{RL}^{\beta\beta}$  and  $\mathcal{T}_{RL}^{\beta\alpha}$ , and therefore only one spin-conserving and one spin-flip transmission are discussed. T-symmetry of  $\mathcal{T}$  originates from the T-symmetry of  $\mathbf{H}_C$ . T-symmetry of  $\mathbf{H}_C$  is maintained for a closed-shell scattering region and non-magnetic electrodes. Considering the effect of  $\Sigma_X$  on  $\mathbf{H}_C$ , the spin-dependent blocks of the corresponding  $\mathbf{G}$  are related as<sup>31</sup>

$$\mathbf{G}^{\alpha\alpha} = \left( \mathbf{G}^{\beta\beta} \right)^T, \quad (5.62)$$

$$\mathbf{G}^{\beta\alpha} = - \left( \mathbf{G}^{\beta\alpha} \right)^T. \quad (5.63)$$

To show the relation between these symmetries and T-symmetry of  $\mathcal{T}$ , it is helpful to look at the transpose of the matrix of which the trace is taken for the calculation of  $\mathcal{T}_{RL}^{\alpha\alpha}$  and  $\mathcal{T}_{RL}^{\alpha\beta}$ ,<sup>32</sup>

$$\mathcal{T}_{RL}^{\alpha\alpha} = \text{Tr} \left[ \left[ (\mathbf{G}^{\alpha\alpha})^\dagger \right]^T (\mathbf{\Gamma}_R^{\alpha\alpha})^T (\mathbf{G}^{\alpha\alpha})^T (\mathbf{\Gamma}_L^{\alpha\alpha})^T \right], \quad (5.64)$$

$$\mathcal{T}_{RL}^{\alpha\beta} = \text{Tr} \left[ \left[ (\mathbf{G}^{\beta\alpha})^\dagger \right]^T (\mathbf{\Gamma}_R^{\alpha\alpha})^T (\mathbf{G}^{\beta\alpha})^T (\mathbf{\Gamma}_L^{\beta\beta})^T \right]. \quad (5.65)$$

Using the relation  $\mathbf{\Gamma}_X^{\alpha\alpha} = \mathbf{\Gamma}_X^{\beta\beta}$  for non-magnetic electrodes, the relation  $\mathbf{\Gamma}_X = (\mathbf{\Gamma}_X)^T$  for the purely imaginary and symmetric self energies, and due to the symmetries in Equation (5.62) and (5.63), T-symmetry for  $\mathcal{T}$  is obtained by reformulating Equations (5.64)

<sup>31</sup> The derivation of the symmetries for  $\mathbf{G}$  within the implemented Landauer approach is given in Appendix C, based on the T-symmetry of  $\mathbf{H}$  given by Reiher *et al.* [198].

<sup>32</sup> This does not change  $\mathcal{T}$ , because  $\text{Tr}[\mathbf{M}] = \text{Tr}[\mathbf{M}^T]$ .

and (5.65) as

$$\mathcal{T}_{RL}^{\alpha\alpha} = \text{Tr} \left[ (\mathbf{G}^{\beta\beta})^\dagger \mathbf{\Gamma}_R^{\beta\beta} \mathbf{G}^{\beta\beta} \mathbf{\Gamma}_L^{\beta\beta} \right] = \mathcal{T}_{LR}^{\beta\beta}, \quad (5.66)$$

$$\mathcal{T}_{RL}^{\alpha\beta} = \text{Tr} \left[ (\mathbf{G}^{\beta\alpha})^\dagger \mathbf{\Gamma}_R^{\beta\beta} \mathbf{G}^{\beta\alpha} \mathbf{\Gamma}_L^{\alpha\alpha} \right] = \mathcal{T}_{LR}^{\alpha\beta}. \quad (5.67)$$

P-symmetry of  $\mathcal{T}$  is present if  $\mathbf{G}$  is symmetric,

$$\mathbf{G}^{\alpha\alpha} = (\mathbf{G}^{\alpha\alpha})^T, \quad (5.68)$$

$$\mathbf{G}^{\alpha\beta} = (\mathbf{G}^{\beta\alpha})^T, \quad (5.69)$$

or Hermitian,

$$\mathbf{G}^{\alpha\alpha} = (\mathbf{G}^{\alpha\alpha})^\dagger, \quad (5.70)$$

$$\mathbf{G}^{\alpha\beta} = (\mathbf{G}^{\beta\alpha})^\dagger. \quad (5.71)$$

This can be shown by rewriting Equation (5.60) and (5.61) and assuming a Hermitian  $\mathbf{G}$ , or by rewriting Equation (5.64) and (5.65) and assuming a symmetric  $\mathbf{G}$ . In both cases, P-symmetry of  $\mathcal{T}$  is obtained as (for details see Appendix C)

$$\mathcal{T}_{RL}^{\alpha\alpha} = \text{Tr} \left[ \mathbf{\Gamma}_L^{\alpha\alpha} (\mathbf{G}^{\alpha\alpha})^\dagger \mathbf{\Gamma}_R^{\alpha\alpha} \mathbf{G}^{\alpha\alpha} \right] = \mathcal{T}_{LR}^{\alpha\alpha}, \quad (5.72)$$

$$\mathcal{T}_{RL}^{\alpha\beta} = \text{Tr} \left[ \mathbf{\Gamma}_L^{\beta\beta} (\mathbf{G}^{\alpha\beta})^\dagger \mathbf{\Gamma}_R^{\alpha\alpha} \mathbf{G}^{\alpha\beta} \right] = \mathcal{T}_{LR}^{\beta\alpha}. \quad (5.73)$$

Based on these conditions, a connection between SOC and the removal of P-symmetry can be done for the Landauer approach, which is discussed next.

#### 5.4.2. Connection between Imaginary Parts of the Effective Single-Particle Hamiltonian Matrix and Removal of P-Symmetry of the Transmission Function

Without SOC,  $\mathbf{H}_C$  for a closed-shell system is symmetric, the spin-up and spin-down blocks are the same, and the spin-flip blocks are zero [20],

$$\mathbf{H}_C = \mathbf{H}_C^T, \quad (5.74)$$

$$\mathbf{H}_C^{\alpha\alpha} = \mathbf{H}_C^{\beta\beta}, \quad (5.75)$$

$$\mathbf{H}_C^{\alpha\beta} = \mathbf{H}_C^{\beta\alpha} = 0. \quad (5.76)$$

Since  $\mathbf{S}_C$  [20],  $\mathbf{\Sigma}_L$ , and  $\mathbf{\Sigma}_R$  are also symmetric,  $\mathbf{G}$  must be symmetric as well,

$$\mathbf{G} = (\mathbf{E}\mathbf{S}_C - \mathbf{H}_C - \mathbf{\Sigma}_L - \mathbf{\Sigma}_R)^{-1} = (\mathbf{E}\mathbf{S}_C^T - \mathbf{H}_C^T - \mathbf{\Sigma}_L^T - \mathbf{\Sigma}_R^T)^{-1} = \mathbf{G}^T. \quad (5.77)$$

As shown before, a symmetric  $\mathbf{G}$  leads to P-symmetry in  $\mathcal{T}$ , and the spin polarization must be zero without SOC because T-symmetry is maintained for a closed-shell system.

If SOC is taken into account,  $\mathbf{H}_C$  becomes complex and Hermitian [35, 36], while  $\mathbf{S}_C$  remains purely real and symmetric. The symmetry properties of these matrices can now be written as

$$\mathbf{H}_C = \mathbf{H}_C^\dagger \neq \mathbf{H}_C^T, \quad (5.78)$$

$$\mathbf{S}_C = \mathbf{S}_C^T = \mathbf{S}_C^\dagger. \quad (5.79)$$

Since  $\mathbf{\Sigma}_L$  and  $\mathbf{\Sigma}_R$  are not Hermitian [24], but symmetric and complex, the combination of  $\mathbf{\Sigma}_L$ ,  $\mathbf{\Sigma}_R$ , and  $\mathbf{H}_C$  results in a  $\mathbf{G}$  which is in general neither Hermitian,

$$\mathbf{G} = \frac{1}{\mathbf{E}\mathbf{S}_C - \mathbf{H}_C - i\text{Im}[\mathbf{\Sigma}_L] - i\text{Im}[\mathbf{\Sigma}_R]} \neq \mathbf{G}^\dagger = \frac{1}{\mathbf{E}\mathbf{S}_C - \mathbf{H}_C + i\text{Im}[\mathbf{\Sigma}_L] + i\text{Im}[\mathbf{\Sigma}_R]}, \quad (5.80)$$

nor symmetric,

$$\mathbf{G} = \frac{1}{\mathbf{E}\mathbf{S} - \mathbf{H}_C - i\text{Im}[\mathbf{\Sigma}_L] - i\text{Im}[\mathbf{\Sigma}_R]} \neq \mathbf{G}^T = \frac{1}{\mathbf{E}\mathbf{S} - \mathbf{H}_C^* - i\text{Im}[\mathbf{\Sigma}_L] - i\text{Im}[\mathbf{\Sigma}_R]}. \quad (5.81)$$

Since a Hermitian or symmetric  $\mathbf{G}$  is necessary to enforce the P-symmetry of  $\mathcal{T}$ , the relation  $T_{RL}^{\alpha\alpha} = T_{RL}^{\beta\beta}$  is no longer enforced. This opens the door for non-zero  $SP$  and a description of CISS effect within the Landauer approach. In other words, SOC, or more precisely  $\text{Im}(\mathbf{H}_C)$ , is a necessary but no sufficient condition for a non-zero  $SP$  within the Landauer approach, because it leads to a non-symmetric, non-Hermitian  $\mathbf{G}$ .

To cover the CISS effect with the Landauer approach, besides SOC, the symmetry of the system should dictate the presence of a non-zero  $SP$ , *i.e.*, non-chiral molecules should show no  $SP$ . To give a relation between the symmetry of the molecule in the scattering region and P-symmetry of  $\mathcal{T}$ , a simple model Hamiltonian is applied in the following.

### 5.4.3. Indications for a Connection between Structural Symmetry of the Molecule and P-Symmetry of the Transmission Function

While  $\text{Im}(\mathbf{H})$  (as induced by SOC) as a necessary condition for non-zero  $P$  has been shown, the effect of the molecule's symmetry on  $SP$  remains open. Since for non-chiral molecules,  $\text{Im}(\mathbf{H})$  is non-zero as well, if SOC is considered, the explicit structure of  $\mathbf{H}$  for a molecule may be responsible for the absence of  $SP$  in non-chiral systems. In the following, a connection between the absence of  $SP$  and a linear symmetry (which represents only a single form of non-chiral symmetry) is derived for a very simple model. This derivation does not prove that no  $SP$  occurs in non-chiral molecules in general, but shows that the symmetry of the molecule can be connected to the absence of  $SP$ , even if SOC is considered.

To investigate the effect of the symmetry of a molecule on the P-symmetry of  $\mathcal{T}$ , a model system consisting of a homoatomic chain with two atoms placed between two leads is used. The two-atomic chain defines the central region, and  $\mathbf{H}_C$  has the form

$$\mathbf{H}_C = \begin{pmatrix} \mathbf{H}_1 & \mathbf{V}_{12} \\ \mathbf{V}_{21} & \mathbf{H}_2 \end{pmatrix} = \begin{pmatrix} \mathbf{H}_1 & \mathbf{V}_{12} \\ \mathbf{V}_{12}^\dagger & \mathbf{H}_2 \end{pmatrix} \quad (5.82)$$

where the block  $\mathbf{H}_x$  describes the coupling between atomic orbitals located on atom  $x$ , and the block  $\mathbf{V}_{xy}$  describes the coupling of all atomic orbitals located on atom  $x$  with all orbitals located on atom  $y$ . Since the chain is homoatomic,  $\mathbf{H}_1$  is equal to  $\mathbf{H}_2$ .

If SOC is considered and the spin-flip terms are ignored,  $\mathbf{H}_C$  becomes

$$\mathbf{H}_C = \begin{pmatrix} \mathbf{H}_1^{\alpha\alpha} & \mathbf{V}_{12}^{\alpha\alpha} & \mathbf{0} & \mathbf{0} \\ (\mathbf{V}_{12}^{\alpha\alpha})^\dagger & \mathbf{H}_2^{\alpha\alpha} & \mathbf{0} & \mathbf{0} \\ \mathbf{0} & \mathbf{0} & \mathbf{H}_1^{\beta\beta} & \mathbf{V}_{12}^{\beta\beta} \\ \mathbf{0} & \mathbf{0} & (\mathbf{V}_{12}^{\beta\beta})^\dagger & \mathbf{H}_2^{\beta\beta} \end{pmatrix}. \quad (5.83)$$

This rough assumption hardly applies to realistic systems, but allows to give a simple connection between  $SP$  and the symmetry of the system. For simplicity,  $\mathbf{\Gamma}_L$  and  $\mathbf{\Gamma}_R$  are

assumed to be

$$\mathbf{\Gamma}_L = \begin{pmatrix} \mathbf{\Gamma} & 0 & 0 & 0 \\ 0 & 0 & 0 & 0 \\ 0 & 0 & \mathbf{\Gamma} & 0 \\ 0 & 0 & 0 & 0 \end{pmatrix}, \quad (5.84)$$

$$\mathbf{\Gamma}_R = \begin{pmatrix} 0 & 0 & 0 & 0 \\ 0 & \mathbf{\Gamma} & 0 & 0 \\ 0 & 0 & 0 & 0 \\ 0 & 0 & 0 & \mathbf{\Gamma} \end{pmatrix}, \quad (5.85)$$

which corresponds to a coupling of the left electrode with atom 1 and a coupling of the right electrode with atom 2, which is equal for  $\alpha$  and  $\beta$  spins.  $\mathbf{V}_{xy}$  is not influenced by the vicinity of the electrodes. This is also a rough approximation, since in most systems the electrode couples to more than one atom, but it allows for a simple formulation of the transmission function.  $\mathcal{T}_{RL}^{\sigma\sigma}$  and  $\mathcal{T}_{LR}^{\sigma\sigma}$  of the model system can then be calculated as

$$T_{LR}^{\sigma\sigma} = \text{Tr} \left[ \mathbf{\Gamma} \mathbf{G}_{12}^{\sigma\sigma} \mathbf{\Gamma} (\mathbf{G}_{12}^{\sigma\sigma})^\dagger \right], \quad (5.86)$$

$$T_{RL}^{\sigma\sigma} = \text{Tr} \left[ \mathbf{\Gamma} \mathbf{G}_{21}^{\sigma\sigma} \mathbf{\Gamma} (\mathbf{G}_{21}^{\sigma\sigma})^\dagger \right]. \quad (5.87)$$

As in Section 5.4.1, P-symmetry is retained if  $(\mathbf{G}_{12}^{\sigma\sigma})^\dagger = \mathbf{G}_{21}^{\sigma\sigma}$  or  $(\mathbf{G}_{12}^{\sigma\sigma})^T = \mathbf{G}_{21}^{\sigma\sigma}$ . However, another relation also can enforce P-symmetry of  $\mathcal{T}$  for the model system, namely  $\mathbf{G}_{12}^{\sigma\sigma} = \mathbf{G}_{21}^{\sigma\sigma}$ . This is consistent with an interpretation for  $\mathbf{G}_{12}$  [199] as a propagator, *i.e.*, as the probability amplitude of an electron's propagation from atom 2 to atom 1 at a certain energy.<sup>33</sup> It makes sense that if the propagator from atom 1 to atom 2 is different from the propagator from atom 2 to atom 1, P-symmetry is broken. In the following, the effect of the model-system's symmetry on  $\mathbf{G}$  is discussed.

In principle,  $\mathbf{H}_C$  always describes a linear system because only two atoms are considered. Therefore, the symmetry in both model systems is modulated artificially by the

---

<sup>33</sup> Probability of a propagation is defined as  $|G|^2$  [199].

relation of  $\mathbf{V}_{12}$  and  $\mathbf{V}_{21}$ . Considering  $p$ -orbitals only, the matrix elements of the form  $\xi_j \langle p_k^\alpha | l_z \cdot s_z | p_l^\alpha \rangle$  (see Equation (2.79)) allow to estimate the relation for a linear system in a linear basis (see Figure 32 part a)

$$\mathbf{V}_{12} = \mathbf{V}_{21} = \mathbf{V}_{12}^\dagger, \quad (5.88)$$

while for a helical system in a helical basis, the relation

$$\mathbf{V}_{12} = \mathbf{V}_{21}^\dagger \quad (5.89)$$

can be estimated (see Figure 32 part b). The reasons for using a symmetry-adapted basis is discussed in Section 5.5.2, and the relations for the nearest-neighbor coupling are validated by DFT calculations for a perfect-helical and perfect-linear carbon chain later on (see Section 5.5.4). These relations determine the symmetry of  $\mathbf{G}$  of the model system.  $\mathbf{H}_C^{\sigma\sigma}$  for the linear model system can be written as

$$\mathbf{H}_C^{\sigma\sigma} = \begin{pmatrix} \mathbf{H}_1^{\sigma\sigma} & \mathbf{V}_{12}^{\sigma\sigma} \\ \mathbf{V}_{12}^{\sigma\sigma} & \mathbf{H}_2^{\sigma\sigma} \end{pmatrix}. \quad (5.90)$$

$\mathbf{G}^{\sigma\sigma}$  can then be calculated as

$$\mathbf{G}^{\sigma\sigma} = \frac{1}{E\mathbf{S}_C^{\sigma\sigma} - \mathbf{H}_C^{\sigma\sigma} - \Sigma_L - \Sigma_R}. \quad (5.91)$$

Since  $\mathbf{S}_C$  has the same block form as  $\mathbf{H}_C^{\sigma\sigma}$ ,

$$\mathbf{S}_C^{\sigma\sigma} = \begin{pmatrix} \mathbf{S}_1^{\sigma\sigma} & \mathbf{S}_{12}^{\sigma\sigma} \\ \mathbf{S}_{12}^{\sigma\sigma} & \mathbf{S}_2^{\sigma\sigma} \end{pmatrix}, \quad (5.92)$$

and because  $\Sigma_L$  manipulates  $\mathbf{H}_1^{\sigma\sigma}$  in the same way as  $\Sigma_R$  manipulates  $\mathbf{H}_2^{\sigma\sigma}$ , the matrix in the denominator also has the same form as  $\mathbf{H}_C$ . The inversion of a  $(2 \times 2)$  block matrix yields [200]

$$\begin{pmatrix} \mathbf{A} & \mathbf{B} \\ \mathbf{C} & \mathbf{D} \end{pmatrix}^{-1} = \begin{pmatrix} (\mathbf{A} - \mathbf{B}\mathbf{D}^{-1}\mathbf{C})^{-1} & -\mathbf{A}^{-1}\mathbf{B}(\mathbf{D} - \mathbf{C}\mathbf{A}^{-1}\mathbf{B})^{-1} \\ -\mathbf{D}^{-1}\mathbf{C}(\mathbf{A} - \mathbf{B}\mathbf{D}^{-1}\mathbf{C})^{-1} & (\mathbf{D} - \mathbf{C}\mathbf{A}^{-1}\mathbf{B})^{-1} \end{pmatrix}, \quad (5.93)$$

and the relation  $\mathbf{G}_{12}^{\sigma\sigma} = \mathbf{G}_{21}^{\sigma\sigma}$  remains valid<sup>34</sup>. Consequently, P-symmetry of  $\mathcal{T}$  for the linear model system is retained and  $SP$  must be zero, even if  $\text{Im}(\mathbf{H})$  is not zero.

---

<sup>34</sup> For the chosen system  $\mathbf{A} = \mathbf{D}$  and  $\mathbf{B} = \mathbf{C}$ .

If the estimated relation  $\mathbf{V}_{12} \neq \mathbf{V}_{21}$  for the helical model is used,  $\mathbf{H}_C^{\sigma\sigma}$  can only be written as

$$\mathbf{H}^{\sigma\sigma} = \begin{pmatrix} \mathbf{H}_1^{\sigma\sigma} & \mathbf{V}_{12}^{\sigma\sigma} \\ (\mathbf{V}_{12}^{\sigma\sigma})^\dagger & \mathbf{H}_2^{\sigma\sigma} \end{pmatrix}. \quad (5.94)$$

As a consequence<sup>35</sup>, neither  $\mathbf{G}_{12} = \mathbf{G}_{21}$  nor  $\mathbf{G}_{12}^\dagger = \mathbf{G}_{21}$  can be assumed to hold, and the P-symmetry of  $\mathcal{T}$  cannot be enforced anymore, resulting in a possible non-zero  $P$ . Therefore, a linear structure of the molecule defining the scattering region can be connected to the absence of  $SP$  within the Landauer approach, while a helical structure can be connected to the removal of P-symmetry of  $\mathcal{T}$ .

The analytical derivations throughout Section 5.4 have given important hints on the origin of the CISS effect within first-principles based electron transport calculations. It is important to emphasize that for the Landauer approach, the imaginary part induced by SOC has been shown to be a necessary condition for any system, while a connection between symmetry and the CISS effect only has been indicated for linear and helical systems, and by using a simple model Hamiltonian. Spin-flip blocks have been neglected and the relations for  $\mathbf{V}_{12}$  and  $\mathbf{V}_{21}$  have been roughly estimated for  $p$ -orbitals only. If atomic  $s$ -orbitals are considered, the relation in Equation (5.88) is not valid anymore, due to the real part of the spin-conserving block (the overlap of the  $s$ -orbitals on atom 1 with the  $p$ -orbitals on atom 2 has the opposite sign as the overlap of the  $s$ -orbitals on atom 2 with the  $p$ -orbitals on atom 1, since  $s$ -orbitals are symmetric under inversion, while  $p$ -orbitals are not). However, results from DFT calculations for a perfect linear carbon chain show (see Section 5.5) that even considering the  $s$ - $p$  coupling for a linear system does not induce spin polarization.

---

<sup>35</sup> For details see Equations (C.13) and C.14. For the chosen system,  $\mathbf{B} \neq \mathbf{C}$  (due to the symmetry) and  $\mathbf{A} \neq \mathbf{A}^\dagger$  (due to the self-energies).

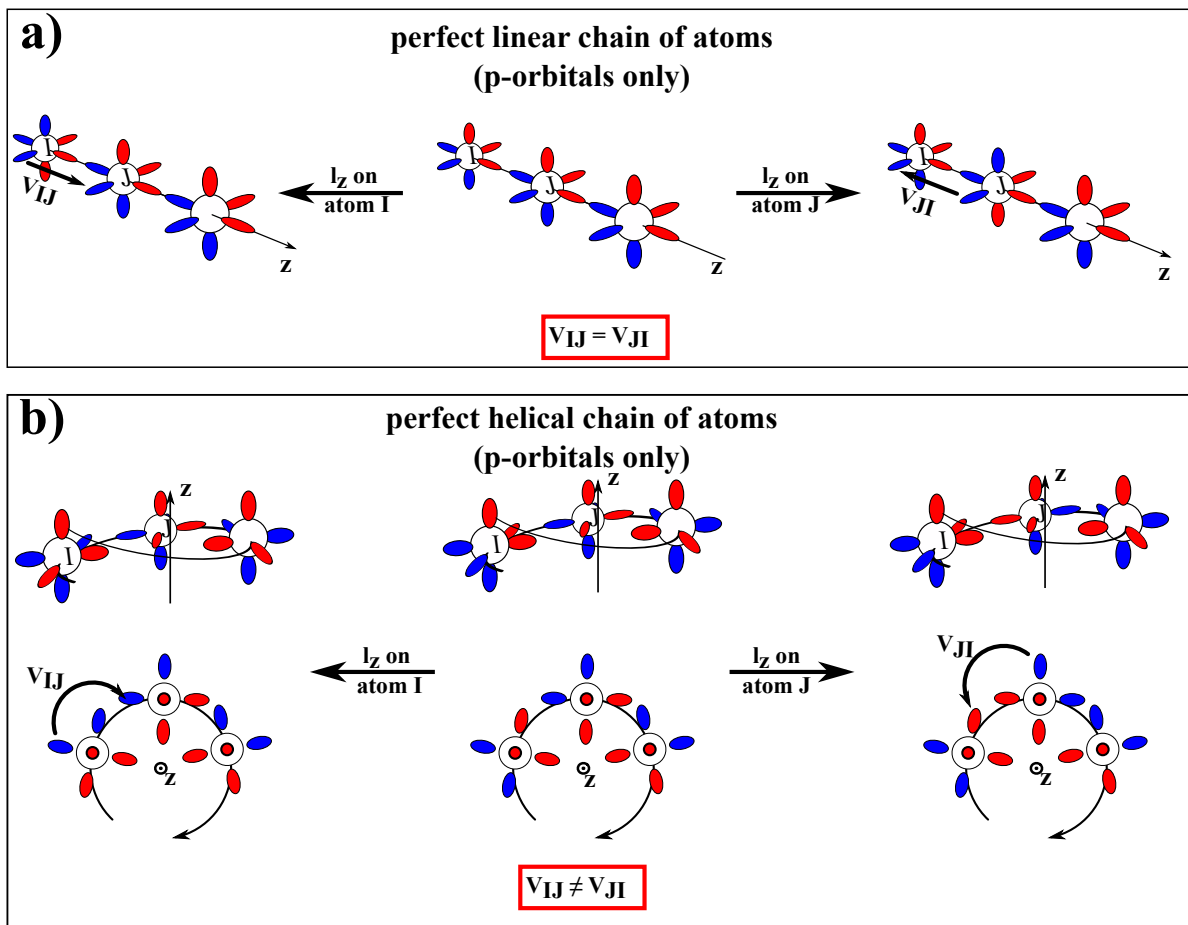


Figure 32: Direction dependence of spin–orbit coupling induced coupling between atom  $I$  and atom  $J$ . Using very simple spin–orbit coupling matrix elements (see Section 2.2.5,  $l_z$  is the  $z$ -component of the orbital angular momentum operator) and a symmetry-adapted basis (linear basis for a linear systems, helical basis for the helical system), for atomic  $p$ -orbitals, the size of such an element can be estimated by the overlap of a rotated  $p$ -orbital with an unrotated  $p$ -orbital. For a perfect linear molecule, the  $p$ - $p$  overlap does not depend on which atom the orbitals are rotated, while for the helical molecule in a helical basis it does. Thus for the helical molecule, the imaginary part of the  $p$ - $p$  coupling of atom  $J$  with atom  $I$  ( $\text{Im}(\mathbf{V}_{IJ})$ ) is not equal to the coupling of atom  $I$  with atom  $J$  ( $\text{Im}(\mathbf{V}_{JI})$ ), while both are the same for the linear molecule.

Nevertheless, the simple diatomic model system shows that the symmetry of the molecule can, in principle, be connected to  $SP$  within the Landauer approach. A more detailed analytical derivation regarding the symmetry has not been done for reasons of time.

To get further insights into a first-principles description of the CISS effect, besides analytical derivations, numerical calculations for perfect symmetrical systems were done, and the results are presented and discussed in the next section. This contains a validation of the derivations shown in this section, as well as the importance of computational parameters which influence the imaginary part of the elements of the effective single-particle Hamiltonian (theses elements have been shown to be very important for the first-principles based description of the CISS effect using the Landauer approach).

## 5.5. Possible Origins of Chiral Induced Spin Selectivity with First-Principles Methods: Insight from Density Functional Theory

To numerically validate that the CISS effect can be described with the Landauer approach in combination with DFT, and to get further insight into a first-principles description of the CISS effect,  $\mathcal{T}^{\sigma\sigma'}$  and  $SP$  for ideal carbon-based helical and linear chains were calculated with DFT<sup>36</sup> at zero bias voltage. Similar systems were already investigated by Cuniberti *et al.* [166] with DFT, but without a detailed analysis of the microscopic origin of the CISS effect within the computational method. Regarding the CISS effect, several trends are expected based on experimental results [146,147]:

- $SP$  for the linear molecule should be much smaller than for the helical molecule.
- $SP$  should change its sign upon changing the handedness of the helix.
- $SP$  should increase with the length of the helical molecule.

---

<sup>36</sup> Scalar-relativistic effects/spin-orbit coupling were considered with the X2C method, as implemented as in TURBOMOLE (neglecting the electron-electron part of SOC). ADF was not used because it employed a different number of basis functions in the scalar-relativistic calculations as in the calculation considering SOC for the linear cumulenes. This prevented the calculation of  $\mathbf{H}$  and  $\mathbf{S}$  (for details on the calculation of  $\mathbf{H}$  and  $\mathbf{S}$ , see Section 5.3.1).

A detailed investigation of  $H$  extracted from DFT might give further insight into the origin of the CISS effect based on first-principles methods.

Since the systems investigated in this part are model systems, the energy scale of the transmission function is not shifted against an estimated  $E_F$ . Regarding  $SP$ , the focus is the most significant extremum  $SP_{\text{extr}}$ .

### 5.5.1. Details on the Calculations and Structures of Perfect Symmetric Cumulenes

The helical molecular structures were created by placing carbon atoms, evenly spaced (1.3 Å), along a perfect helical path with a pitch of 3 Å and a radius of 2 Å (see Figure 33). The linear structures were built by placing carbon atoms evenly spaced (1.3 Å) along a perfect linear path. For both systems, two different lengths (20 and 40 carbon atoms) were studied. The terminal carbon atoms were saturated by adding two hydrogen atoms, resulting in an overall cumulene-like structure. The hydrogen atoms used for the saturation were structurally relaxed, the helical carbon backbone was kept fixed.

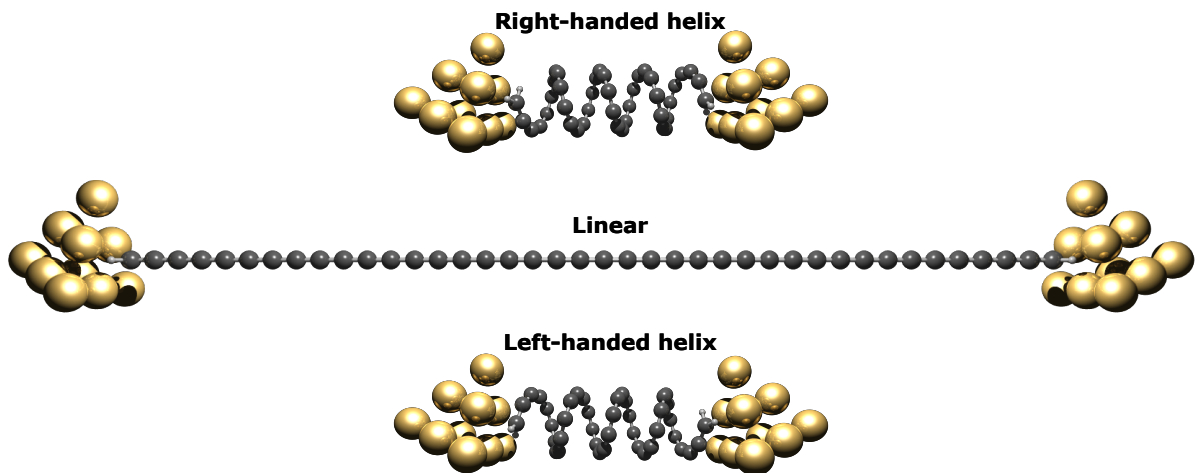


Figure 33: Gold–molecule–gold junctions as used in the DFT calculations consisting of a molecule placed between two 10-atomic gold clusters. 40-atomic left-handed helix (lower system), 40-atomic right-handed helix (upper system), and the 40-atomic chain (middle system) are depicted.

The relaxed structures<sup>37</sup> were placed between two gold clusters of 10 atoms each, mimicking the electrodes ( $d_{\text{Au-Au}} = 2.88 \text{ \AA}$  as in crystalline gold [61]), so that the terminal carbon atoms were in face-centered-cubic adsorption positions with gold-carbon distances of  $2.48 \text{ \AA}$ . The choice of this value was inspired by the sulfur-gold distance based on calculations for phenylthiol from the literature [68].

The transmission functions of the obtained gold-molecule-gold junctions were calculated using the implementation described in Section 5.3.2, and are based on a DFT-single point calculation<sup>38</sup>. The central (scattering) region (see Section 2.3 for details on the Landauer approach) was defined to be the helical/linear molecule only.

### 5.5.2. Details on the Analyzed Matrices of Perfect Symmetric Cumulenes

To give a better understanding of the matrices presented in this work, a short introduction into their structure is given (see Figure 34). This is focused on  $\mathbf{H}$ , but the same structures hold for  $\mathbf{S}$ . The extracted  $\mathbf{H}$  consists of four spin blocks ( $\mathbf{H}^{\alpha\alpha}$ ,  $\mathbf{H}^{\beta\alpha}$ ,  $\mathbf{H}^{\alpha\beta}$ ,  $\mathbf{H}^{\beta\beta}$ ). For each spin block  $\mathbf{H}^{\sigma\sigma'}$ , each atom  $I$  builds a block matrix  $\mathbf{H}_I$ , which contains only matrix elements describing the coupling terms of basis functions located on atom  $I$ . The blocks which contain matrix elements describing the coupling terms of basis functions of atom  $I$  with basis functions located on another atom  $J$  are called  $\mathbf{V}_{IJ}$  in the following. All  $\mathbf{H}_I$  blocks build the diagonal blocks and all  $\mathbf{V}_{IJ}$  blocks build the off-diagonal blocks of  $\mathbf{H}^{\sigma\sigma'}$ . All other spin-dependent blocks have the same structure. The  $\mathbf{H}_I$  blocks are sorted along the helix axis for the helical cumulenes and along the axis connecting the carbon atoms for the linear cumulenes. Both axes were aligned along the  $z$ -axis in the global Cartesian coordinate frame, and  $\mathbf{V}_{(J>I)I}$  describes the coupling of atom  $I$  with atom  $J$  in  $z$ -direction. In terms of electron transport, this is referred to as “in transport direction” in the following, since in the transport calculations the transport direction was chosen to be the  $z$ -axis. Thus, the electron transport from the electrode

---

<sup>37</sup> PBE-D3/def2-TZVP without relativistic effects, for details see Appendix A.

<sup>38</sup> B3LYP/X2C-SVPall-2c with relativistic effects (X2C), for details see Appendix A.

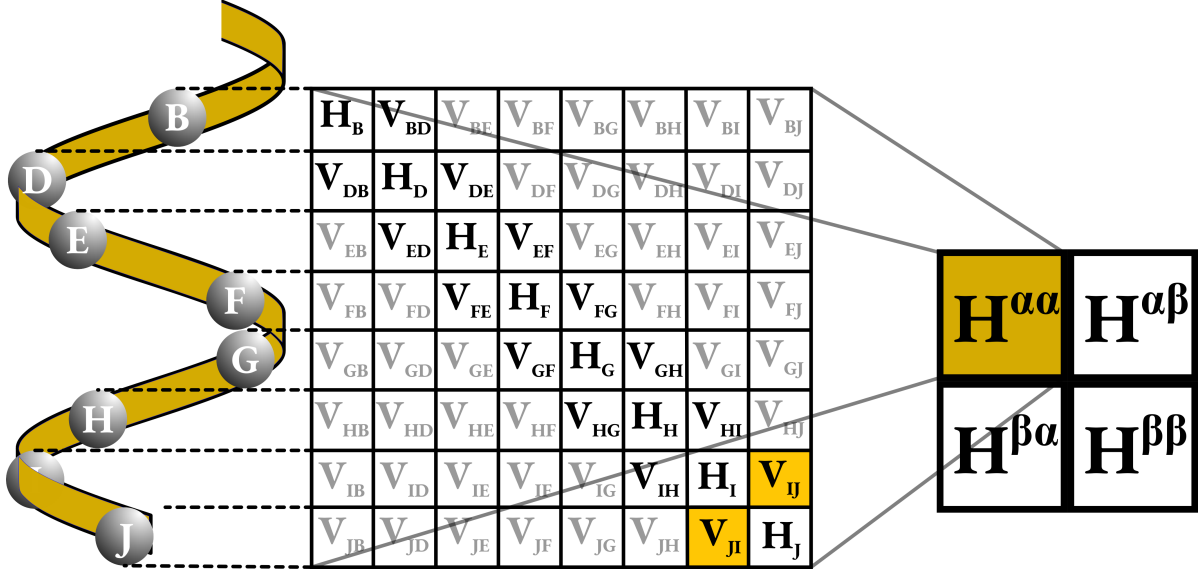


Figure 34: Schematic structure of the investigated matrices. Each matrix consists of four spin-dependent blocks ( $\mathbf{H}^{\alpha\alpha}$ ,  $\mathbf{H}^{\beta\alpha}$ ,  $\mathbf{H}^{\alpha\beta}$ ,  $\mathbf{H}^{\beta\beta}$ ). The focus is  $\mathbf{H}^{\alpha\alpha}$ , which also has a block structure. The diagonal blocks  $\mathbf{H}_N$  contain matrix elements describing the on-site terms and the coupling terms of basis functions located on atom  $N$ , while the off-diagonal blocks  $\mathbf{V}_{NM}$  contain matrix elements describing the coupling terms of basis functions located on atom  $N$  with basis functions located on atom  $M$ . The discussion is limited to a single pair of nearest-neighbor couplings  $\mathbf{V}_{NM}$  and  $\mathbf{V}_{MN}$ .

with a lower  $z$ -coordinate to the electrode with higher  $z$ -coordinate was computed.  $\mathbf{H}_I$  and  $\mathbf{V}_{IJ}$  can further be separated into a real and imaginary part

$$\mathbf{H}_I = \text{Re}(\mathbf{H}_I) + i\text{Im}(\mathbf{H}_I), \quad (5.95)$$

$$\mathbf{V}_{IJ} = \text{Re}(\mathbf{V}_{IJ}) + i\text{Im}(\mathbf{V}_{IJ}). \quad (5.96)$$

Two different types of matrices are analyzed:

To investigate how the symmetries in combination with SOC leads to the CISS effect within the Landauer approach, a single pair of nearest-neighbor couplings ( $\mathbf{V}_{I(I+1)}^{\alpha\alpha}$  and  $\mathbf{V}_{(I+1)I}^{\alpha\alpha}$ ) in  $\mathbf{H}^{\alpha\alpha}$  of the isolated molecules are analyzed (see Section 5.5.4). Since  $\mathbf{H}^{\alpha\alpha}$  is directly related to  $\mathbf{H}^{\beta\beta}$  and should contain all important relations for the P-symmetry

of  $\mathcal{T}$  (as indicated in Section 5.4.3),  $\mathbf{H}^{\beta\beta}$ ,  $\mathbf{H}^{\beta\alpha}$ , and  $\mathbf{H}^{\alpha\beta}$  are not discussed. For simplicity, all polarization functions ( $d$ -orbitals for the carbon atoms and  $p$ -orbitals for the hydrogen atoms) were removed from the basis set for the DFT calculation. An important issue is the orientation of the basis functions provided by TURBOMOLE. The  $p$ -type basis functions are oriented along the  $x$ -,  $y$ -, and  $z$ -axis. For the linear molecule aligned along the  $z$ -axis, such a basis corresponds to the symmetry-adapted basis, *i.e.*, any nearest-neighbor overlap matrix block  $\mathbf{S}_{I(I+1)}^{\alpha\alpha}$  is the same. This is not the case for a helical molecule oriented along the  $z$ -axis, which makes a comparison of the nearest-neighbor coupling from the left-handed and right-handed helix difficult<sup>39</sup>. To circumvent this problem, the basis was transformed into a symmetry-adapted left-handed or right-handed helical basis (see Figure 35 and 36). This results in  $\mathbf{S}_{I(I+1)}^{\alpha\alpha}$  being equal for any atom pair and to  $\mathbf{S}^{\alpha\alpha}$  being equal for the right- hand left-handed helix. The obtained symmetry-adapted bases resulting in those relations is assumed to be the best representation for making a meaningful comparison between the matrices of the linear chain, left-handed, and right-handed helix<sup>40</sup>. An illustration of the procedure is depicted in Figure 36. The linear and helical structures are oriented along the  $z$ -axis, which is defined as the transport direction. In the linear and helical symmetry-adapted bases, the  $p_z$ -orbital remains aligned along the  $z$ -axis, while the  $p_x$ - and  $p_y$ -orbitals remain in the  $xy$ -plane. The  $p_x$ - and  $p_y$ -orbitals of the linear symmetry-adapted basis are aligned along the  $x$ - and  $y$ -axis, while in the helical symmetry-adapted basis, the orientation of the  $p_y$ - and  $p_x$ -orbitals rotate depending on the position in the helix (see Figure 35). A similar scheme was already used by Medina *et al.* [181].

---

<sup>39</sup> Both matrices depend on the exact orientation of the molecule, even if both helix-axes are oriented along the transport direction.

<sup>40</sup> The symmetry-adapted basis transforms  $\mathbf{S}$  of the helical molecules into a pseudo-linear shape. This makes a comparison for the linear chain and both helices independent from the exact orientation of the molecules.

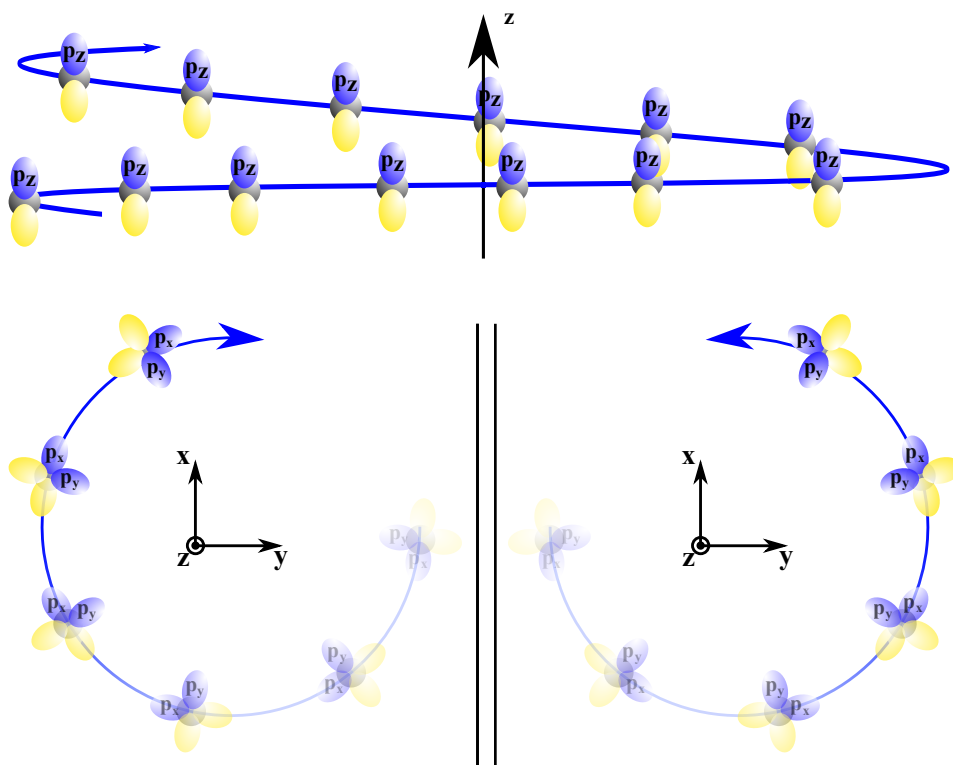


Figure 35: Orientation of the  $p$ -orbitals after transforming the Cartesian basis into a helical basis. The  $p_x$ - and  $p_y$ -orbitals rotate depending on the position in the helix in such way that the positive lobe (blue) of the  $p_x$ -orbitals points into ascending direction of the helix (indicated by the arrowhead) and the positive lobe of the  $p_y$ -orbitals points into the center of the helix. The  $p_z$ -orbitals remain oriented along the helix axis. For details of the construction of this basis, see Figure 36.

To investigate the strength of SOC in the gold–molecule–gold junction of the helical cumulene, and therefore possible origins of the magnitude of the CISS effect, the full  $\mathbf{H}$  of an isolated helical cumulene molecule, as well as  $\mathbf{H}_C$  of the helical cumulene molecule within a gold–molecule–gold junction are analyzed (see Section 5.5.5). Since this analysis is not focused on a detailed nearest-neighbor coupling scheme, but on the character of the full matrix, the basis functions were not transformed as described in Figure 36 and polarization functions were used for carbon and hydrogen atoms during the DFT calculation.

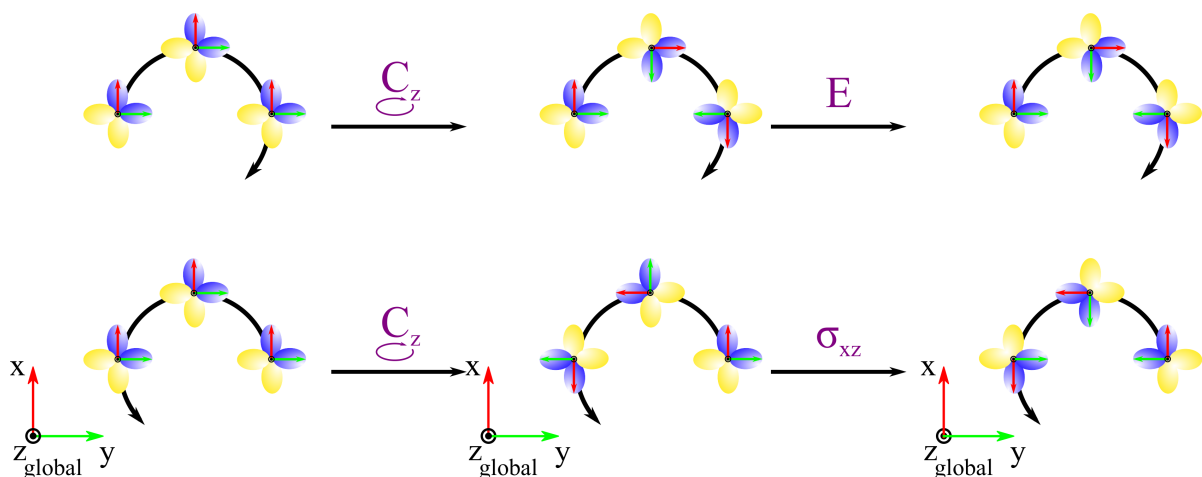


Figure 36: Transformation of the Cartesian basis into a handedness-dependent helical basis, resulting in equal overlap matrices for the helices of both chiralities (left- and right-handed, helix axis =  $z$ -axis). First, the atom-centered basis functions for both chiralities were rotated around the  $z$ -axis, resulting in  $p_x$ -orbitals oriented along the  $xy$ -projection of the vector connecting the nearest-neighboring atoms of the atom on which the  $p_x$ -orbital is located. The vector was chosen to point from the nearest-neighboring atom with the lower value for the  $z$ -coordinate to the nearest-neighboring atom with the larger  $z$ -coordinate. Consequently, the  $p_y$ -orbitals pointed into or away of the helix center (depending on the handedness of the helix) resulting in different overlap matrices for the left- and right-handed helix. Thus, for the right-handed molecule a mirror transformation along the  $xz$ -plane was applied, which led to  $p_y$ -orbitals pointing into the helix center for both chiralities.

### 5.5.3. Spin Polarization of Transmitted Electrons for Perfect Symmetric Cumulenes

To validate the importance of  $\text{Im}(\mathbf{H})$  for  $SP$  and to validate that the implementation done in this work describes CISS in principle,  $SP$  for linear and helical cumulenes were calculated (see Figure 37 for  $SP$ , see Appendix B for transmission functions).

For the 40-atomic left-handed helix,  $SP_{\text{extr}}$  has a positive sign (1.06 %), while for the 40-atomic right-handed helix, the sign is negative ( $-1.05$  %).  $SP$  changes its sign for any energy upon changing the handedness of the helix (see Figure 37 part b). A reduction of the chain length to a 20-atomic helix leads to a decrease of the absolute value of  $SP_{\text{extr}}$  ( $\pm 0.43$  %). For both linear molecules,  $SP$  is close to zero for any energy value (see Figure 37 part a). All calculations are consistent with the expectations for the CISS effect, because  $SP$  is nearly zero for the linear cumulenes and much larger for helical cumulenes, increases with the length of the molecule, and changes its sign upon changing the chirality of the helical molecule. However, a  $SP$  of about 1 % is much smaller than what is observed experimentally, indicating that the magnitude of the effect is not covered within the employed methodology.

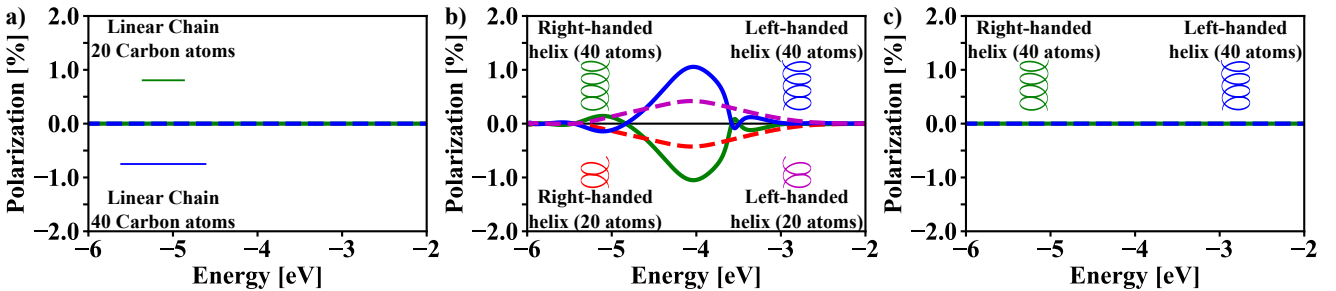


Figure 37: Calculated spin polarization of the transmitted electrons in the range of  $-6.00$  eV to  $-2.00$  eV, using B3LYP/X2C-SVPall-2c. The linear molecules do not show significant spin polarization (a), while for the helical ones the spin polarization can reach absolute values of about 1% (b). The sign of the spin polarization changes upon changing the handedness of the helix. If the calculations are done setting the imaginary part of the Hamiltonian matrix to zero, the spin polarization becomes nearly zero for the whole calculated energy range (c).

To further validate the suggestion that  $SP$  originates from SOC-induced  $\text{Im}(\mathbf{H}_C)$ ,  $SP$  was re-calculated for the helical molecules setting  $\text{Im}(\mathbf{H}_C)$  to zero. This leads to a vanishing of  $SP$  (see Figure 37 part c), confirming the predicted importance of  $\text{Im}(\mathbf{H})$  for the P-symmetry of  $\mathcal{T}$  and for the calculated  $SP$  (see Section 5.4.2).

The electron transport calculations confirm the importance  $\text{Im}(\mathbf{H})$  for the presence of a non-zero  $SP$ , and thus also for CISS, within the Landauer approach. However, although  $\mathcal{T}$  shows the importance of the molecule’s symmetry numerically, it does not give any insight into the microscopical origin. To provide such an insight, an analysis of  $\text{Re}(\mathbf{H})$  and  $\text{Im}(\mathbf{H})$ , calculated for the isolated molecules, is discussed next.

#### **5.5.4. Connection between Symmetry of the Cumulenes and Spin Polarization of the Transmitted Electrons: Analysis of Effective Single-Particle Hamiltonian Matrix**

To get further insights into the origin of the symmetry dependence of  $SP$  within the Landauer approach, a connection between the calculated  $SP$ ,  $\text{Im}(\mathbf{H})$ , and the symmetry of the molecule is investigated (in connection with the diatomic model system, see Section 5.4.3). The focus is the changing sign of  $SP$  for the left- and right-handed helix and the vanishing  $SP$  for the linear molecule. To do so, the spin-conserving nearest-neighbor coupling matrix elements of the isolated cumulene molecules ( $\mathbf{V}_{I(I+1)}^{\alpha\alpha}/\mathbf{V}_{(I+1)I}^{\alpha\alpha}$ ) are discussed for a single pair of nearest-neighbor couplings. The spin-flip nearest-neighbor coupling matrices are neglected because the relations drawn from the diatomic model only allow to draw conclusions for the spin-conserving nearest-neighbor coupling matrices. Additionally, it is assumed that the spin-flip nearest-neighbor coupling blocks does not give any additional information.

The matrices presented and discussed in the following were calculated with the X2C-SVPall-2c basis set, but without the polarization functions for carbon and hydrogen atoms (see Section 5.5.2).

Important to note for the next part is:

- Although the matrices of the isolated molecule are in focus, the terms in and against “transport direction” are used for the helix axis of the helical cumulene or the bonding axis of the linear cumulene ( $z$ -axis). This is consistent with the transport direction for the calculated  $SP$  of the helical and linear cumulene molecules.
- $\mathbf{V}_{I(I+1)}^{\alpha\alpha}$  describes the spin-conserving nearest-neighbor coupling against transport direction
- $\mathbf{V}_{(I+1)I}^{\alpha\alpha}$  describes the spin-conserving nearest-neighbor coupling in transport direction.
- Only  $\mathbf{G}^{\alpha\alpha}$  and  $\mathbf{G}^{\beta\beta}$  are connected to the probability of a spin-conserving propagation [199], and the self energies and  $\mathbf{V}^{\alpha\beta}/\mathbf{V}^{\beta\alpha}$  also influence the spin-conserving transport. Nevertheless, a rough estimation for the spin-conserving transport properties ( $\mathcal{T}_{LR}^{\alpha\alpha}/\mathcal{T}_{RL}^{\alpha\alpha}$ ) based on the shape of  $\mathbf{V}_{I(I+1)}^{\alpha\alpha}$  and  $\mathbf{V}_{(I+1)I}^{\alpha\alpha}$  is done for simplicity.
- Only the signs of the elements in  $\mathbf{V}_{(I+1)I}^{\alpha\alpha}$  and  $\mathbf{V}_{I(I+1)}^{\alpha\alpha}$  are in focus.
- The symmetry of the Hamiltonian dictates that  $\mathbf{V}_{(I+1)I}^{\alpha\alpha} = (\mathbf{V}_{I(I+1)}^{\alpha\alpha})^\dagger$ . The nearest-neighbor coupling is termed direction-dependent if  $\mathbf{V}_{(I+1)I}^{\alpha\alpha} = \mathbf{V}_{I(I+1)}^{\alpha\alpha}$ .

### “Direction-dependence” of Imaginary Hamiltonian Elements

The comparison of the  $p$ - $p$  blocks of  $\mathbf{V}_{I(I+1)}^{\alpha\alpha}$  and  $\mathbf{V}_{(I+1)I}^{\alpha\alpha}$  for the right-handed helical molecule with the  $p$ - $p$  blocks  $\mathbf{V}_{I(I+1)}^{\alpha\alpha}$  and  $\mathbf{V}_{(I+1)I}^{\alpha\alpha}$  of the linear molecule is in agreement with the conclusions drawn from the diatomic model system (see Figure 38 and 39). For the helical cumulene molecule, the  $p$ - $p$  nearest-neighbor coupling in transport direction is different from the  $p$ - $p$  nearest-neighbor coupling against transport direction. For the diatomic model system, this prohibited an enforcement of P-symmetry of  $\mathcal{T}$  and opened the possibility for a non-zero  $SP$ . For the linear cumulene molecule, the  $p$ - $p$  coupling is independent from the transport direction, which enforces P-symmetry in the diatomic model system. Including the  $s$ -orbitals into the analysis leads to a different picture.

# Im( $V^{\alpha\alpha}$ )

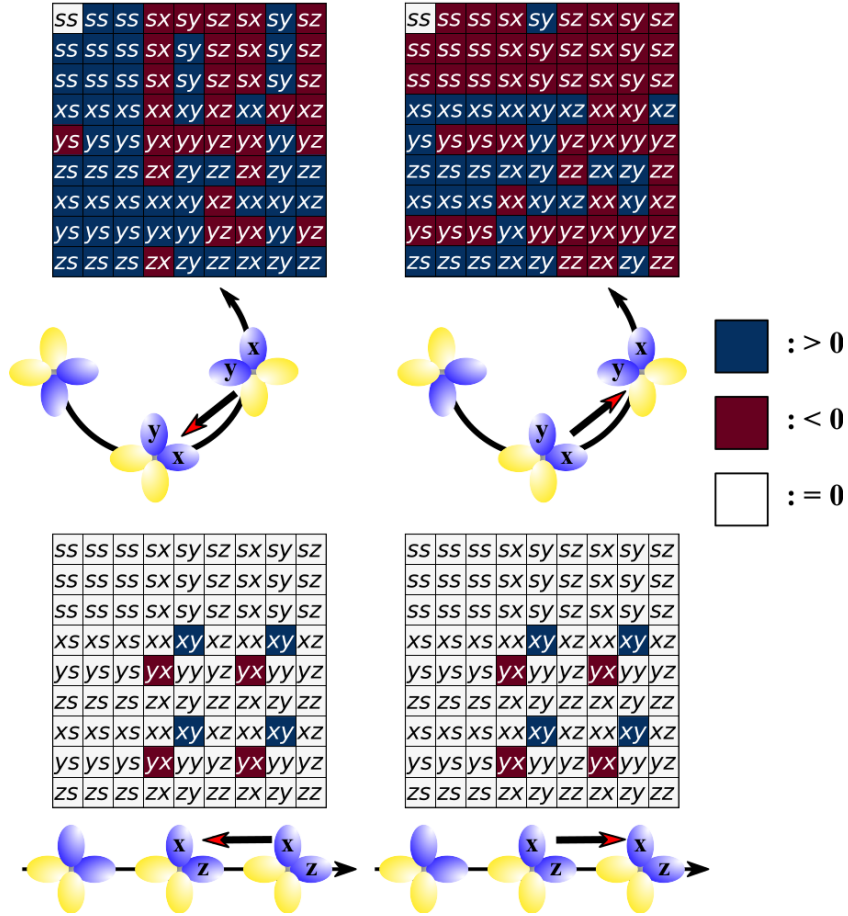


Figure 38: Exemplary nearest-neighbor coupling in  $\text{Im}(\mathbf{H}^{\alpha\alpha})$ :  $\text{Im}(\mathbf{V}_{I(I+1)}^{\alpha\alpha})$  in and  $\text{Im}(\mathbf{V}_{(I+1)I}^{\alpha\alpha})$  against transport direction, illustrating the Hermitian symmetry of the matrix. The  $p$ -orbitals are abbreviated just by their Cartesian index. For the linear molecule, the sign of all elements in transport direction are the same as against transport direction, while for the helix, the sign of some elements in  $\text{Im}(\mathbf{V}_{I(I+1)}^{\alpha\alpha})$  changes compared to  $\text{Im}(\mathbf{V}_{(I+1)I}^{\alpha\alpha})$ . In connection with the diatomic model system (see Section 5.4.3) this implies that  $\mathcal{P}$ -symmetry of  $\mathcal{T}$  is retained for the linear molecule, which would prevent any non-zero  $SP$ , while it is broken for the helical one. Non-zero matrix elements were defined to be larger than  $10^{-8}$  a.u. (positive) and smaller than  $-10^{-8}$  a.u. (negative). Calculations were done using B3LYP/X2C-SVPall-2c without polarization functions.

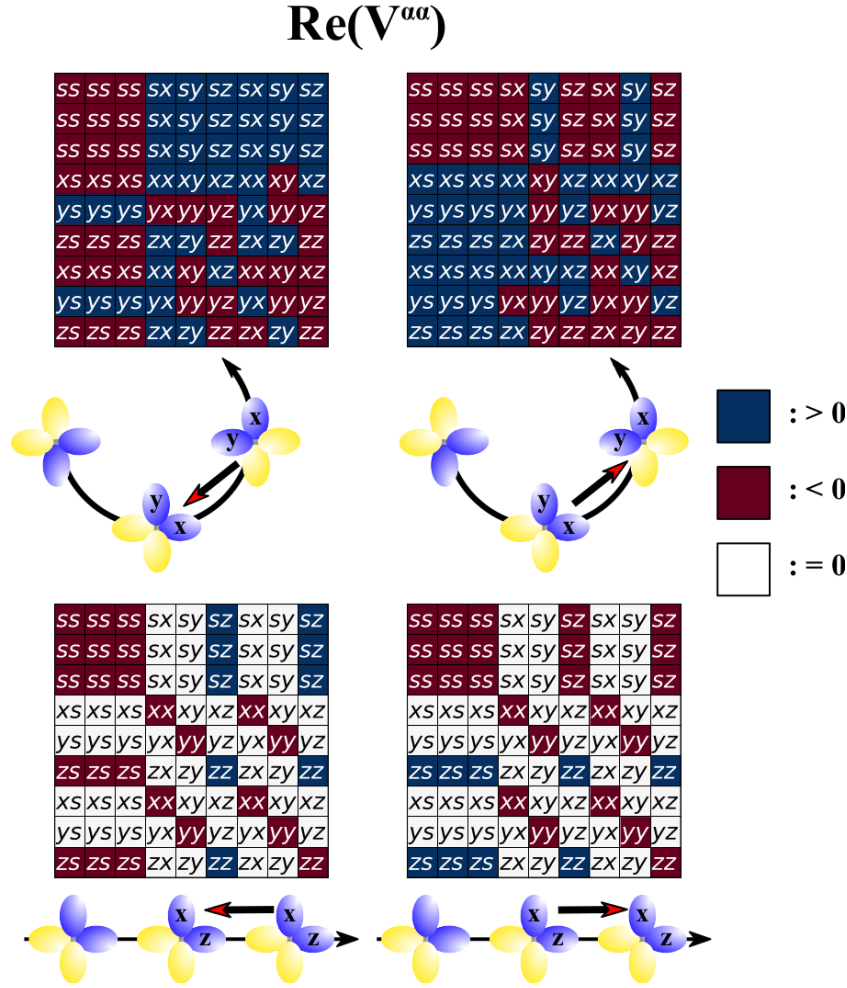


Figure 39: Exemplary nearest-neighbor coupling block in  $\text{Re}(\mathbf{H}^{\alpha\alpha})$ :  $\text{Re}(\mathbf{V}_{I(I+1)}^{\alpha\alpha})$  in and  $\text{Re}(\mathbf{V}_{(I+1)I}^{\alpha\alpha})$  against transport direction. The  $p$ -orbitals are abbreviated just by their Cartesian index. For the linear molecule, the sign of all  $s$ - $s$  and  $p$ - $p$  coupling elements in transport direction are the same as against transport direction, but the sign of the  $s$ - $p$  elements changes. For the helix, the sign of some elements of the  $s$ - $p$  and  $p$ - $p$  blocks of  $\text{Re}(\mathbf{V}_{I(I+1)}^{\alpha\alpha})$  changes compared to  $\text{Re}(\mathbf{V}_{(I+1)I}^{\alpha\alpha})$ . Since the calculated  $SP$  remains zero for the linear molecule, a direction-dependent real part of the coupling in the spin-conserving block does not appear to break P-symmetry of  $\mathcal{T}$ . This consideration is beyond the scope of the diatomic model system (see Section 5.4.3), showing the need of extending the model. Non-zero matrix elements were defined to be larger than  $10^{-8}$  a.u. (positive) and smaller than  $-10^{-8}$  a.u. (negative). Calculations were done using B3LYP/X2C-SVPall-2c without polarization functions.

For the helical cumulene, the direction-dependent coupling is also indicated by the real and imaginary  $s$ - $s$  and  $s$ - $p$  blocks of  $\mathbf{V}_{I(I+1)}^{\alpha\alpha}$  and  $\mathbf{V}_{(I+1)I}^{\alpha\alpha}$ . This is consistent with the removal of P-symmetry for the diatomic model system. However, for the linear cumulene molecule, the  $s$ - $p$  blocks of  $\text{Re}(\mathbf{V}_{I(I+1)}^{\alpha\alpha})$  and  $\text{Re}(\mathbf{V}_{(I+1)I}^{\alpha\alpha})$  indicate a direction dependence of the nearest-neighbor coupling, since they change their sign. This originates from the symmetry relations of the  $s$ - and  $p$ -orbitals;  $s$ -orbitals are symmetric under inversion, while  $p$ -orbitals are not, thus the overlap between the  $s$ -orbital in transport direction has the opposite sign as against transport direction. However, since the calculated  $SP$  for the linear cumulene molecule is zero, the P-symmetry of  $\mathcal{T}$  appears to be maintained. This indicates  $\text{Re}(\mathbf{H}^{\alpha\alpha})$  being unable to break the P-symmetry of  $\mathcal{T}$  which is consistent with the fact that  $\text{Re}(\mathbf{H}^{\alpha\alpha})$  does not originate from SOC and is not related to CISS generation. Additionally, this might also be related to the  $p$ -orbital dominated transport due to the  $\pi$ -system of the cumulene molecules.

The numerical results in combination with a model system (Section 5.4.3) indicate that the relation between the symmetry of the system and the calculated  $SP$  is connected to the relation of  $\mathbf{V}_{IJ}^{\alpha\alpha}$  and  $\mathbf{V}_{JI}^{\alpha\alpha}$ . However, the diatomic model does not cover the whole connection between the vanishing  $SP$  for linear molecules. A more detailed model is needed to cover the relation between the direction-dependent nearest-neighbor coupling and the vanishing  $SP$  for linear and other non-chiral molecules, which is not within the scope of this work.

### “Handedness-dependence” of Imaginary Hamiltonian Elements

To get insight into the changing sign of  $SP$  upon changing the handedness of the helix,  $\mathbf{V}_{I(I+1)}^{\alpha\alpha}$  of the left- and right-handed helix are compared (see Figure 40). Upon changing the handedness of the helix, the signs of the matrix elements of  $\text{Re}(\mathbf{V}_{I(I+1)}^{\alpha\alpha})$  do not change, while the sign of each matrix element of  $\text{Im}(\mathbf{V}_{I(I+1)}^{\alpha\alpha})$  does change<sup>41</sup>.

---

<sup>41</sup> In fact, all imaginary elements of  $\mathbf{H}$  change and all real matrix elements of  $\mathbf{H}$  remain the same upon changing the helix-sense in the helical basis.

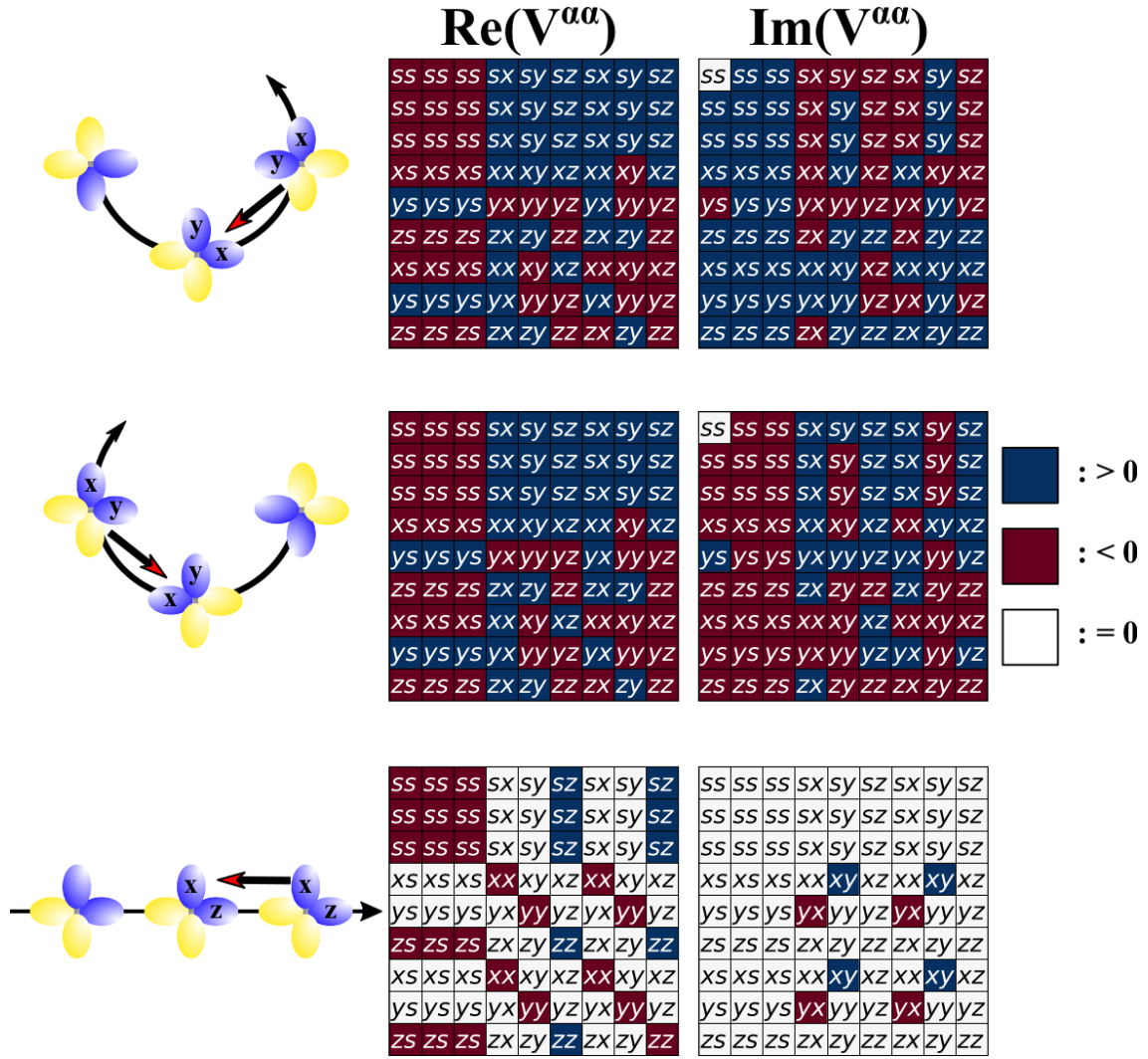


Figure 40: Exemplary blocks of nearest-neighbor coupling part of  $H_C^{\alpha\alpha}$ :  $V_{I(I+1)}^{\alpha\alpha}$  against transport direction for the left- and right-handed helix. The  $p$ -orbitals are abbreviated just by their Cartesian index. While the elements of  $\text{Re}(V_{I(I+1)}^{\alpha\alpha})$  do not change their sign upon changing the handedness, all elements of  $\text{Im}(V_{I(I+1)}^{\alpha\alpha})$  do so. This may be the origin of the changing sign of the spin polarization upon changing the handedness of the helix. Non-zero matrix elements were defined to be larger than  $10^{-8}$  a.u. (positive) and smaller than  $-10^{-8}$  a.u. (negative). Calculations were done using B3LYP/X2C-SVPall-2c without polarization functions.

The changing sign of  $SP$  likely originates from the changing signs of  $\text{Im}(\mathbf{H})$ , which additionally reinforces the importance of  $\text{Im}(\mathbf{H})$  for a non-zero  $SP$  and the hypothesis that  $\text{Re}(\mathbf{H})$  is not connected to the removal of the P-symmetry of  $\mathcal{T}$ .

So far, the results indicate that  $\text{Im}(\mathbf{H})$  is important for the appearance of the CISS effect within a first-principles computational scheme. Besides its principle appearance, the magnitude of the effective SOC for the molecules is important for a first-principles description of the CISS effect, since most theoretical studies indicate that the effective SOC in helical molecules is enhanced. Because the magnitude of  $SP$  for the cumulene molecules is much smaller as expected for the CISS effect, the effective SOC seems to be underestimated. However, the dependence of  $SP$  on several parameters (*e.g.* the amount of HF exchange) might give important insights into what is important in a first-principles description of the CISS effect.

#### **5.5.5. Connection between Magnitude of the Polarization of Transmitted Electrons and Imaginary Parts of the Effective Single-Particle Hamiltonian Matrix**

The magnitude of the elements of  $\text{Im}(\mathbf{H}_C)$  should be connected to the magnitude of the calculated  $SP$ , and therefore also to the strength of SOC. Analyzing the dependence of the magnitude of  $\text{Im}(\mathbf{H}_C)$  and  $SP$  on several parameters within the DFT calculation might give insight into which parameters strongly influence the effective SOC, and thus are possibly important for a systematic first-principles investigation of the CISS effect.

#### **Increase of Imaginary Elements of the Effective Single-Particle Hamiltonian of the Cumulene Molecule due to the Proximity of Gold**

To get further insights into the effective strength of SOC within the helical cumulene in a junction,  $\mathbf{H}_C$  of the gold–molecule–gold junction is compared with  $\mathbf{H}$  of the isolated helical molecule.

Comparing  $\mathbf{H}_C$  and  $\mathbf{H}$  of the isolated molecule, placing the helical cumulene molecule between two gold electrodes has a huge effect on the matrix elements which can be

attributed to SOC (imaginary part of spin-flip and spin-conserving blocks as well as real elements of the spin-flip blocks) (see Figure 41). On the one hand, these matrix elements increase due to the presence of the gold electrodes, on the other hand, the range of the SOC induced interatomic coupling increases (indicated by a less block-diagonal shape of the spin-flip blocks in  $\text{Re}(\mathbf{H}_C)$  and  $\text{Im}(\mathbf{H}_C)$  and the spin-conserving blocks in  $\text{Im}(\mathbf{H}_C)$ ).

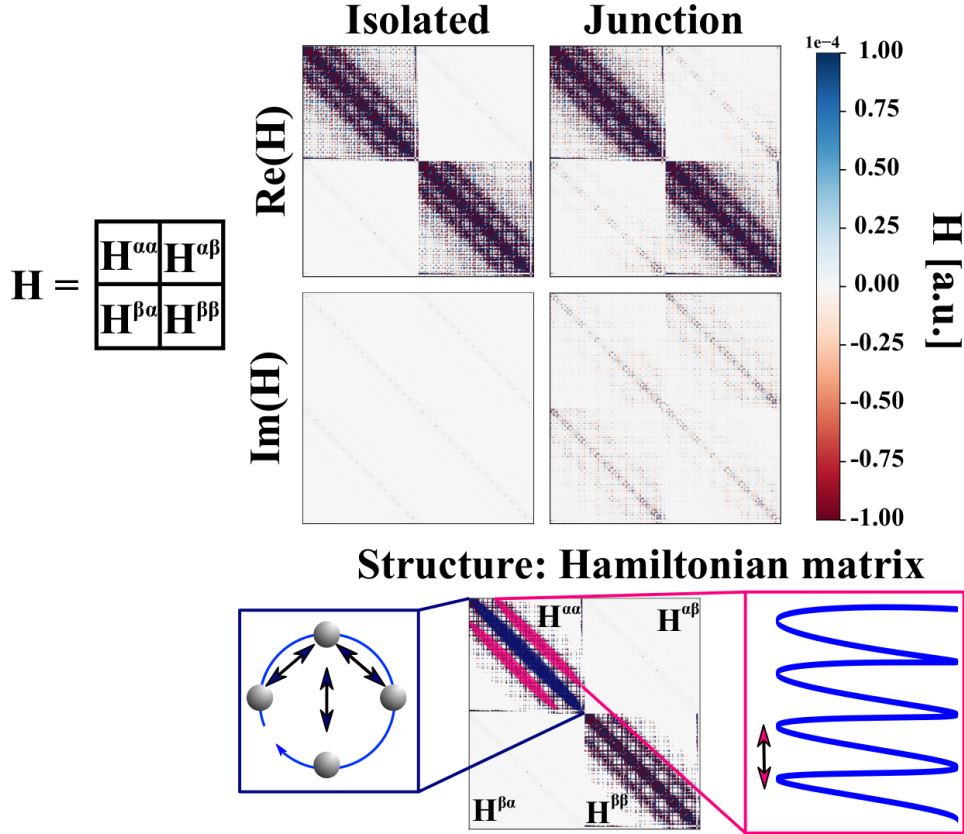


Figure 41: **a)**  $\text{Re}(\mathbf{H})$  (upper part) and  $\text{Im}(\mathbf{H})$  (lower part) for the carbon atoms of the right-handed helical cumulene only. On the left-hand side the matrices are depicted for the isolated molecule, on the right-hand side they are depicted for the gold–molecule–gold junction. The gold electrodes induces a massive increase of  $\text{Im}(\mathbf{H})$ ,  $\text{Re}(\mathbf{H}^{\alpha\beta})$  and  $\text{Re}(\mathbf{H}^{\beta\alpha})$  within the helix. **b)** Schematic overview of the structure of the Hamiltonian matrix. While the main diagonal (marked in blue) arises from the interaction of the closest carbon atoms within a pitch, the off-diagonals arise from the interaction of carbon atoms of different pitches. Calculations were done using B3LYP/X2C-SVPall-2c.

This suggests an increase of effective SOC within the helical cumulene molecule, indicating that SOC may be at least partially inherited by the gold electrodes. This would be similar to the known proximity effects in graphene on gold [201,202].

To further validate the inheritance of the SOC from the gold for the helical cumulene molecule,  $SP$  was recalculated for copper–molecule–copper and silver–molecule–silver junctions. To build the junctions, the atoms of the gold cluster were replaced by copper or silver atoms, without changing the atomic distances in the cluster. Compared to gold, using copper and silver as an electrode material leads to a massive decrease of the absolute value of  $SP_{\text{extr}}$  (see Figure 42).

Since the effective strength of SOC increases with the atomic number, the amount of effective SOC in the perfect helical cumulene inherited by the electrodes also increases with the atomic number of the electrode atoms. Therefore, the absolute value of  $SP_{\text{extr}}$  increases with the atomic number as well. This trend can also be seen in  $\text{Im}(\mathbf{H}_C)$  (see Figure 43), since the range of the SOC-induced interatomic coupling decreases massively as well as the matrix elements of  $\text{Im}(\mathbf{H}_C)$ , if gold is replaced by silver or copper.

An interpretation of the inheritance of SOC of the gold as the origin of the strong SOC observed for the CISS effect cannot be made due to the artificial nature of the cumulene molecules. Experimental observations for helical molecules on aluminum and silver substrates [148,151] in photoelectron emission experiments suggest a similar magnitude of the CISS effect on substrates with much smaller SOC than gold. However, this was never shown to be also the case for the electron transport experiment, and the results suggest that electron transport experiments using copper or silver instead of gold are worthwhile.

Since the size of  $\text{Im}(\mathbf{H}_C)$  seems to affect the amount of  $SP$ , and the predicted strength of the CISS effect within the Landauer approach, another computational parameter should influence the calculated  $SP$ : the amount of HF exchange in the DFT functional, which also induces imaginary terms in  $\mathbf{H}_C$  [35,36]. The dependence of  $SP$  for the perfect helical cumulene on the HF exchange is discussed next.

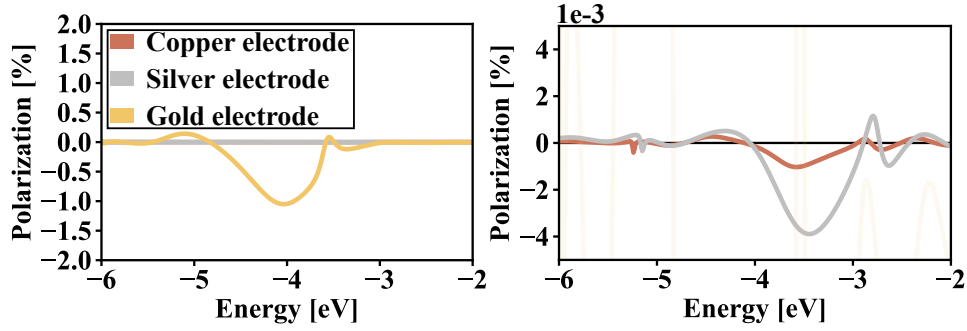


Figure 42: Calculated spin polarization of the transmitted electrons (B3LYP/X2C-SVPall-2c) for the perfect helical cumulene (40 carbon atoms), using different elements (Cu, Ag, Au) to build the electrodes, all with the same interatomic distance. On the left-hand side, the spin polarization for all materials is plotted up to 2.0 %, on the right-hand side it is plotted up to  $5 \cdot 10^{-3}$  %. For clarity, the plot for Au is blurred. The amount of spin polarization is consistent with the effective spin-orbit coupling of the electrode atoms ( $\text{Cu} < \text{Ag} < \text{Au}$ ).

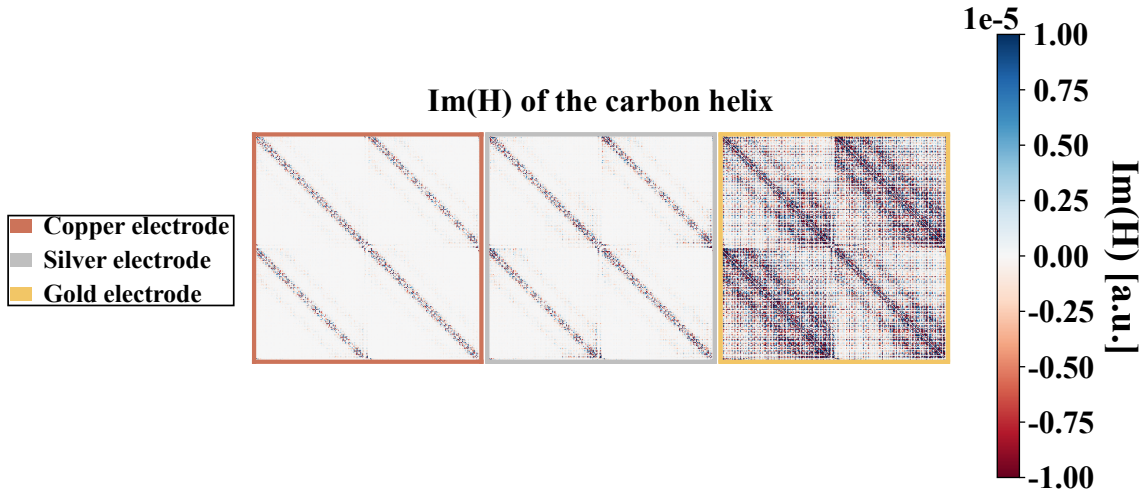


Figure 43:  $\text{Im}(\mathbf{H}_C)$  of the perfect helical cumulene (40 carbon atoms) within an electrode-molecule-electrode junction. The Hamiltonian was calculated using electrodes of different materials (Cu, Ag, Au), all with the same interatomic distance.  $\text{Im}(\mathbf{H}_C)$  increases from copper to gold, confirming the effective SOC in the helical cumulene molecule to be inherited by the electrodes. Calculations were done using B3LYP/X2C-SVPall-2c.

## Change of Calculated Spin Polarization of Transmitted Electrons due to varying Hartree–Fock Exchange

To investigate the influence of the amount of HF exchange on  $SP$ , it was recalculated for the helical cumulene gold–molecule–gold junction with the B3LYP functional and different amounts of HF exchange (5 %, 20 %, 35 %, 50 %, 65 %, 80 %).

The calculated  $SP$  strongly depends on the amount of HF exchange. Starting from 5 %, the absolute value of  $SP_{\text{extr}}$  increases with the amount of HF exchange, until it reaches its maximum at 50 %. A further increase to 65 % and 80 % again leads to a decrease of the absolute value of  $SP_{\text{extr}}$  (see Figure 44). This trend is also represented in  $\text{Im}(\mathbf{H})$  (see Figure 45). Looking at  $\text{Im}(\mathbf{H}_C)$  of the gold–molecule–gold junction, several elements of  $\text{Im}(\mathbf{H})$  increase from 5 % to 50 % HF exchange and again decrease from 50 % to 80 % HF exchange. In contrast, several elements of  $\text{Im}(\mathbf{H})$  of the isolated perfect helical cumulene continuously increase with the amount of HF exchange. This indicates that for the perfect helical cumulene the HF exchange does not influence  $SP$  by increasing the imaginary part directly, but by modifying the gold–molecule coupling.

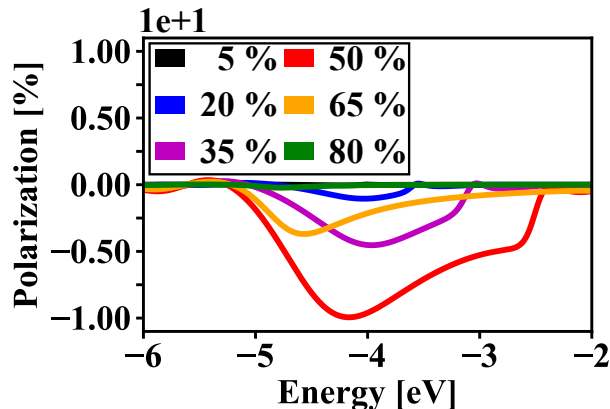


Figure 44: Calculated spin polarization of the transmitted electrons for the perfect helical cumulene (40 carbon atoms), using B3LYP/X2C-SVPall-2c with different amounts of Hartree–Fock exchange. The spin polarization strongly depends on the amount of Hartree–Fock exchange, but it is not strictly proportional to it. This suggests, that testing the influence of the HF exchange on  $SP$  for the prediction of the CISS effect is mandatory.

This shows the importance of testing the amount of HF exchange for the prediction of the CISS effect because it seems to severely influence the predicted amount of  $SP$ . This is especially problematic because several quantum chemistry codes able to calculate transport properties are not able to use hybrid functionals. The dependence of  $SP$  on the amount of HF-exchange might also explain the much larger  $SP$  obtained in this work compared to the results of Cuniberti *et al.* [166], who used a pure functional.

To summarize,  $\text{Im}(\mathbf{H})$  appears to be necessary for the prediction of a non-zero  $SP$  in closed-shell systems, and thus for the description of the CISS effect, employing the Landauer approach in combination with DFT. The relation of the symmetry of the molecule to the shape of the interatomic-coupling elements and to the sign of the elements in  $\text{Im}(\mathbf{H})$ , appears to induce the symmetry dependence of the calculated  $SP$ . In addition, the amount of HF exchange seems to be important in a first-principles description of the CISS effect because it influences the magnitude of the elements in  $\text{Im}(\mathbf{H})$ . Sections 5.4 and 5.5 have given insight into the microscopic origin of the CISS effect using first-principles methods, but only artificial systems have been used. However, comparing the theoretical results with experimental values is mandatory which is done next.

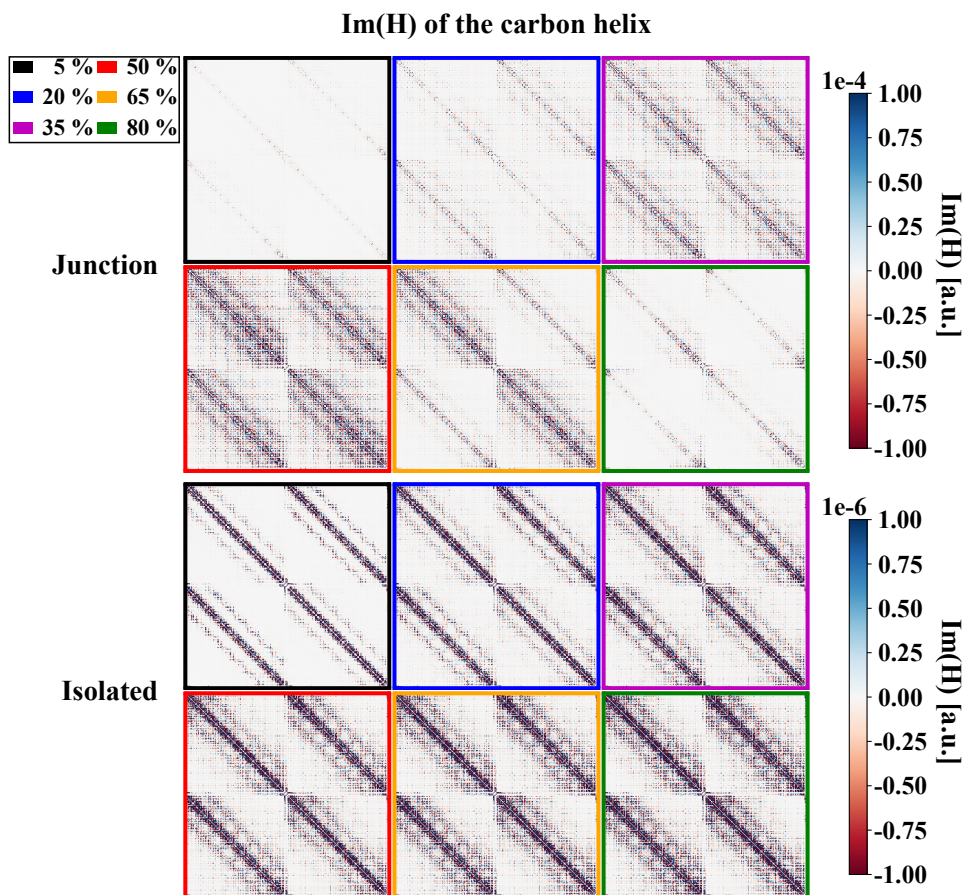


Figure 45:  $\text{Im}(\mathbf{H}_C)$  of the perfect helical cumulene (40 carbon atoms) within an electrode–molecule–electrode junction. The Hamiltonian was calculated from a B3LYP/X2C-SVPall-2c calculation with different amounts of Hartree–Fock exchange. While the magnitude of the imaginary elements in  $\text{Im}(\mathbf{H}_C)$  (“Junction”) shows the same trend as the magnitude of the calculated spin polarization, the magnitude of the elements in  $\text{Im}(\mathbf{H})$  (“Isolated”) increase continuously with the amount of HF exchange. This indicates that the dominant influence of the amount of HF exchange on the spin polarization is an increase of the gold–molecule coupling, thus changing the amount of inherited spin–orbit coupling.

## 5.6. Chiral-Induced Spin Selectivity from Electron Transport Calculations for Experimentally Relevant Systems

The analysis of the matrices and spin polarization calculated for perfect linear and perfect helical cumulene molecules, as well as the analytical derivations regarding the removal of P-symmetry of  $\mathcal{T}$ , which both has been discussed in Section 5.4 and Section 5.5, have shown that the CISS effect is described in principle by the implemented Landauer approach. Although an effective transfer of SOC from the gold electrodes to the helical cumulene molecules has been shown, it does not appear to be the case that DFT in combination with the Landauer approach is able to describe the correct order of magnitude of the CISS effect. However, a direct comparison with experimental data is not sufficiently informative for the artificial systems.

In the following, the application of the Landauer approach in combination with DFT<sup>42</sup> to experimental systems is investigated. A comparison of the calculated  $SP$  with experimentally measured values for  $SP$  is used to evaluate the ability of the Landauer approach to predict the correct order of magnitude of the CISS effect. It is important to note that  $SP$  during this work was calculated for non-magnetic electrodes (see Equation (5.2)), while in the experiments,  $SP$  was evaluated for different orientations of the magnetization of a magnetic electrode either as [149]

$$SP = \frac{I_{\text{Down}} - I_{\text{Up}}}{I_{\text{Down}} + I_{\text{Up}}}, \quad (5.97)$$

where  $I_{\text{Up}}$  is the current with the magnetization in transport direction, and  $I_{\text{Down}}$  is the current with its magnetization against transport direction, or as [147]

$$SP = \frac{G_{\text{L/R}}^+ - G_{\text{L/R}}^-}{G_{\text{L/R}}^+ + G_{\text{L/R}}^-}, \quad (5.98)$$

where  $G_{\text{L/R}}^+$  is the high-conductance orientation of the magnetization, and  $G_{\text{L/R}}^-$  is the low-conductance orientation of the magnetization. Thus, no direct  $SP$  is measured, but

---

<sup>42</sup> B3LYP/ZORA-DZ, scalar-relativistic effects/spin-orbit coupling were considered within the ZORA method. For details see Appendix A.

the magnetoresistance<sup>43</sup> induced by the chiral molecule.

Two different types of molecules are investigated during this part of this work: oligopeptides and a helicene molecule. The structure and the experimental results for such molecules are discussed next.

### 5.6.1. Oligopeptide and Helicene Molecules as Realistic Systems

Oligopeptides are experimentally well studied systems with respect to their spin-filter properties [146, 156, 203–205], even in a single-molecule junction [147]. The CISS effect for oligopeptides was already investigated based on DFT by Cuniberti *et al.* [166] using a pure functional (PBE). Since the exact exchange admixture in the exchange–correlation functional has a great influence on the calculated  $SP$  (see Section 5.5.5), it is worthwhile to compute  $SP$  of oligopeptides using hybrid functionals, and compare the results with results from calculations with pure ones.

Two different oligopeptides were investigated, one consisting of non-chiral glycines only, and one consisting of alternating blocks of leucin and alanin (see Figure 46). The first one was also used by Cuniberti *et al.* [166] in a DFT based electron transport investigation, the second one was used in electron transport experiments by Naaman *et al.* [146]. Since no experimental value for  $SP$  in the conductance experiment is given in Reference [146], the calculated values for  $SP$  are compared to other experiments done by Aragonés *et al.* [147] and Naaman *et al.* [156].

Landauer transport calculations at zero bias voltage correspond to a single-molecule junction experiment at very low biases, and therefore are similar to the measurements done by Aragonés *et al.* [147]. The authors measured  $SP$  at only 50 mV for a single-peptide junction, consisting of three and four Lys-Ala-Ala-Ala-Glu blocks, corresponding to a length of 25.5/33.0 Å. Due to the deviation of the peptide’s length, the measured amount of  $SP$  in their experiment (up to 60 %) is expected to be larger than the cal-

---

<sup>43</sup> Magnetoresistance describes the dependence of the resistance on an external magnetic field.

culated ones for the used peptides. However, results of Naaman *et al.* [156] indicate a *SP* of 60 % for a single-molecular junction to be a reasonable reference because they measured spin polarizations up to 40 % for monolayers of peptides with a similar length as the peptides considered here (five blocks of Ala-Aib). While two gold electrodes were used in the calculations, both experimental setups used magnetic electrodes to contact the peptides, which were adsorbed on a gold surface.

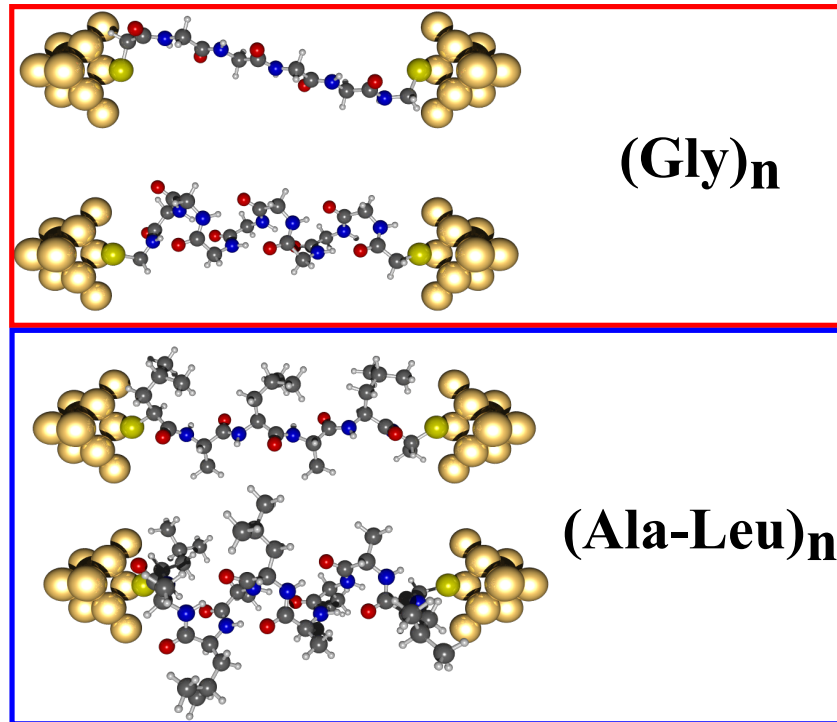


Figure 46: Gold–molecule–gold junctions of the used oligopeptides. The C- and N-termini were replaced by thiol groups. Two different kinds of peptides were investigated, one consisting of glycine only (upper part), and one consisting of Alanin-Leucin blocks (lower part). The isolated molecules were optimized (PBE-D3/def2-TZVP) and placed between two nine-atomic gold clusters, having removed the hydrogen atoms of the thiol groups. The sulfur atoms were placed in fcc-position with a sulfur–gold distance of 2.48 Å. The distance was roughly estimated based on calculations for phenylthiol from the literature [68].

For both investigated peptides, a linear and a helical structure was investigated. To compare oligopeptides of similar length, three Ala-Leu blocks (19.8 Å) or six glycines (18.9 Å) were used for the linear molecules, five Ala-Leu blocks (19.6 Å) or 10 glycines (19.9 Å) were used for the helical ones. The C- and N-termini were substituted by a thiol linker to connect the molecules with gold electrode. The gold–molecule–gold junctions were obtained by optimizing the isolated peptides<sup>44</sup> and placing them between two nine-atomic gold clusters ( $d_{\text{Au–Au}} = 2.88$  Å as in crystalline gold [61]), having removed the hydrogen atoms from the thiol groups (for details on the positioning, see Figure 46).

Helicene molecules also exhibit the CISS effect [149, 151]. A gold–molecule–gold junction of a derivative of the helicene molecule (see Figure 47 part a) was investigated for comparison.  $SP$  for a monolayer of this molecule was measured in conductance experiments by Kiran *et al.* [149], showing  $SP$  to reach values up to 50 %. While the calculations describe a single-molecular junction with two gold electrodes, the experimental setup was different. The molecules were adsorbed on a monolayer of pyrolytic graphite, which was deposited on a gold surface and contacted with a magnetic iron electrode. Thus, deviations between the calculations and the experimental results are to be expected.

The junctions were built by optimizing the isolated helicene<sup>45</sup> and placing it between two 20-atomic gold clusters ( $d_{\text{Au–Au}} = 2.88$  Å as in crystalline gold [61]). For details on the positioning, see Figure 47.

The transmission functions of the obtained gold–molecule–gold junctions were calculated using the implementation described in Section 5.3.2, and are based on a DFT-single point calculation<sup>46</sup>. The central (scattering) region was defined to be the molecules only, if not mentioned otherwise. All energies are shifted against the estimated  $E_F$  (-5 eV [69]),

---

<sup>44</sup> PBE-D3/def2-TZVP, for details see Appendix A.

<sup>45</sup> PBE-D3/def2-TZVP, for details see Appendix A.

<sup>46</sup> B3LYP/ZORA-DZ with relativistic effects (ZORA), for details see Appendix A.

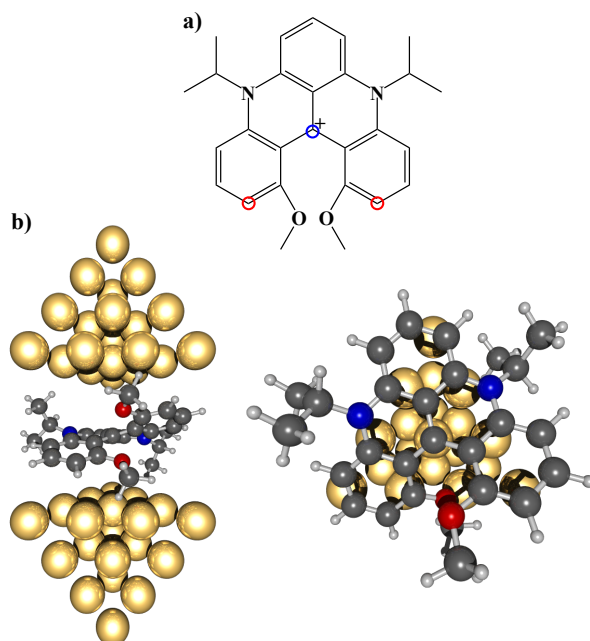


Figure 47: Lewis structure (a) and gold–molecule–gold junction (b) of the helicene molecule. The isolated helicene molecule was optimized (PBE-D3/def2-TZVP), and was placed between two 20-atomic gold clusters. The carbon atom marked blue in the Lewis structure was placed in top position. The upper/lower gold clusters were placed in a distance of 3.1 Å from the carbon atoms marked red in the Lewis structure. The distance was roughly estimate based on a calculated carbon–gold distance for benzene from the literature [206].

and the analysis of  $SP$  is focused on  $SP_{\text{extr}}$  as well as on  $SP$  within an energy range of  $E_F \pm 1$  eV. The oligopeptides are discussed first.

### 5.6.2. Electron Transport Properties of Oligopeptides

The calculated  $\mathcal{T}(E_F)$  at zero bias voltage for both helical peptides is very low ( $< 10^{-8}$ ), and  $SP(E_F)$  is also nearly zero. Within an energy window of  $E_F \pm 1$  eV,  $\mathcal{T}$  does not increase significantly, and  $SP$  remains below 0.1 % (see Figure 48). Therefore, independent of the exact value for  $E_F$ , the transport calculations indicate all considered

oligopeptides to have nearly no conductance within the tunneling regime and to show no CISS at low biases. This is in agreement with the results by Cuniberti *et al.* [166], but contradicts the experimental results of Aragoes *et al.* [147] for a single-molecule junction of a helical peptide. The authors measured histogram features of the conductance at  $2.1 \cdot 10^{-5} G_0$  (length=25.5 Å) and  $2.8 \cdot 10^{-6} G_0$  (length=33.0 Å), and concluded tunneling to be the dominant transport mechanism.  $SP$  was determined to reach values up to 60 % at low biases. Thus, the calculations for the helical peptides cannot reproduce the experimental results.

Another contradiction to the expectations for the CISS effect can be seen by comparing  $SP_{\text{extr}}$  for the linear and the helical oligopeptide.  $SP_{\text{extr}}$  has the same order of magnitude ( $10^{-1}$  %) for both symmetries, which is in contradiction with the expectations for the CISS effect. To get further insight into this problem,  $\mathcal{T}$  and  $SP$  of the inverted structures for the Leucin-Alanin-block oligopeptides (helical and linear) were calculated (see Figure 48). An inversion of the structure leads to a change of sign for the calculated  $SP_{\text{extr}}$ , both for the helical and the linear one. This indicates the calculations to be very sensitive to asymmetries because even the optimized structures of the linear molecules are not symmetric under inversion/mirror operation. This also indicates that influencing factors for the enhancement of the SOC in helical structures are probably missing in the used methodology. The results are not only in contradiction with experimental results, but also with DFT results of Cuniberti *et al.* [166]. Using a similar methodology, the authors reproduced the expected trend for CISS effect regarding the symmetry of the peptide (the calculated  $SP_{\text{extr}}$  for the linear peptide was shown to be much smaller than  $SP_{\text{extr}}$  for the helical one). The reason for the differing results may be deviations in the used structures for the linear peptide. The used linear peptide in the work by Cuniberti *et al.* [166] is much more symmetric and linear than the one used in this work. It is not for sure, whether the peptides in Reference [166] were optimized or were constructed to be completely linear, but the structure optimization always lead to an slightly asymmetric structure during this work. Therefore, the differences might not be grounded in slightly deviating methodologies, but in the deviating symmetries of

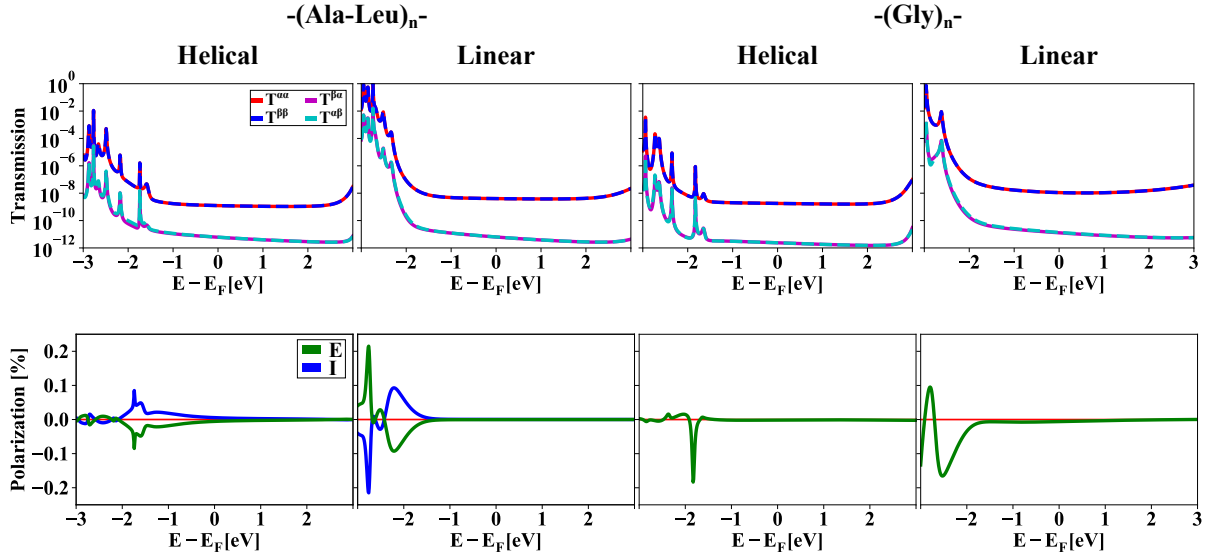


Figure 48: Calculated transmission functions and spin polarizations of the transmitted electrons for gold–molecule–gold junction of the helical and linear peptides (B3LYP/ZORA-DZ). The relative symmetries of the structures are indicated as **E** (identity) and **I** (inverted). All energies are shifted against the estimated  $E_F$  ( $-5$  eV). Within the energy window of  $E_F \pm 1$  eV, the transmission and spin polarization are very low for all peptides. The maximum absolute value for the spin polarization of the linear peptides is larger than for the helical ones, which is in contradiction with the expectations for the CISS effect.  $SP$  changes its sign upon inverting the structure, even for the linear molecule.

the linear peptides.

It is important to note that care has to be taken, if  $SP$  is estimated from small transmissions due to the danger of numerical noise. However, the changing sign after inverting the structures indicate that the  $SP$  for the peptides is beyond numerical noise.

Since the Landauer approach with the chosen structures of the gold–molecule–gold junction and the settings for the DFT calculation does not describe the conductance properties of the oligopeptides very well, no further calculations for the oligopeptides were done. The results indicate that peptides are very problematic systems for a first-principles in-

vestigation of the CISS effect. However, the used methodology might be able to correctly describe CISS for the helicene molecule.

### 5.6.3. Electron Transport Properties of the Helicene Molecule

$SP$  of a gold–helicene–gold junction was calculated using two different amounts of HF exchange admixture (20 % and 50 %, see Figure 49). For both amounts of HF exchange, the computed absolute value for  $SP$  remains below  $10^{-5}$  % within an energy window of  $E_F \pm 1$  eV. For 20 % HF exchange admixture,  $SP_{\text{extr}}$  only reaches values of  $\pm 0.42 \cdot 10^{-4}$  % within the calculated energy range of  $E_F \pm 3$  eV (sign is depending on the handedness of the helicene molecule), and  $SP_{\text{extr}}$  computed with 50 % HF exchange admixture is shifted to energies larger than  $E_F + 3$  eV. However, the increased amount of HF exchange does not appear to influence the magnitude of  $SP$  significantly.

The Landauer approach at zero bias voltage with a scattering region consisting of the molecule only covers the CISS effect for the helicene molecule qualitatively, but cannot reproduce the experimental magnitude of the CISS effect ( $P \approx 50\%$  [149]). This is similar to the shortcomings of the tight-binding models of Cuniberti *et al.* [171, 172]. To address the problem of underestimating the magnitude of the CISS effect, the influence of additional parameters were investigated: an applied external electric field and dephasing. The influence of an external electric field was already discussed by Mujica *et al.* [181], the influence of dephasing was discussed by Guo and Sun [173] and by Mujica *et al.* [191].

The external electric field was approximated by including a linear homogeneous electric field within the SCF calculation, and was applied along the transport direction. The strength of the field corresponded to an applied voltage of 1 V. Similar voltages were applied in conductance experiments for helicene by Kiran *et al.* [149]. Electron–phonon interactions were considered within the effective dephasing model as explained in Section 5.3.3. The effective dephasing parameter was set to a value of 0.2 eV, which is a rough estimate for aromatic molecules at room temperature, given by Frauenheim *et al.* [192].

Neither an external electric field, nor electron–phonon interactions significantly increase  $SP$  for the helicene molecule. An applied electric field and electron–phonon interactions slightly shift the maximum of  $SP$  in energy and slightly increase the absolute value of  $SP_{\text{extr}}$  (see Figure 50). Nevertheless, the absolute value of  $SP_{\text{extr}}$  in both cases remains below  $10^{-4}$  %.

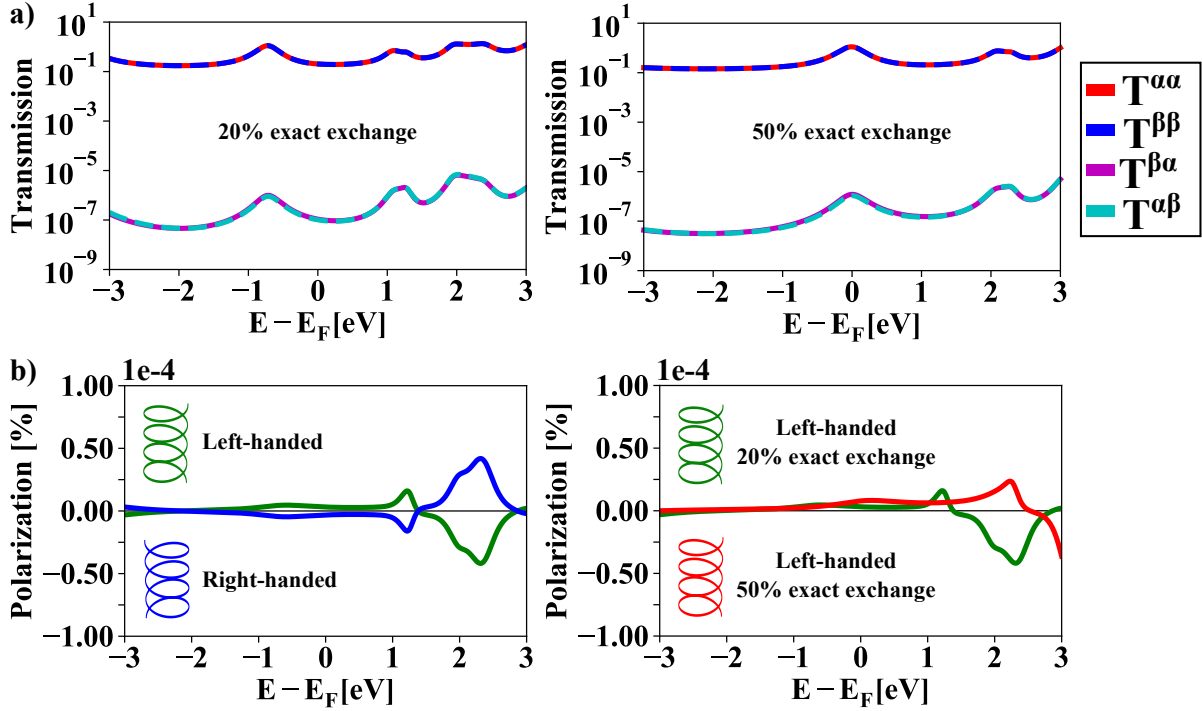


Figure 49: Calculated transmission function (a) and spin polarization of transmitted electrons (b) for gold–molecule–gold junctions of the left- and right-handed helicene molecule, employing two different values for the amount of HF exchange (B3LYP/ZORA-DZ). All energies are shifted against the estimated  $E_F$  ( $-5$  eV). Within the energy window of  $E_F \pm 1$  eV, the spin polarization is very low, and the spin polarization changes its sign upon changing the handedness of the helix. Increasing the amount of HF exchange shifts the spin polarization to higher energies, but does not lead to much higher values for the spin polarization.

The influence of dephasing and an electric field on  $SP$  are both very small, and cannot explain the deviations from the first-principles electron transport calculations with the experimental results. However, all calculations which have been discussed so far have included only the molecule into the scattering region. Including the first layer of both clusters' gold atoms into the scattering region should increase  $SP$  due to the strong SOC of gold. As mentioned before (see Section 5.5.5), the importance of the substrate's strong SOC for the magnitude of the CISS effect was ruled out for the photoelectron emission experiment [148,151]. However, this might be different for transport experiments because they have been done only by using gold substrates.

The inclusion of gold into the scattering region massively influences  $\mathcal{T}$ ,  $SP_{\text{extr}}$ , and  $SP$  (see Figure 51).  $\mathcal{T}$  decreases, and the peaks in the transmission function become less broadened.  $SP$  varies in the range of  $E_F \pm 1$  eV and reaches values in the order of magnitude of  $\pm 0.1$  % (depending on the handedness of the helicene), with  $SP_{\text{extr}}$  reaching values of  $\pm 0.38$  %. Compared to the experimental  $SP$  of about 50 % [149],  $SP$  computed with a scattering region including gold atoms is in better agreement than  $SP$  calculated with a scattering region consisting of the helicene only. Although  $SP$  remains several orders of magnitude smaller than in the experiment, this might indicate the strong SOC of gold to be important in the transport experiment.

To summarize, the results which have been discussed in Section 5.6 show that the first-principles methodology used in this work, despite its ability to describe CISS qualitatively, cannot describe the magnitude of the CISS effect. The SOC-enhancing effect of the helical structures appears to be missing. The deviation might be attributed to missing parts of SOC within the ZORA method, an approximated treatment of the electrodes due to small clusters, neglecting structural changes due to the adsorption on the substrate, or neglecting dynamical effects like structural fluctuations. Additionally, induced magnetic fields due to electron transport might be important.

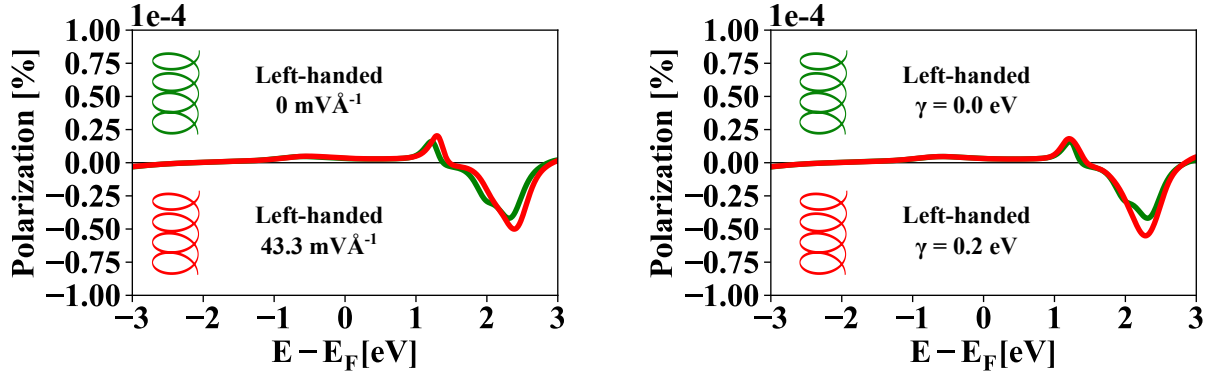


Figure 50: Calculated transmission function and spin polarization of transmitted electrons for gold–molecule–gold junctions of the left-handed helicene molecule (B3LYP/ZORA-DZ), applying an electric field (left) or considering electron–phonon interaction with an effective scaling parameter  $\gamma$  (right). All energies are shifted against the estimated  $E_F$  ( $-5$  eV). Neither an external electric field nor dephasing increases the spin polarization significantly.

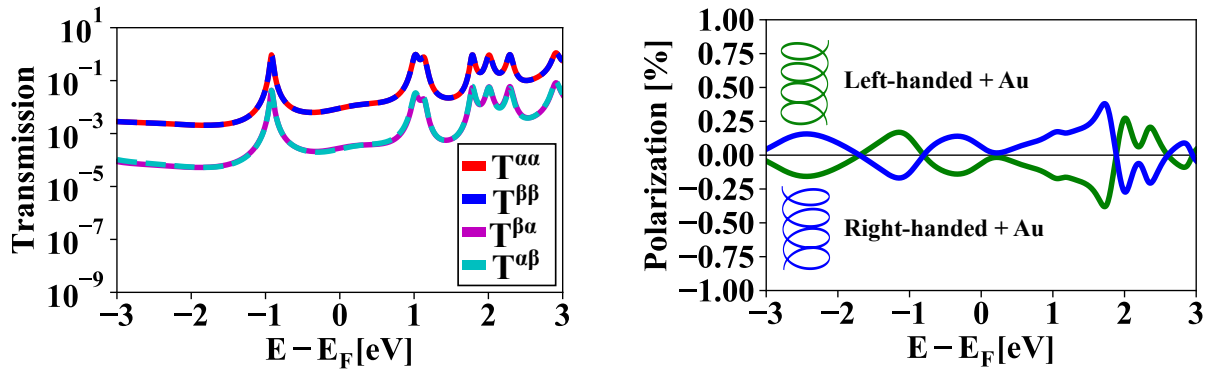


Figure 51: Calculated transmission function and spin polarization of transmitted electrons for gold–molecule–gold junctions of the left- and right-handed helicene molecule, including the first layer of both clusters' gold atoms into the scattering region (B3LYP/ZORA-DZ). All energies are shifted against the estimated  $E_F$  ( $-5$  eV). Gold within the scattering region increases the spin polarization massively. However, the spin polarization remains several orders of magnitude smaller than in the experiment (which was about 50 % [149]).

## 5.7. Conclusion

In this part of this thesis, the applicability and quality of a two-component-DFT-based Landauer approach to describe the CISS effect has been investigated. To do so, this approach and an extension to include dephasing have been successfully implemented in ARTAIOS and have been used for a DFT-based investigation of the CISS effect. The DFT results have been compared with a newly developed symmetry analysis based on analytical considerations.

First, the qualitative origin of the CISS effect has been analyzed, focusing on the removal of the P-symmetry of  $\mathcal{T}$ . For closed-shell systems with non-magnetic electrodes, it has been shown that if  $\mathbf{G}$  is symmetric or Hermitian, P-symmetry of  $\mathcal{T}$  can be enforced and the spin polarization of the transmitted electrons has to be zero. If SOC is considered, imaginary parts in  $\mathbf{H}$  are introduced, which in combination with  $\Sigma_L$  and  $\Sigma_R$  results in a non-symmetric and non-Hermitian  $\mathbf{G}$ . Thus, if SOC is considered, P-symmetry of  $\mathcal{T}$  is not enforced anymore. This opens the possibility of a non-zero spin polarization, and therefore the possibility to describe CISS effect. Using a simplified Hamiltonian for a diatomic model system, it has been shown that the symmetry of the molecule defining the scattering region can be connected to an enforcement of the P-symmetry of  $\mathcal{T}$ , even if SOC is considered (for the definition of P- and T-Symmetry see Section 5.4).

To verify the analytical derivations, the Landauer approach combined with SOC in the electronic structure method has been applied to perfect helical and perfect linear model systems, described with DFT. The resulting spin polarization is in qualitative agreement with all experimental observations for the CISS effect. Additional insight into the connection of symmetry and spin polarization has been gained by analyzing a symmetry-adapted  $\text{Im}(\mathbf{H})$  for the isolated molecules. All elements of  $\text{Im}(\mathbf{H})$  change their sign upon changing the helix sense, and the  $p$ - $p$  spin-conserving nearest-neighbor coupling elements in  $\text{Im}(\mathbf{H})$  of the linear molecule are direction independent, while for the helical molecule they are direction-dependent. The first finding gives a direct link

with the helicity-dependent spin polarization of transmitted electrons in helical structures, while the latter provides a link between the preservation of P-symmetry of  $\mathcal{T}$  for linear molecules and the removal of the P-symmetry of  $\mathcal{T}$  for helical molecules.

Furthermore, it has been shown that the magnitude of  $\text{Im}(\mathbf{H})$  for a helical molecule within a electrode–molecule–electrode junction is connected to the absolute value of the spin polarization. The magnitude of  $\text{Im}(\mathbf{H})$  increases with the atomic number of the atoms which have been used to build the electrode, and strongly depends on the amount of HF exchange admixture in the exchange–correlation functional. The first finding indicates an inheritance of the electrode’s SOC to be important for the absolute amount of the CISS, the latter indicates the importance of considering hybrid-functionals for the prediction of CISS.

At the end of this section, the Landauer approach has been applied to experimental relevant systems. For several oligopeptides, the methodology has not been able to reproduce the experimental findings with respect to the CISS effect. The oligopeptides are predicted to have nearly no conductance within the tunneling regime, the polarization is massively underestimated in comparison with the experiment, and even small asymmetries in linear structures can induce a spin polarization of the same magnitude as for the helical ones. However, an inversion of the structures (linear and helical) has led to a change of sign for the spin polarization, indicating that this effect originates from asymmetries within the molecule. This strongly indicates that the factors which increase the effective SOC in helical molecules are missing in the used approach.

For the helicene molecules, the spin polarization is also underestimated in comparison to the experiment. The addition of an electric field as well as the inclusion of dephasing does not improve the agreement with the experiment. Including gold into the scattering region massively increases the spin polarization, although it remains two orders of magnitude smaller than experimental values. This might indicate an importance of the substrate’s SOC in transport experiments, although such an influence on the CISS effect has been ruled out for the photoelectron emission experiment.

Overall, the results show directly that the CISS effect is described in principle by the Landauer approach combined with SOC in the electronic structure method, but do not elucidate the origin of the enhanced SOC in helical structures. The importance of imaginary quantities following from the results of this work points towards potential new developments for first-principles descriptions of CISS in the future, by including further mechanisms that enhance these imaginary terms.

## 6. Conclusion and Perspectives

The understanding of spin-dependent phenomena based on first-principles calculations is important for both the improvement of existing molecular and nanoscale devices and for the development of new devices in the field of spintronics. In the field of nanoscale spintronics, one faces the challenge that in many cases the physical mechanisms underlying the experimental results are unclear, and simple model descriptions cannot always grasp all relevant aspects of the system. The goal of this work has been to provide insight into three different kinds of experimentally observed effects from the field of spintronics using density functional theory.

### 6.1. Summary

First, the origin of the experimentally observed magnetoresistance for single-molecule junctions of a TEMPO-OPE molecule has been investigated. Electron transport calculations within the Landauer regime indicate that the current does not pass through the TEMPO radical, and therefore a direct interaction between passing electrons and unpaired spins on the molecule cannot explain the observed magnetoresistance. A possible interaction of the gold electrodes with the radical part of the molecules covering the gold electrode has been indicated as a possible alternative explanation: the interaction of these molecules with the electrodes may depend on an external magnetic field, and the magnetoresistance may be induced by a modification of the electrode–molecule interface. It has been computationally shown that indeed for adsorbed TEMPO-OPE molecules on a gold-(111)-surface, the TEMPO radical is close to the surface. Further investigations of the bonding between TEMPO and gold, as well as of the response of such an interaction to a magnetic field, are necessary to confirm such a mechanism.

In addition, modifications of the TEMPO-OPE molecule, like changing the conducting OPE backbone or the TEMPO radical part, have been found to lead to molecules in which the current is directly influenced by the radical. These radicals might exhibit new

types of magnetoresistance behavior, and are therefore worthwhile to be investigated experimentally. Some of these molecules are already studied in the group of Elke Scheer in Konstanz.

In the second part of this work, the origin of photocurrents induced by a circular photogalvanic effect in lead-(II)-sulfide nanosheets has been revealed by calculating the band structures of two-dimensional nanosheets under periodic-boundary conditions. The combination of spin-orbit coupling and an external electric field has been found to introduce a Rashba splitting in the band structure of the nanosheets. A selection mechanism for the creation of an asymmetric charge-carrier distribution under illumination with circularly polarized light has been formulated, based on the Rashba splitting as well as on the orbital character of the bands. This selection mechanism can explain the presence of the photocurrent.

In the last part of this work, the chiral-induced spin selectivity effect and the resulting spin filtering in transport experiments on helical molecules such as DNA or peptides have been investigated using first-principles methods. The overall mechanism behind chiral-induced spin selectivity is likely related to Rashba spin-orbit coupling. However, it is still unclear how the small atomic spin-orbit coupling of the light elements composing the molecules exhibiting the chiral-induced spin selectivity effect can be connected with its surprisingly large magnitude. First-principles investigations could provide essential insight into the mechanisms underlying chiral-induced spin selectivity. For this purpose, a modification of the Landauer approach to include spin-orbit coupling has been implemented within the ARTAIOS code, analyzed, and applied to several systems. The imaginary parts of the effective single-particle Hamiltonian that are induced by spin-orbit coupling have been identified to be responsible for the spin filtering potential of closed-shell molecules. A linear symmetry of a molecule has been connected to the absence of spin filtering, even if spin-orbit coupling is considered, using a simplified molecular model Hamiltonian. The analytical results have been confirmed numerically

for electrode–molecule–electrode junctions of perfect linear and perfect helical carbon chains, reinforcing the importance of the imaginary parts of the effective single-particle Hamiltonian for the symmetry-dependent spin filtering.

Although the presence of the chiral-induced spin selectivity effect has been shown in principle, the origin of the experimentally observed large magnitude of the effect remains unknown. Numerical results show that such an enhancement is not fully described within the methodology which has been used here, as the total amount of spin polarization is underestimated and the same order of magnitude is predicted for the spin polarization of inversion-asymmetric helical and linear peptides. However, by identifying the importance of imaginary terms for chiral-induced spin selectivity a guideline for further theoretical descriptions is suggested, in particular with respect to processes including imaginary terms, such as dephasing and leakage.

## 6.2. Outlook

The results of this work provide starting points for further investigations.

- Since the origin of the large magnetoresistance for the TEMPO-OPE molecule has not been identified in the course of this thesis, further investigations are needed. The results of the structure optimizations of the TEMPO-OPE molecule on a gold surfaces indicate that a detailed analysis of the radical–gold interaction could be very promising in this context. To do so, force field methods or tight-binding DFT could be used to simulate a whole junction with a large ensemble of molecules. Such an investigation could give further insights into the possible adsorption structures of the organic radicals on gold. Based on the adsorption structures, a detailed analysis of the bonding situation of a possible radical–gold interaction could reveal the mechanism underlying the observed magnetoresistance.
- The implemented Landauer approach including spin–orbit coupling could be extended for further investigations of the chiral-induced spin selectivity effect based on density functional theory. Extending the approach beyond the wide-band limit

approximation would allow for the simulation of magnetic electrodes as used in the experimental setups. In addition, the treatment of dephasing could be extended by a more accurate method, which considers the vibrations directly and does not use an effective dephasing parameter (for instance the lowest-order expansion [207]).

- The investigation of the spin filter properties for peptides would benefit from a detailed insight into the tunneling conductance of peptides. The results of Alemán *et al.* [208], Misicka *et al.* [209], and Isied *et al.* [210] indicate that the hopping mechanism is important for longer peptides (about 20 Å to 25 Å), suggesting that tunneling transport may not be the dominant transport mechanism for those oligopeptides. Landauer transport calculations based on density functional theory by Cuevas and Zotti [211] support this assumption. Nevertheless, results by Mujica *et al.* [147] indicate that the tunneling regime is dominant for oligopeptides with a length of 25.5 Å and 33 Å. Environmental effects like solvation and the proximity of other peptides adsorbed on the surface may be also of importance [211] as well as a more accurate adsorption structure (experimentally, non-zero angles between the helix axis and the surface normal were observed [156, 209]).
- The treatment of the spin-orbit coupling in density functional theory calculations is only approximate, ignoring for instance the spin-other-orbit interaction. In addition, the influence of induced magnetic fields due to the current [212] on the transported electrons and the electronic structure of the molecule is neglected. To include the missing contributions of the spin-orbit coupling, the quantum chemistry code DIRAC [213] could be employed. The inclusion of current-induced magnetic fields would require a current-density functional theory treatment, which is quite difficult computationally.

Overall, relevant insight into spin-dependent electron transport phenomena of molecular and nanoscale systems has been gained by using first-principles methods. In one case (circular photogalvanic effect in lead-(II)-sulfide nanosheets), a plausible mechanism has been suggested, in another case (magnetoresistance in TEMPO-OPE junctions), no such mechanism has been identified, but one possible explanation has been excluded, and first steps toward an alternative one have been made. In a third case (chiral-induced spin selectivity in helical systems), the surprisingly high magnitude of the effect remains an open question. However, state-of-the art first-principles methods have been confirmed to be able to explain the effect in principle, and new insights into why this is the case have been gained. These findings suggest additional ingredients which might be necessary to fully understand chiral-induced spin selectivity in helical molecules.

This illustrates both the potential and drawbacks of present-day first-principles methodologies in the field of spin-dependent phenomena. Ideally, it will point the way both toward further insight into relevant processes in molecular and nanoscale spintronic devices, and toward further development of first-principles methodologies for this field.

## 7. Acknowledgment

I would like to acknowledge all the people who supported and accompanied me during the time of my Ph.D. thesis:

First I want to thank Prof. Dr. Carmen Herrmann for supervising me for the time of this thesis. She incited my interest in quantum chemistry during her lectures which motivated me to do my master's and my Ph.D. thesis in her group. The professional discussions with her have given me much support and often have led to new ideas. I am thankful that she has given me the opportunity to work on such an interesting topic and allowed me to spent such a great time in her working group.

I also want to thank Prof. Dr. Robin Santra for agreeing to be my co-examiner.

In addition, I want to express my gratitude to all of my collaborators. Especially to Prof. Dr. Chirstian Klinke and Mohammad Mehdi Ramin Moayed for intense and frequent discussions about lead-(II)-sulfide nanosheets, and to Solmar Varela, Ernesto Medina and Prof. Vladimiro Mujica for all the discussions regarding the chiral-induced spin selectivity effect.

Also thanks to all members of the working group, both former or present, who have accompanied me for the time in the group. Dr. Lynn Groß and Dr. Torben Steenbock were always eager to help with scientific questions, especially when I joint the group. The games of *Doppelkopf* with Dr. Alexander Voigt and Conrad Stork were always a nice distraction from the work. I had the pleasure to support Susanne Kröncke during her master's thesis and afterwards she became appreciated colleague. Michael Deffner, Haitao Zhang, Benjamin Bolbrinker, and Rukan Nasri helped me a lot due to discussions on overlapping topics.

A lot of people have proofread my thesis, and I would like to thank them all. Thanks to

Benjamin Bolbrinker, and Rukan Nasri, Susanne Kröncke, Marcus von der Au, Mareike Krell, and Isabel Sarah Reuter for this.

For technical support and making all the computational resources needed for this thesis available and accessible, I want to thank the IT-service of the chemistry department of the University of Hamburg, the Norddeutscher Verbund für Hoch- und Höchstleistungsrechnen (HLRN), as well as the High-Performance Computing Cluster of the University of Hamburg. Dr. Hinnerk Stüben and Dr. Thomas Orgis spent a lot of time to make an easy access possible and were always ready to help.

I want to thank Susanne Breidohr, Beate Susemihl, Ingke Klemme, and Antje Geilen for all administrative matters I faced during my thesis.

For additional financial support, I would like to thank the “Advanced Imaging of Matter” cluster of the “Hamburg Centre for Ultrafast Imaging” (CUI).

For the whole time of my master’s studies and my Ph.D. thesis, Dr. Marc Philipp Bahlke accompanied me as a colleague and as a friend. I am thankful for both the professional discussions we had and the leisure times we spent. He also proofread my thesis, although he had plenty to do by himself.

For all the support and care of my parents, not only for the time of this thesis, but for the time of my whole life, I am very grateful. The financial and mental support, as well as their guidance made it possible for me to start my chemistry studies and to finally write this thesis. I also want to thank both of my brothers who also accompanied and supported me for my whole life.

My gratitude for huge mental support as a partner and a lot of beautiful moments over the last year goes to Isabel Sarah Reuter. I am very thankful for our time together.

# Appendix

## A. Computational Methodology

Electronic structure calculations and geometry optimizations during this work were done using the program packages TURBOMOLE 7.0 [214–217], TURBOMOLE 7.1 [215–218], ADF 2014 [219–221], GAUSSIAN09 [222], QUANTUM ESPRESSO 5.2 [186, 187], and QUANTUM ESPRESSO 6.0 [186, 187]. The GTO basis sets LANL2DZ [223–226], def2-SVP [227, 228], def2-TZVP [227, 228], and x2c-SVPall-2c [229] as well as the ZORA adapted STO basis sets DZ [230] and DZP [230] were used. Several exchange–correlation functionals were employed like BP86 [231, 232], PBE [233, 234], and B3LYP [232, 235, 236]. Dispersion interactions were either taken into account by using the DFT-D3 method [237] with Becke–Johnson dampending [238] or with the DFT-D2 [239, 240] method and modified  $C_6$  parameters [73]. Relativistic effects were taken into account with the X2C method [241, 242], the ZORA method [32, 243–246], or within the projector-augmented wave (PAW) potentials [247]. The PAW provided by the pslibrary.1.0.0 [248] were used<sup>47</sup>.

### Section (3) Large Magnetoresistance in TEMPO-OPE Single-Molecule Junctions

**(3.3.1 and 3.4)** The transmission functions for the gold–molecule–gold junctions of TEMPO-OPE, OPE, Keto-OPE, and all other radicals were calculated with ARTAIOS [195]. The electronic structure calculations and geometry optimizations were done with the quantum chemistry code TURBOMOLE 7.0. The energy convergence threshold within the self-consistent field algorithm was set to  $10^{-7}$  a.u. and the convergence criteria for structure optimizations were set to  $10^{-6}$  a.u. for the energy change and  $10^{-4}$  a.u. for the gradient.

The structures of the isolated molecules were allowed to relax, employing the BP86 functional, the def2-TZVP basis set, and the dispersion correc-

---

<sup>47</sup> Downloadable at <https://dalcorsio.github.io/pslibrary/>.

tion DFT-D3 including Becke–Johnson damping. To speed-up the structure optimizations, the resolution-of-the-identity method [249, 250] with the corresponding auxiliary basis set was applied.

The electronic structures of the gold–molecule–gold junctions were calculated using the B3LYP functional and the def2-SVP basis set.

**(3.3.2)** The structures of the TEMPO-OPE molecule on a gold surface were calculated with QUANTUM ESPRESSO 6.0. The Brillouine zone was sampled with a  $2 \times 2 \times 1$  grid ( $4 \times 4$  surface cell) or at the  $\Gamma$ -point only ( $7 \times 7$  surface cell) employing a Fermi–Dirac smearing (0.01 Ry). A kinetic-energy cutoff for the wavefunction of 48 Ry and a cutoff for the kinetic-energy of the electronic density of 480 Ry were used. The convergence thresholds for the structure optimization were set to  $10^{-6}$  a.u. for the energy change and  $10^{-4}$  a.u. for the gradient. The energy convergence threshold within the self-consistent field algorithm was set to  $10^{-7}$  a.u..

The structures were optimized using the PBE functional and the corresponding PAW potentials. Scalar-relativistic PAW potentials were used to take relativistic effects into account. Dispersion interactions during the structure optimization were considered within the DFT-D2 method. The  $C_6$  parameter for the gold atoms was set to  $736.368 \frac{\text{Ry}}{a_0^6}$  [73]. A large vacuum was employed by setting the length of the unit cell along the surface normal to 50.24 Å, preventing an interaction of the TEMPO-OPE molecule with the periodic image of the gold slab.

#### Section (4) Circular Photogalvanic Effect in Lead-(II)-Sulfide Nanosheets

- All calculations were done with QUANTUM ESPRESSO 5.2. A kinetic-energy cutoff for the wavefunction of 46 Ry and a cutoff for the kinetic-energy of the electronic density of 460 Ry were used. The Brillouin zone was sampled with a shifted  $8 \times 8 \times 8$  grid for bulk lead-(II)-sulfide and a shifted  $8 \times 8 \times 1$  mesh for two-dimensional (001)-lead(II)-sulfide sheets. The default

convergence thresholds were used for all calculations. The PBE functional in combination with the PAW method was used, and scalar-relativistic as well as full-relativistic PAW potentials were used to take relativistic effects into account.

SOC and dispersion interactions were not considered during the structure and lattice-constant optimizations. The periodic-image of the two-dimensional sheet was separated by a vacuum of 15 Å during the structure optimization. Single-point calculations and band structure calculations with applied external electric fields were done with a larger vacuum layer (20 Å). The fields were simulated with a saw-like potential, changing along the surface normal and the decrease of the saw-like potential to its initial value was set to be in the middle of the vacuum. Symmetry was not used to reduce the number of k-points during the self-consistent field calculation. The pDOS resolved band structure was calculated using a Gaussian smearing with a broadening of 0.0001 Ry. The pDOS was summed over all atoms for any type of orbital.

## Section (5) Chiral-Induced Spin Selectivity in Helical Molecules

(5.3.2) The structures of the *m*-Diethynethiolbenzene and 1,4-Diethynethiol-2-methylbenzene gold–molecule–gold junctions were taken from the example file of ARTAIOS. One- and two-component electronic structure calculations were done using both ADF 2014 (BP86/DZ) and TURBOMOLE 7.1 [36,198] (BP86-def2-SVP). In the case of TURBOMOLE 7.1, the resolution-of-the-identity method with the corresponding auxiliary basis set was applied to speed up the calculation, and a convergence threshold for the total energy during the SCF calculation of  $10^{-7}$  a.u. was used. In the case of the ADF 2014 calculations, scalar-relativistic effects and SOC were taken into account with the ZORA method, and a convergence threshold for the total energy during the SCF calculation of  $10^{-6}$  a.u. was used. The transmission functions were calculated within the Landauer regime using ARTAIOS and the approach implemented in this thesis.

**(5.3.3)** The structures of the anthraquinone molecule were optimized employing the B3LYP functional and the def2-TZVP basis set (TURBOMOLE 7.1). The convergence thresholds for the structure optimization were set to  $10^{-6}$  a.u. for the energy change and  $10^{-4}$  a.u. for the gradient. The energy convergence threshold within the self-consistent field algorithm was set to  $10^{-7}$  a.u..

The electronic structure calculation for the subsequent transport calculation including dephasing was done with ADF 2014, employing the B3LYP functional and the ZORA adapted DZP basis set. Scalar-relativistic effects were taken into account with the ZORA method. Transport calculations including dephasing were done with the approach implemented in this work.

**(5.5)** All one- and two-component DFT calculations and the structure optimizations of the hydrogen atoms in the ideal helical and linear molecules were carried out using TURBOMOLE 7.1. The threshold for the geometry optimizations was set to  $10^{-6}$  a.u. for the energy change and  $10^{-4}$  a.u. for the gradient. The energy convergence threshold within the self-consistent field algorithm was set to  $10^{-7}$  a.u..

For the structure optimization, the PBE functional, the def2-TZVP basis set, and the dispersion correction DFT-D3 including Becke–Johnson damping were used. To speed up the structure optimizations, the resolution-of-the-identity method with the corresponding auxiliary basis set was applied. The one- and two-component DFT calculations for the subsequent Landauer transport calculations were done using the B3LYP functional and the x2c-SVPall-2c basis set. Scalar-relativistic effects and SOC were considered within the X2C method. Transport calculations were done with the approach implemented in this work.

**(5.6)** All structure optimizations for the oligopeptides and helicene molecules were carried out using TURBOMOLE 7.1, employing the PBE functional and the def2-TZVP basis set. Dispersion interactions were considered within the DFT-D3 method using Becke–Johnson dampening. The threshold for the ge-

ometry optimizations was set to  $10^{-6}$  a.u. for the energy change and  $10^{-4}$  a.u. for the gradient. The energy convergence threshold within the self-consistent field algorithm was set to  $10^{-7}$  a.u..

The one- and two-component DFT calculations were done with ADF 2014 using the B3LYP functional and the ZORA adapted DZ basis set. Scalar-relativistic effects and SOC were considered within the ZORA method. The accuracy of the used Becke grid was set to “good”. The energy convergence threshold within the self-consistent field algorithm was set to  $10^{-6}$  a.u.. Transport calculations were done with the approach implemented in this work.

## B. Additional Data

### Optimized structures of the isolated TEMPO-OPE molecule

Figure 52 and 53 show the optimized structures of the *cis*- and *trans*-TEMPO-OPE molecule and the relative energies, comparing an optimization with and without dispersion interactions.

Without dispersion interactions, the OPE backbone of the *cis*- and *trans*-TEMPO-OPE molecule remains planar and the *cis*-isomer is slightly favored energetically (see Figure 52). If dispersion interactions are considered within the structure optimization, one ring of the OPE backbone of the *cis*-TEMPO-OPE molecule is twisted and the *trans*-isomer is slightly favored energetically (see Figure 53).

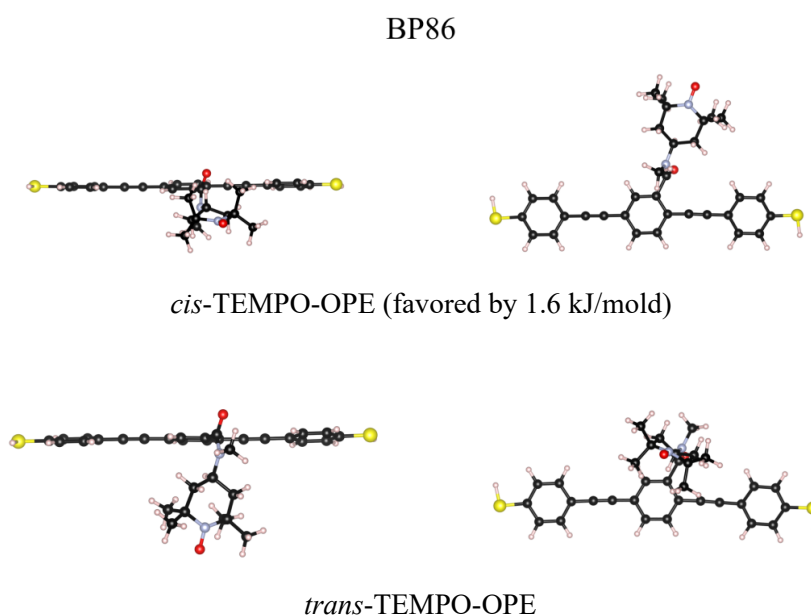


Figure 52: Optimized structures of *cis*- and *trans*-TEMPO-OPE, optimized with BP86/def2-TZVP. Both isomers are close in energy. Without dispersion interactions, the OPE-backbone for both isomers is completely planar. (Adapted with permission from R. Hayakawa, M. A. Karimi, J. Wolf, T. Huhn, M. S. Zöllner, C. Herrmann, and E. Scheer, *Nano Lett.* 2016, 16, 8, 4960-4967. Copyright 2016 American Chemical Society.)

BP86-D3

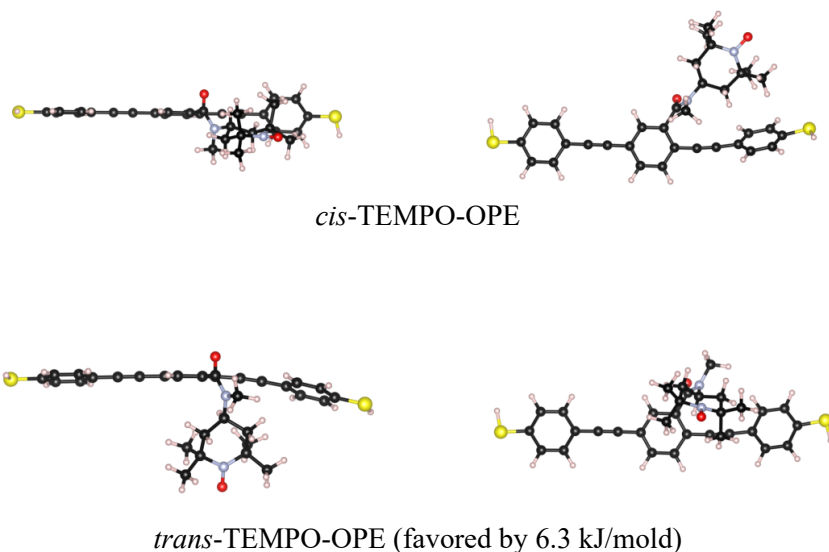


Figure 53: Optimized structures of *cis*- and *trans*-TEMPO-OPE, optimized with BP86-D3/def2-TZVP. Both isomers are close in energy. For the *cis*-isomer, one ring in the OPE-backbone is tilted due to the interaction with the TEMPO-radical. (Adapted with permission from R. Hayakawa, M. A. Karimi, J. Wolf, T. Huhn, M. S. Zöllner, C. Herrmann, and E. Scheer, *Nano Lett.* 2016, 16, 8, 4960-4967. Copyright 2016 American Chemical Society.)

### Transmission function and Breit–Wigner fit for the TEMPO-OPE molecule

Figure 54 shows a transmission function and a Breit–Wigner fit for a gold–molecule–gold junction of the TEMPO-OPE molecule, using a 19-atomic gold cluster to simulate the electrodes (GAUSSIAN09: B3LYP/LANL2DZ). The transmission functions are in qualitative agreement with the transmission functions calculated with the nine-atomic gold cluster (TURBOMOLE 7.0: B3LYP/def2-SVP). The Breit–Wigner fit shows a nearly symmetric electrode coupling for the *trans*-isomer and an asymmetric electrode coupling for the *cis*-isomer of the TEMPO-OPE molecule. This indicates that the preferred configuration of the TEMPO-OPE molecule within the junction is the *trans*-configuration because experimental results also indicate a symmetric electrode coupling [16].

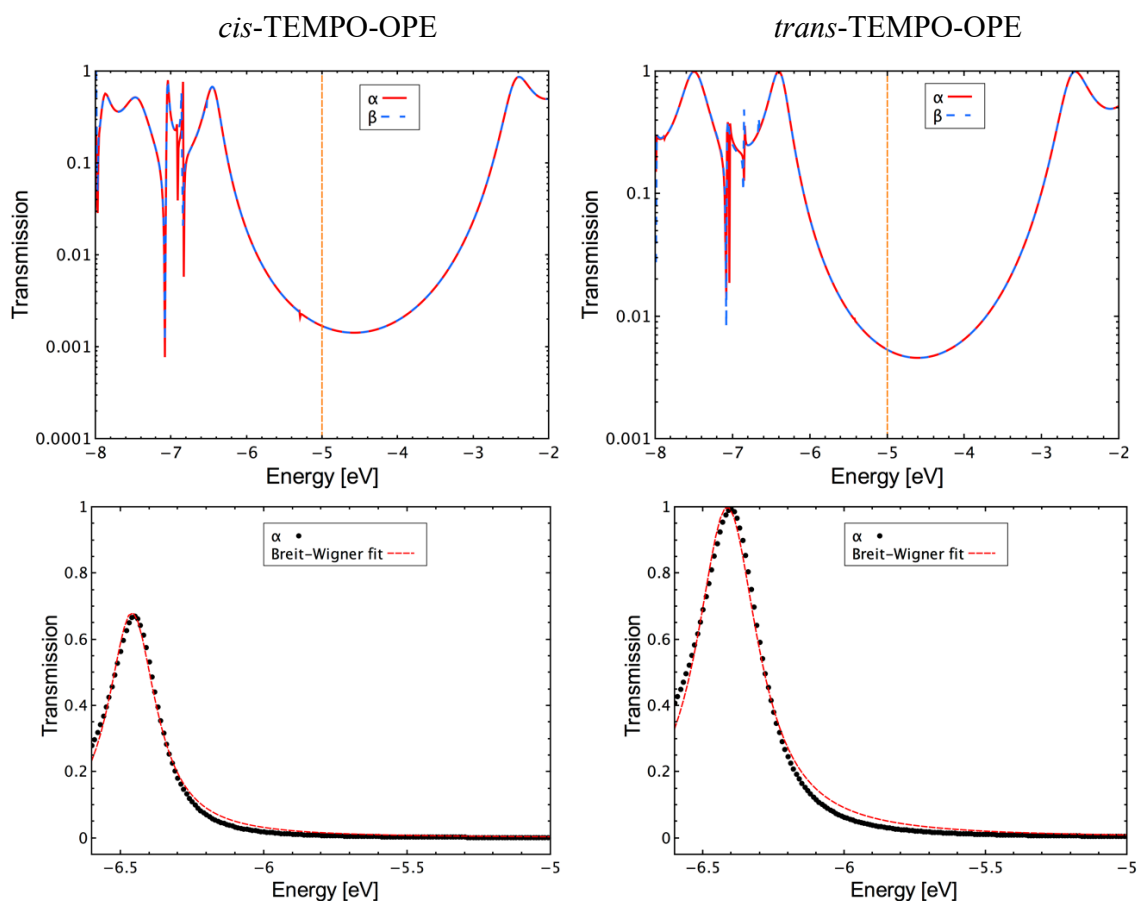


Figure 54: Transmission function and Breit–Wigner fit ( $T = \frac{4\Gamma_L\Gamma_R}{(E-E_0(V))^2+(\Gamma_L+\Gamma_R)^2}$ ) of the HOMO, assuming the transport to be dominated by the HOMO. The transmission function was calculated with GAUSSIAN 09, using 3,6,10-clusters as electrodes (B3LYP/LANL2DZ). The Breit–Wigner fit gives the following parameters; *cis*:  $\Gamma_L=22.0$  meV,  $\Gamma_R=79.1$  meV,  $E_0=-6.46$  meV,  $r^2=0.995$ , RMSE=0.0129, RSS=0.0265; *trans*:  $\Gamma_L=65.4$  meV,  $\Gamma_R=65.4$  meV,  $E_0=-6.41$  meV,  $r^2=0.994$ , RMSE=0.0232, RSS=0.0847. The fit therefore indicates an asymmetric coupling for the *cis*-isomer ( $\frac{\Gamma_L}{\Gamma_R} = 0.28$ ) and a symmetric coupling for the *trans*-isomer ( $\frac{\Gamma_L}{\Gamma_R} = 1.00$ ). (Adapted with permission from R. Hayakawa, M. A. Karimi, J. Wolf, T. Huhn, M. S. Zöllner, C. Herrmann, and E. Scheer, *Nano Lett.* 2016, 16, 8, 4960-4967. Copyright 2016 American Chemical Society.)

### Subsystem molecular orbitals for the *cis*- and *trans*-TEMPO-OPE molecules

Figure 55 and 56 show the molecular orbitals of the central subsystem within a gold–molecule–gold junction (*cis*- and *trans*-TEMPO-OPE molecule). 19-atomic gold cluster were used to mimic the electrodes. The molecular orbitals of the subsystem using a 19-atomic gold cluster (B3LYP/LANL2DZ) are in qualitative agreement with the ones calculated with a nine-atomic gold cluster (B3LYP/def2-SVP). The shape and energy of the  $\alpha$  and  $\beta$  orbitals corresponding to either the HOMO or the LUMO are nearly the same.

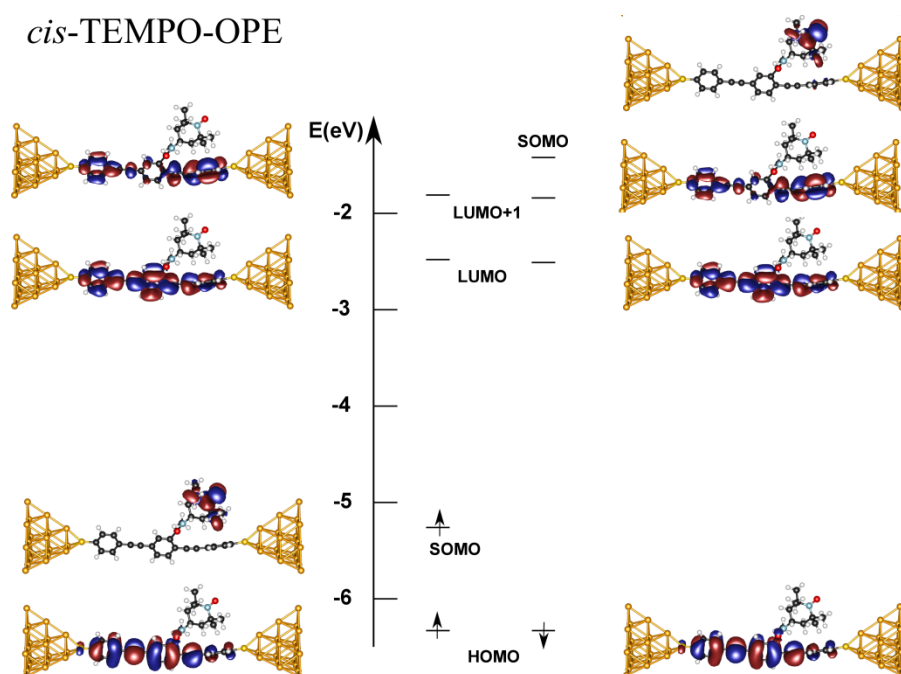


Figure 55: Subsystem molecular orbitals ( $\alpha$  part left,  $\beta$  part right) for the *cis*-TEMPO-OPE molecule within a junction. The gold electrodes were simulated with a 3,6,10-cluster. The orbitals are based on calculations with GAUSSIAN09 (B3LYP/LANL2DZ). (Adapted with permission from R. Hayakawa, M. A. Karimi, J. Wolf, T. Huhn, M. S. Zöllner, C. Herrmann, and E. Scheer, *Nano Lett.* 2016, 16, 8, 4960-4967. Copyright 2016 American Chemical Society.)

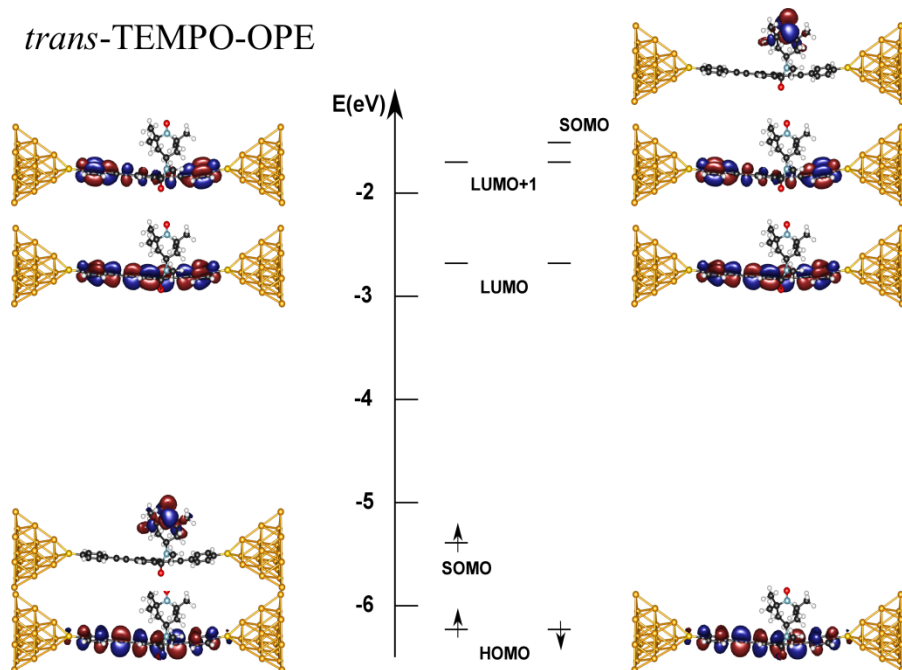


Figure 56: Subsystem molecular orbitals ( $\alpha$  part left,  $\beta$  part right) for the *trans*-TEMPO-OPE molecule within a junction. The gold electrodes were simulated with a 3,6,10-cluster. The orbitals are based on calculations with GAUSSIAN09 (B3LYP/LANL2DZ). (Adapted with permission from R. Hayakawa, M. A. Karimi, J. Wolf, T. Huhn, M. S. Zöllner, C. Herrmann, and E. Scheer, *Nano Lett.* 2016, 16, 8, 4960-4967. Copyright 2016 American Chemical Society.)

### Optimized structures of the TEMPO-OPE molecule on a Au(111) surface

Figure 57 shows the optimized structures of the TEMPO-OPE molecule on a gold surface, including several periodic images. Using a  $7 \times 7$  surface, the OPE backbone of the TEMPO-OPE molecule is lying on the surface. If a  $4 \times 4$  surface is used instead, a ring of the OPE backbone is located on top of the radical part of a neighboring TEMPO-OPE molecule (periodic image), preventing the OPE backbone to get into direct contact with the surface.

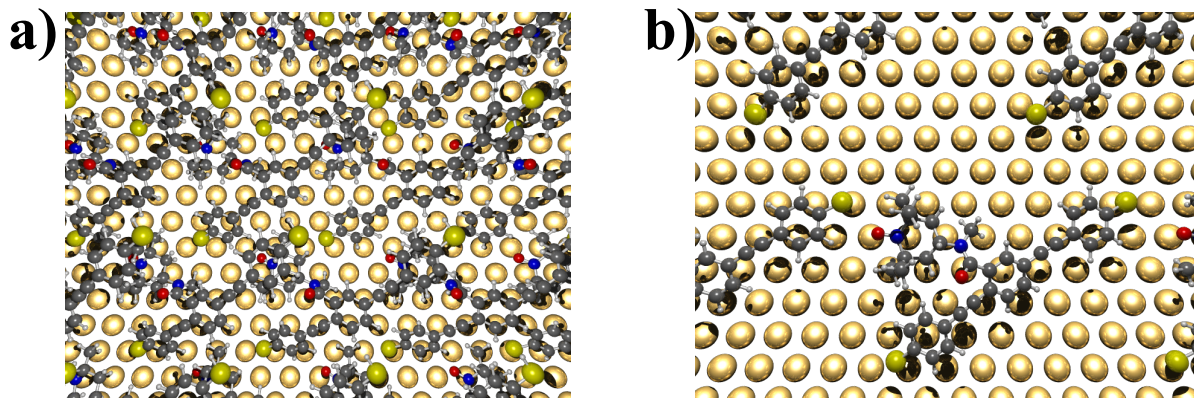


Figure 57: Optimized structures of the TEMPO-OPE molecule on a gold surface using periodic-boundary conditions, PBE, and a modified  $C_6$  parameter of gold for the DFT-D2 method. **a)**: Illustration a TEMPO-OPE molecule on gold using a  $4 \times 4$  surface cell. The interaction of the TEMPO-OPE molecule with its periodic images prevents the TEMPO-OPE to completely adsorb on the gold surface with the OPE backbone. **b)**: Illustration of the nearly isolated TEMPO-OPE molecule adsorbed on a gold surface using a  $7 \times 7$  surface cell. The molecule is lying on the surface and the OPE backbone is nearly planar and nearly parallel to the surface.

### Transmission function of the perfect helical and perfect linear cumulenes

Figure 58 shows the transmission functions calculated for the perfect linear and perfect helical cumulenes. The spin-flip transmissions for the helical cumulenes are much larger than the ones of the linear cumulenes. Nevertheless, the small size of the spin-flip transmissions compared to the spin-conserving transmissions indicate the spin-conserving transmissions to be most important for the spin polarization of the transmitted electrons.

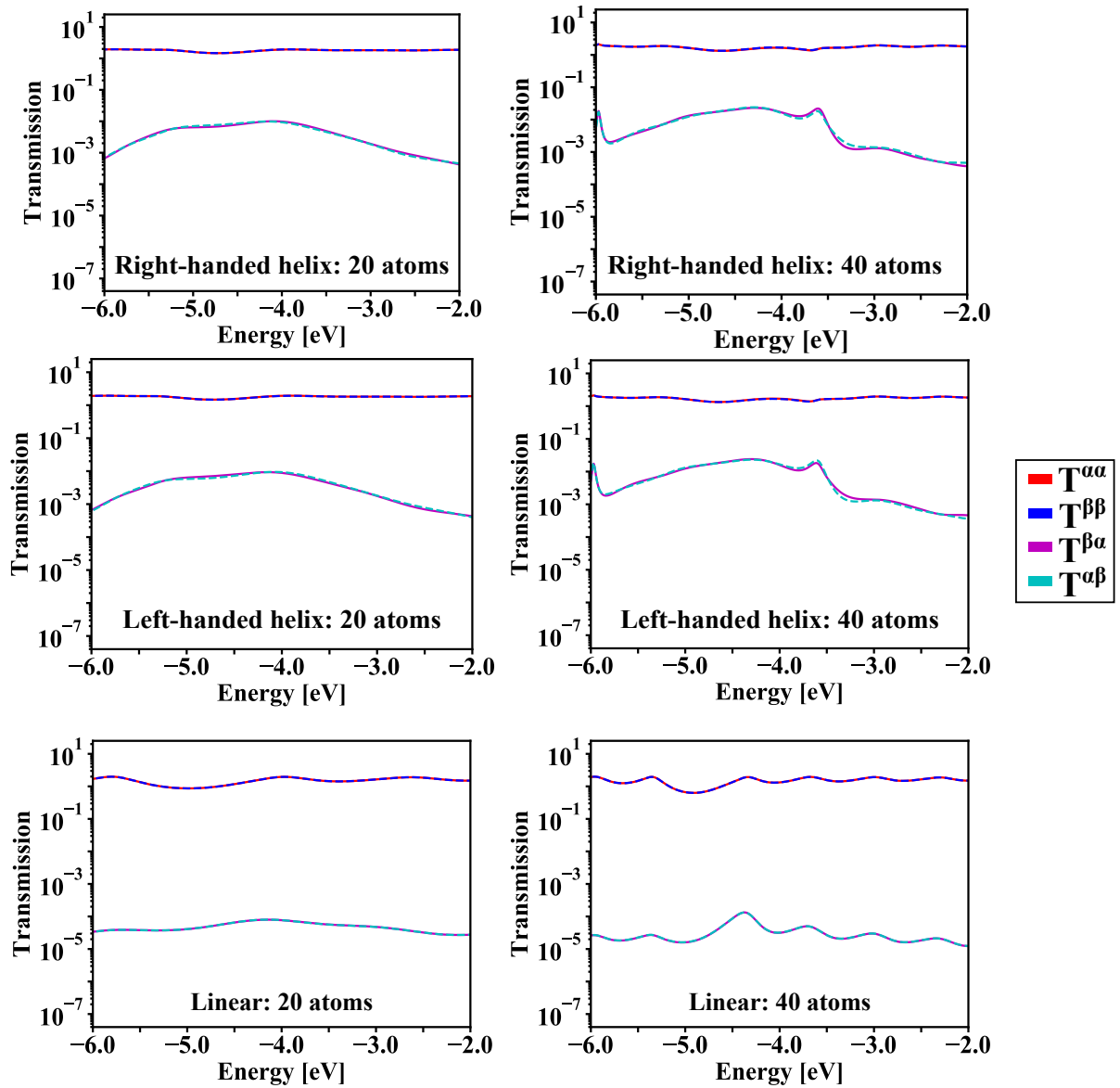


Figure 58: Transmission functions for the cumulenes consisting of 20 carbon atoms (left column) and 40 carbon atoms (right column). The transmission functions for the right-handed helices (upper row), left-handed helices (middle row), and the linear chains (bottom row) are shown.

## C. Additional Derivations

### Derivation of the symmetry of the Green's function

In Section 5.4.1 the symmetries of  $\mathbf{G}$ ,

$$\mathbf{G}^{\alpha\alpha} = (\mathbf{G}^{\beta\beta})^T, \quad (\text{C.1})$$

$$\mathbf{G}^{\alpha\beta} = -(\mathbf{G}^{\alpha\beta})^T, \quad (\text{C.2})$$

were used to derive the T-symmetry of  $\mathcal{T}$  for closed-shell central regions and non-magnetic electrodes. In the following the origin of this symmetry relation is given:

Due to T-symmetry and Hermiticity the spin blocks of  $\mathbf{H}_C$  are related as [198]

$$\mathbf{H}_C = \mathbf{H}_C^\dagger, \quad (\text{C.3})$$

$$\mathbf{H}_C^{\alpha\beta} = (\mathbf{H}_C^{\beta\alpha})^\dagger, \quad (\text{C.4})$$

$$\mathbf{H}_C^{\alpha\alpha} = (\mathbf{H}_C^{\beta\beta})^*, \quad (\text{C.5})$$

$$\mathbf{H}_C^{\alpha\beta} = -(\mathbf{H}_C^{\beta\alpha})^*. \quad (\text{C.6})$$

Using Equations (C.3) and (C.4), Equations (C.5) and (C.6) can be reformulated as

$$\mathbf{H}_C^{\alpha\alpha} = (\mathbf{H}_C^{\beta\beta})^* = ([\mathbf{H}_C^{\beta\beta}]^*)^\dagger = (\mathbf{H}_C^{\beta\beta})^T \quad (\text{C.7})$$

$$\mathbf{H}_C^{\alpha\beta} = -(\mathbf{H}_C^{\beta\alpha})^* = -([\mathbf{H}_C^{\alpha\beta}]^*)^\dagger = -(\mathbf{H}_C^{\alpha\beta})^T. \quad (\text{C.8})$$

Since  $\mathbf{G}$  is calculated as

$$\mathbf{G} = \frac{1}{E\mathbf{S} - \mathbf{H}_C - i\text{Im}[\boldsymbol{\Sigma}_L] - i\text{Im}[\boldsymbol{\Sigma}_R]}, \quad (\text{C.9})$$

the symmetry of the denominator determines the symmetry of  $\mathbf{G}$ . The symmetry of the denominator is determined by  $\boldsymbol{\Sigma}_{L/R}$  and  $\mathbf{H}_C$ . While the relation  $(\mathbf{H}_{\text{eff}}^{\alpha\alpha}) = [(\mathbf{H}_{\text{eff}}^{\beta\beta})]^T$  remains ( $\text{Im}(\boldsymbol{\Sigma}^{\alpha\alpha}) = \text{Im}(\boldsymbol{\Sigma}^{\beta\beta})$  for non-magnetic electrodes and closed-shell central region),

$$\begin{aligned} \mathbf{H}_C^{\alpha\alpha} - \boldsymbol{\Sigma}^{\alpha\alpha} &= \text{Re}(\mathbf{H}_C^{\alpha\alpha}) + i\text{Im}(\mathbf{H}_C^{\alpha\alpha}) - i\text{Im}(\boldsymbol{\Sigma}^{\alpha\alpha}) \\ &= \text{Re}(\mathbf{H}_C^{\beta\beta})^T + i\text{Im}(\mathbf{H}_C^{\beta\beta})^T - i\text{Im}(\boldsymbol{\Sigma}^{\beta\beta})^T = (\mathbf{H}_C^{\beta\beta} - \boldsymbol{\Sigma}^{\beta\beta})^T, \end{aligned} \quad (\text{C.10})$$

the relation  $(\mathbf{H}_{\text{eff}}^{\alpha\alpha}) = [(\mathbf{H}_{\text{eff}}^{\beta\beta})]^*$  does not,

$$\mathbf{H}_C^{\alpha\alpha} - \Sigma^{\alpha\alpha} = \text{Re}(\mathbf{H}_C^{\alpha\alpha}) + i\text{Im}(\mathbf{H}_C^{\alpha\alpha}) - i\text{Im}(\Sigma^{\alpha\alpha}) \quad (\text{C.11})$$

$$\neq \text{Re}(\mathbf{H}_C^{\beta\beta}) - i\text{Im}(\mathbf{H}_C^{\beta\beta}) + i\text{Im}(\Sigma^{\beta\beta}) = (\mathbf{H}_C^{\beta\beta} - \Sigma^{\beta\beta})^*. \quad (\text{C.12})$$

The relations for the spin-flip blocks remain because the self-energy only changes the spin-conserving blocks in the implemented approach.

To continue, a formulation for the inversion to calculate  $\mathbf{G}$  is needed. The inversion of a block matrix can be done as [200]

$$\begin{pmatrix} \mathbf{A} & \mathbf{B} \\ \mathbf{C} & \mathbf{D} \end{pmatrix}^{-1} = \begin{pmatrix} \mathbf{A}^{-1} + \mathbf{A}^{-1}\mathbf{B}(\mathbf{D} - \mathbf{C}\mathbf{A}^{-1}\mathbf{B})^{-1}\mathbf{C}\mathbf{A}^{-1} & -\mathbf{A}^{-1}\mathbf{B}(\mathbf{D} - \mathbf{C}\mathbf{A}^{-1}\mathbf{B})^{-1} \\ -(\mathbf{D} - \mathbf{C}\mathbf{A}^{-1}\mathbf{B})^{-1}\mathbf{C}\mathbf{A}^{-1} & (\mathbf{D} - \mathbf{C}\mathbf{A}^{-1}\mathbf{B})^{-1} \end{pmatrix} \quad (\text{C.13})$$

and [200]

$$\begin{pmatrix} \mathbf{A} & \mathbf{B} \\ \mathbf{C} & \mathbf{D} \end{pmatrix}^{-1} = \begin{pmatrix} (\mathbf{A} - \mathbf{B}\mathbf{D}^{-1}\mathbf{C})^{-1} & -(\mathbf{A} - \mathbf{B}\mathbf{D}^{-1}\mathbf{C})^{-1}\mathbf{B}\mathbf{D}^{-1} \\ -\mathbf{D}^{-1}\mathbf{C}(\mathbf{A} - \mathbf{B}\mathbf{D}^{-1}\mathbf{C})^{-1} & \mathbf{D}^{-1} + \mathbf{D}^{-1}\mathbf{C}(\mathbf{A} - \mathbf{B}\mathbf{D}^{-1}\mathbf{C})^{-1}\mathbf{B}\mathbf{D}^{-1} \end{pmatrix} \quad (\text{C.14})$$

In the following, the relations  $\mathbf{A} = \mathbf{D}^T$ ,  $\mathbf{B} = -\mathbf{B}^T$ , and  $\mathbf{C} = -\mathbf{C}^T$ <sup>48</sup> are used to derive the symmetry of the spin-dependent blocks of  $\mathbf{G}$ .

The relation between the spin-conserving blocks can be shown by looking at  $\mathbf{A}$  and  $\mathbf{D}$  block of the inverse. They can be calculated by combining Equation (C.13) and Equation (C.14) as

$$\begin{pmatrix} \mathbf{I}_A & \mathbf{I}_B \\ \mathbf{I}_C & \mathbf{I}_D \end{pmatrix} = \begin{pmatrix} \mathbf{A} & \mathbf{B} \\ \mathbf{C} & \mathbf{D} \end{pmatrix}^{-1} = \begin{pmatrix} (\mathbf{A} - \mathbf{B}\mathbf{D}^{-1}\mathbf{C})^{-1} & -(\mathbf{A} - \mathbf{B}\mathbf{D}^{-1}\mathbf{C})^{-1}\mathbf{B}\mathbf{D}^{-1} \\ -\mathbf{D}^{-1}\mathbf{C}(\mathbf{A} - \mathbf{B}\mathbf{D}^{-1}\mathbf{C})^{-1} & (\mathbf{D} - \mathbf{C}\mathbf{A}^{-1}\mathbf{B})^{-1} \end{pmatrix}. \quad (\text{C.15})$$

---

<sup>48</sup>  $\mathbf{A} = \mathbf{H}_{\text{eff}}^{\alpha\alpha}$ ,  $\mathbf{B} = \mathbf{H}_{\text{eff}}^{\alpha\beta}$ ,  $\mathbf{C} = \mathbf{H}_{\text{eff}}^{\beta\alpha}$ ,  $\mathbf{D} = \mathbf{H}_{\text{eff}}^{\beta\beta}$ .

Taking the transpose of  $\mathbf{D}$  of the inverse matrix leads to

$$\begin{pmatrix} \mathbf{I}_A & \mathbf{I}_B \\ \mathbf{I}_C & \mathbf{I}_D^T \end{pmatrix} = \begin{pmatrix} (\mathbf{A} - \mathbf{B}\mathbf{D}^{-1}\mathbf{C})^{-1} & -(\mathbf{A} - \mathbf{B}\mathbf{D}^{-1}\mathbf{C})^{-1}\mathbf{B}\mathbf{D}^{-1} \\ -\mathbf{D}^{-1}\mathbf{C}(\mathbf{A} - \mathbf{B}\mathbf{D}^{-1}\mathbf{C})^{-1} & ((\mathbf{D} - \mathbf{C}\mathbf{A}^{-1}\mathbf{B})^{-1})^T \end{pmatrix}, \quad (\text{C.16})$$

which can also be written as

$$\begin{pmatrix} \mathbf{I}_A & \mathbf{I}_B \\ \mathbf{I}_C & \mathbf{I}_D^T \end{pmatrix} = \begin{pmatrix} (\mathbf{A} - \mathbf{B}\mathbf{D}^{-1}\mathbf{C})^{-1} & -(\mathbf{A} - \mathbf{B}\mathbf{D}^{-1}\mathbf{C})^{-1}\mathbf{B}\mathbf{D}^{-1} \\ -\mathbf{D}^{-1}\mathbf{C}(\mathbf{A} - \mathbf{B}\mathbf{D}^{-1}\mathbf{C})^{-1} & (\mathbf{D}^T - \mathbf{B}^T(\mathbf{A}^{-1})^T\mathbf{C}^T)^{-1} \end{pmatrix}. \quad (\text{C.17})$$

Making use of the relations  $\mathbf{D}^T = \mathbf{A}$ ,  $\mathbf{A}^{-1} = (\mathbf{D}^{-1})^T$ ,  $\mathbf{B} = -\mathbf{B}^T$  and  $\mathbf{C} = -\mathbf{C}^T$  leads to<sup>49</sup>,

$$\begin{pmatrix} \mathbf{I}_A & \mathbf{I}_B \\ \mathbf{I}_C & \mathbf{I}_D^T \end{pmatrix} = \begin{pmatrix} (\mathbf{A} - \mathbf{B}\mathbf{D}^{-1}\mathbf{C})^{-1} & -(\mathbf{A} - \mathbf{B}\mathbf{D}^{-1}\mathbf{C})^{-1}\mathbf{B}\mathbf{D}^{-1} \\ -\mathbf{D}^{-1}\mathbf{C}(\mathbf{A} - \mathbf{B}\mathbf{D}^{-1}\mathbf{C})^{-1} & (\mathbf{A} - \mathbf{B}\mathbf{D}^{-1}\mathbf{C})^{-1} \end{pmatrix} \quad (\text{C.18})$$

and consequently  $\mathbf{G}^{\alpha\alpha}$  is the transposed of  $\mathbf{G}^{\beta\beta}$  and vice versa.

The symmetry relations between the spin-flip blocks can be shown by looking at the transpose of  $\mathbf{B}$ ,

$$\begin{pmatrix} \mathbf{I}_A & \mathbf{I}_B^T \\ \mathbf{I}_C & \mathbf{I}_D \end{pmatrix} = \begin{pmatrix} (\mathbf{A} - \mathbf{B}\mathbf{D}^{-1}\mathbf{C})^{-1} & -(\mathbf{A} - \mathbf{B}\mathbf{D}^{-1}\mathbf{C})^{-1}\mathbf{B}\mathbf{D}^{-1})^T \\ -\mathbf{D}^{-1}\mathbf{C}(\mathbf{A} - \mathbf{B}\mathbf{D}^{-1}\mathbf{C})^{-1} & (\mathbf{D} - \mathbf{C}\mathbf{A}^{-1}\mathbf{B})^{-1} \end{pmatrix}, \quad (\text{C.19})$$

which can be written as

$$\begin{pmatrix} \mathbf{I}_A & \mathbf{I}_B^T \\ \mathbf{I}_C & \mathbf{I}_D \end{pmatrix} = \begin{pmatrix} (\mathbf{A} - \mathbf{B}\mathbf{D}^{-1}\mathbf{C})^{-1} & -(\mathbf{D}^{-1})^T\mathbf{B}^T(\mathbf{A}^T - \mathbf{C}^T(\mathbf{D}^{-1})^T\mathbf{B}^T)^{-1} \\ -\mathbf{D}^{-1}\mathbf{C}(\mathbf{A} - \mathbf{B}\mathbf{D}^{-1}\mathbf{C})^{-1} & (\mathbf{D} - \mathbf{C}\mathbf{A}^{-1}\mathbf{B})^{-1} \end{pmatrix}. \quad (\text{C.20})$$

Making use of the symmetries  $\mathbf{A}^T = \mathbf{D}$ ,  $(\mathbf{D}^{-1})^T = \mathbf{A}^{-1}$ ,  $\mathbf{B} = -\mathbf{B}^T$  and  $\mathbf{C} = -\mathbf{C}^T$  one arrives at

$$\begin{pmatrix} \mathbf{I}_A & \mathbf{I}_B^T \\ \mathbf{I}_C & \mathbf{I}_D \end{pmatrix} = \begin{pmatrix} (\mathbf{A} - \mathbf{B}\mathbf{D}^{-1}\mathbf{C})^{-1} & \mathbf{A}^{-1}\mathbf{B}(\mathbf{D} - \mathbf{C}\mathbf{A}^{-1}\mathbf{B})^{-1} \\ -\mathbf{D}^{-1}\mathbf{C}(\mathbf{A} - \mathbf{B}\mathbf{D}^{-1}\mathbf{C})^{-1} & (\mathbf{D} - \mathbf{C}\mathbf{A}^{-1}\mathbf{B})^{-1} \end{pmatrix}. \quad (\text{C.21})$$

---

<sup>49</sup> Since  $\mathbf{A} = \mathbf{D}^T$ ,  $\mathbf{A}^{-1}\mathbf{A} = \mathbf{1}$  can be rewritten as  $\mathbf{A}^{-1}\mathbf{D}^T = \mathbf{1}$  and consequently  $\mathbf{A}^{-1} = (\mathbf{D}^T)^{-1}$ .

Comparing this with the formulation of  $\mathbf{B}$  of the inverse in Equation C.13 shows that the relations  $\mathbf{G}^{\alpha\beta} = -(\mathbf{G}^{\alpha\beta})^T$  and  $\mathbf{G}^{\beta\alpha} = -(\mathbf{G}^{\beta\alpha})^T$  are valid.

Consequently the symmetry of  $\mathbf{G}$  can be written as

$$\begin{pmatrix} \mathbf{G}^{\alpha\alpha} & \mathbf{G}^{\alpha\beta} \\ \mathbf{G}^{\beta\alpha} & \mathbf{G}^{\beta\beta} \end{pmatrix} = \begin{pmatrix} (\mathbf{G}^{\beta\beta})^T & -(\mathbf{G}^{\alpha\beta})^T \\ -(\mathbf{G}^{\beta\alpha})^T & (\mathbf{G}^{\alpha\alpha})^T \end{pmatrix}. \quad (\text{C.22})$$

### Derivation of the Remaining P-Symmetry for Symmetric or Hermitian Green's Functions

To show that a symmetric  $\mathbf{G}$  results in P-Symmetry of  $\mathcal{T}$  to be retained, one has to take the transpose of the matrix of which the trace is taken to calculate  $\mathcal{T}$ ,

$$\mathcal{T}_{RL}^{\alpha\alpha} = \text{Tr} \left[ \mathbf{\Gamma}_L^{\alpha\alpha} \mathbf{G}^{\alpha\alpha} \mathbf{\Gamma}_R^{\alpha\alpha} (\mathbf{G}^{\alpha\alpha})^\dagger \right] = \text{Tr} \left[ [(\mathbf{G}^{\alpha\alpha})^\dagger]^T (\mathbf{\Gamma}_R^{\alpha\alpha})^T (\mathbf{G}^{\alpha\alpha})^T (\mathbf{\Gamma}_L^{\alpha\alpha})^T \right], \quad (\text{C.23})$$

$$\mathcal{T}_{RL}^{\alpha\beta} = \text{Tr} \left[ \mathbf{\Gamma}_L^{\beta\beta} \mathbf{G}^{\beta\alpha} \mathbf{\Gamma}_R^{\alpha\alpha} (\mathbf{G}^{\beta\alpha})^\dagger \right] = \text{Tr} \left[ [(\mathbf{G}^{\beta\alpha})^\dagger]^T (\mathbf{\Gamma}_R^{\alpha\alpha})^T (\mathbf{G}^{\beta\alpha})^T (\mathbf{\Gamma}_L^{\beta\beta})^T \right]. \quad (\text{C.24})$$

$\mathbf{\Gamma}_L$  and  $\mathbf{\Gamma}_R$  are always symmetric in the used approach. If now  $\mathbf{G}$  is symmetric as well, Equation (C.23) and Equation (C.24) can be rewritten as

$$\mathcal{T}_{RL}^{\alpha\alpha} = \text{Tr} \left[ (\mathbf{G}^{\alpha\alpha})^\dagger \mathbf{\Gamma}_R^{\alpha\alpha} \mathbf{G}^{\alpha\alpha} \mathbf{\Gamma}_L^{\alpha\alpha} \right] = \text{Tr} \left[ \mathbf{\Gamma}_R^{\alpha\alpha} \mathbf{G}^{\alpha\alpha} \mathbf{\Gamma}_L^{\alpha\alpha} (\mathbf{G}^{\alpha\alpha})^\dagger \right] = \mathcal{T}_{LR}^{\alpha\alpha}, \quad (\text{C.25})$$

$$\mathcal{T}_{RL}^{\alpha\beta} = \text{Tr} \left[ (\mathbf{G}^{\alpha\beta})^\dagger \mathbf{\Gamma}_R^{\alpha\alpha} \mathbf{G}^{\alpha\beta} \mathbf{\Gamma}_L^{\beta\beta} \right] = \text{Tr} \left[ \mathbf{\Gamma}_R^{\alpha\alpha} \mathbf{G}^{\alpha\beta} \mathbf{\Gamma}_L^{\beta\beta} (\mathbf{G}^{\alpha\beta})^\dagger \right] = \mathcal{T}_{LR}^{\beta\alpha}. \quad (\text{C.26})$$

If  $\mathbf{G}$  is Hermitian, Equation (C.23) and Equation (C.24) can simply be rewritten as

$$\mathcal{T}_{RL}^{\alpha\alpha} = \text{Tr} \left[ \mathbf{\Gamma}_L^{\alpha\alpha} \mathbf{G}^{\alpha\alpha} \mathbf{\Gamma}_R^{\alpha\alpha} (\mathbf{G}^{\alpha\alpha})^\dagger \right] = \text{Tr} \left[ \mathbf{\Gamma}_L^{\alpha\alpha} (\mathbf{G}^{\alpha\alpha})^\dagger \mathbf{\Gamma}_R^{\alpha\alpha} \mathbf{G}^{\alpha\alpha} \right] = \mathcal{T}_{LR}^{\alpha\alpha}, \quad (\text{C.27})$$

$$\mathcal{T}_{RL}^{\alpha\beta} = \text{Tr} \left[ \mathbf{\Gamma}_L^{\beta\beta} \mathbf{G}^{\beta\alpha} \mathbf{\Gamma}_R^{\alpha\alpha} (\mathbf{G}^{\beta\alpha})^\dagger \right] = \text{Tr} \left[ \mathbf{\Gamma}_L^{\beta\beta} (\mathbf{G}^{\alpha\beta})^\dagger \mathbf{\Gamma}_R^{\alpha\alpha} \mathbf{G}^{\alpha\beta} \right] = \mathcal{T}_{LR}^{\beta\alpha}. \quad (\text{C.28})$$

Thus, both a symmetric  $\mathbf{G}$  and a Hermitian  $\mathbf{G}$  results in P-Symmetry of  $\mathcal{T}$ .

## D. List of Publications

### D.1. Published

1. Ryoma Hayakawa, Mohammad Amin Karimi, Jannic Wolf, Thomas Huhn, Martin Sebastian Zöllner, Carmen Herrmann, and Elke Scheer, *Large Magnetoresistance in Single-Radical Molecular Junctions*, *Nano Lett.* **2016**, 16, 4960. (Based on parts of Section 3.3 and parts of Appendix B, <http://pubs.acs.org/articlesonrequest/AOR-ihMEKniDzvXGMfnw7GQ8>)
2. Mohammad Mehdi Ramin Moayed, Thomas Bielewicz, Martin Sebastian Zöllner, Carmen Herrmann, and Christian Klinke, *Towards colloidal spintronics through Rashba spin-orbit interaction in lead sulphide nanosheets*, *Nat. Commun.* **2017**, 8, 15721. (Based on parts of Section 4.3, DOI: <https://doi.org/10.1038/ncomms15721>)

### D.2. In Preparation

3. Zöllner, Martin Sebastian; Varela, Solmar; Medina, Ernesto; Mujica, Vladimiro; Herrmann, Carmen (2019): Chiral-Induced Spin Selectivity: A Symmetry Analysis of Electronic Transmission. ChemRxiv. Preprint. (Based on parts of Section 5.4 and parts of Section 5.5 , <https://doi.org/10.26434/chemrxiv.8325248.v2>)

## **E. List of Chemicals**

No hazardous chemicals according to the Globally Harmonized System of Classification and Labelling of Chemicals (GHS) have been used for the preparation of this thesis.

## References

- [1] V. Marx, *Nature* **2013**, 498, 255.
- [2] M. M. Waldrop, *Nature* **2016**, 530, 144.
- [3] *Nat. Electron.* **2018**, 1, 205.
- [4] R. Naaman, Y. Paltiel, D. H. Waldeck, *Nat. Rev. Chem.* **2019**, 3, 250.
- [5] V. K. Joshi, *Eng. Sci. Technol. Int. J.* **2016**, 19, 1503.
- [6] H. Gu, X. Zhang, H. Wei, Y. Huang, S. Wei, Z. Guo, *Chem. Soc. Rev.* **2013**, 42, 5907.
- [7] M. N. Baibich, J. M. Broto, A. Fert, F. N. Van Dau, F. Petroff, P. Etienne, G. Creuzet, A. Friederich, J. Chazelas, *Phys. Rev. Lett.* **1988**, 61, 2472.
- [8] G. Binasch, P. Grünberg, F. Saurenbach, W. Zinn, *Phys. Rev. B* **1989**, 39, 4828.
- [9] M. Jullière, *Phys. Lett. A* **1975**, 54, 225.
- [10] T. Miyazaki, N. Tezuka, *J. Magn. Magn. Mater.* **1995**, 139, L231.
- [11] J. S. Moodera, L. R. Kinder, T. M. Wong, R. Meservey, *Phys. Rev. Lett.* **1995**, 74, 3273.
- [12] C. Chappert, A. Fert, F. N. Van Dau, *Nat. Mater.* **2007**, 6, 813.
- [13] *Nat. Nanotechnol.* **2015**, 10, 185.
- [14] S. Bandyopadhyay, M. Cahay, *Nanotechnology* **2009**, 20, 412001.
- [15] A. A. Khajetoorians, J. Wiebe, B. Chilian, R. Wiesendanger, *Science* **2011**, 332, 1062.
- [16] R. Hayakawa, M. A. Karimi, J. Wolf, T. Huhn, M. S. Zöllner, C. Herrmann, E. Scheer, *Nano Lett.* **2016**, 16, 4960.

- [17] M. M. R. Moayed, T. Bielewicz, M. S. Zöllner, C. Herrmann, C. Klinke, *Nat. Commun.* **2017**, *8*, 15721.
- [18] S. Sanvito, *arXiv:cond-mat/0503445* **2005**.
- [19] M. D. Segall, P. J. D. Lindan, M. J. Probert, C. J. Pickard, P. J. Hasnip, S. J. Clark, M. C. Payne, *J. Phys.: Condens. Matter* **2002**, *14*, 2717.
- [20] A. Szabo, N. S. Ostlund, *Modern Quantum Chemistry: Introduction to Advanced Electronic Structure Theory*; Dover Publications Inc.: New York, 1996.
- [21] K. G. Dyall, K. Faegri Jr., *Introduction to Relativistic Quantum Chemistry*; Oxford University Press: New York, 2007.
- [22] M. Reiher, A. Wolf, *Relativistic Quantum Chemistry: The Fundamental Theory of Molecular Science*; Wiley-VCH: Weinheim, 2014.
- [23] J. Reinhold, *Quantentheorie der Moleküle*; Springer: Wiesbaden, 2012.
- [24] M. D. Ventra, *Electrical Transport in Nanoscale Systems*; Cambridge University Press: New York, 2009.
- [25] U. von Barth, *Phys. Scr.* **2004**, *T109*, 9.
- [26] P. Pyykkö, *Annu. Rev. Phys. Chem.* **2012**, *63*, 45.
- [27] T. Nakajima, K. Hirao, *Chem. Rev.* **2012**, *112*, 385.
- [28] A. Petrone, D. B. Williams-Young, S. Sun, T. F. Stetina, X. Li, *Eur. Phys. J. B* **2018**, *91*, 169.
- [29] D. Peng, M. Reiher, *Theor. Chem. Acc.* **2012**, *131*, 1081.
- [30] E. van Lenthe, E. J. Baerends, J. G. Snijders, *J. Chem. Phys.* **1993**, *99*, 4597.
- [31] C. van Wüllen, *J. Chem. Phys.* **1998**, *109*, 392.
- [32] E. van Lenthe, E. J. Baerends, J. G. Snijders, *J. Chem. Phys.* **1994**, *101*, 9783.

- [33] E. van Lenthe, J. G. Snijders, E. J. Baerends, *J. Chem. Phys.* **1996**, *105*, 6505.
- [34] F. Neese, *J. Chem. Phys.* **2005**, *122*, 034107.
- [35] C. van Wüllen, *Z. Phys. Chem.* **2010**, *224*, 413.
- [36] M. K. Armbruster, F. Weigend, C. van Wüllen, W. Klopper, *Phys. Chem. Chem. Phys.* **2008**, *10*, 1748.
- [37] A. M. Steane, *arXiv:1312.3824* **2013**.
- [38] F. E. Mabbs, D. J. Machin, *Magnetism and Transition Metal Complexes*; Dover Publications Inc: New York, 2008.
- [39] A. N. Rudenko, V. V. Mazurenko, V. I. Anisimov, A. I. Lichtenstein, *Phys. Rev. B* **2009**, *79*, 144418.
- [40] T. Helgaker, J. Olsen, P. Jorgensen, *Molecular Electronic-Structure Theory*; Wiley-Blackwell: West Sussex, 2013.
- [41] R. Landauer, *IBM J. Res. Dev.* **1957**, *1*, 223.
- [42] M. Büttiker, Y. Imry, R. Landauer, S. Pinhas, *Phys. Rev. B* **1985**, *31*, 6207.
- [43] V. Mujica, M. Kemp, M. A. Ratner, *J. Chem. Phys.* **1994**, *101*, 6849.
- [44] M. A. Reed, *Mater. Today* **2008**, *11*, 46.
- [45] J. Camarero, E. Coronado, *J. Mater. Chem.* **2009**, *19*, 1678.
- [46] M. Mas-Torrent, N. Crivillers, V. Mugnaini, I. Ratera, C. Rovira, J. Veciana, *J. Mater. Chem.* **2009**, *19*, 1691.
- [47] C. Boehme, *Nat. Phys.* **2017**, *13*, 928.
- [48] I. Ratera, J. Veciana, *Chem. Soc. Rev.* **2012**, *41*, 303.
- [49] A. R. Rocha, V. M. García-Suárez, S. W. Bailey, C. J. Lambert, J. Ferrer, S. Sanvito, *Nat. Mater.* **2005**, *4*, 335.

- [50] M. Gobbi, E. Orgiu, *J. Mater. Chem. C* **2017**, *5*, 5572.
- [51] T. Sugawara, M. Minamoto, M. M. Matsushita, P. Nickels, S. Komiyama, *Phys. Rev. B* **2008**, *77*, 235316.
- [52] H. Komatsu, M. M. Matsushita, S. Yamamura, Y. Sugawara, K. Suzuki, T. Sugawara, *J. Am. Chem. Soc.* **2010**, *132*, 4528.
- [53] T. Sugawara, M. M. Matsushita, *J. Mater. Chem.* **2009**, *19*, 1738.
- [54] M. Matsushita, H. Kawakami, T. Sugawara, M. Ogata, *Phys. Rev. B* **2008**, *77*, 195208.
- [55] C. Herrmann, G. C. Solomon, M. A. Ratner, *J. Am. Chem. Soc.* **2010**, *132*, 3682.
- [56] C. Herrmann, G. C. Solomon, M. A. Ratner, *J. Chem. Phys.* **2011**, *134*, 224306.
- [57] K. Tagami, M. Tsukada, *J. Phys. Chem. B* **2004**, *108*, 6441.
- [58] J. Lee, E. Lee, S. Kim, G. S. Bang, D. A. Shultz, R. D. Schmidt, M. D. Forbes, H. Lee, *Angew. Chem. Int. Ed. Engl.* **2011**, *50*, 4414.
- [59] Y. Yonekuta, K. Susuki, K. Oyaizu, K. Honda, H. Nishide, *J. Am. Chem. Soc.* **2007**, *129*, 14128.
- [60] K. Oyaizu, H. Nishide, *Adv. Mater.* **2009**, *21*, 2339.
- [61] C. Herrmann, G. C. Solomon, J. E. Subotnik, V. Mujica, M. A. Ratner, *J. Chem. Phys.* **2010**, *132*, 024103.
- [62] D. Nozaki, S. M. Avdoshenko, H. Sevinçli, R. Gutierrez, G. Cuniberti, *J. Phys. Conf. Ser.* **2013**, *427*, 012013.
- [63] D. Nozaki, S. M. Avdoshenko, H. Sevinçli, G. Cuniberti, *J. Appl. Phys.* **2014**, *116*, 074308.
- [64] T. Shiozaki, *Wiley Interdiscip. Rev.: Comput. Mol. Sci.* **2018**, *8*, e1331.

- [65] T. S. for more information), “BAGEL, Brilliantly Advanced General Electronic-structure Library. <http://www.nubakery.org> under the GNU General Public License”.
- [66] E. I. Tellgren, A. Soncini, T. Helgaker, K. K. Lange, A. M. Teale, U. E. Ekström, S. Stopkowicz, J. H. Austad, “LONDON: A quantum-chemistry program for plane-wave/GTO hybrid basis sets and finite magnetic field calculations (see [londonprogram.org](http://londonprogram.org) for more information)”.
- [67] M. A. Reed, C. Zhou, C. Muller, T. Burgin, J. Tour, *Science* **1997**, *278*, 252.
- [68] A. Bilić, J. R. Reimers, N. S. Hush, *J. Chem. Phys.* **2005**, *122*, 094708.
- [69] J. Proppe, C. Herrmann, *J. Comput. Chem.* **2015**, *36*, 201.
- [70] R.-W. Yan, X. Jin, S.-Y. Guan, X.-G. Zhang, R. Pang, Z.-Q. Tian, D.-Y. Wu, B.-W. Mao, *J. Phys. Chem. C* **2016**, *120*, 11820.
- [71] V. Kaliginedi, P. Moreno-García, H. Valkenier, W. Hong, V. M. García-Suárez, P. Buitter, J. L. H. Otten, J. C. Hummelen, C. J. Lambert, T. Wandlowski, *J. Am. Chem. Soc.* **2012**, *134*, 5262.
- [72] Z. Wei, T. Li, K. Jennum, M. Santella, N. Bovet, W. Hu, M. B. Nielsen, T. Bjørnholm, G. C. Solomon, B. W. Laursen, K. Nørgaard, *Langmuir* **2012**, *28*, 4016.
- [73] K. Tonigold, A. Groß, *J. Chem. Phys.* **2010**, *132*, 224701.
- [74] Y.-h. Zhang, S. Kahle, T. Herden, C. Stroh, M. Mayor, U. Schlickum, M. Ternes, P. Wahl, K. Kern, *Nat. Commun.* **2013**, *4*, 2110.
- [75] A. Manchon, H. C. Koo, J. Nitta, S. M. Frolov, R. A. Duine, *Nat. Mater.* **2015**, *14*, 871.
- [76] H. Nakayama, Y. Kanno, H. An, T. Tashiro, S. Haku, A. Nomura, K. Ando, *Phys. Rev. Lett.* **2016**, *117*, 116602.

- [77] W. Han, Y. Otani, S. Maekawa, *NPJ Quantum Mater.* **2018**, *3*, 27.
- [78] Y. A. Bychkov, E. I. Rasbha, *Pis'ma Zh. Eksp. Teor. Fiz.* **1984**, *39*, 66.
- [79] R. Winkler, *Spin-orbit Coupling Effects in Two-Dimensional Electron and Hole Systems*; Springer: New York, 2003.
- [80] N. Pournaghavi, M. Esmailzadeh, A. Abrishamifar, S. Ahmadi, *J. Phys.: Condens. Matter* **2017**, *29*, 145501.
- [81] H. C. Koo, J. H. Kwon, J. Eom, J. Chang, S. H. Han, M. Johnson, *Science* **2009**, *325*, 1515.
- [82] H. Nakayama, T. Yamamoto, H. An, K. Tsuda, Y. Einaga, K. Ando, *Sci. Adv.* **2018**, *4*, 3899.
- [83] J. C. R. Sánchez, L. Vila, G. Desfonds, S. Gambarelli, J. P. Attané, J. M. D. Teresa, C. Magén, A. Fert, *Nat. Commun.* **2013**, *4*, 2944.
- [84] R. Friedrich, V. Caciuc, G. Bihlmayer, N. Atodiresei, S. Blügel, *New J. Phys.* **2017**, *19*, 043017.
- [85] J. Li, P. M. Haney, *Appl. Phys. Lett.* **2016**, *109*, 193903.
- [86] S. D. Ganichev, W. Prettl, *J. Phys.: Condens. Matter* **2003**, *15*, R935.
- [87] C. Yin, H. Yuan, X. Wang, S. Liu, S. Zhang, N. Tang, F. Xu, Z. Chen, H. Shimotani, Y. Iwasa, Y. Chen, W. Ge, B. Shen, W. Ge, B. Shen, *Nano Lett.* **2013**, *13*, 2024.
- [88] M. I. D. (ed), *Spin Physics in Semiconductors*; Springer: 2017.
- [89] Q. Zhang, X. Q. Wang, C. M. Yin, F. J. Xu, N. Tang, B. Shen, Y. H. Chen, K. Chang, W. K. Ge, Y. Ishitani, A. Yoshikawa, *Appl. Phys. Lett.* **2010**, *97*, 041907.
- [90] A. Bansil, H. Lin, T. Das, *Rev. Mod. Phys.* **2016**, *88*, 021004.

- [91] H. Yu, Y. Wu, G.-B. Liu, X. Xu, W. Yao, *Phys. Rev. Lett.* **2014**, *113*, 156603.
- [92] D. Xiao, G.-B. Liu, W. Feng, X. Xu, W. Yao, *Phys. Rev. Lett.* **2012**, *108*, 196802.
- [93] M. Eginligil, B. Cao, Z. Wang, X. Shen, C. Cong, J. Shang, C. Soci, T. Yu, *Nat. Commun.* **2015**, *6*, 7636.
- [94] H. Yuan, X. Wang, B. Lian, H. Zhang, X. Fang, B. Shen, G. Xu, Y. Xu, S.-C. Zhang, H. Y. Hwang, Y. Cui, *Nat. Nanotechnol.* **2014**, *9*, 851.
- [95] P. W. Atkins, R. S. Friedman, *Molecular Quantum Mechanics*; Oxford University Press: New York, 2010.
- [96] M. Frazier, J. G. Cates, J. A. Waugh, J. J. Heremans, M. B. Santos, X. Liu, G. A. Khodaparast, *J. Appl. Phys.* **2009**, *106*, 103513.
- [97] J. Yu, S. Cheng, Y. Lai, Q. Zheng, L. Zhu, Y. Chen, J. Ren, *Opt. Express* **2015**, *23*, 27250.
- [98] Y. Q. Huang, Y. X. Song, S. M. Wang, I. A. Buyanova, W. M. Chen, *Nat. Commun.* **2017**, *8*, 15401.
- [99] C. Kastl, C. Karnetzky, H. Karl, A. W. Holleitner, *Nat. Commun.* **2015**, *6*, 6617.
- [100] J. McIver, D. Hsieh, H. Steinberg, P. Jarillo-Herrero, N. Gedik, *Nat. Nanotechnol.* **2012**, *7*, 96.
- [101] L. Liu, E. J. Lenferink, G. Wei, T. K. Stanev, N. Speiser, N. P. Stern, *ACS Appl. Mater. Interfaces* **2019**, *11*, 3334.
- [102] C. Tusche, A. Krasnyuk, J. Kirschner, *Ultramicroscopy* **2015**, *159*, 520.
- [103] L. Leppert, S. E. Reyes-Lillo, J. B. Neaton, *J. Phys. Chem. Lett.* **2016**, *7*, 3683.
- [104] K. Frischwasser, I. Yulevich, V. Kleiner, E. Hasman, *Opt. Express* **2011**, *19*, 23475.
- [105] G. Bihlmayer, O. R. , R. Winkler, *New J. Phys.* **2015**, *17*, 050202.

- [106] K. V. Shanavas, S. Satpathy, *Phys. Rev. Lett.* **2014**, *112*, 086802.
- [107] H. Weng, X. Dai, Z. Fang, *MRS Bulletin* **2014**, *39*, 849.
- [108] L. Muechler, H. Zhang, S. Chadov, B. Yan, F. Casper, J. Kübler, S.-C. Zhang, C. Felser, *Angew. Chem. Int. Ed. Engl.* **2012**, *51*, 7221.
- [109] Q. Liu, X. Zhang, L. B. Abdalla, A. Fazzio, A. Zunger, *Nano Lett.* **2015**, *15*, 1222.
- [110] H. Steinberg, D. R. Gardner, Y. S. Lee, P. Jarillo-Herrero, *Nano Lett.* **2010**, *10*, 5032.
- [111] K. V. Mitrofanov, A. V. Kolobov, P. Fons, M. Krbal, J. Tominaga, T. Uruga, *J. Phys.: Condens. Matter* **2014**, *26*, 475502.
- [112] J. R. Schaibley, H. Yu, G. Clark, P. Rivera, J. S. Ross, K. L. Seyler, W. Yao, X. Xu, *Nat. Rev. Mater.* **2016**, *1*, 16055.
- [113] C. Jiang, F. Liu, J. Cuadra, Z. Huang, K. Li, A. Rasmita, A. Srivastava, Z. Liu, W.-B. Gao, *Nat. Commun.* **2017**, *8*, 802.
- [114] N. C. Gerhardt, M. R. Hoffmann, *Adv. Opt. Technol.* **2012**, *2012*, 268949.
- [115] H. Eschrig, K. Kikoin, V. Kohn, *Solid State Commun.* **1985**, *56*, 773.
- [116] T. W. Hollins, S. J. Clark, *Phys. Rev. B* **2012**, *85*, 235126.
- [117] A. Svane, N. E. Christensen, M. Cardona, A. N. Chantis, M. van Schilfgaarde, T. Kotani, *Phys. Rev. B* **2010**, *81*, 245120.
- [118] K. Hummer, A. Grüneis, G. Kresse, *Phys. Rev. B* **2007**, *75*, 195211.
- [119] J. Vidal, X. Zhang, L. Yu, J.-W. Luo, A. Zunger, *Phys. Rev. B* **2011**, *84*, 041109(R).
- [120] J. Kim, S.-H. Jhi, *Phys. Rev. B* **2015**, *92*, 125142.
- [121] E. O. Wrasse, T. M. Schmidt, *Nano Lett.* **2014**, *14*, 5717.

- [122] T. Kosugi, T. Miyake, S. Ishibashi, *J. Phys. Soc. Jpn.* **2011**, *80*, 074713.
- [123] S.-J. Gong, C.-G. Duan, Y. Zhu, Z.-Q. Zhu, J.-H. Chu, *Phys. Rev. B* **2013**, *87*, 035403.
- [124] K. Frohna, T. Deshpande, J. Harter, W. Peng, B. A. Barker, J. B. Neaton, S. G. Louie, O. M. Bakr, D. Hsieh, M. Bernardi, *Nat. Commun.* **2018**, *9*, 1829.
- [125] X. Che, B. Traore, C. Katan, M. Kepenekian, J. Even, *Phys. Chem. Chem. Phys.* **2018**, *20*, 9638.
- [126] S. Picozzi, *Front. Phys.* **2014**, *2*, 10.
- [127] L. Ponet, S. Artyukhin, *Phys. Rev. B* **2018**, *98*, 174102.
- [128] S. Eremeev, I. A. Nechaev, Y. M. Koroteev, P. M. Echenique, E. Chulkov, *Phys. Rev. Lett.* **2012**, *108*, 246802.
- [129] Z. Wu, S. Xu, H. Lu, A. Khamoshi, G.-B. Liu, T. Han, Y. Wu, J. Lin, G. Long, Y. He, Y. Cai, Y. Yao, F. Zhang, N. Wang, *Nat. Commun.* **2016**, *7*, 12955.
- [130] A. Kormányos, V. Zólyomi, N. D. Drummond, G. Burkard, *Phys. Rev. X* **2014**, *4*, 039901.
- [131] T. H. Hsieh, H. Lin, J. Liu, W. Duan, A. Bansil, L. Fu, *Nat. Commun.* **2012**, *3*, No. 982.
- [132] L. Tao, E. Y. Tsymbal, *Nat. Commun.* **2018**, *9*, 2763.
- [133] J. Clayden, N. Greeves, S. Warren, P. Wothers, *Organic Chemistry*; Oxford University Press: New York, 2011.
- [134] T. Eriksson, S. Björkman, P. Höglund, *Eur. J. Pharmacol.* **2001**, *57*, 365.
- [135] L. D. Barron, *Molecular Light Scattering and Optical Activity*; Cambridge University Press: Cambridge, 2009.

- [136] P. J. Stephens, *J. Phys. Chem.* **1985**, 89, 748.
- [137] P. S. Farago, *J. Phys. B: At. Mol. Phys.* **1980**, 13, L567.
- [138] P. S. Farago, *J. Phys. B: At. Mol. Phys.* **1981**, 14, L743.
- [139] R. Fandreyer, D. Thompson, K. Blum, *J. Phys. B: At., Mol. Opt. Phys.* **1990**, 23, 3031.
- [140] D. M. Campbell, P. S. Farago, *Nature* **1985**, 318, 52.
- [141] D. M. Campbell, P. S. Farago, *J. Phys. B: At. Mol. Phys.* **1987**, 20, 5133.
- [142] Z. Xie, T. Z. Markus, S. R. Cohen, Z. Vager, R. Gutierrez, R. Naaman, *Nano Lett.* **2011**, 11, 4652.
- [143] B. Göhler, V. Hamelbeck, T. Z. Markus, M. Kettner, G. F. Hanne, Z. Vager, R. Naaman, H. Zacharias, *Science* **2011**, 331, 894.
- [144] R. Naaman, D. H. Waldeck, *J. Phys. Chem. Lett.* **2012**, 3, 2178.
- [145] R. Naaman, D. H. Waldeck, *Annu. Rev. Phys. Chem.* **2015**, 66, 263.
- [146] M. Kettner, B. Göhler, H. Zacharias, D. Mishra, V. Kiran, R. Naaman, C. Fontanesi, D. H. Waldeck, S. Sęk, J. Pawłowski, J. Juhaniewicz, *J. Phys. Chem. C* **2015**, 119, 14542.
- [147] A. C. Aragonès, E. Medina, M. Ferrer-Huerta, N. Gimeno, M. Teixidó, J. L. Palma, N. Tao, J. M. Ugalde, E. Giralt, I. Díez-Pérez, V. Mujica, *Small* **2016**, 13, 1602519.
- [148] D. Mishra, T. Z. Markus, R. Naaman, M. Kettner, B. Göhler, H. Zacharias, N. Friedman, M. Sheves, C. Fontanesi, *PNAS* **2013**, 110, 14872.
- [149] V. Kiran, S. P. Mathew, S. R. Cohen, I. H. Delgado, J. Lacour, R. Naaman, *Adv. Mater.* **2016**, 28, 1957.

- [150] P. C. Mondal, N. Kantor-Uriel, S. P. Mathew, F. Tassinari, C. Fontanesi, R. Naaman, *Adv. Mater.* **2015**, *27*, 1924.
- [151] M. Kettner, V. V. Maslyuk, D. Nürenberg, J. Seibel, R. Gutierrez, G. Cuniberti, K.-H. Ernst, H. Zacharias, *J. Phys. Chem. Lett.* **2018**, *9*, 2025.
- [152] P. C. Mondal, C. Fontanesi, D. H. Waldeck, R. Naaman, *Acc. Chem. Res.* **2016**, *49*, 2560.
- [153] P. Roy, N. Kantor-Uriel, D. Mishra, S. Dutta, N. Friedman, M. Sheves, R. Naaman, *ACS Nano* **2016**, *10*, 4525.
- [154] J. I. Santos, I. Rivilla, F. P. Cossío, J. M. Matxain, M. Grzelczak, S. K. S. Mazinani, J. M. Ugalde, V. Mujica, *ACS Nano* **2018**, *12*, 11426.
- [155] K. S. Kumar, N. Kantor-Uriel, S. P. Mathew, R. Guliamov, R. Naaman, *Phys. Chem. Chem. Phys.* **2013**, *15*, 18357.
- [156] V. Kiran, S. R. Cohen, R. Naaman, *J. Chem. Phys.* **2017**, *146*, 092302.
- [157] O. B. Dor, S. Yochelis, S. P. Mathew, R. Naaman, Y. Paltiel, *Nat. Commun.* **2013**, *4*, 2256.
- [158] K. Michaeli, V. Varade, R. Naaman, D. H. Waldeck, *J. Phys.: Condens. Matter* **2017**, *29*, 103002.
- [159] V. Varade, T. Markus, K. Vankayala, N. Friedman, M. Sheves, D. H. Waldeck, R. Naaman, *Phys. Chem. Chem. Phys.* **2018**, *20*, 1091.
- [160] H. Al-Bustami, G. Koplovitz, D. Primc, S. Yochelis, E. Capua, D. Porath, R. Naaman, Y. Paltiel, *Small* **2018**, *14*, 1801249.
- [161] C. Fontanesi, E. Capua, Y. Paltiel, D. H. Waldeck, R. Naaman, *Adv. Mater.* **2018**, *30*, 1707390.

- [162] K. Banerjee-Ghosh, O. B. Dor, F. Tassinari, E. Capua, S. Yochelis, A. Capua, S.-H. Yang, S. S. P. Parkin, S. Sarkar, L. Kronik, L. T. Baczewski, R. Naaman, Y. Paltiel, *Science* **2018**, *360*, 1331.
- [163] K. B. Ghosh, W. Zhang, F. Tassinari, Y. Mastai, O. Lidor-Shalev, R. Naaman, P. Möllers, D. Nürenberg, H. Zacharias, J. Wei, E. Wierzbinski, D. H. Waldeck, *J. Phys. Chem. C* **2019**, *123*, 3024.
- [164] W. Zhang, K. Banerjee-Ghosh, F. Tassinari, R. Naaman, *ACS Energy Lett.* **2018**, *3*, 2308.
- [165] K. Michaeli, N. Kantor-Uriel, R. Naaman, D. H. Waldeck, *Chem. Soc. Rev.* **2016**, *45*, 6478.
- [166] V. V. Maslyuk, R. Gutierrez, A. Dianat, V. Mujica, G. Cuniberti, *J. Phys. Chem. Lett.* **2018**, *9*, 5453.
- [167] S. Yeganeh, M. A. Ratner, E. Medina, V. Mujica, *J. Chem. Phys.* **2009**, *131*, 014707.
- [168] E. Medina, F. López, M. A. Ratner, V. Mujica, *EPL* **2012**, *99*, 17006.
- [169] R. A. Rosenberg, J. M. Symonds, V. Kalyanaraman, T. Markus, T. M. Orlando, R. Naaman, E. A. Medina, F. A. López, V. Mujica, *J. Phys. Chem. C* **2013**, *117*, 22307.
- [170] S. Varela, E. Medina, F. López, V. Mujica, *J. Phys.: Condens. Matter* **2014**, *26*, 015008.
- [171] R. Gutierrez, E. Díaz, R. Naaman, G. Cuniberti, *Phys. Rev. B* **2012**, *85*, 081404(R).
- [172] R. Gutierrez, E. Díaz, C. Gaul, T. Brumme, F. Domínguez-Adame, G. Cuniberti, *J. Phys. Chem. C* **2013**, *117*, 22276.
- [173] A.-M. Guo, Q.-F. Sun, *Phys. Rev. Lett.* **2012**, *108*, 218102.

- [174] A.-M. Guo, Q.-F. Sun, *Phys. Rev. B* **2012**, *86*, 115441.
- [175] A.-M. Guo, Q.-F. Sun, *Phys. Rev. B* **2012**, *86*, 035424.
- [176] A.-M. Guo, E. Díaz, C. Gaul, R. Gutierrez, F. Domínguez-Adame, G. Cuniberti, Q.-F. Sun, *Phys. Rev. B* **2014**, *89*, 205434.
- [177] A.-M. Guo, Q.-F. Sun, *PNAS* **2014**, *111*, 11658.
- [178] T.-R. Pan, A.-M. Guo, Q.-F. Sun, *Phys. Rev. B* **2016**, *94*, 235448.
- [179] S. Matityahu, Y. Utsumi, A. Aharony, O. Entin-Wohlman, C. A. Balseiro, *Phys. Rev. B* **2016**, *93*, 075407.
- [180] E. Medina, L. A. González-Arraga, D. Finkelstein-Shapiro, B. Berche, V. Mujica, *J. Chem. Phys.* **2015**, *142*, 194308.
- [181] S. Varela, V. Mujica, E. Medina, *Phys. Rev. B* **2016**, *93*, 155436.
- [182] S. Varela, V. Mujica, E. Medina, *arXiv:1710.07204* **2017**.
- [183] K. Michaeli, R. Naaman, *arXiv:1512.03435* **2015**.
- [184] J. Gersten, K. Kaasbjerg, A. Nitzan, *J. Chem. Phys.* **2013**, *139*, 114111.
- [185] J. M. Soler, E. Artacho, J. D. Gale, A. García, J. Junquera, P. Ordejón, D. Sánchez-Portal, *Journal of Physics: Condensed Matter* **2002**, *14*, 2745.
- [186] P. Giannozzi, *et al. J. Phys.: Condens. Matter* **2009**, *21*, 395502.
- [187] P. Giannozzi, *et al. J. Phys.: Condens. Matter* **2017**, *29*, 465901.
- [188] <http://www.openmx-square.org/>.
- [189] S. Bhattacharya, A. Akande, S. Sanvito, *Chem. Commun.* **2014**, *50*, 6626.
- [190] J. Wilhelm, M. Walz, F. Evers, *Phys. Rev. B* **2015**, *92*, 014405.

- [191] E. Díaz, F. Domínguez-Adame, R. Gutierrez, G. Cuniberti, V. Mujica, *J. Phys. Chem. Lett.* **2018**, *9*, 5753.
- [192] G. Penazzi, A. Pecchia, V. Gupta, T. Frauenheim, *J. Phys. Chem. C* **2016**, *120*, 16383.
- [193] <http://www.netlib.org/blas/>.
- [194] <http://www.netlib.org/lapack/>.
- [195] M. Deffner, L. Groß, T. Steenbock, B. A. Voigt, G. C. Solomon, C. Herrmann, “Artaios – a code for postprocessing quantum chemical electronic structure calculations, available from <https://www.chemie.uni-hamburg.de/ac/herrmann/software/index.html>”, (2008-2017).
- [196] C. J. O. Verziyl, J. S. Seldenthuis, J. M. Thijssen, *J. Chem. Phys.* **2013**, *138*, 094102.
- [197] Y. Jiang, X. Lu, F. Zhai, *arXiv:1310.3733v2* **2013**.
- [198] D. Peng, N. Middendorf, F. Weigend, M. Reiher, *J. Chem. Phys.* **2013**, *138*, 184105.
- [199] R. D. Mattuck, *A Guide to Feynman Diagrams in the Many-Body Problem*; Dover Publications Inc.: New York, 1992.
- [200] T.-T. Lu, S.-H. Shiou, *Comput. Math. Appl.* **2002**, *43*, 119.
- [201] A. López, L. Colmenárez, M. Peralta, F. Mireles, E. Medina, *Phys. Rev. B* **2019**, *99*, 085411.
- [202] D. Marchenko, A. Varykhalov, M. R. Scholz, G. Bihlmayer, E. I. Rashba, A. Rybkin, A. M. Shikin, O. Rader, *Nat. Commun.* **2012**, *3*, 1232.
- [203] F. Tassinari, D. R. Jayarathna, N. Kantor-Uriel, K. L. Davis, V. Varade, C. Achim, R. Naaman, *Adv. Mater.* **2018**, *30*, 1706423.

- [204] P. C. Mondal, C. Fontanesi, D. H. Waldeck, R. Naaman, *ACS Nano* **2015**, *9*, 3377.
- [205] M. Eckshtain-Levi, E. Capua, S. Refaely-Abramson, S. Sarkar, Y. Gavrilov, S. P. Mathew, Y. Paltiel, Y. Levy, L. Kronik, R. Naaman, *Nat. Commun.* **2016**, *7*, 10744.
- [206] K. Toyoda, I. Hamada, K. Lee, S. Yanagisawa, Y. Morikawa, *J. Chem. Phys.* **2010**, *132*, 134703.
- [207] T. Frederiksen, M. Paulsson, M. Brandbyge, A.-P. Jauho, *Phys. Rev. B* **2007**, *75*, 205413.
- [208] D. E. López-Pérez, G. Revilla-López, D. Jacquemin, D. Zanuy, B. Palys, S. Sek, C. Alemán, *Phys. Chem. Chem. Phys.* **2012**, *14*, 10332.
- [209] S. Sek, K. Swiatek, A. Misicka, *J. Phys. Chem. B* **2005**, *109*, 23121.
- [210] R. A. Malak, Z. Gao, J. F. Wishart, S. S. Isied, *J. Am. Chem. Soc.* **2004**, *126*, 13888.
- [211] L. A. Zotti, J. C. Cuevas, *ACS Omega* **2018**, *3*, 3778.
- [212] M. Walz, A. Bagrets, F. Evers, *J. Chem. Theory Comput.* **2015**, *11*, 5161.
- [213] DIRAC, a relativistic ab initio electronic structure program, Release DIRAC18 (2018), written by T. Saue, L. Visscher, H. J. Aa. Jensen, and R. Bast, with contributions from V. Bakken, K. G. Dyall, S. Dubillard, U. Ekström, E. Eliav, T. Enevoldsen, E. Faßhauer, T. Fleig, O. Fossgaard, A. S. P. Gomes, E. D. Hedegård, T. Helgaker, J. Henriksson, M. Iliaš, Ch. R. Jacob, S. Knecht, S. Komorovský, O. Kullie, J. K. Lærdahl, C. V. Larsen, Y. S. Lee, H. S. Nataraj, M. K. Nayak, P. Norman, G. Olejniczak, J. Olsen, J. M. H. Olsen, Y. C. Park, J. K. Pedersen, M. Pernpointner, R. di Remigio, K. Ruud, P. Sałek, B. Schimmelpennig, A. Shee, J. Sikkema, A. J. Thorvaldsen, J. Thyssen, J. van Stralen, S. Villaume, O. Visser, T. Winther, and S. Yamamoto (available at <https://doi.org/10.5281/zenodo.2253986>, see also <http://www.diracprogram.org>).

- [214] “TURBOMOLE V7.0, a development of University of Karlsruhe and Forschungszentrum Karlsruhe GmbH, 1989-2007, TURBOMOLE GmbH, since 2015; available from <http://www.turbomole.com>.”, 2016.
- [215] R. Ahlrichs, M. Bär, M. Häser, H. Horn, C. Kölmel, *Chem. Phys. Lett.* **1989**, *162*, 165.
- [216] O. Treutler, R. Ahlrichs, *J. Chem. Phys.* **1995**, *102*, 346.
- [217] M. von Arnim, R. Ahlrichs, *J. Comput. Chem.* **1998**, *19*, 1746.
- [218] “TURBOMOLE V7.1, a development of University of Karlsruhe and Forschungszentrum Karlsruhe GmbH, 1989-2007, TURBOMOLE GmbH, since 2007; available from <http://www.turbomole.com>.”, 2016.
- [219] E. J. Baerends, *et al.* “ADF2014, SCM, Theoretical Chemistry, Vrije Universiteit, Amsterdam, The Netherlands, <https://www.scm.com>”.
- [220] G. te Velde, F. M. Bickelhaupt, E. J. Baerends, C. Fonseca Guerra, S. J. A. van Gisbergen, J. G. Snijders, T. Ziegler, *J. Comput. Chem.* **2001**, *22*, 931.
- [221] C. Fonseca Guerra, J. G. Snijders, G. te Velde, E. J. Baerends, *Theor. Chem. Acc.* **1998**, *99*, 391.
- [222] M. J. Frisch, *et al.* “Gaussian 09 (Gaussian, Inc., Wallingford CT, 2009)”.
- [223] T. H. Dunning Jr., P. J. Hay, Modern Theoretical Chemistry. In , Vol. 3; H. F. Schaefer III, (Ed.), New York, 1977.
- [224] P. J. Hay, W. R. Wadt, *J. Chem. Phys.* **1985**, *82*, 270.
- [225] W. R. Wadt, P. J. Hay, *J. Chem. Phys.* **1985**, *82*, 284.
- [226] P. J. Hay, W. R. Wadt, *J. Chem. Phys.* **1985**, *82*, 299.
- [227] F. Weigend, R. Ahlrichs, *Phys. Chem. Chem. Phys.* **2005**, *7*, 3297.

- [228] F. Weigend, *Phys. Chem. Chem. Phys.* **2006**, *8*, 1057.
- [229] P. Pollak, F. Weigend, *J. Chem. Theory Comput.* **2017**, *13*, 3696.
- [230] E. Van Lenthe, E. J. Baerends, *J. Comput. Chem.* **2003**, *24*, 1142.
- [231] J. P. Perdew, *Phys. Rev. B* **1986**, *33*, 8822.
- [232] A. D. Becke, *Phys. Rev. A* **1988**, *38*, 3098.
- [233] J. P. Perdew, K. Burke, M. Ernzerhof, *Phys. Rev. Lett.* **1996**, *77*, 3865.
- [234] J. P. Perdew, K. Burke, M. Ernzerhof, *Phys. Rev. Lett.* **1997**, *78*, 1396.
- [235] C. Lee, W. Yang, R. G. Parr, *Phys. Rev. B* **1988**, *37*, 785.
- [236] A. D. Becke, *J. Chem. Phys.* **1993**, *98*, 5648.
- [237] S. Grimme, J. Antony, S. Ehrlich, H. Krieg, *J. Chem. Phys.* **2010**, *132*, 154104.
- [238] S. Grimme, S. Ehrlich, L. Goerigk, *J. Comput. Chem.* **2011**, *32*, 1456.
- [239] V. Barone, M. Casarin, D. Forrer, M. Pavone, M. Sambi, A. Vittadini, *J. Comput. Chem.* **2009**, *30*, 934.
- [240] S. Grimme, *J. Comput. Chem.* **2006**, *27*, 1787.
- [241] K. G. Dyall, *J. Chem. Phys.* **1997**, *106*, 9618.
- [242] W. Kutzelnigg, W. Liu, *J. Chem. Phys.* **2005**, *123*, 241102.
- [243] E. van Lenthe, E. J. Baerends, J. G. Snijders, *J. Chem. Phys.* **1993**, *99*, 4597.
- [244] E. van Lenthe, A. Ehlers, E.-J. Baerends, *J. Chem. Phys.* **1999**, *110*, 8943.
- [245] E. van Lenthe, J. G. Snijders, E. J. Baerends, *J. Chem. Phys.* **1996**, *105*, 6505.
- [246] E. van Lenthe, R. van Leeuwen, E. J. Baerends, J. G. Snijders, *Int. J. Quantum Chem.* **1996**, *57*, 281.

- [247] P. E. Blöchl, *Phys. Rev. B* **1994**, *50*, 17953.
- [248] A. Dal Corso, *Comput. Mater. Sci.* **2014**, *95*, 337.
- [249] K. Eichkorn, O. Treutler, H. Öhm, M. Häser, R. Ahlrichs, *Chem. Phys. Lett.* **1995**, *240*, 283.
- [250] K. Eichkorn, F. Weigend, O. Treutler, R. Ahlrichs, *Theor. Chem. Acc.* **1997**, *97*, 119.

### **Declaration on Oath**

I hereby declare, on oath, that I have written the present dissertation by my own and have not used other than the mentioned source materials and aids. The written version submitted corresponds to the one on the electronic storage medium. I hereby declare that I have not previously applied or pursued for a doctorate (Ph.D. studies) with this thesis.

Hiermit versichere ich an Eides statt, die vorliegende Dissertation selbst verfasst und keine anderen als die angegebenen Hilfsmittel benutzt zu haben. Die eingereichte schriftliche Fassung entspricht der auf dem elektronischen Speichermedium. Ich versichere, dass diese Dissertation nicht in einem früheren Promotionsverfahren eingereicht wurde.

Hamburg, September 4, 2019

---

Martin Sebastian Zöllner